
# Pt and Pt-Pd cluster interaction with graphene and $TiO_2$ based supports: A DFT study

By

**Molefi Matsutsu**

Thesis presented to the University of Cape Town

in fulfilment of the requirements

for the degree of

Doctor of Philosophy

Centre for Catalysis Research

Department of Chemical Engineering

University of Cape Town

November 2016

# Acknowledgments

First and for most I would like to thank God the almighty Father for having guided, protected and given me the courage to pursue the long academic journey from beginning to end.

My sincere appreciation goes to my supervisor Professor Eric van Steen who has provided me with guidance and encouragement throughout my entire postgraduate journey. Thanks for introducing me to the field of molecular modelling which I had not heard of before I commenced my postgraduate studies. It would be amiss of me if I would not express my appreciation to my co-supervisor Dr. Melissa Petersen for her assistance and explanations on how things work in VASP, guidance and for her scientific rigorousness. I will surely miss the Thursday afternoon molecular modelling meetings.

I am indebted to HySA Catalysis for funding my studies, without their funding this dream would not have been achieved. I would also like to express my sincere appreciation to Dr. Pieter Levecque who provided funding for me to present my work at an international conference in Germany, thank you for the experience. Without computational resources this work would not have been possible, in this regard access to computational resources from the University of Cape Town High Performance Computing (UCT-HPC), the Centre for High Performance Computing (CHPC) at the CSIR and our local departmental cluster (chimera) are highly appreciated. A big thank you goes to Graham Inggs the system administrator of chimera for assistance with my many request and allowing me to run sun calculations on the new mech-eng node. Thanks to the various administrators who assisted with my requests at the CHPC and to Andrew Lewis of UCT-HPC for assistance.

I would like to thank my mother Mrs. ‘Mamatsutsu Matsutsu for the encouragement and also keeping in contact with me to check how my studies are going. Thanks for always saying a prayer each time I left home for Cape Town, the prayers kept me going. Special appreciation goes to my brother (Matsutsu Matsutsu), sister (‘Mamosebetsi Matsutsu), nephew (Kefuoe Matsutsu) and niece (Keletso Matsutsu) for always encouraging me. Special mention goes to my grandmother Mrs. ‘Mangoejane Molaoa for always encouraging me and saying a prayer for me each time I left home for Cape Town, the prayers have been my pillar of strength during tough moments.

Lastly I would like to thank my friends who have always been there to cheer me on during this long marathon. I have too many friends to mention all of them here but will mention a few of them, Lusani, Ts'epo, Mali Manono, Sakhile, Jafaru, Ben, Motlokoa, Avela, Malebelo, Thuli, Lere, Moeketsi aka Kakana, Monyakane, Ramonate, Chakala, Ts'epang, Mopeli, Malunga and many more. Special mention to my country men whom we shared lunch with and occasionally discussed science during lunch meetings, Gerard aka Tapole and Lebohang. Special mention also goes to Thobani Gambu, my fellow molecular modelling colleague for his generous assistance with my many requests.

# Plagiarism declaration

**Declaration**

I, **Molefi Matsutsu** , hereby declare that the work on which this thesis is based is my original work (except where acknowledgements indicate otherwise) and that neither the whole work nor part of it has been, is being, or is to be submitted for another degree in this or any university. I authorise the University to reproduce for the purpose of research either the whole or any portion of the contents in any manner whatsoever.

Signature …… Signature removed …….. Date……23 November 2016…….

# Abstract

Density functional theory (DFT) calculations have been performed to gain insight into the role of defects present on the surface of graphene and $TiO_2$ based supports on supported metal clusters. The clusters considered are a $Pt_{38}$ cluster and a bimetallic $Pt_{32}Pd_6$ alloy. The defects considered on graphene based supports are monovacancy defective graphene, OH and COOH functionalised graphene. The defects considered on $TiO_2$ based supports are a partially reduced $TiO_2$(110) surface with a surface oxygen bridge vacancy and hydroxylated $TiO_2$(110) surface with surface OH groups. The defect free graphene and $TiO_2$ surfaces were also considered.

For both the $Pt_{38}$ and $Pt_{32}Pd_6$ cluster, and on both defect containing graphene and $TiO_2$ (except on hydroxylated $TiO_2$(110) surface) the binding of the clusters is enhanced relative to binding on the defect free supports. Enhanced binding at the defects imply that the clusters are bound strongly to the support and thus less likely to detach from the support material relative to binding on the defect free supports. Therefore, the defects may improve the durability of the catalyst by limiting particle detachment.

The electronic properties of the cluster are modified differently depending on the identity of the defect present on the support. On the graphene based supports, OH functionalisation is expected to result in weaker binding energy of adsorbate molecules, whereas COOH functionalisation is expected to result in stronger binding energy of adsorbates for the supported $Pt_{38}$ cluster. This is due to different shifts in d-band centre of the facets on the cluster supported on these supports. Therefore, it can be expected that the $Pt_{38}$ cluster supported on OH functionalised graphene will be more tolerant to poison molecules. This is due to reduced binding strength of adsorbates on OH functionalised graphene compared to adsorption on COOH functionalised graphene. For the $Pt_{32}Pd_6$ cluster the OH and COOH functional groups do not appreciably modify the d-band centre of the facets available to reactants, and thus is expected not to significantly modify the binding strength of adsorbate molecules relative to binding on the free unsupported $Pt_{32}Pd_6$ cluster.

The binding energy of adsorbate molecules on the $Pt_{38}$ cluster supported on defect containing $TiO_2$ is expected to be stronger than on the $Pt_{38}$ cluster supported on defective graphene

based supports, due to higher extent of upward shift of the d-band centre of the exposed facets. The enhanced binding energy of adsorbates on the $Pt_{38}$ cluster supported on $TiO_2$ supports may be detrimental to catalyst durability and activity. This can be due to strong binding of poison molecules and reaction intermediates which maybe too strongly bound on the surface such that they cannot participate in further reaction steps. Overall it might turn out that the functionalised graphene based supports are better support materials over the $TiO_2$ based materials for particular reactions.

The Nb-doped partially reduced $TiO_2$(110) surface attaches the $Pt_{32}Pd_6$ cluster strongly to the support compared to the functionalised graphene supports. Furthermore, the binding energy of adsorbate molecules is expected to be weaker on the $Pt_{32}Pd_6$ cluster supported on the Nb-doped partially reduced $TiO_2$(110) surface compared to the functionalised graphene supports. This might be beneficial as poison molecules may be weakly bound to the cluster resulting in high resistance to poisoning which can also have a positive effect on catalyst activity.

In addition to enhancing binding of the cluster to the support and affecting the binding energy of adsorbates on the supported clusters, some of the defects can also alter the ordering pattern of Pd and Pt atoms within the $Pt_{32}Pd_6$ cluster. OH functionalised graphene and Nb-doped partially reduced $TiO_2$(110) surface result in segregation of Pd towards the cluster-support interface, thereby exposing more Pt atoms at the surface facets of the cluster. The modified arrangement of Pt and Pd atoms may result in modification of the reactivity of the $Pt_{32}Pd_6$ cluster.

The results of this study indicate that the defects can play a vital role in determining the activity and durability of the catalyst. By having the right combination of defects on the support material, the durability and catalytic activity of the catalyst can be fine-tuned simultaneously. This can lead to better design of catalysts.

# Table of Contents

# List of Figures

# List of Tables

# Chapter 1: Introduction

## 1.1 Background

Late transition metals Pt and Pd are used as catalysts for a variety of processes such as hydrocarbon reforming (Yu et al., 2012), electrocatalysts for application in polymer electrolyte fuel cells (PEFCs) (Marković et al., 2001), photocatalysts (Campbell, 2012), for pollution control in car exhaust for the reduction of $NO_x$ (Chen et al., 2012) and many other applications. Pt and Pd catalysts are used as solid catalysts in the form of nanoparticles. Nanoparticles are attractive due to their high surface area to volume ratio resulting in high catalytic activity in particular for particle size dependent reactions (Lee et al., 2010). However, nanoparticles are inherently unstable due to their high surface energy, this results in a large driving force to sinter and thereby minimising their surface energy (Fortunelli & Barcaro, 2012). To stabilise and minimise coalescing, nanoparticles are often supported on materials, such as carbon or transition metal oxides. It has been observed that support materials do not only act as an inert material to disperse the active material but can also influence the catalytic activity of the active material (Haro et al., 1976; Juszczyk et al., 1995; Goodman, 1995; Kesavana et al., 2011; Campbell, 2012; Edwards et al., 2014; Willinger et al., 2014). The type of support used for a particular reaction can also have an effect on the activity of the active metal, Edwards et al. (2014) observed the activity for the Pd-Au bimetallic catalyst for the reaction of $H_2O_2$ production to follow the order C > $TiO_2$ > $Al_2O_3$ with respect to the support.

Kaneeda et al. (2009) observed a higher activity and resistance to poisoning of the Pd-Pt/$Al_2O_3$ catalyst for the reduction of $NO_x$ relative to the Pd/$Al_2O_3$ and Pt/$Al_2O_3$ catalysts. Kakade et al. (2013) and Zhang et al. (2004) observed higher activity and durability of the Pd-Pt/C catalyst over the Pt/C and Pd/C for the oxygen reduction reaction in polymer electrolyte fuel cells. The improved activity of the Pd-Pt bimetallic system over the pure Pd and Pt catalysts is subject to debate with a variety of explanations being proposed depending on the reaction being considered. Rousset et al. (2001) suggested that there is no synergistic effect in the Pd-Pt/$Al_2O_3$ system as catalyst for toluene hydrogenation and the activity of the bimetallic system is just the addition of the activity of the individual pure elements. Other suggestions are that the improved activity of the Pd-Pt/$Al_2O_3$ system as catalyst for the dehydrogenation of cyclohexane is due to the preference of the Pd atoms to occupy the metal-support interface (Haro et al., 1976). It has also been proposed that the higher activity of the Pd-Pt/C alloy

catalyst relative to the pure elements used as oxygen reduction reaction catalyst in PEFCs is due to the electronic and structural modification of Pt upon alloying (Lopes et al., 2008).

## 1.2 Carbon supports

Carbon based support materials are amongst the most commonly used support materials owing to their relatively low cost, availability, light weight and ease of depositing metals (Burgess et al., 2015). Some of the preparation techniques for carbon supported nanoparticles involve a pretreatment step of the carbon support with acid e.g. HCl and $HNO_3$ or $H_2O_2$ prior to metal deposition (Prado-Burguete et al., 1989; Edwards et al., 2014; Burgess et al., 2015). The oxidation pretreatment steps using $HNO_3$ and $H_2O_2$ result in the formation of functional groups containing oxygen in the surface of the carbon support. The series of papers about oxygen on acid washed carbon indicating the presence of oxygen surface functional groups observed through a variety of techniques, includes XPS (Burgess et al., 2015), infra-red spectroscopy (Prado-Burguete et al., 1989), near edge X-ray absorption fine structure spectroscopy (NEXAFS) (Kuznetsova et al., 2001) and absorption X-ray spectroscopy (XAS) (Coleman et al., 2008). The type of oxygen containing surface functional groups identified on carbon supports upon acid or $H_2O_2$ treatment include carboxylic acid group –COOH, hydroxyl –OH, carbonyl –C=O group and C-O group (Prado-Burguete et al., 1989; Burgess et al., 2015). The pretreatment of carbon based support materials is thought to result in defects, which may be in the form of atomic vacancies to which the surface oxygen functional groups are attached to (Schniepp et al., 2006; Burgess et al., 2015). The functional groups containing oxygen on the surface have been observed to result in higher dispersion of the active material deposited onto the surface of the carbon support (Prado-Burguete et al., 1989; Edwards et al., 2014; Burgess et al., 2015).

Prado-Burguete et al. (1989) proposed that the order of importance of the oxygen surface groups in determining a well dispersed catalyst can be arranged in order of decreasing acidity; the carboxylic acid group –COOH is representative of the most acidic group and the most important one for attaining good dispersion and the phenolic –OH group representing the least acidic groups. The carbonyl group (-C=O) and the ether group (-C-O) were found not to play a dominant role in determining dispersion of the catalyst. These functional groups containing oxygen have been postulated to be the anchoring sites for metals (Prado-Burguete et al., 1989; Burgess et al., 2015). Recently it has been observed by Burgess et al. (2015) that for highly oriented pyrolytic graphite (HOPG) mildly treated with $HNO_3$, the dominant oxygen surface functional group is the OH group and gold nanoparticles were located around the OH

functional group on this treated HOPG. Edwards et al. (2014) also observed that the activity for the production of $H_2O_2$ on Pd-Au bimetallic catalyst supported on acid pretreated carbon is higher than the activity on the untreated carbon support. It was concluded that the pretreatment acid wash step is not only to remove contaminants on the support but also has an effect on the activity of the catalyst.

Density functional theory (DFT) calculations performed by Burgess et al. (2015) indicated that the binding energy of a Au atom on OH functionalised HOPG is more exothermic than the binding energy on pristine HOPG. The higher binding on OH functionalised HOPG was considered to be indication that the Au atom will be preferentially anchored at the oxygen functionalised sites not on the pristine sites of HOPG. The OH functionalised HOPG was modelled as a bilayer graphene with zig zag edges functionalised with OH.

## 1.3 Metal oxide supports

The activity of metallic and bimetallic nanoparticles supported on transition metal oxides can be affected by the support material. The interaction between the metal oxide support and the active metal is expected to alter both the electronic properties of the catalytically active material and the morphology. In the case of bimetallic particles, the segregation pattern can be affected as well (Koningsberger & Gates, 1992). The interaction between metal particles and the oxide support can be unusually strong, leading to what has classically been termed as strong metal-support interaction (SMSI). This has traditionally been linked to the detrimental effect of the metal support interaction, e.g. when the $TiO_2$ support migrate over the metal particles thereby blocking the active sites (Tauster, 1987). However, the effect of the strong metal-support interaction is not only linked to negative effects, but can also have a positive effect on the activity of the supported active material. Through a combined experimental and DFT study, Bruix et al. (2012) were able to show that the activity of Pt supported on $CeO_2$ and of Pt supported on $CeO_2$ mixed with nanoparticles of $TiO_2$ was high for the dissociation of water. From DFT calculations, the strong chemical bonds between a $Pt_8$ cluster and the $CeO_2$ support resulted in electronic perturbation of the electronic structure of the $Pt_8$ cluster. The electronic perturbation of the $Pt_8$ cluster facilitated dissociation of water on the supported cluster. The electronic perturbation of the electronic structure of the supported $Pt_8$ cluster has been termed the electronic metal-support interaction (EMSI) (Campbell, 2012).

Transition metal alloy particles supported on metal oxide supports have been observed to undergo preferential segregation of one of the alloy components towards the metal-support

interface, a few examples of such cases will be briefly highlighted. Preferential segregation of Pd towards the metal-support interface and the formation of palladium silicites from Pd-Au/$SiO_2$ has been suggested to occur by Juszczyk et al. (1995). Preferential segregation of Co leading to the formation of CoO as the stable cobalt phase preventing the formation of surface Pt-O-Al bonds has been suggested to occur for the Pt-Co/$Al_2O_3$ catalyst (*Zsoldos* et al., 1996). Furthermore, competition between Pd and Pt to occupy oxidizing centres of the alumina support during reduction has been postulated. Pd is proposed to migrate and occupy the oxidising centres of the alumina surface for the Pd-Pt/$Al_2O_3$ catalyst (Haro et al., 1976). Using DFT studies Han et al. (2012) observed preferential segregation of Pd towards the cluster-support-interface, exposing Ag on the surface of a 5 atom $Ag_nPd_m$ cluster supported on anatase $TiO_2$(101) surface.

Freund (2002) indicated that anchoring sites for metal particles on metal oxide surfaces are defects on the surface; the defects can include surface oxygen monovacancy, surface oxygen divacancy, steps, kinks and corners. Diebold et al. (2010) and Matthey et al. (2007) have indicated that the surface oxygen vacancies on $TiO_2$ are highly reactive towards the dissociation of water. Therefore, some of the surface oxygen vacancies can be occupied by OH groups from the dissociation of water. Little knowledge from fundamental DFT studies exists on the role of surface OH groups on the surface of the $TiO_2$ support in relation to binding of monometallic and bimetallic nanoparticles to the support.

From the summarised background on carbon supports discussed above, the presence of surface oxygen functional groups has been identified and proposed to be the anchoring site for metal deposition on the support. However, knowledge on the two most important surface oxygen functional groups, i.e. OH and COOH groups on binding of metal nanoparticles and the effect on the reactivity of the supported nanoparticles is lacking. In addition, for the case of supported bimetallic nanoparticles the effect of the surface oxygen functional groups on the segregation pattern of the supported bimetallic nanoparticles, and the resulting effect on the reactivity of the supported bimetallic nanoparticles is still lacking.

For supported nanoparticles on $TiO_2$, the role of the surface oxygen vacancy and the presence of surface OH groups on the attachment of metal nanoparticles is not well understood. The effect of the surface composition (i.e. identity of defects) on the $TiO_2$ support on reactivity of supported nanoparticles is also not well understood. Moreover, DFT calculations have been limited to small cluster sizes to investigate ordering in bimetallic metal oxide supported nanoparticles. Most of the cluster sizes are around 5 atoms and the cluster morphologies considered are different to those of a real catalyst particle. Hence there is a need to consider

larger cluster sizes which have morphology close to that of the real catalyst in order to investigate the ordering arrangement of the bimetallic cluster supported on $TiO_2$ based supports.

## 1.4 Aims and Objectives

The aim of the present study is to obtain through DFT calculations a fundamental understanding of the role of OH and COOH presence on the surface of a carbon based support on the binding of a Pt and Pt-Pd cluster. The study seeks to understand the effect of the presence of OH or COOH on the electronic properties of the supported clusters (Pt and Pt-Pd). Furthermore, the role of OH and COOH on the segregation pattern of the supported Pt-Pd bimetallic nanocluster will be explored. The model for the carbon based support will be a single graphene sheet, presence of the OH group will be modelled as a single OH group attached to the graphene sheet and similarly the COOH group presence will be modelled as a single COOH group attached to the graphene sheet. Monometallic Pt nanoparticle will be modelled as a $Pt_{38}$ truncated octahedron cluster and the Pt-Pd bimetallic nanoparticle will be modelled as a $Pt_{32}Pd_6$ truncated octahedron cluster.

The study further seeks to gain insight into the binding of a monometallic and bimetallic nanoparticle on a pristine $TiO_2$ support surface, partially reduced surface with a surface oxygen vacancy and the presence of hydroxyl groups on the surface of $TiO_2$. The rutile $TiO_2$(110) surface will be considered for the $TiO_2$ support. The $TiO_2$ support is investigated since it is used in many catalytic processes owing to its good mechanical stability, and its resistance in both acidic and oxidative environments (Liu et al., 2005). Nb-doped rutile $TiO_2$(110) surface will also be studied as support for the Pt-Pd alloy cluster.

**Hypothesis 1**

The presence of the oxygen surface functional groups OH and COOH on graphene will lead to enhanced binding of the $Pt_{38}$ and $Pt_{32}Pd_6$ clusters on functionalised graphene relative to binding on pristine graphene. The enhanced binding on functionalised graphene is due to the surface oxygen functional groups modifying the electronic properties of the carbon atoms in the vicinity of the attached functional group, therefore leading to stronger binding of the clusters.

**Hypothesis 2**

The modified electronic properties of the carbon atoms in the vicinity of the surface oxygen functional group (i.e. OH and COOH) on functionalised graphene will lead to a different chemical ordering of the $Pt_{32}Pd_6$ cluster compared to the ordering in the unsupported $Pt_{32}Pd_6$ cluster. The preference of either Pt or Pd to bind to the support is expected to change the ordering in the $Pt_{32}Pd_6$ cluster supported on functionalised graphene.

**Hypothesis 3**

Pd will segregate towards the cluster-support interface when the $Pt_{32}Pd_6$ cluster is supported on Nb-doped $TiO_2$(110). Pd will preferentially segregate towards the cluster-support interface due to its higher affinity for oxygen compared to Pt. The segregation of Pd towards the cluster-support interface will result in less Pd being exposed on the surface of the $Pt_{32}Pd_6$ cluster.

# 1.5 References

Bruix, A., Rodriguez, J.A., Ramírez, P.J., Senanayake, S.D., Evans, J., Park, J.B., Stacchiola, D., Liu, P., Hrbek, J, & Illas, F. (2012) A new type of strong metal-support interaction and the production of $H_2$ through the transformation of water on Pt/$CeO_2$(111) and Pt/CeOx/$TiO_2$(110) catalysts. *J. Am. Chem. Soc.* **134**, 8968-8974.

Burgess, R., Buono, C., Davies, P.R., Davies, R.J., Legge, T., Lai, A., Lewis, R., Morgan, D.J. & Willock, D.J. (2015) The functionalisation of graphite surfaces with nitric acid: identification of functional groups and their effects on gold. *J. Catal.* **323**, 10-18.

Campbell, C.T. (2012) Electronic pertubations. *Nat. Chem.* **4**, 597-598.

Chen, J., Lim, B., Lee, E.P. & Xia, Y. (2009) Shape-controlled synthesis of platinum nanocrystals for catalytic and electrocatalytic applications. *Nano Today* **4**, 81-95.

Coleman, V.A., Knut, R., Karis, O., Grennberg, H., Jansson, U., Quinlan, R., Holloway, B.C., Sanyal, B. & Eriksson, O. (2008) Defect formation in graphene nanosheets by acid treatment: an x-ray absorption spectroscopy and density functional theory study. *J. Phys. D: Appl. Phys.* **41**, 062001-062004.

Diebold, U., Li, S.C. & Schmid, M. (2010) Oxide surface science. *Annu. Rev. Phys. Chem.* **61**, 129-148.

Edwards, K.K., Freakly, S.J., Carley, A.F., Kiely, C.J. & Hutchings, G.J. (2014) Strategies for designing supported gold-palladium bimetallic catalysts for the direct synthesis for hydrogen peroxide. *Acc. Chem. Res*. **473**, 845-854.

Freund, H.J. (2002) Clusters and islands on oxides: from catalysis via electronics and magnetism to optics. *Surf. Sci.* **500**, 271-299.

Goodman, D.W. (1995) Model studies in catalysis using surface science probes. *Chem. Rev*. **95**, 523-536.

Han, Y., Zhang, M., Li, W. & Zhang, J. (2012) Effect of $TiO_2$ support on the structural and electronic properties of $Pd_mAg_n$ clusters: a first-principles study. *Phys. Chem. Chem. Phys.* **14**, 8683-8692.

Haro, J., Gómez, R. & Ferreira, J.M. (1976) The role of palladium in dehydrogenation of cyclohexane over Pt-Pd/$Al_2O_3$ bimetallic catalysts. *J. Catal.* **45**, 326-331.

Juszczyk, W. Karpiński, Z., Łomot, D., Pielaszek, J. & Sobczak, J.W. (1995) Pd-Au/$SiO_2$: characterisation and catalytic activity. *J.Catal.* **151**, 67-76.

Kakade, B.A., Wang, H., Tamaki, T., Ohashi, H. & Yamaguchi, T. (2013) Enhanced oxygen reduction reaction by bimetallic CoPt and PdPt nanocrystals. *RCS Advances* **3**, 10487-10496.

Kaneeda, M., Iizuka, H., Hiratsuka, T., Shinotsuka, N. & Arai, M. (2009) Improvement of thermal stability of NO oxidation Pt/$Al_2O_3$ catalyst by addition of Pd. *Appl. Catal. B: Environment* **90**, 564-569.

Kesavan, I., Tiruvalam, R., Rahim, M.H.A., Saiman, M.I.B., Enache, D.I., Jenkins, R.L., Dimitratos, N., Lopez-Sanchez, J.A., Taylor, S.H., Knight, D.W., Kiely, C.J. & Hutchings, G.J. (2011) Solvent-free oxidation of primary carbon-hydrogen bonds in toluene using Au-Pd alloy nanoparticles. *Science* **331**, 195-1999.

Koningsberger, D.C. & Gates, B.C. (1992) Nature of metal-support interface in supported metal catalysts: results from X-ray absorption spectroscopy. *Catal. Lett.* **14**, 271-277.

Kuznetsova, A., Popova, I., Yates Jr., J.T., Bronikowski, M.J., Huffman, C.B., Liu, J., Smalley, R.E., Hwu, H.H. & Chen, J.G. (2001) Oxygen-containing functional groups on single-wall carbon nanotubes: NEXAFS and vibrational spectroscopic studies. *J. Am. Chem. Soc.* **123**, 10699-10704.

Lee, K., Kim, M. & Kim, H. (2010) Catalytic nanoparticles being facet-controlled. *J. Mater. Chem.* **20**, 3791-3798.

Lopes, T., Antolini, E.& Gonzalez, E.R. (2008) Carbon supported Pt-Pd alloy as an ethanol tolerant oxygen reduction electrocatalysts for direct ethanol fuel cells. *Int. J. Hydrogen Energy* **33**, 5563-5570.

Liu, Z., Zhang, J., Han, B., Du, J., Mu, T., Wang, Y. & Sun, Z. (2005) Solvothermal synthesis of mesoporous $Eu_2O_3$-$TiO_2$ composites. *Microporous Mesoporous Mater.* **81**, 169-174.

Marković, N.M., Schmidt, T.J., Stamenkovíc, V. & Ross, P.N. (2001) Oxygen reduction reaction on Pt and Pt bimetallic surfaces: a selective review. *Fuel Cells* **1**,105-116.

Matthey, D., Wang, J.G., Wendt, S., Matthiesen, J., Schaub, R., Laegsgaard, E., Hammer, B. & Besenbacher, F. (2007) Enhanced bonding of gold nanoparticles on oxidized $TiO_2$(110). *Science* **315**, 1692-1696.

Prado-Burguete, C., Linares-Solano, A., Rodríguez-Reinoso, F. & Salinas-Martinez De Lecea, C. (1989) The effect of oxygen surface groups of the support on platinum dispersion in Pt/carbon catalysts. *J. Catal.* **115**, 98-106.

Rousset, J.L., Stievano, L., Cadate Santos Aires, F.J., Geantet, C., Renouprez, A.J. & Pellarami, M. (2001) Hydrogenation of toluene over $\gamma$-$Al_2O_3$ supported Pt, Pd, and Pd-Pt model catalysts obtained by laser vaporization of bulk metals. *J. Catal.* **197**, 335-343.

Schniepp, H.C., Li, J., McAllister, M.J., Sai, H., Herrera-Alonso, M., Adamson, D.H., Prud'homme, R.K., Car, R., Saville, D.A. & Aksay, I.A. (2006) Functionalized single graphene sheets derived from splitting graphite oxide. *J. Phys. Chem. B* **110**, 8535-8539.

Tauster, S.J. (1987) Strong metal-support interactions. *Acc. Chem. Res*. **20**, 389-394.

Willinger, M.G., Zhang, W., Bondarchuk, O., Shaikhutdinov, S., Freund, H. & Schlögl, R. (2014) A case of strong metal-support interactions: combining advanced microscopy and model systems to elucidate the atomic structure of interfaces. *Angew. Chem. Int. Ed.* **53**, 5998-6001.

Yu, W., Porosoff, M.D. & Chen, J.C. (2012) Review of Pt-based catalysis: from model surfaces to supported catalysts. *Chem. Rev*. **112**, 5780-5817.

Zhang, J., Mo, Y., Vukmirovic, M.B., Klie, R., Sasaki, K. & Adzic, R.R. (2004) Platinum monolayer electrocatalysts for $O_2$ reduction: Pt monolayer on Pd(111) and on carbon-supported Pd nanoparticles. *J. Phys. Chem. B* **108**, 10955-10964.

Zsoldos, Z., Garin, F., Hilaire, L. & Guczi, L. (1996) Genesis of cobalt oxide-induced surface structure in $PtCo_x/Al_2O_3$ catalysts. *J. Mol. Catal. A: Chemical* **111**,113-122.

# Chapter 2: Computational Chemistry Methodology

## 2.1 Introduction

The most fundamental process in chemistry as well as in catalysis is the process of bond breaking and bond formation (Becke, 2014). The accurate description of bond breaking and making processes requires electronic structure methods based on quantum mechanics. The quantity of interest in the electronic structure description is the energy of the system as a function of the nuclear coordinates (Burke, 2012), from which other quantities of interest can be derived such as reaction energies, transition state energies, bond lengths, bond angles, vibrational frequencies and many other properties. The quantum mechanical description of the system requires solving the time dependent or time independent Schrödinger equation.

## 2.2 Schrödinger equation

The total energy of the system of interacting particles can be obtained by solving the time independent Schrödinger equation (Schrödinger,1926):

$$\widehat{H}\Psi = E\Psi \quad (2.1)$$

$$\hat{H} = \hat{T} + \hat{V} \quad (2.2)$$

Where: $\hat{H}$ is defined as the Hamiltonian operator which is the sum of the kinetic energy operator $\hat{T}$ , and the potential energy operator $\hat{V}$ and $\Psi$ is the wavefunction. The kinetic energy operator $\hat{T}$ includes the kinetic energy of the electrons and the nuclei separately. The potential energy operator $\hat{V}$ consists of the electrostatic interaction between the electrons and nuclei, the repulsive electron-electron potential and the repulsive potential of nucleus-nucleus interactions. The solution of the Schrödinger equation can only be accurately solved for the one electron system of the H atom, for other systems approximation to the solution of the Schrödinger equation has to be made.

One such approximation to solving the Schrödinger equation is to make use of the Born-Oppenheimer approximation (Born & Oppenheimer, 1927). The Born-Oppenheimer approximation makes use of the difference in mass between nuclei and electrons. In the Born-

Oppenheimer approximation the wavefunction can be decoupled into the electronic and the nuclear wavefunction contributions. The Born-Oppenheimer approximation reduces to the electronic structure problem where the electronic wavefunction is solved for by fixing the nucleus at fixed positions (owing to their heavier mass relative to the electrons), and in turn allowing the electrons to move around the fixed nuclear positions, thereby creating a potential energy surface for the movement of electrons (Fortunelli & Barcaro, 2013). The Schrödinger equation then reduces to the electronic structure problem defined as:

$$\widehat{H}_{elec}\Psi_{elec} = E_{elec}\Psi_{elec} \tag{2.3}$$

$$\widehat{H}_{elec} = T_e + V_{ee} + V_{ext} \tag{2.4}$$

with $T_e$ being the kinetic energy of the electrons, $V_{ee}$ the potential energy due to the electron-electron interaction and $V_{ext}$ the external potential, e.g. due to external filed and due to electron and nuclear interactions, $\widehat{H}_{elec}$ is the electronic Hamiltonian operator and $\Psi_{elec}$ is the electronic wavefunction. In electronic structure calculations utilising the Born-Oppenheimer approximation the kinetic energy contribution of the nucleus is neglected and the nuclear-nuclear interactions are treated as a constant.

The downfall of the electronic Schrödinger equation is that the electronic wave function has a many-body character (Fortunelli & Barcaro, 2013). Solution of the electronic Schrödinger equation is cumbersome since it involves solving for $\Psi$ which depends on position and spin of the N-electrons, thus a function of 6N-dimensional coordinates (Kohn, 1999). Thus if the same problem would be reformulated in terms of the electron density $n(r)$ which is a function of the 3 dimensional spatial coordinates, then solution of the electronic structure would become less cumbersome. The reformulation of the electronic structure problem in terms of the electron density $n(r)$ as opposed to the wavefunction $\Psi$ is at the heart of the density functional theory (Kohn, 1999). The density functional theory is realised through the Hohenberg–Kohn theorem (1964) and the Kohn–Sham formalism (1965).

## 2.3 Density functional theory

The density functional theory (DFT) is derived from the hypothesis that knowledge of the ground state electron density $n(r)$ for any electronic system, whether it includes or excludes interactions uniquely defines that system (Kohn, 1999). DFT is derived from its predecessor the Thomas Fermi Dirac (TFD) theory (Thomas, 1927; Fermi, 1927; Dirac, 1930) which is a crude electronic structure method based on the electron density distribution. The TFD theory considers interacting electrons moving in an external potential $v_{ext}(r)$ and assumes an overly

simple one to one relation between the external potential $v_{ext}(r)$ and the electron density distribution $n(r)$.

### 2.3.1 Hohenberg–Kohn theorem

The Hohenberg–Kohn theorem is based on the electron density as the basic variable to describe the electronic structure theory. The Hohenberg–Kohn theorem (1964) is based on two key concepts. The first key concept is that the ground state density $n(r)$ of a system of interacting electrons in some external potential $v_{ext}(r)$ determines the external potential uniquely. This implies that there is a unique ground state density $n(r)$ associated with the ground state wavefunction $\Psi$, and if the mapping of $v_{ext}(r)$ to $n(r)$ is one to one then the relation $n(r) \rightarrow v_{ext}(r) \rightarrow \Psi$ should hold (Becke, 2014).

The second key concept of the Hohenberg–Kohn theorem is the variational principle. The principle states that for a non–degenerate ground state, the minimum energy is obtained when the electron density $n(r)$ is the ground state density. For the degenerate ground state, the minimum energy is obtained when the electron density $n(r)$ is any of the ground state densities. The principle is valid subject to the constraint that the number of electrons is preserved in the formulations, i.e. N = $\int n(r)dr$.

From the Rayleigh–Ritz minimization principle and the constrained search method of Levy (1982) and Leib (1982) it can be shown that the minimum energy functional in a given potential can be expressed as:

$$E_{v\,min}[n(r)] = \min_{n(r)}\{\int v(r)n(r)dr + F[n(r)]\} \quad (2.5)$$

$$F[n(r)] = (\Psi, (T + U)\Psi) \quad (2.6)$$

$F[n(r)]$ is a universal functional valid for any number of electrons (N) and external potential $v(r)$. $T$ and $U$ in the definition of $F[n(r)]$ are functionals of the electron density $n(r)$. Hohenberg and Kohn formulates the problem of the ground state (e.g. energy) of the many body interacting system entirely in terms of the electron density $n(r)$ and a well defined but not explicitly known functional of the electron density $F[n(r)]$ (Kohn, 1999). The main complexities of the many-electron systems rely on the determination of the explicitly unknown universal functional $F[n(r)]$. DFT calculations are made physically realisable through the Kohn–Sham formulation (1965).

## 2.3.2 Kohn–Sham theorem

The central theme in the Kohn–Sham formulation is to solve the system of interacting electrons in an external potential $v_{ext}(r)$ by using a fictitious system of non-interacting Kohn–Sham particles in an effective potential $v_{eff}(r)$ (Mattsson et al., 2005). Thus, the single effective single-particle potential $v_{eff}(r)$ of the Kohn–Sham theory can be regarded as that unique, fictitious external potential which leads for non-interacting particles, to the same physical density $n(r)$ as that of the interacting electrons in the physical external potential $v_{ext}(r)$ (Wang & Parr, 1993). For a mathematical description for the link between the fictitious effective potential and the external potential see Appendix A.

The Kohn–Sham equations consists of the following 3 equations:

$$\left(-\frac{1}{2}\nabla^2 + v_{eff}(r)\right)\varphi_j(r) = \epsilon_j\varphi_j \tag{2.7}$$

$$v_{eff}(r) = v(r) + \int \frac{n(r')}{|r-r'|}dr' + v_{xc}(r) \tag{2.8}$$

$$n(r) = \sum_{i=1}^{N} |\varphi_j(r)|^2 \tag{2.9}$$

The equations 2.7, 2.8 and 2.9 are collectively termed the self-consistent Kohn-Sham equations which are solved iteratively until a desired convergence is satisfied. Figure 2.1 illustrates the self-consistent iteration procedure for solving the Kohn Sham equations. The ground state energy of the system is given by:

$$E = \sum_j \epsilon_j + E_{xc}[n(r)] - \int v_{xc}(r)n(r)dr - \frac{1}{2}\int \frac{n(r)n(r')}{|r-r'|}drdr' \tag{2.10}$$

Where $E_{xc}[n(r)]$ is the exchange correlation energy and $v_{xc}(r) = \frac{\delta}{\delta n(r)}E_{xc}[n(r)]$ . The Kohn–Sham density functional theory in principle results in an exact electron density and the exact total energy of any interacting, correlated system (Becke, 2014). The accuracy of Kohn–Sham density functional theory calculations depend on the accuracy of the approximation of the exchange correlation energy functional, since there is no known explicit expression for it.

## 2.3.3 Exchange correlation functional

The exchange correlation energy $E_{xc}[n(r)]$ can be separated into its separate part of exchange and correlation, i.e. $E_{xc}[n(r)] = E_x[n(r)] + E_c[n(r)]$ . The exchange energy is a consequence of the Pauli exclusion principle, it arises from the fact that same-spin electrons tend to avoid each other (Capelle, 2006). The correlation energy is described as the additional energy lowering obtained in a real system of interacting electrons due to the mutual avoidance

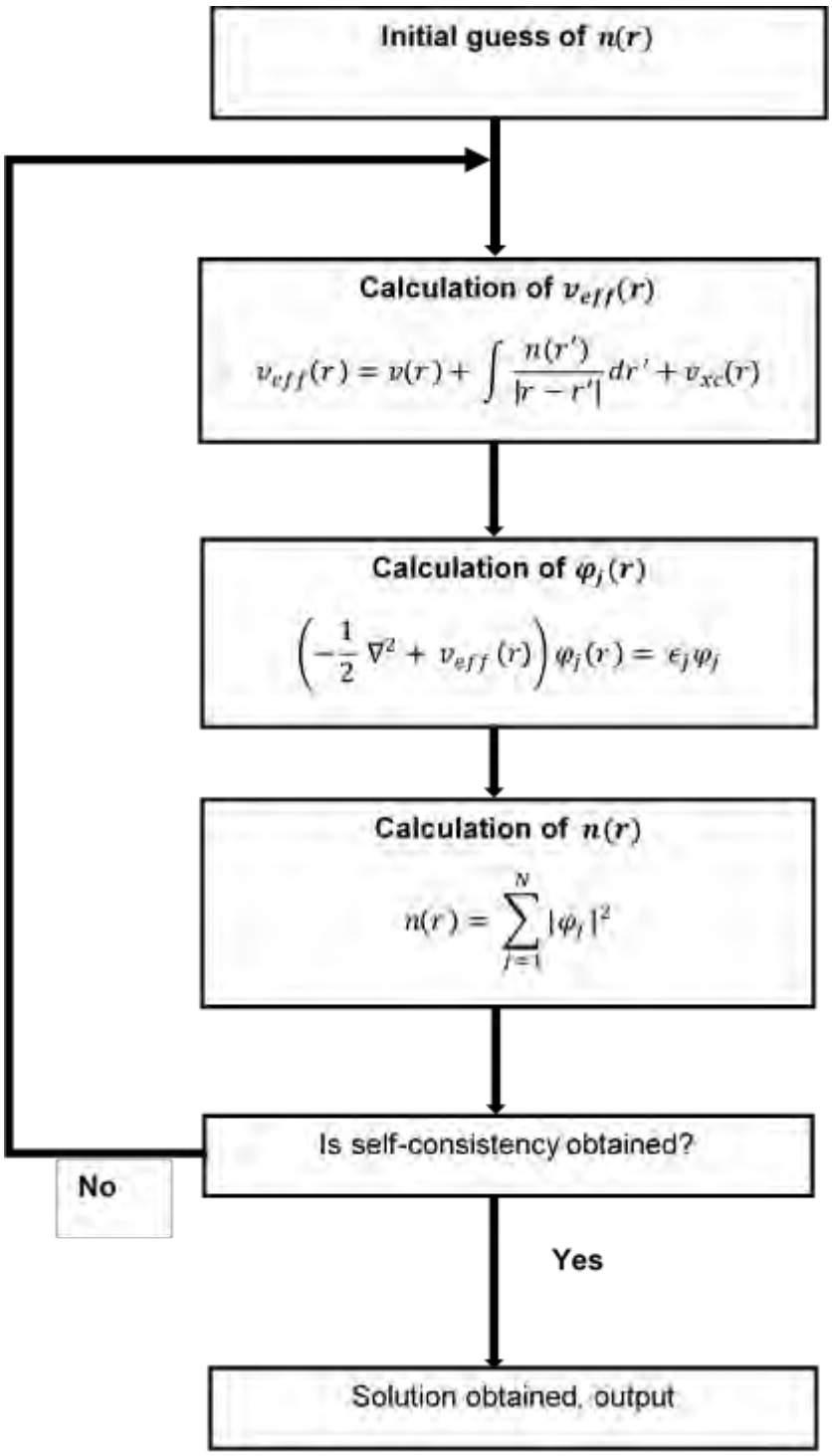


Figure 2.1: Self consistent iteration procedure for solving Kohn–Sham equations (adapted from Mattsson et al. 2005)

of interacting electrons (Capelle, 2006). The exchange energy can be obtained exactly in terms of single particle orbitals from Hartree Fock orbitals or Kohn–Sham orbitals, whereas no exact description of correlation energy can be derived (Capelle, 2006). Correlation effects are smaller than exchange effects, i.e. $|E_x| > |E_c|$ (Becke, 2014).

Two of the most commonly applied exchange correlation functionals are the local density approximation (LDA) and the generalized gradient approximation (GGA). The LDA approximation is based on the assumption of a slow varying density $n(r)$. The exchange correlation functional is given by:

$$E_{xc}^{LDA}[n(r)] = \int n(r)\epsilon_{xc}\big(n(r)\big)dr \quad (2.11)$$

$\epsilon_{xc}$ is the exchange and correlation energy per electron of a uniform electron gas of density $n(r)$. The exchange energy in terms of atomic units is given as (Kohn, 1999):

$$e_x\big(n(r)\big) = \frac{-0.485}{\left(\frac{3}{4\pi n(r)}\right)^{\frac{1}{3}}} \quad (2.12)$$

The correlation part $\epsilon_c(n(r))$ is obtained from high precision Monte Carlo methods of Ceperly and Alder (1980) and Ceperly (1978). LDA approximations result in inaccuracies of the order of 10 – 20 % for some chemical properties such as atomic energies, dissociation energy of molecules and cohesive energies, and these errors are too high (Kohn, 1999). LDA's however give accurate bond lengths and geometries of molecules to an accuracy of 1% (Kohn, 1999).

The generalized gradient approximation (GGA) is a correction to the LDA method which does not consider the electron density as a constant but also incorporates gradients of the electron density. The exchange correlation energy functional for the GGA takes the form:

$$E_{xc}^{GGA}[n(r)] = \int f(n(r), |\nabla n(r)|)n(r)dr \quad (2.13)$$

$|\nabla n(r)|$ is the gradient of the electron density. Different GGA functionals differ in the construction of the function $f(n(r), |\nabla n(r)|$ (Kohn, 1999). Some of the commonly used GGA functionals include the PW91 functional (Perdew & Wang, 1992; Perdew *et al*. 1992), PBE functional (Perdew et al., 1996a; Perdew et al., 1996b) and the RPBE functional (Hammer et al., 1991).

The LDA and GGA functionals inherently suffer from the drawback of self-interaction correction (SIC), which is an erroneous attribution of correlation energy even to a single electron system (Perdew & Zunger, 1981). The standard approximations, i.e. LDA and GGA have well documented shortcomings concerning the prediction of insulators or systems with wide HOMO-LUMO gaps such as oxides, due to over-delocalizing of the d-electrons (Burke, 2012). To correct for over-delocalization of d-electrons, the DFT+ U method (Anisimov et al., 1991) can be used where the U term is added to the DFT Hamiltonian. The U term known as the Hubbard term (Hubbard, 1961) is added as a form of energy penalty for the double occupation of specific orbitals, thereby improving the description of localized electronic states in systems such as transition metal oxides (Fortunelli & Barcaro, 2013).

Hybrid exchange correlation functionals can also be used to correct for over-delocalization of d-electrons. Hybrid functionals consists of a mixture of a certain fraction of exact exchange from Hartree Fock with GGA exchange correlation. An example of a hybrid exchange correlation functional is the PBE0 (Perdew et al., 1996), which consists of 25 % exact exchange.

Other exchange correlation functionals beyond the LDA and GGA, include the meta-GGA functionals. Meta-GGA include the kinetic energy density together with electron density gradients to the function of the exchange correlation functional. According to Jacob's ladder method (Perdew & Schmidt, 2001) of ranking density functionals, approximations above the meta-GGA are the hyper-GGA methods which consists of exact exchange and exact partial correlation methods. The highest ranked methods on Jacobs ladder is the random phase approximation (RPA) method which utilises all the Kohn–Sham orbitals, i.e. occupied and unoccupied orbitals. As one moves up the ladder to higher ranking functionals, the computational time for the methods increases drastically.

## 2.4 van der Waals interactions DFT methods

Up until recent times the standard LDA and GGA approximations for exchange correlation and the hybrid functionals were unable to describe long range electron correlation, i.e. electronic dispersion forces also commonly referred to as van der Waals forces. Van der Waals interactions are dominant in graphene systems which will be investigated in the present study.

Various methods for the implementation of the van der Waals interaction within DFT are in existence and are discussed extensively in various references (Cooper et al., 2010; Tkatchenko et al., 2010; Klimeš & Michaelides, 2012; Ramalho et al., 2013; DiStasio Jr. et al., 2014; Berland et al., 2015).

The methods of incorporating dispersion effects are broadly categorised into three main categories (Berland et al., 2015); namely explicit density functional methods, implicit DFT extended with atom-pair potential methods and the computationally expensive methods based on the perturbation theory typically in the random phase approximation.

The so called $C_6$ method of the density functional theory with dispersion (DFT-D), is an implicit method, where dispersion effects are added to the DFT energy to give a total energy $E_{tot} =$

$E_{DFT} + E_{disp}$. Where $E_{tot}$ is the total energy, $E_{DFT}$ is the DFT calculated energy and $E_{disp}$ is the dispersion energy. In DFT-D methods the dispersion energy is assumed to be a pairwise addition of all the pairwise interactions between atom A and B. The dispersion energy is calculated as:

$$E_{disp} = -\sum_{A,B} f(r_{AB}, A, B)\, C_6^{A,B} / r^6_{A,B} \quad (2.14)$$

Where $C_6^{A,B}$ is the dispersion coefficient between atoms A and B, $r^6_{A,B}$ is the distance between atom A and B and $f(r_{AB}, A, B)$ is the damping function to correct for the divergence of the dispersion energy at short interatomic distances. The $C_6^{A,B}$ coefficients are kept constant during calculations. An example of a DFT-D method is the Grimme method DFT-D2 (Grimme, 2006). Drawbacks of the DFT-D approach in describing van der Waals interactions are that it is not clear how to work out or obtain the dispersion coefficients. Moreover, constant dispersion coefficients in calculations mean different chemical states of the atom and the influence of the environment are neglected (Klimeš & Michaelides, 2012).

An improvement to the constant dispersion coefficient method is methods which consider the change of the dispersion coefficient with change in chemical environment, i.e. the dispersion coefficient changes with change in hybridization of an atom. The dispersion energy is obtained from equation 2.14, with the dispersion coefficients calculated from some reference data such as the atomic polarizability. Two common methods under this treatment of the van der Waals interaction is the DFT-D3 of Grimme (Grimme et al., 2010) and the method of Tkatchenko and Scheffler (Tkatchenko & Scheffler, 2009) which will be referred to as vdW–TS in the present study.

In the present study the vdW-TS method is used, so a short description of this method is provided. The vdW-TS method relies on reference atomic polarizability and dispersion coefficient data from the database by Meath and co-workers (Zeiss & Meath, 1977; Margoliash & Meath, 1978) to calculate the dispersion energy. The dispersion coefficients as calculated within the vdW-TS method for an atom in a molecule depends on the effective volume of the atom. The central theme in the vdW-TS method is that the dispersion coefficient $C_6$, and the van der Waals radii are determined from the mean-field ground state density. The electron density is used to calculate the relative atomic polarizability not the absolute polarizability of an atom in a molecule. In the vdW-TS method the relation between the polarizability and the volume of an atom in a molecule termed the effective volume is used, the link between polarizability and the volume is realised through the Hirschfeld partitioning of electron density (Tkatchenko & Scheffler, 2009).

$$\frac{\kappa_A^{eff}}{\kappa_A^{free}} \frac{\alpha_A^{eff}}{\alpha_A^{free}} = \frac{V_A^{eff}}{V_A^{free}} = \left(\frac{\int r^3 w_A(r) n(r) d^3r}{\int r^3 n_A^{free}(r) d^3r}\right) \quad (2.15)$$

$$w_A(r) = \frac{{n_A}^{free}(r)}{\Sigma_B {n_B}^{free}(r)} \quad (2.16)$$

Where the variables are defined as: ${\kappa_A}^{eff}$: proportionality constant between volume and polarizability for atom A in a molecule, ${\kappa_A}^{free}$: proportionality constant between volume and polarizability for free atom A, ${\alpha_A}^{eff}$: effective polarizability of atom A in a molecule, ${\alpha_A}^{free}$: polarizability of free atom A (obtained from reference data), ${V_A}^{eff}$: effective volume of atom A in a molecule, ${V_A}^{free}$: volume of free atom A, $r$: distance from the nucleus of an atom A, $w_A(r)$: Hirshfeld atomic partitioning weight for atom A, $n(r)$: total electron density and ${n_A}^{free}(r)$: electron density for the free atom A.

The total electron density $n(r)$ and the free atom electron density ${n_A}^{free}(r)$ are calculated from DFT using the exchange correlation energy functional. With the link between the effective volume and the electron density established, the dispersion coefficient as a function of electron density can be calculated from equation 2.17:

$${C_{6AA}}^{eff} = \frac{{\eta_A}^{eff}}{{\eta_A}^{free}} \left(\frac{{\kappa_A}^{free}}{{\kappa_A}^{eff}}\right)^2 \left(\frac{{V_A}^{eff}}{{V_A}^{free}}\right)^2 {C_{6AA}}^{free} \quad (2.17)$$

Where the variables are defined as: ${C_{6AA}}^{eff}$: effective dispersion coefficient for atom A in a molecule, ${\eta_A}^{eff}$: effective frequency for atom A in a molecule, ${\eta_A}^{free}$: frequency for free atom A and ${C_{6AA}}^{free}$: dispersion coefficient for free atom A (obtained from reference data).

The dispersion coefficient between two atoms A and B in a molecule $C_{6A,B}$ is obtained by adding ${C_{6AA}}^{eff}$ and ${C_{6BB}}^{eff}$ since dispersion coefficients are additive. The dispersion coefficients calculated using the vdW-TS method account for the different hybridization that an atom can have and calculates the dispersion coefficient without a need of empirical parameters for the different hybridization states (Tkatchenko & Scheffler, 2009). Tkatchenko et al. (2009) cautions that the vdW-TS method maybe inaccurate for systems where the atom in molecules cannot be applied, e.g. in metals where there is delocalised electrons. Systems which cannot be described with the atom in molecules approach, requires the inclusion of many-body terms to describe which are non-additive like the pairwise summation which applies for atom in molecules approach.

The atomic polarizabilities calculated in the vdW-TS method do not include long range electrostatic screening effects. In addition, the vdW-TS method neglects the non-additive many-body van der Waals (vdW) energy contribution beyond the pairwise approximation (Tkatchenko et al., 2012). The two body vdW energy, e.g. pairwise additive methods stem from an electrostatic interaction of atomic dipolar fluctuations. An atom embedded in a condensed phase, e.g. solid or in a large molecule experiences dipolar fluctuations different

to the free atom case. The atom experiences a dynamic electric field generated by surrounding atoms giving rise to polarization and depolarization effects. Thus the short and long range effects of the environment act to screen the atomic dipolar fluctuations hence the screening effects need to be considered in first principles calculations (Tkatchenko et al., 2012). In materials where there is a sea of delocalized electrons such as metals, screening effects become important to include in the calculations.

The many-body energy contribution to the van der Waals energy in the vdW-TS method is accounted for by incorporating long range screening effects (Tkatchenko et al., 2012). The vdW-TS method including long range screening effects will be referred to as vdW-TS-SCS in the present study. The equations in the vdW-TS-SCS method are derived from approximations of the adiabatic-connection fluctuation-dissipation theorem (ACFDT) (Langreth & Perdew, 1977) which is an exact expression for the total electron correlation energy and contains the full many-body vdW energy (Tkatchenko et al., 2012).

The long range screening effects are included by microscopically modelling the environment as a dipole field and solving the resultant classical electrodynamics self-consistent screening (SCS) equation.

$$\alpha^{SCS}(r;i\omega) = \alpha^{TS}(r;i\omega) + \alpha^{TS}(r;i\omega) \int dr' \, \tilde{\mathrm{I}}\,(r-r')\, \alpha^{SCS}(r';i\omega) \quad (2.18)$$

Where the variables are defined as: $\alpha^{TS}(r;i\omega)$: sum of the vdW-TS effective atomic polarizabilities, and $\tilde{\mathrm{I}}\,(r-r')$: dipole-dipole interaction tensor.

The effective frequency dependent dipole polarizability is defined as:

$$\alpha_A(i\omega) = \frac{\alpha_A[n(r)]}{1+\{{}^{\omega}/_{\omega_A[n(r)]}\}^2} \quad (2.19)$$

Where $\alpha_A[n(r)]$ is the static polarizability of atom A and $\omega_A[n(r)]$ is the characteristic excitation frequency.

The dispersion coefficients are calculated from the Casimir-Polder integral (Casimir, 1948):

$$C_{6AA} = \frac{3}{\pi}\int_0^{\infty} \alpha_A^{SCS}(i\omega)\, \alpha_A^{SCS}(i\omega) d(i\omega) \quad (2.20)$$

Where $\alpha_A^{SCS}$ is the frequency dependent screened polarizability of atom A.

The coefficient $\alpha_A^{SCS}$ consists of both short range (through the vdW-TS method) and long range (through the SCS equation) electrostatic screening (Tkatchenko et al., 2012).

A second category to approximate van der Waals interactions is the explicit methods in which the long-range van der Waals energy is calculated *ab*-initio. The pioneering work in this regard is the van der Waals density functional (vdW-DF) method of Dion et al. (2004). In the vdW-DF

method the exchange correlation energy is split into separate exchange and correlation terms, with the correlation term further split into a local and a non-local component.

$$E_{xc}[n(r)] = E_x{}^{GGA}[n(r)] + E_c[n(r)] \quad (2.21)$$

$$E_c[n(r)] = E_C{}^{LDA}[n(r)] + E_C{}^{nl}[n(r)] \quad (2.22)$$

Where the variables are defined as: $E_C{}^{LDA}[n(r)]$: is the local correlation contribution obtained from LDA and $E_C{}^{nl}[n(r)]$: is the non-local long range correlation energy.

Using the adiabatic-connection fluctuation-dissipation theorem approximations the non-local correlation energy functional in the full potential approximation result in the expression:

$$E_C{}^{nl}[n(r)] = \int_0^\infty \frac{du}{2\pi} tr\left[\ln\left(1 - V\tilde{X}\right) - ln\boldsymbol{\epsilon}\right] \quad (2.23)$$

Where the variables are defined as: $\tilde{X}$: density response to a fully self-consistent potential with long range interfragment spectator contributions omitted, $V$: inter-electronic Coulomb interaction, $\boldsymbol{\epsilon}$**:** approximated dielectric function, and $u$: imaginary frequency.

In the vdW-DF method of Dion et al. (2004) the exchange energy is obtained from a GGA functional, and the vdW-DF method depends on the exchange functional. The vdW energy is a correlation effect and not an exchange effect (Langreth et al., 2005). Therefore, the choice of the GGA functional for exchange in the vdW-DF method should be such that the functional does not predict binding in the van der Waals regime when treated with exact change (Langreth et al., 2005). For the vdW-DF method the exchange energy is calculated using the revPBE functional (Zhang & Yang, 1998) which was tested on a couple of vdW systems and did not show a tendency to bind those systems (Langreth et al., 2005). The vdW-DF method has been found not to be accurate due to a too steep repulsive potential at short distances (Klimeš & Michaelides, 2012).

Several modifications to the vdW-DF method are in existence, in the present study we use the OptPBE functional (Klimeš et al., 2010) to approximate the vdW energy. The exchange part of the energy in the OptPBE-vdW functional is described using the OptPBE functional and the correlation part is described using PBE (Perdew et al., 1996). The OptPBE-vdW functional is a GGA functional for exchange which is a combination of PBE and RPBE.

The GGA exchange energy is related to the LDA exchange energy density by the following relationship:

$$\varepsilon_x(n,s) = \varepsilon_x{}^{LDA}(n)F_x(s) \quad (2.24)$$

Where the variables are defined as: $\varepsilon_x{}^{LDA}(n)$ : LDA exchange energy density and $F_x(s)$: is the enhancement factor. The enhancement factor depends on the reduced gradient density s.

$$s = \frac{|\nabla n|}{2k_F n} \quad (2.25)$$

$$k_F{}^3 = 3\pi^2 n \tag{2.26}$$

The enhancement factor for the PBE and RPBE functionals are of the form:

$$F_x{}^{PBE}(s) = 1 + \kappa - \frac{\kappa}{\left(1+\frac{\mu s^2}{\kappa}\right)} \tag{2.27}$$

The OptPBE-vdW functional has the above form for the enhancement factor with $\mu = 0.175519$ and $\kappa = 1.04804$. The composition of the OptPBE-vdW functional is $x = 94.5268\%$ PBE and $(100 - x)\%$ RPBE, thus it consists of a single empirical parameter $x$ which is a mixing ratio of PBE and RPBE (Klimeš et al., 2010).

## 2.5 Practical implementation of DFT

Practical implementation of DFT simulations for electronic structure calculations for materials such as molecules, solids and surfaces is achieved through various computer packages. In the present study the computational code employed to perform the DFT calculations is the Vienna ab-initio simulation Package (VASP) (Kresse & Hafner, 1993; Kresse & Furthmüller, 1996a; Kresse & Furthmüller, 1996b; Kresse & Jourbert, 1999). VASP uses the plane wave basis set to practically solve the Kohn–Sham orbital equations. Some parameters which need to be considered in performing electronic structure calculations are the k-point density, the plane wave basis set and the pseudopotentials.

In practice the Kohn–Sham orbitals $\varphi_i(r)$ are expanded using basis set functions. The basis set functions are of two main types, the atom centred functions and the non-atom centred functions. The atom centred functions includes the linear combination of atomic orbitals (LCOA), forms of the basis set in this class include the slater type orbitals (STO) and the Gaussian type orbitals (GTO). The non-atom centred functions are delocalised and extends over all space. The non-atom centred functions make use of plane waves as the basis set. The type of basis set used is vital as is sets the accuracy and the computational time for an electronic structure calculation (Mattsson et al., 2005).

To perform an electronic structure calculation on a solid using the Kohn–Sham formalism translate to having to deal with an infinite number of non–interacting electrons moving in a static potential of an infinite number of ions or nuclei (Payne et al., 1992). This amounts to having to solve the wavefunction for each of the electrons in the system and would correspond to an infinite basis set for each wavefunction since the wave function extends over the entire solid (Payne et al., 1992). The above mentioned challenges can be overcome by performing

calculations on periodic systems and making use of Blöch's theorem to the electronic wavefunction (Kittel, 2005).

A crystalline solid consists of lots of electrons which is not practical to include all of them in a calculation. In a crystalline solid the ions within the crystal are arranged in a regular periodic arrangement, hence the external potential felt by the electrons is also periodic in nature (Kittel, 2005). By making use of the periodic boundary conditions the system of the crystalline solid is reduced to a system of a unit cell which is periodically repeated in three dimensions. This allows for the reduction of the infinite number of electrons in the solid to only the number of electrons in the single unit cell of the crystal (Mattsson et al., 2005).

## 2.5.1 Blöch's theorem

Blöch's theorem states that in a periodic solid, each electronic wave function can be written as the product of a cell-periodic part and a wavelike part (Ashcroft & Mermin, 1976).

$$\Psi_i\,(r) = \sum_G c_{i,k+G}\ \exp[i(k+G).r] \tag{2.28}$$

Where $k$ is the wave vector, $G$ is the reciprocal lattice vectors given by $G.l = 2\pi m$ , with $l$ being the lattice vector of the crystal and *m* an integer. Each electronic wavefunction is written as a sum of plane waves. In principle the exact representation of the orbitals, i.e. each wavefunction requires an infinite number of plane waves (Mattsson et al., 2005).

## 2.5.2 k-point sampling

By applying the periodic boundary conditions which apply to the solid, the number of k-points needed to determine the properties of the solid can be reduced from an infinite number to a finite number. To determine the properties of the solid, e.g. the electronic potential and the total energy, the number of occupied electronic states at each k-point need to be calculated. The electronic states are allowed only on a set of k-points determined by the boundary conditions that apply to the bulk solid (Payne et al., 1992). There is a finite number of occupied electronic states at each k-point.

The electronic wavefunction at k-points that are very close to each other will be almost identical, therefore reducing the need to calculate the electronic wavefunction at each k-point (Payne et al., 1992). Thus the electronic wavefunction over a region of k-space can be represented by the electronic wavefunction at a single k-point. In general, for an insulator or a semiconductor a few k-points are required to determine the electronic and the total energy of

the system, whilst for metals a large number of k-points is required in order to precisely define the Fermi surface (Payne et al., 1992).

Various approximate methods for the sampling of special sets of k-points in the Brillouin zone from which the electronic potential and total energy can be determined from the occupied electronic states include methods by Chadi & Cohen, 1973; Joanno-Poulos & Cohen, 1973; Monkhorst & Pack, 1976; Evarestov & Smirnov, 1983. The amount of error in the total energy (and other properties of the system under investigation) introduced by insufficient k-point sampling can be remedied by using a denser set of k-points. The k-point density can be increased until the property is converged to a desired tolerance, though the downside of an increase in k-point density is an increase in computational time.

### 2.5.3 Plane wave basis set

The plane wave representation of the Kohn–Sham orbitals is given by equation 2.28, and the exact representation of the orbitals would need an infinite number of plane waves. The expansion coefficients $c_{i,k+G}$ in equation 2.28 for the plane waves with small kinetic energy $E = \left(\frac{\hbar^2}{2m}\right)|k+G|^2$ are in general more important than those with large kinetic energy (Payne et al., 1992). For practical applications, the plane wave basis set is truncated to include only plane waves that have kinetic energies less than some particular cutoff energy $E \leq E_{cut}$. Thus by truncating to a certain cutoff energy, the basis set is reduced from an infinite size to a finite size. Truncation of the plane wave basis set at a finite cutoff energy will lead to an error in the computed properties of the system, this error can be minimised by increasing the value of the cutoff energy until the calculated property is converged to a desired tolerance. Like for the case of the k-point set, increasing the cutoff energy result in an increase in computational time.

### 2.5.4 Pseudopotentials

To perform an all electron calculation would require an extremely large plane wave basis set, also it would require vast amounts of computational time in order to calculate the electronic wavefunction (Payne et al., 1992). Most physical properties of the solids are dependent on the valence electrons and to a lesser extent to the core electrons which are tightly bound and closest to the nucleus. The pseudopotential approximation (Phillips, 1958; Yin & Cohen, 1982) freezes the core electrons and replaces the strong Coulomb potential of the nucleus and the effects of the tightly bound core electrons by an effective ionic potential acting on the valence electrons (Troullier & Martins, 1991). By using the pseudopotential approximation, the number

of electrons that need to be described in the system is decreased, thus a smaller number of plane wave basis set and therefore large systems with many atoms can be simulated. Various types of pseudopotential approximations are in existence and include projector augmented waves PAW (Blöch, 1994; Kresse & Joubert, 1999), norm-conserving pseudopotentials (Hamman et al., 1979), and ultrasoft pseudopotentials (Vanderbilt, 1990).

## 2.6 References

Ashcroft, N.W. & Mermin, N.D. (1976) *Solid State Physics* (Holt Saunders, Philadelphia), p.113.

Anisimov, V.I., Zaanen, J. & Anderson, O.K. (1991) Band theory and Mott insulators: Hubbard U instead of stoner I. *Phys. Rev. B* **44**, 943-954.

Becke, A.D. (2014) Perspective: Fifty years of density-functional theory in chemical physics. *J. Chem. Phys.***140**, 18A301-18A318.

Berland, K., Cooper, V.R., Lee, K., Schröder, E., Thonhanser, T., Hyldgaard, P. & Lundqvist, B.I. (2015) van der Waals forces in density functional theory: a review of the vdW-DF method. *Rep. Prog. Phys*. **78**, 066501-066542.

Blöch, P.E. (1994) Projector augmented-wave method. Physical Review B **50**, 17953-17979.

Born, M. & Oppenheimer. R. (1927) Zur Quantentheorie der Molekeln. *Annalen Der Physik* **84**, 457-484.

Burke, K. (2012) Perspective on density functional theory. *J. Chem. Phys.* **136**, 150901-150909.

Capelle, K. (2006) A bird's-eye view of density-functional theory. http://arXiv:cond-mat/0211443 (cond.mat.mtrl.sci).

Casimir, H.B.G. (1948) On the attraction between two perfectly conducting planes. *Proc. Kon. Ned. Akad. Wetensch*. **51**, 793-795.

Ceperly, D.M. & Alder, B.J. (1980) Ground state of the electron gas by a stochastic method. *Phys. Rev. Lett.* **45**, 566-569.

Ceperly, D. (1978) Ground state of the fermion one-component plasma: a Monte Carlo study in two and three dimensions. *Phys. Rev. B* **18**, 3126-3138.

Chadi, D.J. & Cohen, M.L. (1973) Special points in the Brillouin zone. *Phys. Rev. B* **8**,

5747-5753.

Cooper, V.R., Kong, L. & Langreth, D.C. (2010) Computing dispersion interactions in density functional theory. *Physica Procedia* **3**,1417-1430.

Dion, M., Rydberg, H., Schröder, E., Langreth, D.C. & Lundqvist, B.I. (2004) Van der Waals density functional for general geometries. *Phys. Rev. Lett.* **92**, 246401-246405.

Dirac, P.A.M. (1930) Note on the exchange phenomena in the Thomas atom. *Mathematical Proceedings of the Cambridge Philosophical Society* **26**, 376-385.

DiStasio Jr., R.A., Gobre, V.V. & Tkatchenko, A. (2014) Many-body van der Waals interactions in molecules and condensed matter. *J. Phys.: Condens. Matter* **26**, 213202-213218.

Evarestov, R.A. & Smirnov, V.P. (1983) Special points of the Brillouin Zone and their use in the solid state theory. *Phys. Status Solidi B* **119**, 9-40.

Fermi, E. (1927) Un metodo statistic per la determinazione di alcune prioprietà dell'Atomo'. *Rend. Accad. Naz. Lincei* **6**, 602-607.

Grimme, S. (2006) Semi-empirical GGA-type density functional constructed with a long-range dispersion correction. *J. Comput. Chem.* **27**, 1787-1799.

Grimme, S., Antony, J., Ehrlich, S. & Krieg, H. (2010) A consistent and accurate ab initio parametrization of density functional dispersion correction (DFT-D) for the 94 elements H-Pu. *J. Chem. Phys*. **132**,154104-154123.

Fortunelli, A. & Barcaro, G. (2013) Density Functional Theory of Free and Supported Metal Nanoclusters and Nanoalloys, in Mariscal, M.M., Leiva, E. P. M. and Oviedo, O. A. (ed.*), Metal Clusters and Nanoalloys: From Modelling to Applications*, Springer, New York, pp. 29-79.

Hamann, D.R., Schlüter, M. & Chiang, C. (1999) Norm-conserving pseudopotential. *Phys. Rev. Lett.* **43**, 1494-1497.

Hammer, B., Hansen, L.B. & Nørskov, J.K. (1999) Improved adsorption energetics within density-functional theory using revised Perdew-Burke-Ernzerhof functionals. *Phys. Rev. B* **59**, 7413-7421.

Hohenberg, P. & Kohn, W. (1964) Inhomogenous electron gas. *Phys. Rev.* **136**, B864-B870.

Hubbard, S.H. (1961) Quantum-mechanical and semiclassical forms of the density operator theory of relaxation. *Rev. Modern Phys.* **33**, 249-264.

Joannopoulos, J.D. & Cohen, M.L. (1973) Electronic charge densities for ZnS in the wurtzite and zincblende structures. *J. Phys. C: Sol. State Phys.* **6**, 1572-1585.

Jurečka, P., Šponer, J., Černý, J. & Hobza, P. (2006) Benchmark database of accurate (MP2 and CCSD(T) complete basis set limit) interaction energies of small model complexes, DNA base pairs, and amino acid pairs. *Phys. Chem. Chem. Phys*. **8**, 1985-1993.

Klimeš, J. & Michaelides, A. (2012). Perspective: advances and challenges in treating van der Waals dispersion forces in density functional theory. *J. Chem. Phys.* **137**, 120901-120912.

Klimeš, J., Bowler, D.R. & Michaelides, A. (2010) Chemical accuracy for the van der Waals density functional. *J. Phys.: Condens. Matter* **22**, 022201-022206.

Kittel, C. (2005) *Introduction to Solid State Physics*. 8th Edition. John Wiley and Sons Inc.: New York, pp 167-170.

Kohn, W. (1999) Nobel lecture: electronic structure of matter–wave functions and density functionals. *Rev. Modern Phys.* **71**, 1253-1266.

Kohn, W. & Sham, L.J. (1965) Self-consistent equations including exchange and correlation effects. *Phys. Rev.* **140**, A1133-A1138.

Kresse, G. & Joubert, D. (1999) From ultrasoft pseudopotentials to the projector augmented-wave method. *Phys. Rev. B* **59**, 1758-1775.

Kresse, G. & Hafner, J. (1993) *Ab* initio molecular dynamics for liquid metals. *Phys. Rev. B* **47**, 558-561.

Kresse, G. & Furthmüller, J. (1996a) Efficiency of ab initio total energy calculations for metals and semiconductors using a plane-wave set. *Comput. Mater. Sci.* **6**, 15-50.

Kresse, G. & Furthmüller, J. (1996b) Efficient iterative schemes for ab initio total-energy calculations using a plane-wave basis set. *Phys. Rev. B* **54**, 11169-11186.

Langreth, D.C. & Perdew, J.P. (1977) Exchange-correlation energy of a metallic surface: wave-vector analysis. *Phys. Rev. B* **15**, 2884-2901.

Langreth, D.C., Dion, M., Rydberg, H., Schröder, E., Hyldgaard, P. & Lundqvist, B.I. (2005) Van der Waals density functional theory with applications. *Int. J. Quantum Chem.* **101**, 599-610.

Leib, E. (1982) Physics as natural philosophy: essays in honor of Laszlo Tisza on his 75$^{th}$ Birthday, edited by Shimony, A. & Feshbach (MIT, Cambridge, MA) p.111.

Levy, M. (1982) Electron densities in search of Hamiltonians. *Phys. Rev. A* **26**,1200-1206.

Margoliash, D.J. & Meath, W.J. (1978) Pseudopotential dipole oscillator strength distributions and some related two body interaction coefficients for H, He, Li, N, O, $H_2$, $N_2$, $O_2$, NO, $N_2O$, $H_2O$, $NH_3$ and $CH_4$. *J. Chem. Phys*. **68**, 1426.

Mattsson, A.E., Schultz, P.A., Desjarlias, M.P., Mattsson, T.R. & Leung, K. (2005) Designing meaningful density functional theory calculations in material science - a primer. *Modell. Simul. Mater. Sci. and Eng.* **13**, R1-R3.

Monkhorst, H.J. & Pack, J.D. (1976) Special points for Brillouin-zone integrations. *Phys. Rev. B* **13**, 5188-5192.

Payne, M.C., Teter, M.P., Allan, D.C., Arias, T.A. & Joannopoulos, J.D. (1992) Iterative minimization techniques for *ab* initio total-energy calculations: molecular dynamics and conjugate gradients. *Rev. Modern Phys.* **64**, 1046-1097.

Perdew, J.P. & Wang, Y. (1992) Accurate and simple analytic representation of the electron-gas correlation energy. *Phys. Rev. B* **45**,13244-13249.

Perdew, J.P., Chevary, J.A., Vosko, S.H., Jackson, K.A., Pederson, M.R., Singh, D.J. & Fiolhais, C. (1992) Atoms, molecules, solids, and surfaces: applications of the generalized gradient approximation for exchange and correlation. *Phys. Rev. B* **46**, 6672-6687.

Perdew, J.P., Burke, K. & Ernzerhof, M. (1996) Generalized gradient approximation made simple. *Phys. Rev. Lett.* **77**, 3865-3868.

Perdew, J.P., Ernzerhof, M. & Burke, K. (1996) Rationale for mixing exact exchange with density functional approximations. *J. Chem. Phys.* **105**, 9982-9985.

Perdew, J.P. & Schmidt, K. (2001) Jacob's ladder of density functional approximations for the exchange correlation energy. *AIP Conference Proceedings* **577**, 1-20.

Perdew, J.P. & Zunger, A. (1981) Self-interaction correction to density-functional approximations for many-electron systems. *Phys. Rev. B* **23**, 5048 – 5078.

Phillips, J.C. (1958) Energy-band interpolation scheme based on a pseudopotential. *Phys. Rev.***112**, 687-695.

Ramalho, J.P.P., Gomes, J.R. & Llas, F. (2008) Accounting for van der Waals interactions between adsorbates and surfaces in density functional theory based calculations: selected examples. *RSC Advances* **3**, 13085-13100.

Schrödinger, E. (1926) An undulatory theory of the mechanics of atoms and molecules. *Phys. Rev. **28***, 1049-1070.

Thomas, L.H. (1927) The calculation of atomic field. *Mathematical Proceedings of the Cambridge Philosophical Society* **23**, 542-548.

Tkatchenko, A., DiStasio Jr., R.A., Car, R. & Scheffler, M. (2012) Accurate and efficient method for many-body van der Waals interactions. *Phys. Rev. Lett*. **108**, 236402-236407.

Tkatchenko, A., Romaner, L., Hofmann, O.T., Zojer, E., Ambrosch-Draxl, C. & Scheffler, M. (2010) Van der Waals interactions between organic adsorbates and at organic/inorganic interfaces. *MRS Bull.* **35**, 435-442.

Tkatchenko, A. & Scheffler, M. (2009) Accurate molecular van der Waals interactions from ground-state electron density and free-atom reference data. *Phys. Rev. Lett*. **102**, 073005-073009.

Tomàš, B., Hafner, J., Lebègue, S. & Ángyán, J.G. (2010) Improved description of the structure of molecular and layered crystals: Ab initio DFT calculations with van der Waals corrections. *J. Phys. Chem. A* **114**, 11814-11824.

Troullier, N. & Martins, J.S. (1991) Efficient pseudopotentials for plane-wave calculations. *Phys. Rev. B* **43**, 1993 - 2006.

Vanderbilt, D. (1990) Soft self-consistent pseudopotentials in a generalized eigenvalue formalism. *Phys. Rev. B* **41**, 7892-7895.

Wang, Y. & Parr, R.G. (1993) Construction of exact Kohn-Sham orbitals from a given electron density. *Phys. Rev. A* **47**, R1591-R1593.

Yin, M.T. & Cohen, M.L. (1982) Theory of *ab initio* pseudopotential calculations. *Phys. Rev. B* **25**, 7408-7412.

Zeiss, G.D. & Meath, W.J. (1977) Dispersion energy constants $C_6$(A,B), dipole oscillator strength sums and refractivities for Li, N, O, $H_2$, $N_2$, $O_2$, $NH_3$, $H_2O$, NO and $N_2O$. *Mol. Phys*. **33**,1155.

Zhang, Y. & Yang, W. (1998) Comments on 'Generalized gradient approximation made simple. *Phys. Rev. Lett.* **80**, 890.

# Chapter 3: Chemical ordering in unsupported $Pt_{32}Pd_6$ cluster

## 3.1 Introduction

The surface composition of bimetallic nanoclusters can be different from the bulk composition as a result of segregation processes (van der Oetelaar et al., 1998). Knowledge of the surface composition of bimetallic nanoclusters is vital since the chemical reactivity and its effectiveness as a catalyst depends critically on the surface composition. Furthermore, the surface composition of the bimetallic nanoalloy also plays a crucial role in relation to its catalytic properties such as selectivity and lifetime/durability of the catalyst (van der Oetelaar et al., 1998). The chemical properties of the nanoalloy which are of significance for catalytic applications may be fine-tuned by varying the nanocluster size, composition and chemical ordering of the constituents of the bimetallic nanoalloy (Johnston, 2003). Knowledge of the chemical ordering in unsupported bimetallic nanoparticles can be used to assess if the support material modifies the chemical ordering of bimetallic nanoparticles, which subsequently may affect the chemical reactivity of the supported bimetallic nanoparticles.

The kind of mixing or atom arrangement in nanoalloys can be categorised into three general groups (Johnston, 2003) depicted in Figure 3.1: mixed, segregated and core shell.

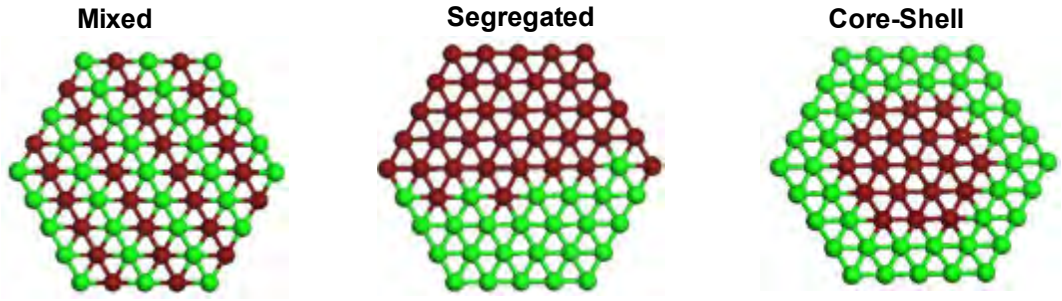


Figure 3.1: Different structures for the ordering in bimetallic alloys.

**Mixed nanoalloys**: This type of arrangement can consist of either randomly mixed (solid solution) or ordered mixing of the alloy constituents.
**Segregated**: This type of arrangement consists of atom type A and atom type B subclusters. The subclusters may share a mixed interface or have only a small number of A-B bonds.
**Core-shell:** In this type of arrangement a shell of atom type A surrounds a core of atom type B. There may be some mixing between the shell and interior.

Several factors are known to affect the ordering of the constituents of a nanoalloy. Depending on the size, geometry, composition of the cluster, chemical identity of the alloy constituents, preparation and experimental conditions the factors can enhance or counter each other (Massen et al., 2002; Lloyd et al., 2004; Ferrando et al., 2008a). The factors affecting the ordering in nanoalloys are (Ferrando et al., 2008a): maximisation of the strongest interatomic interactions, minimisation of the cluster surface energy, minimisation of bulk strain, charge transfer between alloy constituents, specific electronic or magnetic effects, strength of binding to surface ligands and the preference of one of the alloy constituent to bind a particular reactant, e.g. water, hydrogen, carbon monoxide or oxygen. In addition, van der Oetelaar et al. (1998) proposed that the metal-support interaction may influence surface segregation within supported nanoclusters by preferential anchoring of one of the alloy constituents at the cluster-support interface.

## 3.2 Modelling of binary nanoalloys as clusters

The main aim of structural search strategies is to obtain the arrangement of atoms corresponding to the lowest energy (i.e. global minimum) on the potential energy hypersurface (Johnston, 2003). The ability to predict the structure of binary alloys becomes a complicated exercise as the size of the cluster increases due to the many possible arrangements of the alloy constituents (Johnston, 2003). Therefore, the use of a high level of theory such as DFT to determine all the possible structural arrangements becomes prohibitive as the cluster size increases.

To overcome this complexity the possible low energy structures are identified using a low level theory such as a semi-empirical method to locate the minimum energy structures. The minimum energy structures obtained at the semi-empirical level are further refined using the DFT technique to obtain the absolute local minimum structures (Ferrando et al., 2008a). In the semi-empirical approach the metal-metal interactions are described using empirical potentials such as the many-body Gupta potential. The disadvantage of the semi-empirical methods such as the one employing the many-body Gupta potential is that the results obtained are dependent on the fitting parameters used to generate the potentials (Massen et al., 2002).

Different search approaches are used for determining the atomic arrangements in both monometallic and bimetallic nanoclusters. The search techniques include: genetic algorithm methods which mimic the biological mutating process to locate structures low energy

structures (Wales & Doye, 1997; Johnston, 2003) and Basin Hopping Monte Carlo algorithms which uses Monte Carlo steps to determine the lowest energy arrangement structures (Wales & Doye, 1997; Rossi & Ferrando, 2009). The Basin Hoping Monte Carlo can be coupled with a structure recognition algorithm and parallel excitable walker algorithm (Rossi & Ferrando, 2009) and many more structural search algorithms.

## 3.3 Symmetry as a tool for structural search of nanoclusters

One way to minimise the number of structural arrangements for a binary nanocluster is to use symmetry as a criterion for structural search. Wales (1998) and Oakley et al. (2013) have shown qualitatively that structures with high or approximate symmetry are expected to lie at the extremes of the potential energy distribution, i.e. global minima often have a significant number of symmetry elements.

High symmetry structural search makes use of magic structures, i.e. high symmetry structures which result in geometric shell closure. The number of atoms in a cluster resulting in a magic structure is referred to as a magic number. For the case of a binary nanocluster the composition resulting in a magic structure is termed a magic composition. Symmetry considerably reduces the number of compositional isomers (homotops)[1] to be investigated. For a binary nanocluster consisting of $N_A$ atoms of type A and $N_B$ atoms of type B with total atoms $N$, the number of homotops ignoring point group symmetry is given by (Wilson & Johnston, 2002):

$$^{N}P_{A,B} = \frac{N!}{N_A!N_B!} \approx 2^N \tag{3.1}$$

By including symmetry constraints, the number of homotops is reduced significantly, e.g. for the $Pt_{32}Pd_6$ cluster considered in the present study, the number of possible homotops = $2^{38} = 2.75 \times 10^{11}$ and by including symmetry constraints the homotops are reduced to $2^S = 2^3 = 8$. Where S is the number of atomic orbits of the cluster. For high symmetry constraint methods, the cluster is divided into a set of symmetry equivalent atoms which are referred to as atomic shells or orbits (Wilson & Johnston, 2002; Paz Borbón et al., 2007). The different atomic shells or orbits in a 38 atom truncated octahedron cluster (this cluster will be used in the present study) are illustrated in Figure 3.2, where the green atoms represent the core orbit which consists of 6 atoms. The second orbit is represented by the blue atoms consisting of 8 atoms

[1] Homotops are defined as isomers which have the same geometrical arrangement of atoms, but differ in the way in which type $A$ and $B$ atoms are arranged (Jellinek & Krissinel, 1996).

on the centre of the hexagonal (111)-like facets. The third orbit is represented by the yellow atoms consisting of 24 atoms at the corners.

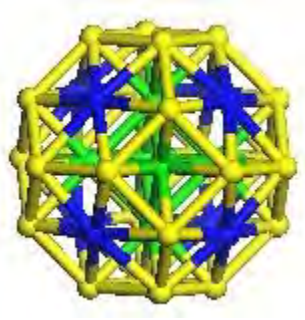

Figure 3.2: Different atomic orbits in a 38 atom truncated octahedron cluster, the three different orbits are represented by the green (coordination number 12), blue (coordination number 9) and yellow atoms (coordination number 6).

Ferrando et al. (2008a) and Massen et al. (2002) cautions that it can never be guaranteed that the absolute lowest energy homotops have been found for a particular geometry, but search methods should enable structures close to the global minimum structure to be obtained.

## 3.4 Previous studies on ordering in Pt-Pd clusters

Generally the search for the chemical ordering of the elements Pd and Pt in Pt-Pd nanoalloys can either follow a symmetry constrained search or a non-symmetry constrained search. In symmetry constraint search techniques the particle/cluster morphology/shape is known apriori whereas in non-symmetry constraint search techniques the particle morphology is not known beforehand.

Several computational studies have been undertaken to investigate the ordering in the unsupported Pt-Pd nanoalloy. The main conclusion is that the ordering of the elements is found to be independent of the cluster size and shape investigated. The preferred ordering in the unsupported Pt-Pd nanoalloy is the Pt core–Pd shell arrangement with the surface enriched in Pd and Pt preferring the interior. In the present study we make use of the high symmetry $Pt_{32}Pd_6$ cluster hence the literature survey on the arrangement of the Pt-Pd nanoalloy is biased towards the symmetry constrained search methods.

**Symmetry constrained search methods**

The truncated octahedron shape has been used to study ordering in the Pt-Pd nanoalloy. Using the empirical potential coupled with Monte Carlo simulations, Rousset et al. (1998) investigated ordering in the truncated octahedron cluster using the magic numbers 201, 586, 1289 and 2406 atoms. These magic numbers corresponded approximately to 1.8 nm, 2.6 nm, 3.4 nm and 4.2 nm particle sizes respectively. For both Pd and Pt rich compositions there was a strong tendency of Pd to migrate to the surface, with the surface composition of Pd being above 90 % regardless of the cluster size. For small cluster sizes the surface Pd occupies the low coordination sites, i.e. corners and edges. Whereas, for larger cluster sizes the Pd migrates/segregates to the planar (111) and (100) facets.

Barcaro et al. (2011) used DFT to investigate ordering in the Pt-Pd nanoalloy using the truncated octahedron of cluster size 38, 79, 116 and 201 atoms. The tendency of Pd to surface segregate was obtained wherein a single Pd dopant atom preferentially occupied the surface relative to the interior with an energy difference of 0.23 eV. A similar result has been obtained by Lloyd et al. (2004) where a single Pd dopant atom in 13 atom, 55 atom and 147 atom icosahedral and cuboctahedral clusters occupied a surface site. For the 38 atom cluster the composition $Pd_{32}Pt_6$ was calculated by Barcaro et al. (2011) to result in a perfect core shell arrangement with Pd on the shell and Pt in the core. A similar result was obtained by Paz Borbón et al. (2008).

At other cluster sizes, i.e. 79 and 116 atoms Barcaro et al. (2011) results indicated that at low Pt concentrations, Pt prefers the interior. At high Pt concentrations the Pd atoms prefers to segregate to the (100) facet or the corner atoms. For the 201 atom cluster an onion-like type arrangement was obtained around a composition of 50:50. The onion-like arrangement/multilayer was such that the centre of the surface (111) facets is occupied by Pt atoms whereas the Pd atoms were on the surface (100) facets and the edges. In the sublayers the arrangement was reversed with the Pd at the centre of the (111) facets and the Pt atoms at the (100) facets and edges, the arrangements alternated from shell to shell within the interior of the cluster. Barcaro et al. (2011) postulated that a probable explanation for the peculiar chemical ordering is due to the different behaviour of site energetics of the Pd and Pt atoms as a function of the coordination number, i.e. preferential strengthening of Pt-Pt (Pt-Pd) intrasurface and Pd-Pd (Pt-Pd) surface–subsurface bonds.

Tan et al. (2012) investigated using DFT Pt-Pd segregation in a 55 atom cuboctahedron cluster. The ground state was found to exhibit Pt core Pd shell properties across all compositions. At composition $Pt_{13}Pd_{42}$ the lowest energy structure was obtained which was a perfect core shell structure with all 13 Pt atoms in the core. For Pd rich compositions the

preferred Pd sites were the surface edges followed by face centre sites. Conversely, for Pt rich compositions, Pt preferred the core followed by inner shell sites before the surface sites can be occupied. With further increase in Pt concentration the surface edges become occupied. In addition, Rubinovich & Polak, (2009) using empirical potentials coupled with the free energy concentration expansion method (FCEM) calculated Pd surface segregation in a 923 atom cuboctahedral cluster of composition $Pt_{24}Pd_{899}$.

A recent study by Ishimoto & Koyama (2016) employed a 711 atoms cuboctahedron cluster (approximately 3nm particle) to investigate the ordering in a Pt-Pd alloy using DFT. The study revealed that for Pt rich compositions, a solid solution (mixed alloy) is the preferred arrangement. Whereas for Pd rich compositions a core shell arrangement with Pt in the core is the preferred arrangement and for intermediate compositions there is competition between the core shell and the solid solution arrangements. The configurational entropy contribution was found to be vital in determining whether the core shell or the solid solution arrangement is dominant. In addition, electron transfer between Pt and Pd atoms at the interfacial layers was found to play a dominant role in the ordering pattern.

## 3.5 Model description

In the present chapter the chemical ordering in the unsupported Pt-Pd nanoparticle will be investigated. The Pt-Pd nanoparticle will be modelled as a high symmetry 38 atom truncated octahedron cluster. The aim of this chapter is not to perform a thorough investigation of the ordering of Pt and Pd atoms in a binary cluster of these elements, but to use high symmetry and non-symmetry arrangements to investigate the preferred arrangement of Pt and Pd atoms at a fixed composition ($Pt_{32}Pd_6$) and shape (truncated octahedron). The $Pt_{32}Pd_6$ composition is chosen as the inverse Pt-rich composition of the $Pt_6Pd_{32}$ composition which results in a perfect core shell arrangement (Paz Borbón et al., 2008; Barcaro et al., 2011). In addition, the magic composition of 32:6 in a previous study by West et al. (2010) was chosen as a composition which allowed for the study of the different mixing patterns (i.e. mixed, core–shell and segregated) within the 38 atom truncated octahedron shape.

## 3.6 Computational methodology

DFT spin-polarised calculations were performed using the Vienna *ab-initio* Simulation package (VASP) (Kresse & Hafner, 1993; Kresse & Hafner, 1994; Kresse & Furthmüller,

1996a; Kresse & Furthmüller, 1996b). Periodic boundary conditions were utilised in the calculations by placing the cluster into a periodic supercell. The 38 atom truncated octahedron clusters, i.e. $Pt_{38}$, $Pd_{38}$ and $Pt_{32}Pd_6$ were placed in a periodic asymmetric box of dimensions (15×15×27) Å. The exchange and correlation effects were described using the PW91 functional (Perdew et al., 1992) within the generalised gradient approximation GGA method. The electron-ion interactions were described using the plane wave based projected augmented wave (PAW) pseudopotentials (Blöchl, 1994; Kresse & Joubert, 1999). A plane wave basis set cut off energy of 400 eV was used for the geometry optimisation of the clusters. The gamma centred single k-point was utilised because the clusters are isolated from periodic images so that there is no need for reciprocal space representation of the band structure states.

All atoms of the cluster were allowed to relax to their lowest energy state during the geometry optimisation calculations. The atoms were relaxed to their ground state energy using the conjugate gradient algorithm (Press et al., 1986). The convergence criteria for the geometry optimisation calculations were energy differences below $1\times10^{-5}$ eV and forces below 0.03 eV / Å. To speed up convergence the method of Methfessel Paxton (Methfessel & Paxton, 1989) with a smearing width σ = 0.2 eV was used.

The excess energy as defined by Ferrando et al. (2005) is used to assess if the mixing or chemical ordering of the $Pt_{32}Pd_6$ cluster is energetically favourable. The excess energy represents the energy gain or loss upon forming the bimetallic cluster relative to the pure metallic clusters of the same size and geometry. The excess energy is synonymous to the enthalpy change upon mixing at 0 K. The excess energy for the $Pt_{32}Pd_6$ cluster is calculated using the equation:

$$E_{excess} = E_{Pt_{32}Pd_6} - \frac{6}{38} \times E_{Pd_{38}} - \frac{32}{38} \times E_{Pt_{38}} \quad (3.2)$$

With $E_{Pt_{32}Pd_6}$ the energy of the optimised $Pt_{32}Pd_6$ cluster, $E_{Pd_{38}}$ the energy of the optimised $Pd_{38}$ cluster and $E_{Pt_{38}}$ the energy of the optimised $Pt_{38}$ cluster. An exothermic excess energy indicates that mixing or the chemical ordering of the structure is favoured relative to the separate state of the pure clusters of the same size. A highly exothermic excess energy corresponds to a more energetically stable chemical ordering.

## 3.7 Results and Discussion

A few select high symmetry arrangements of the $Pt_{32}Pd_6$ cluster are presented in Figure 3.3, whilst the rest of the investigated arrangements of the $Pt_{32}Pd_6$ cluster are presented in Appendix B.1. The least preferred arrangement of the Pt and Pd atoms in the $Pt_{32}Pd_6$ cluster is the perfect core shell arrangement with all 6 Pd atoms in the core. This arrangement has the most endothermic excess energy of 0.82 eV. This result is consistent with previous studies, and the unfavourable arrangement has been explained to be due to the preference of Pd to be on the surface due to its lower surface energy compared to Pt (Lloyd et al., 2004; Cheng et al., 2006; West et al., 2010).

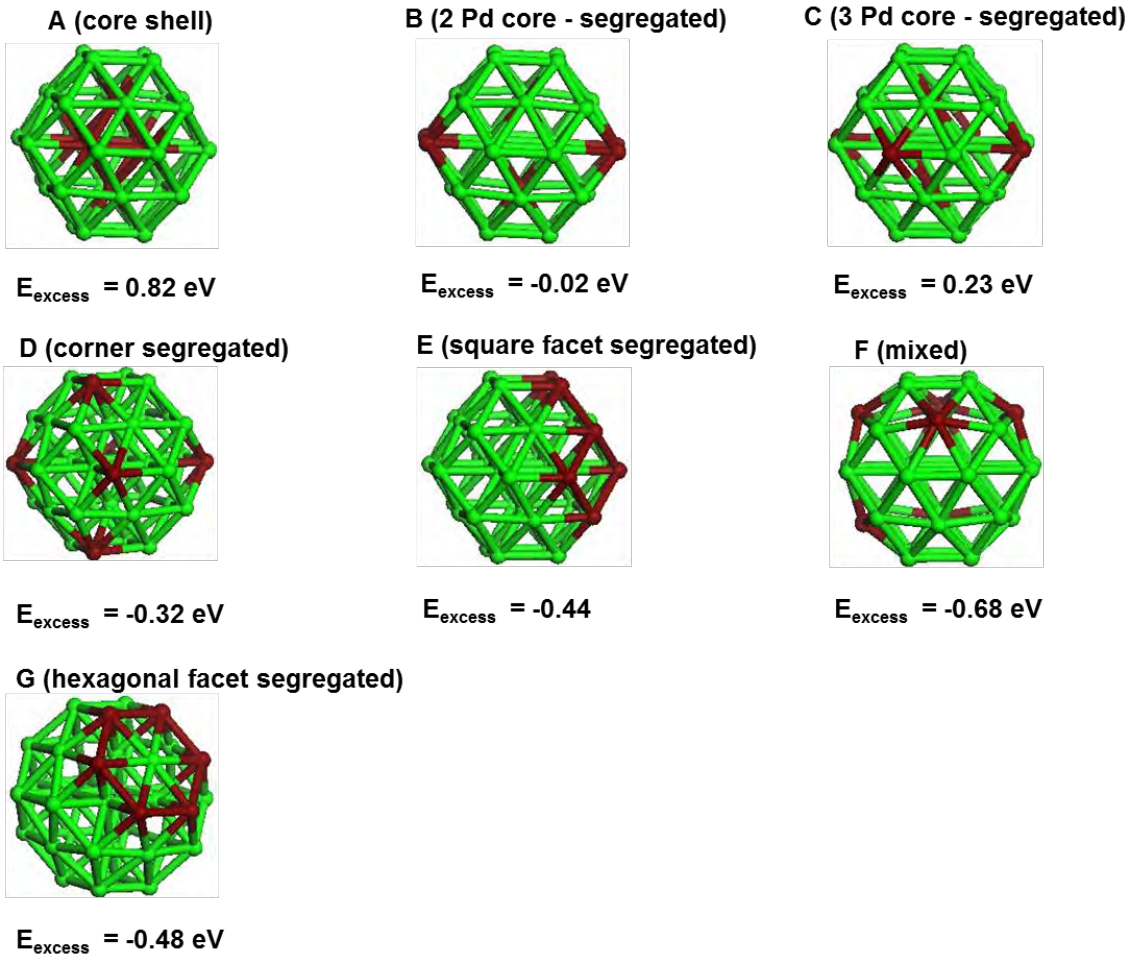


Figure 3.3: Structures of the different arrangements of the $Pt_{32}Pd_6$ truncated octahedron cluster with the calculated excess energy. The green atoms represent Pt atoms and the maroon colour represents Pd atoms.

From Figure 3.3 and Figure 3.4 (a) and (b) it is observed that the excess energy for arrangements in which some of the Pd atoms remain in the core region whilst the rest are on

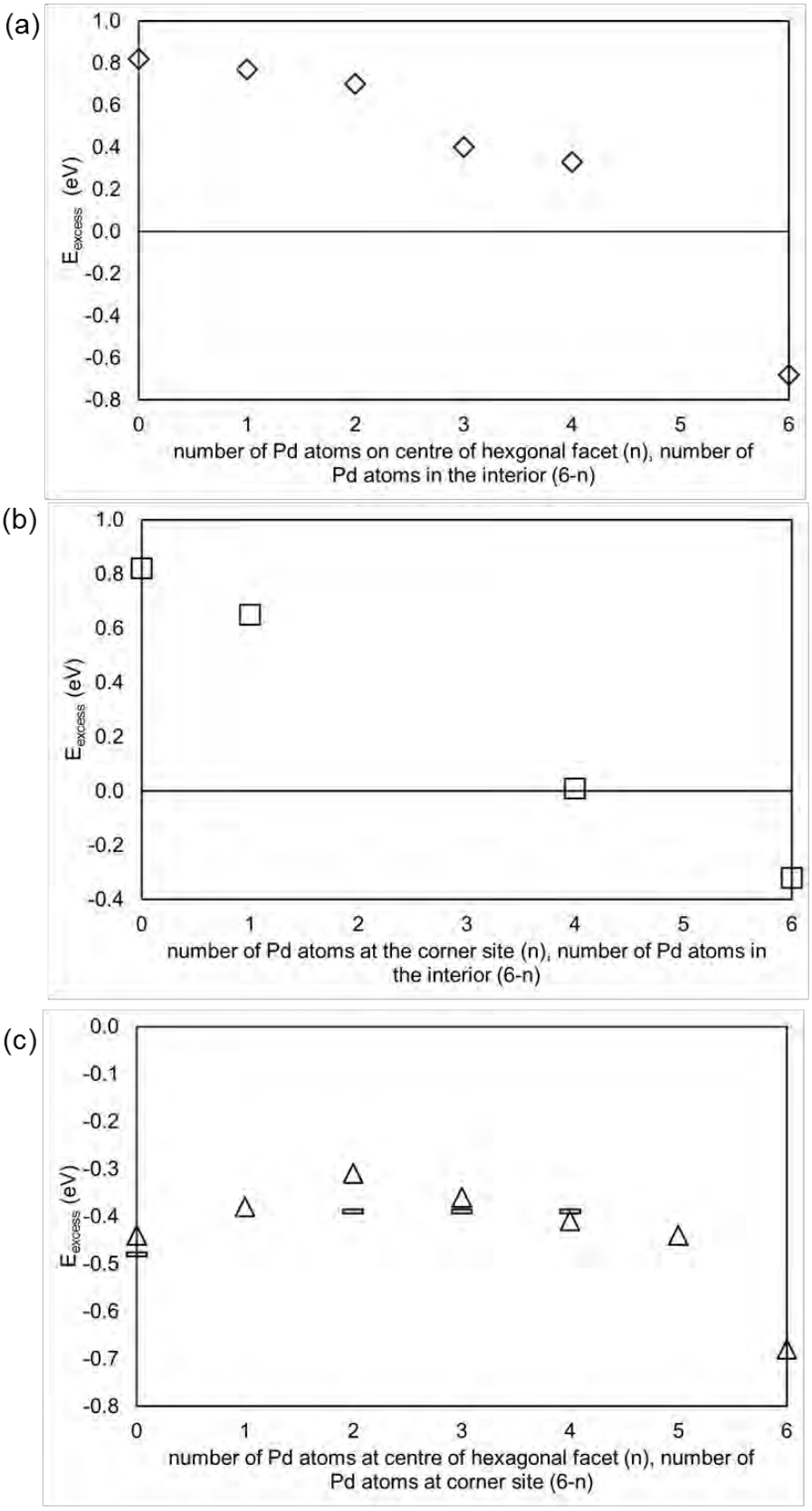


Figure 3.4: Plot of excess energy: (a) excess energy as a function of number of Pd atoms on centre of hexagonal facet, (b) excess energy as a function of number of Pd atoms at the corner site, (c) excess energy as a function of the distribution of Pd atoms at the corner and centre of hexagonal facet.

the surface (i.e. 2 Pd–core segregated and 3 Pd–core segregated structures) have endothermic excess energies. As the surface concentration of Pd atoms increases and the core concentration decreases the excess energy becomes less endothermic. The decrease in endothermicity of the excess energy with increase in surface concentration of Pd indicates the preference of Pd to be on the surface. In previous studies it has also been calculated that Pd surface segregate in Pt-Pd alloys in which Pt is the majority element (Rousset et al., 1998; Johnston, 2003; Lloyd et al., 2004; Rossi et al., 2005; Cheng et al., 2006; Paz Borbón et al., 2007; Rubinovich & Polak, 2009; Barcaro et al., 2011; Ishimoto & Koyama, 2016).

Structures in which all Pd atoms are located on the surface have exothermic excess energies (see Figure 3.4 (c) and Appendix B.1). This indicates that these are energetically preferred arrangements. The extent of the exothermicity of the excess energy depends on the location of the Pd atoms on the surface.

The structure which has the highest exothermic excess energy of -0.68 eV is the one in which all six Pd atoms are located at the centre of the hexagonal facets (mixed arrangement structure), i.e. coordination number 9. The arrangement in which all Pd atoms are located at the corner sites and far away from each other (corner segregated structure) has an excess energy of -0.32 eV. Comparing the lowest energy structure in which all Pd atoms are at the centre of the hexagonal facet (mixed structure) and the structure in which the Pd atoms are at the corner sites and away from each other (corner segregated structure) indicates that the stability and excess energy of the $Pt_{32}Pd_6$ cluster is dependent on the site of location hence the coordination number of the site. Previous studies have also observed that the stability in Pt-Pd alloys depends on the site of location of the Pt or Pd atoms (Barcaro et al., 2011; Tan et al., 2012).

Structures in which the Pd atoms on the surface are distributed between the corner site and the centre of the hexagonal facet site have lower excess energies than the lowest energy arrangement where all Pd atoms are at the centre of the hexagonal facet. Arrangements in which all surface Pd atoms occupy the corner sites, are in close proximity to each other and maximises the number of surface Pd-Pd bonds have more exothermic excess energies than when all 6 Pd atoms are at the corner sites without any surface Pd-Pd bonds (See Fig. 3.3 square segregated structure (-0.44 eV), hexagonal facet segregated structure (-0.48 eV) vs (-0.32 eV) corner segregated structure). This observation seems to contradict a previous study by Lloyd et al. (2004) which indicated that the preferred arrangements are the ones in which surface Pd-Pd bonds are minimised. In the present case the maximisation of surface Pd-Pd

bonds seems to compensate for the location of Pd at a low coordination site. Location at the low coordination site has a destabilising effect on the calculated excess energy of the cluster.

From Figure 3.4 (c) it is observed that the excess energy of structures in which Pd on the surface is distributed between the corner and the centre of the hexagonal facet sites depend on the concentration in the respective sites. Structures in which there is a higher concentration of Pd at the centre of the hexagonal facet sites than at the corner sites have slightly more exothermic excess energies than the cases where the concentration at the corner sites is higher. Arrangements in which the Pd atoms are at the corner sites and have a higher number of surface Pd-Pd bonds have slightly more exothermic excess energies than arrangements where there are few surface Pd-Pd bonds with Pd located at the corner sites. This is indicated in Figure 3.4 (c) by the data points represented by rectangles.

Having established that the excess energy is highly dependent on the location of Pd atoms, the excess energy was quantified depending on the location of the Pd atoms. The least energetically preferred arrangement of the core shell arrangement with all Pd atoms in the core region is found to have the most endothermic segregation energy per site, the excess energy per Pd atom occupying the core region is calculated to be 0.14 eV/ Pd atom. For the most energetically preferred arrangement where all the Pd atoms are located at the centre of the hexagonal facet (mixed structure), the excess energy per Pd atom occupying the centre of the hexagonal facet site is calculated to be -0.11 eV/Pd atom.

The calculated excess energy per corner site depends on whether the Pd atom at the corner site is bonded to another surface Pd atom. For the case where the Pd atoms are located at the corner site but without bonding to other surface Pd atoms (corner segregated structure) the excess energy per corner site is calculated to be -0.05 eV/Pd atom. This indicates why there is a strong preference of Pd atoms to occupy the central sites on the hexagonal facet compared to the corner sites, since at the central site the excess energy per atom is twice that at the corner site. The excess energy for the Pd atoms at the corner site slightly increases when the Pd atoms at the corner sites form Pd-Pd bonds with other surface Pd atoms at corner sites (see square facet segregated and hexagonal facet segregated structures in Figure 3.3). For the square facet segregated structure and hexagonal facet segregated structures in Figure 3.3 the excess energy per Pd atom are -0.07 eV/ Pd atom and -0.08 eV/Pd atom respectively.

In Tables 3.1 – 3.3 the bond lengths of the unique facets of the core shell structure, hexagonal facet segregated structure and mixed structure are presented. These structures are taken as representative examples to elucidate the effect of relaxation on the final structure of the

cluster. The facets are unique in the sense that the other facets of the cluster have identical bond lengths to the unique facet hence they are representative of those other identical facets. A description of labelling of the unique facets in the mixed structure is presented in Appendix B.2. This structure is the most stable arrangement of the $Pt_{32}Pd_6$ cluster which will be used in other chapters of this study.

Table 3.1: Bond lengths of the unique facets for the core shell structure (structure A).

| **core shell (structure A)** | | | | | |
|---|---|---|---|---|---|
| **Square Facet** | | **Hexagonal facet** | | | |
| | | *Side length* | | *Diagonal length* | |
| $d_{Pt-Pt}$ (Å) | | $d_{Pt-Pt}$ (Å) | 2.70 | $d_{Pt-Pt}$ (Å) | 2.69 |
| | 2.71 | | 2.66 | | 2.69 |
| | 2.71 | | 2.71 | | 2.70 |
| | 2.70 | | 2.66 | | 2.69 |
| | 2.70 | | 2.71 | | 2.69 |
| | | | 2.66 | | 2.70 |

Structures in which Pd atoms are located at the centre of the hexagonal facet appear to be somewhat distorted and swelling out upon relaxation. The central Pd atom is pushed out of plane relative to the Pt atoms making up the hexagonal facet. Structures in which the Pd atoms are not occupying the central site on the hexagonal facet retain the almost perfect truncated octahedron shape without bulging upon structural relaxation.

Of all investigated structures of the $Pt_{32}Pd_6$ cluster, the structure which undergoes the highest extent of structural change upon relaxation is the lowest energy structure with an excess energy of -0.68 eV. The structural change in this structure is clearly visible as evidenced by distortion from the perfect truncated octahedron cluster to a ball like structure, with central Pd atoms elevated out of plane relative to other Pt atoms of the hexagonal facet.

To quantify the extent of distortion upon relaxation the bond lengths reported in Tables 3.1 – 3.3 are compared. Comparison of hexagonal facets bound by Pt atoms in all three structures indicates that in the core shell structure (structure A) and hexagonal facet segregated structure (structure G), the side lengths of these hexagonal facets are almost identical. Juxtaposing these side bond lengths (for Pt only bound hexagonal facets in core shell structure (structure A) and hexagonal facet segregated structure (structure G)) to the side lengths for facet C in the mixed structure (structure F), it is observed that on facet C the side lengths are slightly

contracted. Thus, location of Pd atoms at the centre of the hexagonal facet in facet C results in compressive strain on the Pt-Pt side bond lengths as evidenced by the shorter Pt-Pt bond lengths.

Table 3.2: Bond lengths of the unique facets for the hexagonal facet segregated structure (structure G)

| **hexagonal facet segregated structure (structure G)** | | | | | | | |
|---|---|---|---|---|---|---|---|
| **Square Facets** | | | | | | | |
| $d_{Pt\text{-}Pd}$ (Å) | 2.73 | | $d_{Pt\text{-}Pt}$ (Å) | 2.66 | | | |
| $d_{Pt\text{-}Pd}$ (Å) | 2.73 | | | 2.71 | | | |
| $d_{Pt\text{-}Pt}$ (Å) | 2.67 | | | 2.71 | | | |
| $d_{Pd\text{-}Pd}$ (Å) | 2.77 | | | 2.71 | | | |
| **Hexagonal Facets** | | | | | | | |
| *Side length* | | *Diagonal length* | | *Side length* | | *Diagonal length* | |
| $d_{Pd\text{-}Pd}$ (Å) | 2.77 | $d_{Pt\text{-}Pd}$ (Å) | 2.75 | $d_{Pt\text{-}Pd}$ (Å) | 2.73 | $d_{Pt\text{-}Pd}$ (Å) | 2.71 |
| | 2.71 | | 2.75 | | 2.73 | | 2.71 |
| | 2.77 | | 2.75 | $d_{Pd\text{-}Pd}$ (Å) | 2.71 | $d_{Pt\text{-}Pt}$ (Å) | 2.69 |
| | 2.71 | | 2.75 | $d_{Pt\text{-}Pt}$ (Å) | 2.66 | | 2.71 |
| | 2.77 | | 2.75 | | 2.66 | | 2.71 |
| | 2.71 | | 2.75 | | 2.66 | | 2.69 |
| | | | | | | | |
| *Side length* | | *Diagonal length* | | | | | |
| $d_{Pt\text{-}Pt}$ (Å) | 2.66 | $d_{Pt\text{-}Pt}$ (Å) | 2.67 | | | | |
| | 2.71 | | 2.73 | | | | |
| | 2.64 | | 2.69 | | | | |
| | 2.71 | | 2.69 | | | | |
| | 2.66 | | 2.73 | | | | |
| | 2.67 | | 2.67 | | | | |

The compressive strain can be rationalised by the difference in atomic size between Pt (1.77 Å) and Pd (1.69 Å) (Clementi et al., 1967). Placing the smaller Pd atom at the centre of the hexagonal facet consisting of Pt atoms only will contract the Pt-Pt side bond lengths. The effect of compressive strain is the central Pd atom is pushed out of plane in order to relieve the strain. This in turn results in elongation of diagonal Pt-Pd bond lengths leading to observed structural distortion and swelling. Distortion upon locating the Pd atom at the centre of the hexagonal facet bound by Pt atoms only is also observed from the shorter Pt-Pt side bond

lengths of facet D in the mixed structure (structure F) compared to those in the core shell structure (structure A) and hexagonal facet segregated structure (structure G).

Table 3.3: Bond lengths of the unique facets for the mixed structure (structure F)

| **mixed structure (structure F)** | | | | | | | |
|---|---|---|---|---|---|---|---|
| **Square Facets** | | | | | | | |
| **Facet A** | | | | **Facet B** | | | |
| $d_{Pt-Pt}$ (Å) | 2.64 | | $d_{Pt-Pt}$ (Å) | 2.65 | | | |
| | 2.64 | | | 2.65 | | | |
| | 2.66 | | | 2.70 | | | |
| | 2.66 | | | 2.70 | | | |
| **Hexagonal Facets** | | | | | | | |
| **Facet C** | | | | **Facet D** | | | |
| *Side length* | | *Diagonal length* | | *Side length* | | *Diagonal length* | |
| $d_{Pt-Pt}$ (Å) | 2.64 | $d_{Pt-Pd}$ (Å) | 2.78 | $d_{Pt-Pt}$ (Å) | 2.57 | $d_{Pt-Pd}$ (Å) | 2.75 |
| | 2.56 | | 2.79 | | 2.66 | | 2.74 |
| | 2.65 | | 2.79 | | 2.61 | | 2.76 |
| | 2.57 | | 2.78 | | 2.65 | | 2.75 |
| | 2.64 | | 2.77 | | 2.60 | | 2.76 |
| | 2.57 | | 2.77 | | 2.66 | | 2.74 |
| | | | | | | | |
| **Facet E** | | | | | | | |
| *Side length* | | *Diagonal length* | | | | | |
| $d_{Pt-Pt}$ (Å) | 2.61 | $d_{Pt-Pt}$ (Å) | 2.70 | | | | |
| | 2.68 | | 2.70 | | | | |
| | 2.61 | | 2.70 | | | | |
| | 2.69 | | 2.70 | | | | |
| | 2.62 | | 2.70 | | | | |
| | 2.69 | | 2.69 | | | | |

The Pt-Pt side bond lengths in facet D of the mixed structure (structure F) are shorter than the side lengths for the hexagonal facets bordered by Pt atoms only in the core shell structure (structure A) and hexagonal facet segregated structure (structure G).

Furthermore, structural distortion in the mixed structure (structure F) is evident from the Pt-Pt bond distances on facet E which consists only of Pt atoms. The side lengths in facet E are slightly shortened relative to those of the hexagonal facet in the core shell structure (structure

A) whilst the diagonal bond length in facet E are similar to those in the core shell structure (structure A). Moreover, the Pt-Pt bond lengths of the square facets in the mixed structure (structure F), i.e. facets A and B are shorter than the calculated Pt-Pt bond lengths of the square facets consisting only of Pt atoms in the core shell structure (structure A) and hexagonal facet segregated structure (structure G). This further strengthens the observation that there is compressive strain on the Pt-Pt bonds in the mixed structure (structure F).

The Pd-Pd side bond lengths of the hexagonal facet bound by Pd atoms only in structure G (hexagonal facet segregated structure) are longer than the Pt-Pt side bond lengths for hexagonal facets bound by Pt atoms only in structures A (core shell structure) and F (mixed structure). This is rationalised by the slightly bigger Pt atom occupying the centre of the hexagonal facet consisting of smaller Pd atoms. The effect of the bigger Pt atom is to elongate the Pd-Pd side lengths. Therefore, the Pd-Pd bonds on the hexagonal facet bound by Pd atoms are under tensile strain. The diagonal Pt-Pd bond lengths of the hexagonal facet bound by Pd atoms only in the hexagonal facet segregated structure (structure G) (see Table 3.2) are slightly shorter than the diagonal Pt-Pd bond lengths of facet C (see Table 3.3) and almost identical to the diagonal bond lengths of facet D (see Table 3.3) in the mixed structure (structure F). Tensile strain on the hexagonal facet bound by Pd atoms only in the hexagonal facet segregated structure (structure G) does not result in the central Pt atom being elevated out of plane relative to other atoms of the hexagonal facet. Thus, there is no observable structural change and swelling of the structure upon relaxation.

## 3.8 Conclusions

The preferred arrangement for the $Pt_{32}Pd_6$ cluster is the solid solution arrangement where the Pd atoms are mixed with Pt atoms and are located on the surface. The least preferred arrangement of the $Pt_{32}Pd_6$ cluster is the core shell arrangement with all the Pd atoms located in the core. Distribution of Pd atoms on the surface between the corner and centre of hexagonal facet site lowers the excess energy of the cluster.

On the surface, Pd atoms prefer to be at the centre of the hexagonal facet where the excess energy per site is more exothermic than at the corner site. The excess energy per site is exothermic for the surface sites, i.e. centre of hexagonal facet and corner sites whilst for the interior site the excess energy per site is endothermic. This indicates that the interior site is the least stable site for Pd location.

The structural arrangement with all Pd atoms located at the centre of the hexagonal facet undergoes the highest extent of structural change and distortion upon relaxation. The high degree of structural change is due to compressive strain experienced by Pt atoms bounding the hexagonal facet which has a Pd atom at the centre. The compressive strain is relieved by pushing the central Pd atom out of plane relative to Pt atoms of the facet.

# 3.9 References

Barcaro, G., Fortunelli, A., Polak, M. & Rubinovich, L. (2011) Patchy multishell segregation in Pt-Pd alloy nanoparticles. *Nano Lett.* **11**, 1766-1769.

Blöch, P.E. (1994) Projector augmented-wave method*. Phys. Rev. B* **50**, 17953-17979.

Cheng, D., Huang, S. & Wang, W. (2006) Structures of small Pt-Pd bimetallic clusters by Monte Carlo simulation. *Chem. Phys.* **330**, 423-430.

Clementi, E., Raimondi, D.L. & Reinhardt, W.P. (1967) Atomic screening constants from SCF functions. II Atoms with 37 to 86 electrons. *J. Chem. Phys*. **47**, 1300-1307.

Ferrando, R., Fortunelli, A. & Rossi, G. (2005) Quantum effects on the structure of pure and binary metallic nanoclusters. Phys. Rev. B **72**, 085449-085458.

Ferrando, R., Jellenik, J. & Johnston, R.L. (2008a) Nanoalloys: From theory to applications of alloy clusters and nanoparticles. *Chem. Rev.* **108**, 845-909.

Ferrando, R., Fortunelli, A. & Johnston, R.L. (2008b) Searching for the optimum structures of alloy nanoclusters. *Phys. Chem. Chem. Phys*. **10**, 640-649.

Ishimoto, T. & Koyama, M. (2016) Electronic structure and phase stability of PdPt nanoparticles. *J. Phys. Chem. Lett*. **7**, 736-740.

Jellinek, J. & Krissinel, E.B. (1996) $Ni_n Al_m$ alloy clusters: analysis of structural forms and their energy ordering. *Chem. Phys. Lett.* **258**, 283-292.

Johnston, R.L. (2003) Evolving better nanoparticles: Genetic algorithms for optimising cluster geometries. *Dalton Trans*.: 4193-4207.

Kresse, G. & Hafner, J. (1993) *Ab initio* molecular dynamics for liquid metals. *Phys. Rev. B* **47**, 558-561.

Kresse, G. & Joubert, D. (1999) From ultrasoft pseudopotentials to the projector augmented-wave method. *Phys. Rev. B* **59**, 1758-1775.

Kresse, G. & Hafner, J. (1994) Ab initio molecular-dynamics simulation of the liquid-metal-amorphous-semiconductor transition in germanium. *Phys. Rev. B* **49**, 14251-14269.

Kresse, G. & Furthmüller, J. (1996a) Efficiency of ab initio total energy calculations for metals and semiconductors using a plane-wave set. *Comput. Mater. Sci.* **6**, 15-50.

Kresse, G. & Furthmüller, J. (1996b) Efficient iterative schemes for ab initio total-energy calculations using a plane-wave basis set. *Phys. Rev. B* **54**, 11169-11186.

Lloyd, L.D., Johnston, R.L., Salhi, S. & Wilson, N.T. (2004) Theoretical investigation of isomer stability in platinum-palladium nanoalloy clusters. *J. Mater. Chem.* **14**, 1691-1704.

Massen, C., Mortimer-Jones, T. & Johnston, R.L. (2002) Geometries and segregation properties of platinum-palladium nanoalloy clusters. *Dalton Trans*.: 4375-4388.

Methfessel, M. & Paxton, A.T. (1989) High-precision sampling for Brillouin-zone integration in metals. *Phys. Rev. B* **40**, 3616-3621.

Oakley, M.T., Johnston, R.L. & Wales, D.J. (2013) Symmetrisation schemes for global optimisation of atomic clusters. *Phys. Chem. Chem. Phys*. **15**, 3965-3976.

Paz-Borbón, L.O., Johnston, R.L., Barcaro, G. & Fortunelli, A. (2007) A mixed structural motif in 34-atom Pt-Pd clusters. *J. Phys. Chem. C* **111**, 2936-2941.

Paz- Borbón, L.O., Johnston, R.L., Barcaro, G. & Fortunelli, A. (2008) Structural motifs, mixing, and segregation effects in 38-atom binary clusters. *J. Chem. Phys*. **128**, 134517-134529.

Perdew, J.P., Chevary, J.A., Vosko, S.H., Jackson, K.A., Pederson, M.R., Singh, D.J. & Fiolhais, C. (1992) Atoms, molecules, solids, and surfaces. Applications of the generalized gradient approximation for exchange and correlation. *Phys. Rev. B* **46**, 6671-6687.

Press, W.H., Flannery, B.P., Tenkolsky, S.A. & Vetterling, W.T. (1986) *em Numerical Recipes*. Cambridge University Press: New York.

Rossi, G. & Ferrando, R. (2009) Searching for low-energy structures of nanoparticles: a comparison of different methods and algorithms. *J. Phys.: Condes. Matter* **21**, 084208-084219.

Rossi, G., Ferrando, R., Rapallo, A., Fortunelli, A., Curley, B.C., Lloyd, L.D. & Johnston, R.L. (2005) Global optimization of bimetallic cluster structures. II Size-matched Ag-Pd, Ag-Au and Pt-Pd systems. *J. Chem. Phys.* **122**, 194309-194318.

Rousset, J.L., Renouprez, A.J. & Cadrot, A.M. (1998) Ion-scattering study and Monte-Carlo simulations of surface segregation in Pt-Pd nanoclusters obtained by laser vaporization of bulk alloys. *Phys. Rev. B* **58**, 2150-2156.

Rubinovich, L. & Polak, M. (2009) Prediction of distinct surface segregation effects due to coordination-dependent bond-energy variations in alloy nanoclusters. *Phys. Rev. B* **80**, 045404-045412.

Tan, T.L., Wang, L.L., Johnson, D.D. & Bai, K. (2012) A comprehensive search for stable Pt-Pd nanoalloy configurations and their use as tunable catalysts. *Nano Lett.* **12**, 4875-4880.

van der Oetelaar, L.C.A., Nooij, O.W., Oerlemans, S., Denier van der Gon, A.W., Brongersma, H.H., Lefferts, L., Roosenbrand, A.G. & van Veen, J.A.R. (1998) Surface segregation in supported Pt-Pd nanoclusters and alloys. *J. Phys. Chem. B* **102**, 3445-3455.

Wales, D.J. & Doye, J.P.K. (1997) Global optimization by basin-hopping and the lowest energy structures of Lennard-Jones clusters containing upto 110 atoms. *J. Phys. Chem. A* **101**, 5111-5116.

Wales, D. J. (1998) Symmetry, near-symmetry and energetics. *Chem. Phys. Lett.* **285**, 330-336.

West, P.S., Johnston, R.L., Barcaro, G. & Fortunelli, A. (2010) The effect of CO and H chemisorption on the chemical ordering of bimetallic clusters. *J. Phys. Chem. C*. **114**, 19678-19686.

Wilson, N.T. & Johnston, R.L. (2002) A theoretical study of atom ordering in copper-gold nanoalloy clusters. *J. Mater. Chem.* **12**, 2913-2922.

# Chapter 4: $Pt_{38}$ cluster interaction with pristine, monovacancy and functionalised graphene

## 4.1 Introduction

Carbon in its different forms can be utilised as a support for the active metal in heterogeneous catalysts (Rodríguez-Reinoso et al., 1986; Kou et al., 2011). In some applications carbon is preferred as a support material because it does not interact strongly with the active material as a metal oxide support would (Rodríguez-Reinoso et al., 1986). Further, in other applications such as polymer electrolyte fuel cells, carbon is preferred as a support material because of its high surface area and electrical conductivity (Wissler, 2006; Shao et al., 2009; Kou et al., 2011). Different forms of carbon which are used as support material include: carbon black, e.g. Vulcan, Ketjen Black etc., single walled or multi walled carbon nanotubes, carbon nanospheres, graphene and graphitized carbon (Shao et al., 2009).

Carbon materials can have a variety of functional groups, the source of which can vary, some are naturally occurring within the material whilst others are a result of the synthesis method of the carbon materials (Rodríguez-Reinoso et al., 1986; Prado-Burguete et al., 1989) and some can be intentionally added to the material via functionalisation (Chen et al., 1998; Kuznetsova et al., 2001; Schniep et al., 2006; Coleman et al., 2008; Kou et al., 2009; Burgess et al., 2015). For the present study we will only focus on the oxygen surface functional groups. Spectroscopic techniques have indicated that the surface oxygen functional groups on the carbon framework can be in the form of the following groups, OH, C-O, C=O, COOH, epoxides and many other forms (Prado-Burguete et al., 1989; Chen et al., 1998; Kuznetsova et al., 2001; Coleman et al., 2008; Burgess et al., 2015). The synthesis of supported catalysts involves deposition of the catalytically active material onto the support via e.g. incipient wetness impregnation or deposition of a colloid of the active metal onto the support. The functional groups present on the surface of the carbon support have been postulated to act as nucleation sites or anchoring sites for the deposition of the active metal and hence assist in the dispersion of the catalytically active material on the catalyst support (Prado-Burguete et al., 1989).

One of the steps in the synthesis of carbon supported catalysts can involve a pretreatment step where the carbon support is treated with $HNO_3$ acid and or $H_2O_2$. The treatment step results in the formation of surface defects in the form of atom vacancies which are occupied by functional groups (Balasubramaniam & Burghard, 2005; Coleman et al., 2008). Recently a study by Burgess et al. (2015) has shown that mild treatment with low concentration of $HNO_3$ of highly oriented pyrolytic graphite HOPG results in the generation of OH groups on the HOPG surface. Treatment of the HOPG with higher concentrations of $HNO_3$ was observed to result in formation of the COOH functional group. Burgess et al. (2015) further investigated the influence of the functional groups on the growth of gold nanoparticles on functionalised HOPG, and observed that gold nanoparticles grew close to the OH functional group which were located on the terrace of the basal graphene plane and not at the edges. Edwards et al. (2014) observed that a Pd-Au/C catalyst for $H_2O_2$ synthesis whose carbon support had been pretreated with acid showed higher catalytic activity than the catalyst whose carbon support was not pretreated in acid. It was proposed that the pretreatment step of the carbon support is not only to remove contaminants but also affects the activity of the catalyst (Edwards et al., 2014). Therefore, there is need to investigate further the role of the surface oxygen functional groups in relation to the activity of supported clusters.

Density functional theory studies have been performed to study interaction between graphene and Pt particles. Most of the studies are limited to small size clusters ranging from a single atom to n = 13 atoms (Kong et al., 2006; Okamoto, 2006; Okazaki-Maeda et al., 2010; Lim & Wilcox, 2011; Fampiou & Ramasubramaniam, 2012; Fampiou & Ramasubramaniam, 2013). Pt interaction with pristine graphene is found to be weak due to the high cohesive energy of Pt and thus Pt-Pt bonds are stronger compared to Pt-C bonds (Maiti & Ricca, 2004). Defective graphene with a monovacancy has been observed to bind Pt clusters stronger than pristine graphene (Lim & Wilcox, 2011; Fampiou & Ramasubramaniam, 2012). The strong binding energy on monovacancy graphene is due to the formation of strong Pt-C bonds at the vacancy site between Pt and carbon atoms which are coordinatively unsaturated at the vacancy (Fampiou & Ramasubramaniam, 2012).

DFT studies which investigate the binding of Pt clusters on oxygen functionalised graphene have focussed on edge functionalisation and not on terrace functionalisation. However, the experimental study of Burgess et al. (2015) has shown that the functional groups can be located on the terrace. The oxygen functional groups were calculated to stabilise binding of Pt clusters relative to pristine graphene (Vedala et al., 2011; Kou et al., 2011; Chutia et al., 2014). Vedala et al. (2011) observed through DFT calculations that edge epoxide functionalised graphene has a stronger stabilising effect on the $Pt_{27}$ cluster than OH-edge functionalised

graphene. However, the study did not elucidate further what was the source of the difference in stabilising effect between the epoxide and OH functional groups.

Denis & Iribarne (2013) showed using DFT calculations that monovacancy graphene is the most reactive type of defect towards functional group addition compared to other types of defects such as 585 double vacancy, 555-777 reconstructed double vacancy, Stone-Wales defect, hydrogenated zig zag and hydrogenated armchair edge (see Figure 4.1). Therefore, we believe that despite monovacancy defective graphene binding the Pt cluster strongly, the monovacancy is unlikely to exist in isolation under reaction conditions. Surface oxygen functional groups will attach to the monovacancy site since it is highly reactive. Hence, it is vital to investigate the interaction of the Pt cluster with the oxygen functional group attached to the vacancy site on graphene as model for the functionalised graphene support.

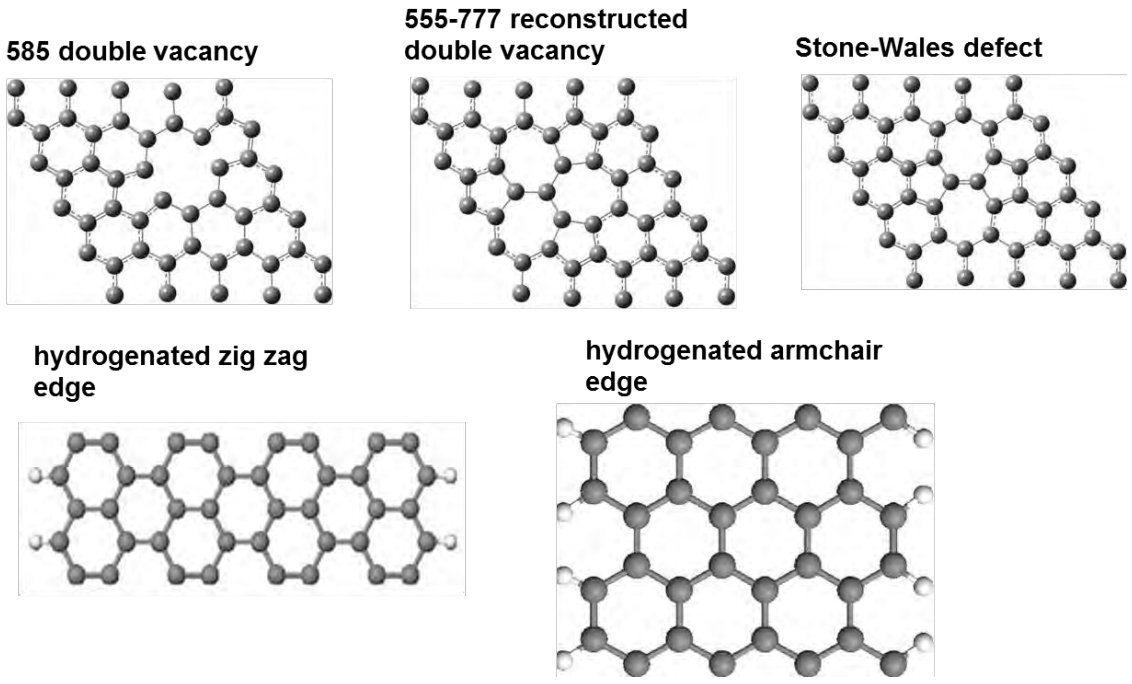


Figure 4.1: Different type of defects on graphene.

Vanin et al. (2010) observed through GGA calculations utilising the revPBE functional that the was no binding of graphene to a Pt (111) slab. However, experimental observations for graphite monolayer (which is equivalent to a graphene sheet) on metal (111) surfaces including Pt (111) indicates that there is weak interaction between graphene and the Pt (111) surface (Preobrajenski et al., 2008; Sutter et al., 2009). Prediction of non-binding at the GGA level has been described to be due to the absence of non-local correlation effects in local and semi-local GGA functionals (Vanin et al., 2010). Long range correlation effects are important

for weak interacting systems such as graphene on metal surfaces since these systems are dominated by weak dispersion forces such as the van der Waals forces (Fuentes-Cabrera et al., 2008; Vanin et al., 2010).

The weak interaction between graphene and the Pt (111) surface has been experimentally observed from the C 1s spectrum from NEXAFS. The C 1s peak of highly oriented pyrolytic graphite (HOPG) was found to be the same as the C 1s peak of graphene atoms bound to the Pt (111) surface (Preobrajenski et al., 2008). The similarity of the electronic structure of the bare HOPG and that of the graphene atoms bonded to the Pt (111) was considered an indication of no orbital interaction between the C 2p states and the Pt 5d states, hence the weak interaction between graphene and Pt (111) (Preobrajenski et al., 2008).

LDA calculations have been performed to investigate the binding of graphene to Pt (111), the LDA method is known to result in overestimation of the binding energy (Vanin et al., 2010). van der Waals density functional vdW-DF (Dion et al., 2004) which incorporates non-local correlations effects was used to determine the binding of graphene to Pt (111) and an exothermic binding energy was obtained (Vanin et al., 2010).

From the literature survey it is evident that the Pt-graphene interaction is dominated by van der Waals interactions due to the weak interaction between graphene and Pt. Moreover, standard DFT calculations have been found to be inadequate to account for van der Waals interactions, thus DFT methods incorporating van der Waals interactions are sought to describe the Pt-graphene interaction. Standard DFT and DFT incorporating van der Waals corrections will be utilised in this chapter.

In this chapter the interaction of the $Pt_{38}$ cluster with different graphene based support materials will be investigated with the aim of gaining more insight into the metal–substrate interaction for carbon supported materials. The graphene based supports to be investigated are pristine graphene, monovacancy defective graphene, OH and COOH functionalised graphene. The carbon support is represented by a single graphene layer. The functional groups (i.e. OH and COOH) in the present study will be positioned on the terrace of the graphene and not at the edges as in previous DFT studies. The rationale for placing the functional groups on the terrace is from the study by Burgess et al. (2015) which indicated that for $HNO_3$ mildly treated HOPG, the OH groups are located at the terrace sites and Au clusters deposited at the terrace sites. The Pt nanoparticle will be represented by a 38 atom truncated octahedron cluster. The truncated octahedron cluster is utilised since it has face centre cubic

packaging which is the bulk crystal structure packing of metallic Pt (Paz-Borbón et al., 2008). The $Pt_{38}$ truncated octahedron cluster is approximately 1 nm in diameter.

# 4.2 Methodology

## 4.2.1 Models for the support materials

Pristine graphene is represented by a single graphene sheet of periodicity (6 × 6). To create a monovacancy defective graphene, a single carbon atom at the centre of the graphene sheet is removed resulting in three dangling bonds at the vacancy site. The OH and COOH functionalised graphene are generated from the monovacancy defective graphene. OH functionalised graphene is generated by adding a single OH group to one of the 3 carbon atoms with dangling bonds with the two remaining carbon atoms saturated with atomic hydrogen each.

Different combinations of the OH and the H atoms at the vacancy site were investigated and relaxed through geometry optimisation. The investigated combinations are: OH group and one H atom on one side of the graphene pointing out of plane with the other H atom on the opposite side of graphene and pointing in the opposite direction, the OH group and the two H atoms located on the same side of the graphene and pointing in the same direction and the final configuration was where the OH group was on one side of the graphene pointing out of plane with the two H atoms on the opposite side of the graphene plane and pointing in the opposite direction as the OH group.

COOH functionalised graphene was constructed the same way as the OH functionalised graphene with the COOH functional group replacing the OH group. As for the case of OH functionalised graphene, different starting configurations similar to those for OH were investigated for the COOH functionalised graphene support.

## 4.2.2 Pt nanoparticle model

The Pt nanoparticle is represented by a 38 atom truncated octahedron cluster which has been optimised in an asymmetric box of dimensions (15 × 15 × 28) Å. The $Pt_{38}$ cluster consists of square (100)-like facets and hexagonal (111)-like facets shown in Figure 4.2.

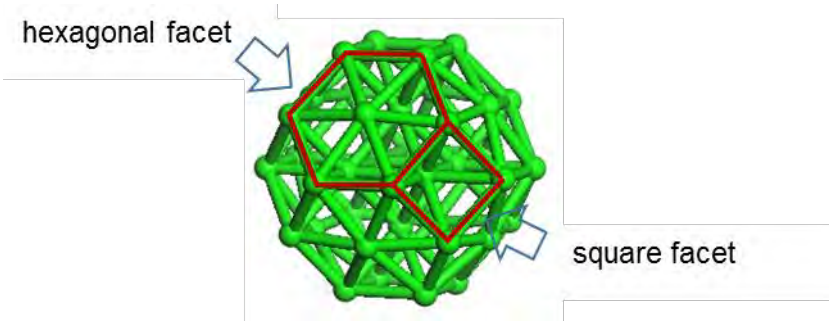


Figure 4.2: $Pt_{38}$ cluster with hexagonal and square facets highlighted

### 4.2.3 $Pt_{38}$ interaction with the different graphene support materials

For adsorption of the $Pt_{38}$ cluster on the different graphene supports, the only investigated geometries of approach of the cluster to the support is through the facets not through edge or corner atoms. According to Ramos-Sanchez & Balbuena (2013) the facet approach is expected to be a stable adsorption state. However, we are aware that the facet approach may not necessarily lead to a global minimum adsorption state, but may result in a local minimum adsorption state. Approach of the $Pt_{38}$ cluster to the support was investigated through the square (100)-like facet and the hexagonal (111)-like facet of the $Pt_{38}$ cluster.

#### 4.2.3.1 $Pt_{38}$ interaction with pristine and monovacancy defective graphene

For adsorption on both pristine and monovacancy graphene, two adsorption configurations were investigated. One adsorption geometry was adsorption via the square facet and the other geometry was through the hexagonal facet. Adsorption was investigated on only one side of the graphene sheet since adsorption from the top and from underneath should be the same owing to symmetry of the graphene sheet. The initial geometries were such that the atoms on the facet of the cluster approaching the support were placed atop the carbon atoms of the support.

#### 4.2.3.2 $Pt_{38}$ interaction with OH and COOH functionalised graphene

For adsorption on OH and COOH functionalised graphene two different adsorption approaches were investigated. The first approach was approach from the atop position of the graphene on the side bearing the OH or COOH functional group. For the atop position the investigated geometry of interaction was limited to the case where the cluster is directly atop the oxygen atom of the OH or COOH functional group, with a bond formed between the metal cluster and the OH or COOH functional group. Adsorption geometries where the cluster was

close by but not interacting with the functional group were not investigated, since the aim was to establish the direct role of the functional group on the binding of the cluster. Adsorption geometries where the cluster was binding to carbon atoms not in the vicinity of the attached functional group at the vacancy site are not considered. This is due to the large size of the unit cell used and the large $Pt_{38}$ cluster.

The second approach was from the underneath side, from this side the cluster is approaching from below the functional group and is not directly bonded to the functional group. The adsorption geometries were confined to those where the cluster via its interacting facet were close to the carbon atoms around the vicinity of the added functional group and the saturating H atoms at the vacancy site of the graphene. Only the local region around the added functional group to the graphene was investigated for the binding of the cluster to the support.

On OH functionalised graphene a total of 4 adsorption geometries were investigated. Two atop geometries and 2 underneath approach geometries. The atop geometries consists of the square facet and hexagonal facet approach, with the facet of approach atop the OH functional group. For the underneath approach geometries both the square and the hexagonal facet approaches were investigated as can be seen later in Figure 4.7.

On COOH functionalised graphene a total of 6 adsorption geometries were investigated, with 4 atop geometries and 2 underneath approach geometries. For the atop geometries two variants for both the square and hexagonal facet approach were investigated. For the square facet approach, the first variant is where the square facet approaching the support is at the same level as the COOH group with the O of the C=O group closer to one bridge site of the square facet. The second variant of the square facet approach is the geometry where the square facet approaching the support is not at the same height as the COOH group, but closer to the support with a central Pt atom of the hexagonal facet closest to the O of the C=O group as can be seen later in Figure 4.8 (c). The two variants for the hexagonal facet approach are identical to those for the square facet approach with the only difference being the hexagonal facet approaching the support instead of the square facet as can be seen later in Figure 4.8 (b) and (f).

### 4.2.4 Computational method

The calculations were performed using the Vienna ab initio simulation package VASP (Kresse & Hafner, 1993; Kresse & Hafner, 1994; Kresse & Furthmüller, 1996a; Kresse & Furthmüller, 1996b). To identify the facet of the $Pt_{38}$ cluster which interacts favourably with the support

materials, the Generalised Gradient Approximation GGA-PW91 functional (Perdew et al., 1992) was used for the exchange-correlation energy. Once the lowest energy structures are identified at the standard DFT GGA level, the two lowest energy structures on each support were re-optimised by incorporating van der Waals correction using the vdW-TS-SCS method (Tkatchenko et al., 2012; Bučko et al., 2013) and the vdW-OptPBE method (Dion et al., 2004; Thonhauser et al., 2007; Romàn-Pérez & Soler, 2009; Klimeš et al., 2010) as implemented in VASP. The electron-ion interactions were described by the projector augmented wave (PAW) method (Blöchl, 1994; Kresse & Jourbert, 1999) pseudopotentials. A plane wave basis set cut-off energy of 400 eV was utilised. Applying a higher cut-off energy of 500 eV let to binding energy differences of 0.08 eV for adsorption on pristine and mono-vacancy graphene, and 0.16 eV for adsorption on OH-functionalised and COOH-functionalised graphene. The difference in binding energy between the 400 eV and 500 eV cut-off energy is not large enough to affect the trends in binding energy, hence a cut-off energy of 400 eV was utilised. The method of Methfessel-Paxton (Methfessel & Paxton, 1989) smearing was employed with a smearing width $\sigma = 0.05$ eV.

For adsorption calculations of the $Pt_{38}$ cluster on pristine graphene, monovacancy defective graphene and OH functionalised graphene, a (6 × 6) periodic surface unit cell of graphene was used. Adsorption calculations on COOH functionalised graphene were performed on a slightly larger periodic unit cell of (7 × 7) due to the bulkier COOH group. Test calculations with larger unit cells of (7 × 7) and (8 × 8) respectively resulted in binding energies which are 0.12 eV more negative than for the smaller unit cells. Using larger unit cells does not significantly alter the binding energies hence the smaller unit cells were used. In all cases, one defect was introduced per (6 × 6) or (7 × 7) unit cell. A vacuum region of 25 Å was utilised to avoid spurious interactions between periodic images. The optimised lattice parameter for graphene was found to be identical to the experimental value of 2.46 Å (Lide, 2004) similar to previous results (Ramos-Sanchez & Balbuena, 2013). The Brillouin zone sampling was sampled at a single Γ-point in k-space owing to the size of the unit cell used for the geometry optimisation calculations. Using a larger k-point grid of (5 × 5 × 1) resulted in differences in calculated binding energies of 0.10 eV. The difference in binding energy due to using a finer k-point grid is insignificant to affect the observed trends as it lies within the accuracy of DFT calculations of 0.10 eV. Geometry optimisation calculations were performed for adsorption calculations, with an electronic convergence criterion of energies below $10^{-5}$ eV and forces below 0.03 eV/Å on the unconstrained atoms. During geometry optimisation all atoms of the support and the $Pt_{38}$ cluster were allowed to relax to the lowest energy state. The dipole

correction in the z-direction as implemented within the VASP manual was utilised to correct for any induced dipoles which may have resulted from adsorption of the $Pt_{38}$ cluster.

The binding energy of the $Pt_{38}$ cluster on the different supports is calculated using the relation:

$$E_{bind} = E_{Pt_{38}+\,support} - E_{support} - E_{Pt_{38}} \quad (4.1)$$

Where $E_{Pt_{38}+\,support}$ is energy of the optimised support with the $Pt_{38}$ cluster bound to it, $E_{support}$ is energy of the optimised support without any $Pt_{38}$ cluster adsorbed, $E_{support}$ is energy of pristine graphene, monovacancy defective graphene, OH and COOH functionalised graphene depending on the support considered. $E_{Pt_{38}}$ is energy of the free standing optimised $Pt_{38}$ cluster.

To gain further insight into the interaction of the $Pt_{38}$ cluster with the different supports, Bader charge analysis determined using Bader charge partitioning method (Bader, 1991; Henkelman et al., 2006; Sanville et al., 2007; Tang et al., 2009), projected density of states (PDOS) analysis, and electron density difference plot analysis calculations were also performed to assess changes to the electronic structure upon adsorption of the $Pt_{38}$ cluster to the support. For the PDOS, Bader and charge density difference plot analysis a Monkhorst Pack (Monkhorst & Pack, 1976) k-point grid of (6 × 6 × 1) was utilised to sample the Brillouin zone. For the above analysis, single point energy calculations using a (6 × 6 × 1) k-point grid on the optimised low energy adsorption structures were performed. The charge density difference was determined from the relation:

$$\Delta\rho = \rho_{Pt_{38}+\,support} - \rho_{support} - \rho_{Pt_{38}} \quad (4.2)$$

Where $\rho_{Pt_{38}+\,support}$ is the charge density of the optimised support with the $Pt_{38}$ cluster adsorbed, $\rho_{support}$ is the charge density of the support without the $Pt_{38}$ cluster in the same position as in the optimised geometry with the adsorbed $Pt_{38}$ cluster and $\rho_{Pt_{38}}$ is the charge density of the $Pt_{38}$ cluster in the same position as in the optimised geometry with the support.

The atom resolved change in the Bader charge on the carbon, oxygen and hydrogen atoms upon adsorption is calculated from:

$$\Delta q = q_{Pt_{38}+\,support} - q_{support} \quad (4.3)$$

Where $q_{Pt_{38}+\,support}$ is the atom resolved Bader charge on the carbon, oxygen and hydrogen atoms in the optimised geometry of the support together with the adsorbed $Pt_{38}$ cluster, $q_{support}$ is the atom resolved Bader charge on the corresponding carbon, oxygen and hydrogen atoms of the support without the $Pt_{38}$ cluster in the same position as in the optimised geometry. The atom resolved change in the Bader charge on Pt atoms of the $Pt_{38}$ cluster upon

adsorption is calculated in a similar manner to how the change in Bader charge on the carbon, oxygen and hydrogen atoms was calculated.

$$\Delta q = q_{Pt_{38}+\ support} - q_{Pt_{38}} \quad (4.4)$$

Where $q_{Pt_{38}+\ support}$ is the atom resolved Bader charge on Pt atoms in the optimised geometry of the support together with the adsorbed $Pt_{38}$ cluster and $q_{Pt_{38}}$ is the atom resolved Bader charge on the corresponding Pt atoms of the $Pt_{38}$ cluster without the support in the same position as in the optimised geometry.

# 4.3 Results and Discussion

## 4.3.1 Optimised supports

Figure 4.3 presents monovacancy defective graphene with the numbering of the carbon atoms at the vacancy site. The numbering at the vacancy site is to aid in describing the geometry of the functionalised graphene support.

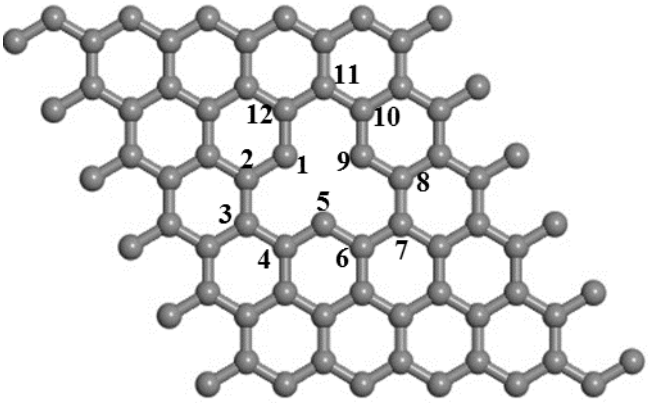


Figure 4.3: Labelling of carbon atoms around the defect site on monovacancy defective graphene

The optimised structures of the different types of support structures are presented in Figure 4.4. The relaxed structure of the pristine and monovacancy supports are planar and flat throughout with no observable lifting out of plane of carbon atoms (see Figure 4.4 (a) and (b)).

The three different investigated arrangements of the OH and the two H atoms at the vacancy all converged to the same structure shown in Figure 4.4 (c). The optimised geometry of the bare OH functionalised graphene is such that the hydrogen atom attached at carbon C9 is pointing into plane and below the graphene sheet. The hydrogen atom at C5 has an opposite arrangement to that at C9 and points out of plane as can be seen in the side view of Figure

4.4 (c). The side view and top view of OH functionalised graphene also indicates that the OH group is optimised to an angle of 40.35 ° from a plane normal to graphene. In addition, it is observed that carbon C1 to which the OH functional group is attached and carbon atoms C9 – C10 are elevated out of plane relative to the other carbon atoms in the graphene network. This result obtained in the present study is consistent with previous DFT studies where a similar elevation of the carbon bearing the OH group on functionalised graphene was observed (Schneipp et al., 2006) on a 585 defective graphene with the hydroxyl group (Kou et al., 2011). Therefore, the region around the attached OH group is not flat but bent-like thus introducing topological defects in the basal graphene plane. The calculated geometric parameters of the OH group in the optimised OH functionalised graphene are $d_{O\text{-}H}$ = 0.98 Å and the OH group distance to carbon C1 is $d_{C\text{-}OH}$ = 1.36 Å.

Similar to the case of optimised OH functionalised graphene the attached COOH group on COOH functionalised graphene is optimised to an angle 28.29 ° from a plane normal to graphene. Similarly, the hydrogen atoms at C5 and C9 have opposite orientations to each other like in OH functionalised graphene as can be seen in the side view of Figure 4.4 (d). The hydrogen at C5 is pointing into plane whilst the hydrogen at C9 is pointing out of plane. Also carbon C1 bearing the functional group and carbon atoms C9-C12 are elevated above plane relative to other carbon atoms within the graphene sheet. The extent of elevation of C1 and carbon atoms C9-C12 in COOH functionalised graphene is lesser than that in OH functionalised graphene resulting is less bending in the vicinity of the defect site. The optimised parameters of the COOH group of the optimised COOH functionalised graphene are: $d_{C=O}$ = 1.23 Å, $d_{C\text{-}O(H)}$ = 1.38 Å, $d_{O\text{-}H}$ = 0.98 Å and $\angle_{O=C-OH} = 120.8^{\circ}$. The COOH group is a distance $d_{C\text{-}COOH}$ = 1.47 Å above the graphene sheet.

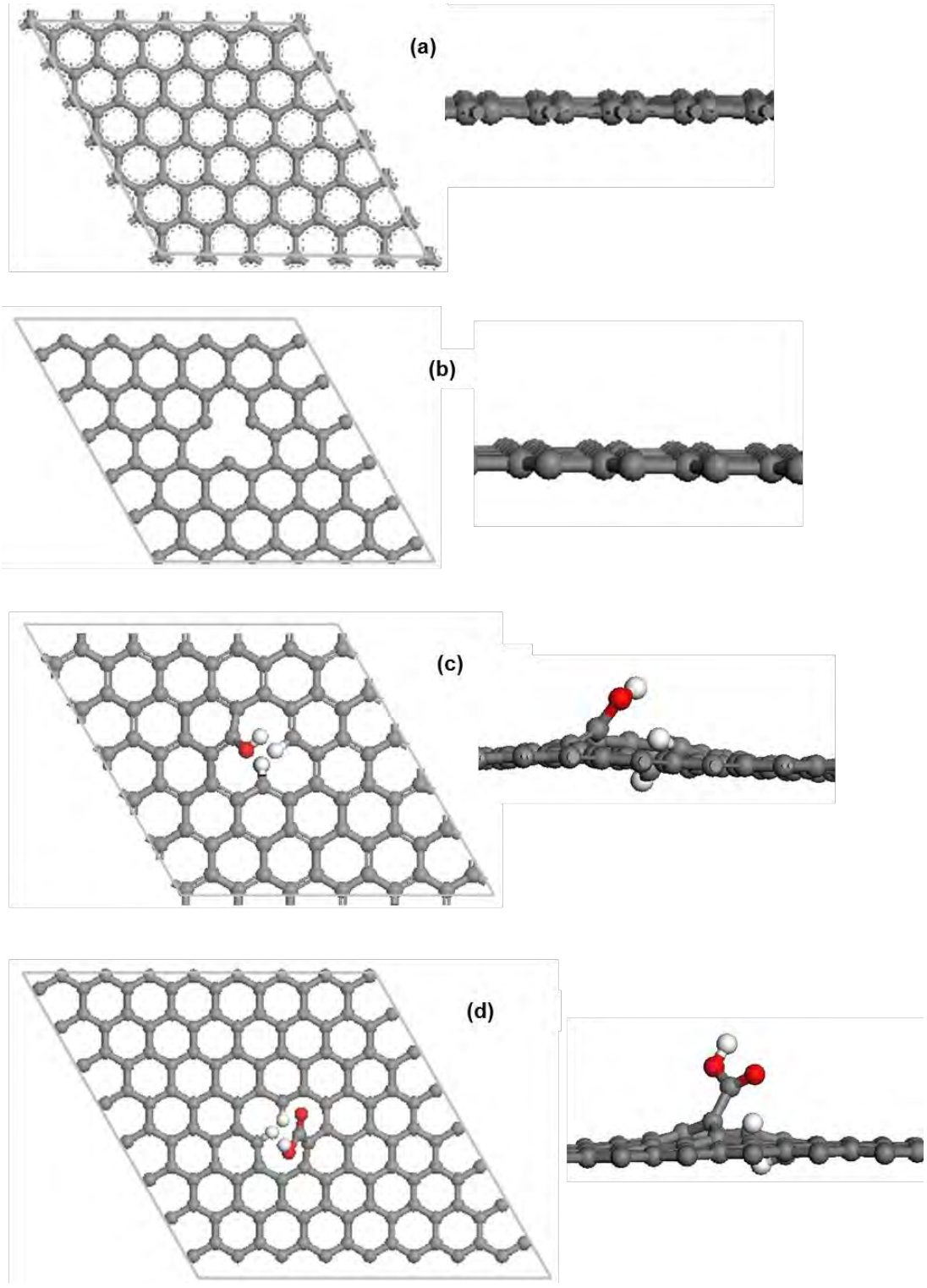


Figure 4.4: Top and side view of the optimised structures for the carbon support (a) pristine graphene, (b) monovacancy defective graphene, (c) OH functionalised graphene and (d) COOH functionalised graphene.

## 4.3.2 $Pt_{38}$ interaction with pristine graphene

The optimised structures for the $Pt_{38}$ cluster interaction with pristine graphene are presented in Figure 4.5.

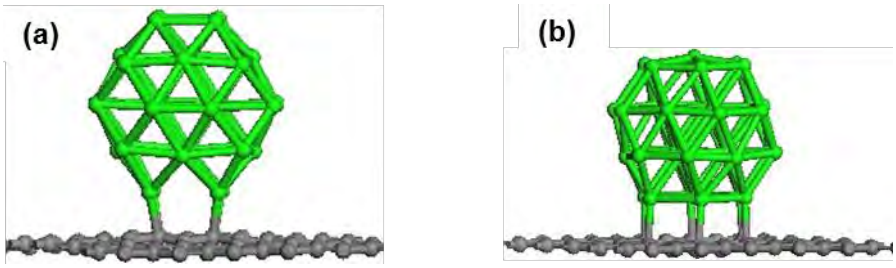


Figure 4.5: Optimised geometries for the $Pt_{38}$ cluster on pristine graphene approaching via (a) square facet and (b) hexagonal facet.

The binding of the $Pt_{38}$ cluster to pristine graphene results in minimum distortion around the contact region between the cluster and the support, with the support retaining its flat orientation (see Figure 4.5). From the reported binding energies in Table 4.1 the calculated binding energy with the GGA-PW91 functional of the $Pt_{38}$ cluster on pristine graphene is endothermic and non-binding, i.e. repulsive for both the square and the hexagonal facet approach. This result is consistent with the result obtained by Vanin et al. (2010) where they also reported non-binding of the Pt (111) surface to a graphene sheet at the GGA level using the revPBE functional. This result is not surprising since the Pt-graphene interaction is weak and is considered a classical van der Waals system (Fuentes-Cabrera et al., 2008), for which the standard GGA functionals fail to predict the van der Waals interaction.

Including van der Waals corrections in DFT with the different implementation methods, viz. vdW-TS, vdW-TS-SCS and vdW-OptPBE it is observed in Table 4.1 that exothermic binding energy is obtained for all the different implementations of the van der Waals correction. An exothermic binding energy (-6.63 eV) for the adsorption of a truncated octahedron 38 atom Pt cluster on two layers of graphene has also been calculated by Ramos-Sanchez & Balbuena (2013) using the semi-empirical van der Waals correction method of Grimme of DFT-D2. The highly stable binding energy of -6.63 eV calculated by Ramos-Sanchez & Balbuena (2013) compared to the one calculated presently (-3.16 eV) may be due to two graphene layers they utilised, and a different implementation of the van der Waals method. The difference in binding energy between the two studies is too big to ignore.

Table 4.1: Optimised parameters for geometric structures of the $Pt_{38}$ cluster adsorbed on pristine graphene. Side length corresponds to corner to corner length while diagonal length corresponds to corner to central Pt atom on the hexagonal facet.

| | **Square Facet** | | **Hexagonal Facet** | | | |
|---|---|---|---|---|---|---|
| **$E_{bind}$ (eV)** | | | | | | |
| GGA-PW91 | 0.14 | | 1.31 | | | |
| vdW-TS | -2.26 | | -1.64 | | | |
| vdW-TS-SCS | -2.47 | | -2.06 | | | |
| vdW-OptPBE | -3.16 | | -2.70 | | | |
| | **PW91** | **vdW-OptPBE** | **PW91** | | **vdW-OptPBE** | |
| | | | Side length | Diagonal length | Side length | Diagonal length |
| $d_{Pt\text{-}Pt}$ [1], Å | 2.76 | 2.74 | 3.39 | 2.83 | 3.32 | 2.76 |
| | 3.12 | 3.10 | 2.75 | 2.84 | 2.80 | 2.75 |
| | 2.76 | 2.75 | 2.75 | 2.83 | 2.79 | 2.76 |
| | 3.12 | 3.10 | 2.69 | 2.86 | 2.72 | 2.75 |
| | | | 2.72 | 2.89 | 2.72 | 2.76 |
| | | | 2.71 | 2.80 | 2.72 | 2.76 |
| | **PW91** | **vdW-OptPBE** | **PW91** | | **vdW-OptPBE** | |
| | | | Side length | Diagonal length | Side length | Diagonal length |
| $d_{Pt\text{-}Pt}$ [2], Å | 2.69 | 2.69 | 2.64 | 2.69 | 2.63 | 2.69 |
| | 2.69 | 2.69 | 2.69 | 2.70 | 2.70 | 2.70 |
| | 2.69 | 2.69 | 2.64 | 2.71 | 2.63 | 2.70 |
| | 2.69 | 2.68 | 2.71 | 2.69 | 2.71 | 2.69 |
| | | | 2.64 | 2.71 | 2.63 | 2.70 |
| | | | 2.71 | 2.69 | 2.71 | 2.69 |
| | **PW91** | **vdW-OptPBE** | **PW91** | | **vdW-OptPBE** | |
| | | | | | | |
| $d_{Pt\text{-}C}$ , Å | 2.20 | 2.18 | 2.24 | | 2.29 | |
| | 2.19 | 2.18 | 2.30 | | 2.32 | |
| | 2.19 | 2.18 | 2.33 | | 2.32 | |
| | 2.20 | 2.18 | 2.30 | | 2.29 | |
| | | | 2.44 | | 2.32 | |
| | | | 2.26 | | 2.29 | |

[1]Pt-Pt distance of the facet closest to graphene

[2] Pt-Pt distance of the facet opposite and furthest to the one interacting with the graphene

Vanin et al. (2010) calculated a binding energy of 30 meV / carbon atom for interaction of graphene with a Pt (111) surface using the vdW-DF method of Dion et al. (2004), in the present study for the square facet approach a binding energy of 43.8 meV / carbon atom is obtained using the vdW-OptPBE method which is derived from the vdW-DF method, and 34.2 meV / carbon atom for the vdW-TS-SCS method. The binding energy/carbon atom obtained in the

present study and the previous study by Vanin et al. (2010) are of the same order of magnitude and are thus consistent with each other. Van der Waals contribution to binding for the $Pt_{38}$ cluster adsorbed through the square facet is 45.8 meV /C (0.83 eV/ Pt atom in contact with graphene) for the vdW-TS-SCS method and 36.2 meV/C (0.65 eV/ Pt atom in contact with the support) for the vdW-OptPBE method in the present study. Van der Waals contribution to binding on pristine graphene in the present study are of the order of magnitude expected of van der Waals contribution of 5 – 10 kJ/mol (Tonigold & Groß, 2010; Rubeš et al., 2010; Klimeš & Michaelides, 2012).

Comparison of the geometries calculated with the GGA-PW91 functional and the vdW-OptPBE functional as represented by the bond lengths of the interacting and opposite facets are reported in Table 4.1. The geometries obtained with both functionals are identical to within a general bond length error of ± 0.02 Å for the square facet approach. The difference in bond lengths between the GGA-PW91 and the vdW-OptPBE functionals for the hexagonal facet approach is 0.05 Å with shorter bond lengths for the interacting facet calculated with the vdW-OptPBE functional. Other than this discrepancy, other bond lengths for the opposite facet are within the error range of ± 0.02 Å for the hexagonal facet approach.

Binding of the $Pt_{38}$ cluster via the square facet results in bond elongation of 15 % for two sides of the square facet relative to the optimised bond lengths in the free standing $Pt_{38}$ cluster. The bond lengths of the opposite square facet not interacting with the cluster remain identical to within an error of ± 0.01 Å to the free standing optimised $Pt_{38}$ bond lengths. For the hexagonal facet approach there is an average bond increase of 0.05 Å relative to the bond lengths of the optimised free standing $Pt_{38}$ cluster. Similar to the square facet approach, the bond lengths of the opposite hexagonal facet are identical to within the error range of ± 0.01 Å of the values of the optimised free standing $Pt_{38}$ cluster.

From Table 4.1 it is further observed that the square facet approach results in shorter Pt-C distances compared to the hexagonal facet approach. The shorter Pt-C bond lengths for the square facet approach compared to the hexagonal facet approach corroborate with the slightly more exothermic binding energy of the square facet. The vdW-OptPBE Pt-C bond lengths for the hexagonal facet approach are in general longer than the GGA-PW91 values, though there are some few exceptions.

### 4.3.3 $Pt_{38}$ interaction with monovacancy defective graphene

For both the square facet approach and hexagonal facet approach the binding of the cluster results in structural distortion of the support in the contact region as can be seen in Figure 4.6.

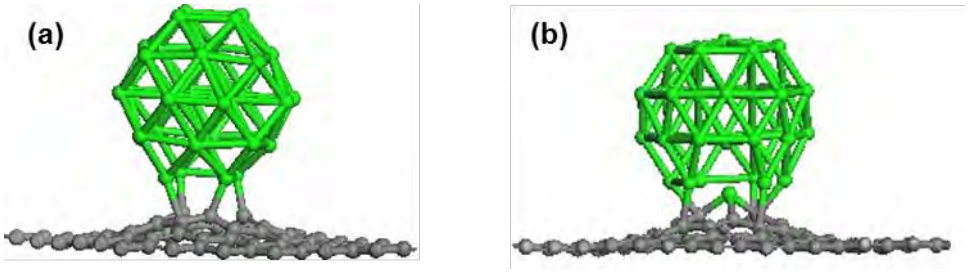


Figure 4.6: Optimised geometries for the $Pt_{38}$ cluster on monovacancy defective graphene approaching via (a) square facet and (b) hexagonal facet.

The extent of distortion is higher for the hexagonal facet approach than the square face approach. In both cases the atoms around the vacancy site are elevated out of plane towards the approaching cluster facet. The distortion of monovacancy graphene upon adsorption of Pt clusters has also been observed by Okazaki-Maeda et al. (2010) for $Pt_n$ clusters where n = 1-13, and by Fampiou & Ramasubramaniam (2012) for Pt, $Pt_2$, $Pt_3$, $Pt_4$ and $Pt_{13}$ clusters. From Figure 4.6 (b) it can be observed for the hexagonal facet approach that the central Pt atom on the hexagonal facet approaching the cluster is pulled out of plane towards the vacant site of the defective graphene. This central Pt atom is bonded to the three coordinatively unsaturated carbon atoms at the vacancy, i.e. C1, C5 and C9.

The reported binding energies for adsorption on monovacancy defective graphene in Table 4.2 indicate that the binding energy through the hexagonal facet is more exothermic than through the square facet. The binding energy of the $Pt_{38}$ cluster on monovacancy graphene is highly exothermic compared to the endothermic binding energy on pristine graphene calculated with the GGA-PW91 functional. The strong binding on defective graphene relative to pristine graphene has been observed in previous studies by Maiti & Rica (2004), Okazaki-Maeda et al. (2010) and Fampiou & Ramasubramaniam (2012). The stable binding on monovacancy graphene has been attributed to formation of strong Pt-C bonds at the coordinatively unsaturated carbon atoms at the defect. Inclusion of the van der Waals forces does not change the stability order between the square and hexagonal facet approach to the defective graphene as can be seen in Table 4.2. The van der Waals contribution to bonding on defective graphene for approach through the hexagonal facet is 25.2 meV/C (0.26 eV/Pt

atom in contact with the support) for the vdW-OptPBE functional and 46.2 meV/C (0.43 eV/Pt atom in contact with the support) for vdW-TS-SCS.

Table 4.2: Optimised parameters for geometric structures of the $Pt_{38}$ cluster adsorbed onto monovacancy defective graphene. Side length corresponds to corner to corner length while diagonal length corresponds to corner to central Pt atom on the hexagonal facet.

| | **Square Facet** | | **Hexagonal Facet** | | | |
|---|---|---|---|---|---|---|
| **$E_{bind}$ (eV)** | | | | | | |
| GGA-PW91 | -4.31 | | -6.67 | | | |
| vdW-TS | -6.76 | | -9.54 | | | |
| vdW-TS-SCS | -6.99 | | -9.95 | | | |
| vdW-OptPBE | -5.88 | | -8.46 | | | |
| $d_{Pt-Pt}$ [1], Å | **PW91** | **vdW-OptPBE** | **PW91** | | **vdW-OptPBE** | |
| | | | Side length | Diagonal length | Side length | Diagonal length |
| | 2.98 | 3.04 | 3.39 | 2.84 | 3.74 | 2.93 |
| | 2.84 | 2.88 | 2.71 | 2.83 | 2.76 | 2.89 |
| | 2.77 | 2.76 | 2.72 | 2.80 | 2.84 | 2.81 |
| | 2.76 | 2.75 | 2.69 | 2.89 | 2.75 | 3.38 |
| | | | 2.75 | 2.86 | 2.85 | 3.03 |
| | | | 2.75 | 2.83 | 2.85 | 3.35 |
| $d_{Pt-Pt}$ [2], Å | **PW91** | **vdW-OptPBE** | **PW91** | | **vdW-OptPBE** | |
| | | | Side length | Diagonal length | Side length | Diagonal length |
| | 2.75 | 2.73 | 2.66 | 3.16 | 2.65 | 2.72 |
| | 2.74 | 2.73 | 2.69 | 3.02 | 2.71 | 2.71 |
| | 2.70 | 2.71 | 2.66 | 3.26 | 2.66 | 2.71 |
| | 2.72 | 2.71 | 2.71 | 2.84 | 2.71 | 2.69 |
| | | | 2.66 | 2.80 | 2.68 | 2.69 |
| | | | 2.70 | 2.98 | 2.70 | 2.70 |
| $d_{Pt-C}$ , Å | **PW91** | **vdW-OptPBE** | **PW91** | | **vdW-OptPBE** | |
| | | | | | | |
| | 1.97 | 1.97 | 2.25 | | 2.25 | |
| | 2.25 | 2.25 | 2.29 | | 2.28 | |
| | 2.00 | 1.99 | 2.26 | | 2.26 | |
| | 1.98 | 1.98 | 2.26 | | 2.25 | |
| | | | 2.25 | | 2.23 | |
| | | | 2.26 | | 2.20 | |

[1]Pt-Pt distance of the facet closest to monovacancy graphene

[2] Pt-Pt distance of the facet opposite to the one interacting with the monovacancy graphene

The bond lengths reported in Table 4.2 indicates that for the square facet approach the bond lengths calculated using the vdW-OptPBE functional are within 0.04 Å of the values calculated with the GGA-PW91 functional. Therefore, the geometries can be considered to be identical.

For the square facet approach, on average the Pt-Pt bond lengths of the facet are increased by 5% compared to the average Pt-Pt bond distance of 2.70 Å for the square facet in the optimised free standing $Pt_{38}$ cluster. For the square facet approach, there is less structural change to the opposite square facet not in contact with the support, since on average the Pt-Pt bonds change by less than 1% relative to the free standing $Pt_{38}$ cluster bond lengths.

For the hexagonal facet approach, the bond lengths calculated using the vdW-OptPBE functional are longer than those calculated using the GGA-PW91 functional. The highest difference in bond lengths between the two functionals is 0.35 Å for the long side lengths of the hexagonal facet with the other sides being on average 0.10 Å longer. The diagonal lengths on the hexagonal facet are 0.10 Å longer for the vdW-OptPBE functional than the GGA-PW91 functional. The GGA-PW91 values are in turn 0.10 Å longer than the optimised diagonal lengths of 2.70 Å in the optimised free standing $Pt_{38}$ cluster. Thus, distortion of the hexagonal facet upon interaction with defective graphene is higher than for the square facet approach, this can be seen by the visible distortion of the hexagonal facet in Figure 4.6 (b). For the opposite hexagonal facet not interacting with the support, the vdW-OptPBE calculated bonds lengths are shorter than the GGA-PW91 functional values. The lengths for the sides of the hexagonal facet are similar to the optimised free standing $Pt_{38}$ cluster (long side = 2.70 Å and short side = 2.65 Å) for the vdW-OptPBE functional and the GGA-PW91 functional. Whereas, the diagonal lengths of the hexagonal facet are elongated relative to the free standing optimised $Pt_{38}$ cluster bond length of 2.70 Å in the case of the GGA-PW91 functional. For the vdW-OptPBE functional, the diagonal lengths are similar to the optimised free standing $Pt_{38}$ cluster bond lengths. Therefore, it appears that the vdW-OptPBE functional leads to a slightly different geometry to that predicted by the GGA-PW91 functional for the hexagonal facet approach of the $Pt_{38}$ cluster on monovacancy graphene.

The Pt-C distances for the square facet are shorter than the calculated Pt-C bond lengths for the hexagonal facet approach (see Table 4.2). This is despite the cluster being closer to the support while approaching via the square facet, which does not result in the most stable binding energy on monovacancy graphene. For both the square and hexagonal facet approach, the calculated Pt-C distance using the GGA-PW91 functional and the vdW-OptPBE functional are identical, indicating similar prediction of the metal–carbon distances.

### 4.3.4 $Pt_{38}$ interaction with OH functionalised graphene

Of the investigated adsorption geometries, the binding energies where the cluster approaches the support from underneath are more exothermic than the atop approach structures (see

Figure 4.7). Approach from underneath results in the cluster being optimised closer to the support while for the atop approach the cluster is optimised a distance away from the functional group. The binding energies calculated using the GGA-PW91 functional are exothermic compared to the calculated binding energies of the cluster on pristine graphene. Hence, the OH functional group stabilises binding of the cluster to the support unlike the repulsive interaction on pristine graphene calculated with the GGA-PW91 functional. The present result of enhanced binding on OH functionalised graphene relative to adsorption on pristine graphene is consistent with previous theoretical studies of Chutia et al. (2014) where binding of a $Pt_4$ cluster on OH edge decorated graphene was enhanced relative to adsorption on pristine graphene. A similar result has been obtained by Vedala et al. (2011) for the enhanced adsorption of a $Pt_{27}$ cluster on OH edge decorated graphene relative to adsorption on pristine graphene.

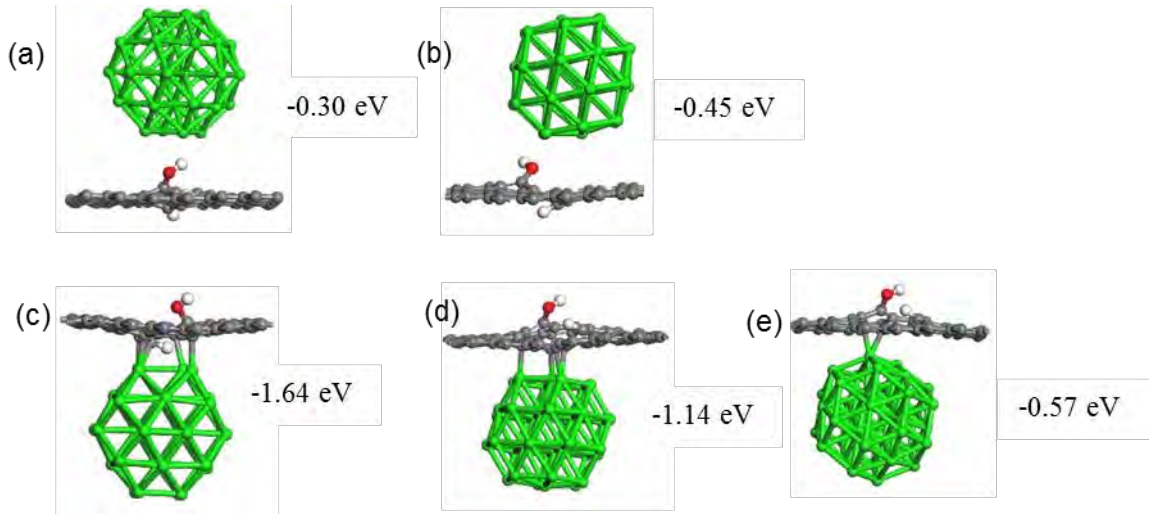


Figure 4.7: Optimised geometries for the $Pt_{38}$ cluster on OH functionalised graphene together with the binding energies calculated with the GGA-PW91 functional.

The lowest energy structures obtained using the GGA-PW91 functional shown in Figure 4.7, i.e. Figure 4.7 (c) and (d) were re-optimised with the inclusion of the van der Waals contribution. The structure shown in Figure 4.7 (a) was also re-optimised using the van der Waals methods to assess if the energy ordering of the atop approach being less exothermic relative to the bottom approach would be retained with the inclusion of van der Waals contribution. The inclusion of the van der Waals contribution does not alter the energy ordering between the square facet and hexagonal facet approach from underneath as seen in Table 4.3.

Furthermore, the calculated binding energy of the structure in Figure 4.7 (a) is -2.75 eV with the vdW-OptPBE functional and -3.03 eV with vdW-TS-SCS method. This shows that

incorporating the van der Waals contribution does not lead to the atop approach binding more strongly than the bottom approach. For underneath approach through the square facet, van der Waals contribution to bonding is 30.1 meV/C (0.54 eV/Pt atom in contact with the support) for the vdW-OptPBE method and 40.3 meV/C (0.72 eV / Pt atom in contact with the support) for the vdW-TS-SCS method.

Table 4.3: Optimised parameters for the lowest energy geometric structures of the $Pt_{38}$ cluster adsorbed onto OH functionalised graphene. Side length corresponds to corner to corner length while diagonal length corresponds to corner to central Pt atom on hexagonal facet.

| | **Square Facet** | | **Hexagonal Facet** | | | |
|---|---|---|---|---|---|---|
| **$E_{bind}$ (eV)** | | | | | | |
| GGA-PW91 | -1.64 | | -1.14 | | | |
| vdW-TS | -4.66 | | -3.73 | | | |
| vdW-TS-SCS | -4.50 | | -3.82 | | | |
| vdW-OptPBE | -3.78 | | -3.45 | | | |
| $d_{Pt-Pt}$ [1], Å | **PW91** | **vdW-OptPBE** | **PW91** | | **vdW-OptPBE** | |
| | | | Side length | Diagonal length | Side length | Diagonal length |
| | 3.31 | 3.06 | 2.69 | 2.74 | 2.65 | 2.71 |
| | 3.11 | 2.76 | 2.74 | 2.78 | 2.70 | 2.78 |
| | 2.81 | 2.84 | 2.74 | 2.86 | 2.70 | 2.83 |
| | 3.18 | 2.96 | 2.99 | 2.83 | 2.93 | 2.82 |
| | | | 2.75 | 2.77 | 2.70 | 2.76 |
| | | | 2.72 | 2.75 | 2.70 | 2.71 |
| $d_{Pt-Pt}$ [2], Å | **PW91** | **vdW-OptPBE** | **PW91** | | **vdW-OptPBE** | |
| | | | Side length | Diagonal length | Side length | Diagonal length |
| | 2.72 | 2.70 | 2.99 | 2.86 | 2.69 | 2.71 |
| | 2.73 | 2.69 | 2.74 | 2.83 | 2.69 | 2.70 |
| | 2.71 | 2.67 | 2.72 | 2.77 | 2.64 | 2.69 |
| | 2.71 | 2.67 | 2.69 | 2.75 | 2.63 | 2.65 |
| | | | 2.74 | 2.74 | 2.67 | 2.65 |
| | | | 2.74 | 2.79 | 2.62 | 2.70 |
| $d_{Pt-C}$ , Å | **PW91** | **vdW-OptPBE** | **PW91** | | **vdW-OptPBE** | |
| | | | | | | |
| | 2.17 | 2.14 | 2.17 | | 2.15 | |
| | 2.25 | 2.25 | 2.27 | | 2.27 | |
| | 2.16 | 2.14 | 2.26 | | 2.25 | |
| | 2.26 | 2.26 | | | | |
| | 2.25 | 2.21 | | | | |
| | 2.24 | 2.20 | | | | |

[1]Pt-Pt distance of the facet closest to OH functionalised graphene

[2] Pt-Pt distance of the facet opposite to the one interacting with the OH functionalised graphene

The van der Waals contribution to the binding energy on OH functionalised graphene per Pt atom in contact with the support is lower than the contribution to the binding energy on pristine graphene. On both OH functionalised graphene and pristine graphene, the cluster attaches to the support through a square facet consisting of 4 Pt atoms.

The lowest energy geometry with the square facet approaching from underneath has the highest structural distortion for both the approaching facet and the support. For this structure it can be observed from Figure 4.7 (c) that the graphene support is bent inwards towards the approaching square facet of the cluster. The square facet interacting with the support loses its square shape as can be seen from the calculated Pt-Pt bond lengths of the square facet in Table 4.3.

The opposite square facet not interacting with the support retains its almost square shape as deduced from the calculated Pt-Pt bond lengths in Table 4.3 as these values are similar to the calculated bond lengths in the optimised free standing $Pt_{38}$ cluster for the square facet. There is less structural distortion around the contact region for the underneath approach through the hexagonal facet as can be seen in Figure 4.7(d). The hexagonal facet approach geometry is such that the cluster is adsorbed in a tilted position with one end of the hexagonal facet closer to the support than the other. The diagonal bond lengths for the hexagonal facet approach are elongated on average by 0.05 Å relative to the optimised free standing $Pt_{38}$ cluster bond lengths for the facet interacting with the support. This indicates less structural distortion upon binding to the support. For the opposite hexagonal facet there is minimal change to the Pt-Pt bond distances.

The geometry as reflected by the calculated bond lengths of the interacting and opposite facets presented in Table 4.3 indicate that the calculated bond lengths using the GGA-PW91 functional are longer than those calculated with the vdW-OptPBE functional. The extent of difference in bond lengths differ between the hexagonal facet and square facet approach. For the square facet approach, the GGA-PW91 functional bond lengths for the interacting facet are on average 0.20 Å longer than the vdW-OptPBE functional. For the opposite facet they are merely 0.04 Å longer. On the contrary, for the hexagonal facet approach, for the interacting facet on average the GGA-PW91 functional calculated bond lengths are 0.04 Å longer than the vdW-OptPBE functional, whilst for the opposite non-interacting facet the GGA-PW91 functional bond lengths are 0.11 Å longer. Comparison of the Pt-C bond lengths for the GGA-PW91 functional and the vdW-OptPBE functional presented in Table 4.3 indicates that the two methods predicts the same metal-carbon bond distances.

### 4.3.5 $Pt_{38}$ interaction with COOH functionalised graphene

The optimised structures for $Pt_{38}$ interaction with COOH functionalised graphene are presented in Figure 4.8.

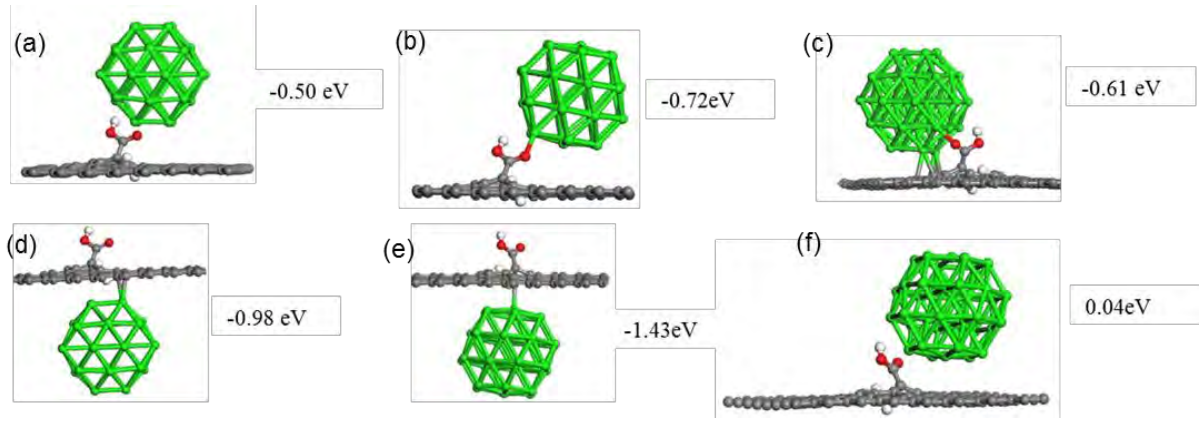


Figure 4.8: Optimised geometries for the $Pt_{38}$ cluster on COOH functionalised graphene together with the binding energies calculated with the GGA-PW91 functional.

Similar to the case of $Pt_{38}$ interaction with OH functionalised graphene, it can be observed from Figure 4.8 that underneath approach results in more exothermic binding energies than the atop approach.

In contrast to $Pt_{38}$ adsorption on OH functionalised graphene where the square facet approach from underneath is more stable than the hexagonal facet approach, on COOH functionalised graphene the underneath approach via the hexagonal facet has a binding energy which is 0.45 eV more stable than the underneath approach via the square facet calculated with the GGA-PW91 functional. For the atop approach, the hexagonal facet approach binds more strongly than the square facet by 0.11 eV and 0.22 eV for the two investigated variants of the square facet approach. The hexagonal facet approach from the top where the cluster is positioned on the side of the COOH functional group is weakly repulsive with a binding energy of 0.04 eV.

The difference in energy between the two lowest energy structures calculated with the vdW-OptPBE functional is 0.18 eV compared to 0.45 eV calculated with the GGA-PW91 functional. The van der Waals contribution to the binding energy for approach through the hexagonal facet is 16.3 meV/C (0.30 eV/Pt atom in contact with the support) for the vdW-OptPBE functional and 30.8 meV/C (0.56 eV/Pt atom in contact with the support) for the vdW-TS-SCS

method. This indicates that the van der Waals contribution to the binding energy on COOH functionalised graphene is higher than on monovacancy graphene. On both supports the cluster interacts with the support through the hexagonal facet consisting of 7 Pt atoms. Thus, the van der Waals contribution play a more dominant role on COOH functionalised graphene than on graphene with a monovacancy site.

Table 4.4: Optimised parameters for the lowest energy geometric structures of the $Pt_{38}$ cluster adsorbed onto COOH functionalised graphene. Side length corresponds to corner to corner length while diagonal length corresponds to corner to central Pt atom on the hexagonal facet.

| | **Square Facet** | | **Hexagonal Facet** | | | |
|---|---|---|---|---|---|---|
| **$E_{bind}$ (eV)** | | | | | | |
| GGA-PW91 | -0.98 | | -1.43 | | | |
| vdW-TS-SCS | -5.27 | | -5.37 | | | |
| vdW-OptPBE | -3.34 | | -3.52 | | | |
| $d_{Pt-Pt}$ [1], Å | **PW91** | **vdW-OptPBE** | **PW91** | | **vdW-OptPBE** | |
| | | | Side length | Diagonal length | Side length | Diagonal length |
| | 2.91 | 2.87 | 2.76 | 2.73 | 2.81 | 2.70 |
| | 2.77 | 2.78 | 2.72 | 3.05 | 2.70 | 3.36 |
| | 2.72 | 2.73 | 2.80 | 2.78 | 2.85 | 2.79 |
| | 2.79 | 2.78 | 2.69 | 2.73 | 2.68 | 2.70 |
| | | | 2.73 | 2.68 | 2.80 | 2.66 |
| | | | 2.67 | 2.69 | 2.73 | 2.69 |
| $d_{Pt-Pt}$ [2], Å | **PW91** | **vdW-OptPBE** | **PW91** | | **vdW-OptPBE** | |
| | | | Side length | Diagonal length | Side length | Diagonal length |
| | 2.72 | 2.69 | 2.64 | 2.71 | 2.62 | 2.73 |
| | 2.72 | 2.69 | 2.69 | 2.68 | 2.68 | 2.66 |
| | 2.68 | 2.65 | 2.65 | 2.68 | 2.63 | 2.67 |
| | 2.72 | 2.68 | 2.69 | 2.71 | 2.66 | 2.72 |
| | | | 2.65 | 2.68 | 2.64 | 2.63 |
| | | | 2.69 | 2.69 | 2.70 | 2.69 |
| $d_{Pt-C}$ , Å | **PW91** | **vdW-OptPBE** | **PW91** | | **vdW-OptPBE** | |
| | | | | | | |
| | 2.45 | 2.36 | 2.20 | | 2.18 | |
| | 2.24 | 2.24 | 2.29 | | 2.30 | |
| | 2.30 | 2.25 | 2.15 | | 2.15 | |
| | 2.33 | 2.30 | | | | |
| | | | | | | |
| | | | | | | |

[1]Pt-Pt distance of the facet closest to the COOH functionalised graphene

[2] Pt-Pt distance of the facet opposite to the one interacting with the COOH functionalised graphene

There is elongation of Pt-Pt bond lengths for the interacting facet relative to Pt-Pt bond lengths of the free standing $Pt_{38}$ cluster, for both the square facet and underneath hexagonal facet approach structures (see Table 4.4). The extent of Pt-Pt bond length elongation on the opposite facet is small compared to the interacting facet for both the square and underneath hexagonal facet structures.

For both the square and hexagonal facet underneath approach structures, and for the interacting facets, the GGA-PW91 functional and vdW-OptPBE functional Pt-Pt bond lengths are similar to each other to within ± 0.03 Å. This indicates that both the GGA-PW91 functional and vdW-OptPBE functional predict identical geometries.

Identical Pt-C bond lengths are calculated using the GGA-PW91 functional and vdW-OptPBE functional. Shorter Pt-C bond lengths are calculated for the underneath approach through the hexagonal facet, and this correlates with the more stable binding energy for this approach.

### 4.3.6. Electronic structure analysis

Electronic structure analysis was performed on the lowest energy adsorption geometries on the different supports to gain insight into the interaction of the $Pt_{38}$ cluster with the support. The considered structures for electronic structure analysis are; square facet approach for $Pt_{38}$ interaction with pristine graphene, hexagonal facet approach for $Pt_{38}$ interaction with monovacancy defective graphene, underneath square facet approach for $Pt_{38}$ interaction with OH functionalised graphene and underneath hexagonal facet approach for $Pt_{38}$ interaction with COOH functionalised graphene.

On all the different supports it can be observed in Figure 4.9 that most of the charge redistribution occurs around the contact region between the support and the $Pt_{38}$ cluster facet interacting with the support. The contact region between the cluster and the support consists of an interlock of regions of charge accumulation and depletion which is an indication of covalent bond formation. Charge redistribution to the opposite facet opposite not in direct contact with the support is less compared to the facet interacting with the support, this is observed on all the different supports.

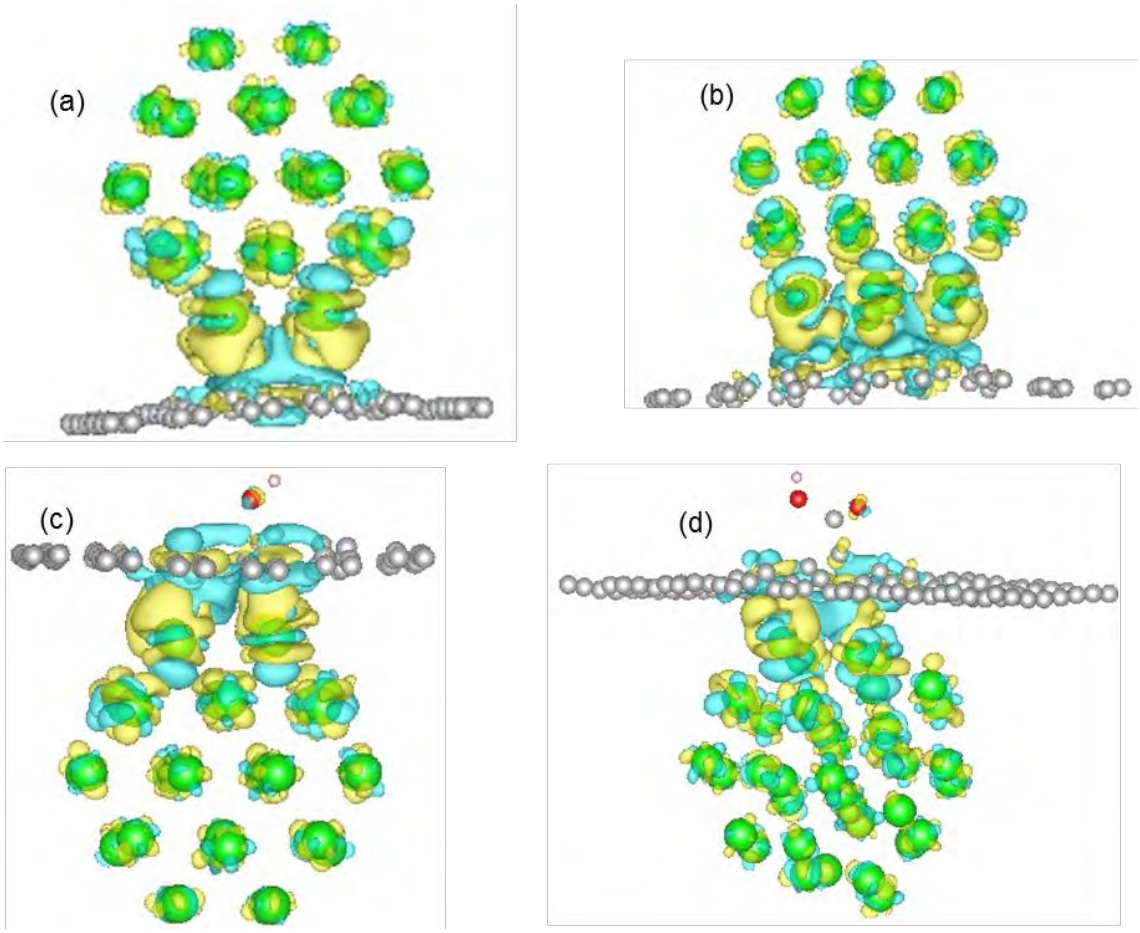


Figure 4.9: Charge density difference plots for the adsorption of the $Pt_{38}$ cluster; (a) pristine graphene, (b) monovacancy defective graphene, (c) OH functionalised graphene and (d) COOH functionalised graphene. Isosurface level is 0.0025 e/Å$^3$. Blue Isosurface represents charge depletion and yellow Isosurface represent charge accumulation.

The Bader charge partitioning method was used to quantify the amount of charge transfer upon adsorption by determining the atom resolved charges on the individual atoms. From the reported $\Delta q_{\text{interacting facet}}$ in Table 4.5, there is charge loss from the facet interacting with the support on all the graphene based supports. This is despite an overall charge transfer to the $Pt_{38}$ cluster for adsorption on pristine graphene, OH functionalised and COOH functionalised graphene. The overall charge transfer upon adsorption is not only a contribution by anchoring Pt atoms, for the total charge loss of the anchoring Pt atoms on the interacting facet is not equivalent to the overall quantity of charge transfer. This indicates that the carbon and the Pt atoms far away from the contact region participate in the overall charge transfer process upon adsorption. A similar conclusion has been made by Chutia et al. (2014) for a $Pt_4$ cluster adsorbed on OH edge decorated graphene.

In the present study a net overall charge transfer from the pristine graphene support to the $Pt_{38}$ cluster is observed, this is consistent with the calculations by Subrahmanyam *et al*. (2010)

for a $Pt_{40}$ cluster on graphene where 2.47 e charge was transferred to the cluster and Vanin et al. (2010) who calculated charge transfer from graphene to Pt (111) surface albeit being a small amount of 0.005 e. Consistent with findings of the present study, Fampiou & Ramasubramaniam (2012) calculated net charge transfer of 0.35 e to monovacancy graphene from a $Pt_{13}$ cluster upon adsorption. In the present study a total net charge transfer of 0.44 e to the monovacancy graphene support is calculated. A similar result of charge transfer to monovacancy graphene of 0.24 e upon $Pt_{13}$ cluster adsorption has been calculated by Lim & Wilcox (2011). The variation in charge transfer between graphene and Pt in the different references are due to cluster size (Ramos-Sanchez & Balbuena, 2013 $Pt_{38}$, Fampiou & Ramasubramaniam, 2012 $Pt_{13}$, Vanin et al., 2010 Pt (111) slab and Subrahmanyam et al., 2010 $Pt_{40}$), pseudopotentials (PAW pseudopotentials (for all references except Subrahmanyam et al. (2010) who utilises norm conserving pseudopotentials) and charge partitioning method (Bader for all references except Subrahmanyam et al. (2010) who uses Mulliken population analysis).

Table 4.5: Summary of change in Bader charge for $Pt_{38}$ adsorption on different supports. For the overall Δq column a negative value indicates charge loss from the $Pt_{38}$ cluster and a positive value indicates charge transfer to the $Pt_{38}$ cluster.

| **Support** | **$\Delta q_{overall}$ (e)** | **$\Delta q_{interacting\ facet}$ (e)** |
|---|---|---|
| Pristine graphene | 0.16 | -0.40 |
| | | |
| Monovacancy graphene | -0.44 | -1.14 |
| | | |
| OH functionalised graphene | 0.19 | -0.40 |
| | | |
| COOH functionalised graphene | 0.28 | -0.33 |

The overall amount of charge transfer does not to correlate directly with the binding energy of the cluster, since a higher magnitude of overall charge does not correspond to a more exothermic binding energy, e.g. see $\Delta q_{overall}$ for OH and COOH functionalised graphene in Table 4.5.

Projected density of states (PDOS) analysis was also performed to further gain insight into changes of the electronic structure upon adsorption on the different supports. For the PDOS analysis, the PDOS was projected onto the C 2p states for the carbon atoms and the 5d states for Pt atoms. The PDOS is calculated for carbon atoms within the vicinity of the defect for the supports: monovacancy graphene, OH and COOH functionalised graphene. For the pristine

graphene support the PDOS for the carbon atoms around the contact region is considered. The PDOS for the entire $Pt_{38}$ cluster is considered for the PDOS analysis.

The projected PDOS for the carbon atoms of the different supports are presented in Figure 4.10 showing the projected PDOS before and after adsorption of the $Pt_{38}$ cluster. The PDOS for the Pt 5d states for the entire $Pt_{38}$ cluster on the different supports is presented in Figure 4.11. From Figure 4.11 it is seen that pre adsorption the PDOS of the $Pt_{38}$ cluster is discrete-like. However, upon interaction with the different supports, the PDOS of the entire $Pt_{38}$ cluster is transformed from discrete-like to continuous. The transformation of the PDOS of the Pt cluster from discrete to continuous upon adsorption has been observed by Fampiou & Ramasubramaniam (2012) for $Pt_{13}$ adsorption on monovacancy, divacancy, 555-777 vacancy, and by Okazaki et al. (2010) for other small $Pt_n$ (n = 1-13) cluster adsorbed on defective and non-defective graphene.

The PDOS for graphene before adsorption shows the Dirac shape (i.e. inverted cone shape) around the Fermi level consistent with previous calculations (Giovannetti et al., 2008; Sutter et al., 2009; Amft et al., 2011; Gao et al., 2014). Upon adsorption of the $Pt_{38}$ cluster the PDOS still maintains the same features as before adsorption except the appearance of new small peaks around and near the Fermi level (energy range -2 to +2 eV). The new states originate from the hybridization between the carbon states and Pt states leading to formation of covalent bonds (Ramos-Sanchez & Balbuena, 2013). The interaction of the $Pt_{38}$ cluster with pristine graphene results in the appearance of Pt 5d states around the Fermi level in the PDOS of the $Pt_{38}$ cluster (see Figure 4.11 (b)). The changes to the PDOS of the $Pt_{38}$ cluster and the carbon 2p states around the Fermi level is indicative of bond formation between the pristine graphene and the $Pt_{38}$ cluster upon adsorption.

On monovacancy graphene the carbon PDOS before adsorption is similar to that of pristine graphene except that at the Fermi level there is appearance of two almost discrete states which manifests itself as two peaks. The two peaks in the PDOS spectrum of the carbon atoms at the Fermi level on monovacancy defective graphene have also been calculated by Fampiou & Ramasubramaniam (2012). The two peaks were attributed to the dangling bonds at the vacancy site due to missing bonds. Post adsorption there is appearance of new peaks in the vicinity of the Fermi level (energy range -2 to +2 eV). The PDOS of the Pt 5d states of the $Pt_{38}$ cluster adsorbed on monovacancy graphene differs to that of the free standing $Pt_{38}$ cluster (see Figure 4.11 (c)). There is appearance of Pt 5d states around the Fermi level and there is also a relative number of states above the Fermi level with an increase in the degree of dispersion of the energy levels below the Fermi energy. These changes in the PDOS of the

carbon 2p states and the Pt 5d states indicates formation of bonds between carbon 2p states and Pt 5d states.

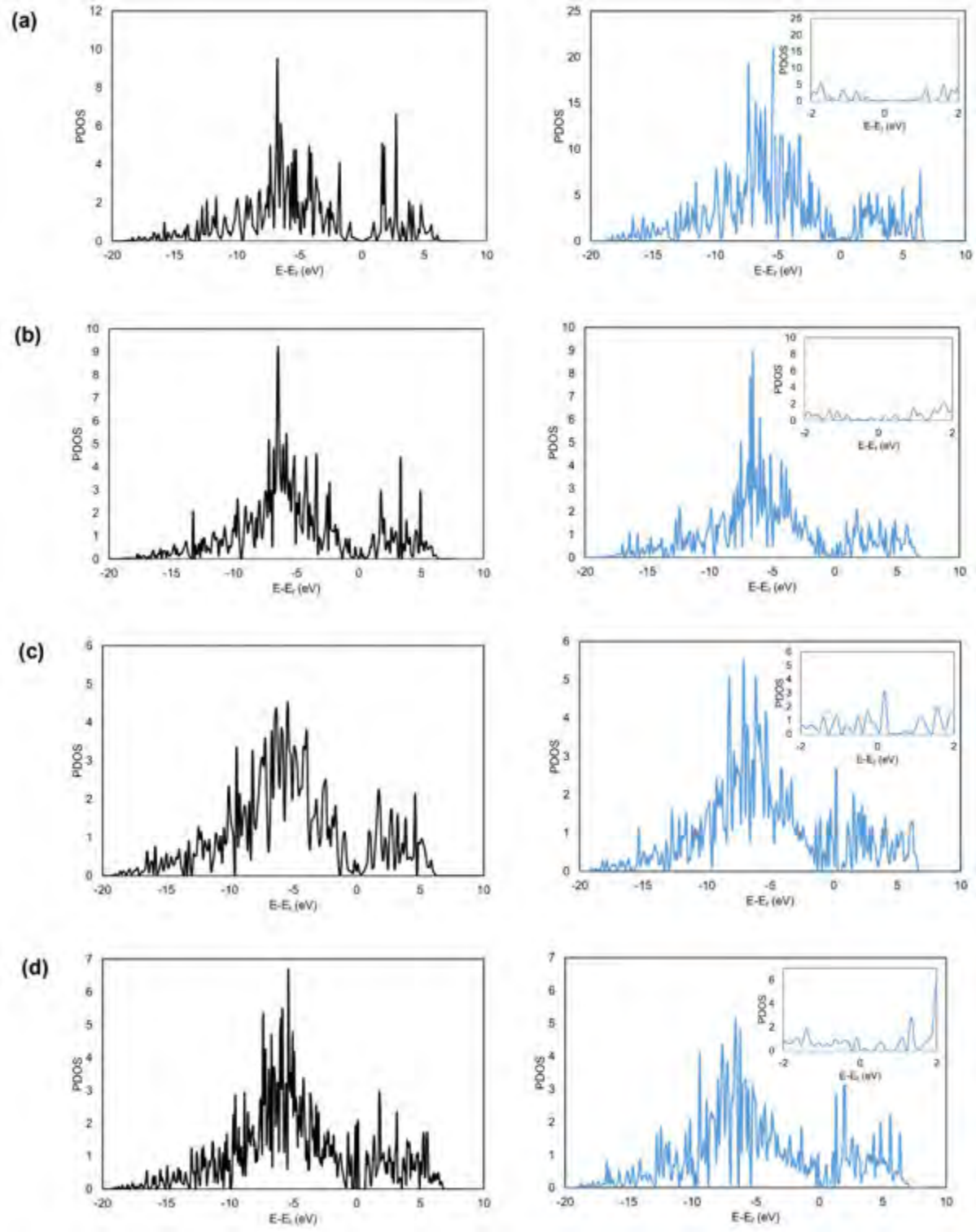


Figure 4.10: PDOS for the carbon atoms of the support at the contact region pre adsorption (black curve) and post adsorption (blue curve); (a) $Pt_{38}$ on pristine graphene (b) $Pt_{38}$ on monovacancy graphene, (c) $Pt_{38}$ on OH functionalised graphene and (d) $Pt_{38}$ on COOH functionalised graphene. The energy scale is relative to the Fermi level. Inserts show zoomed view of PDOS around Fermi level.

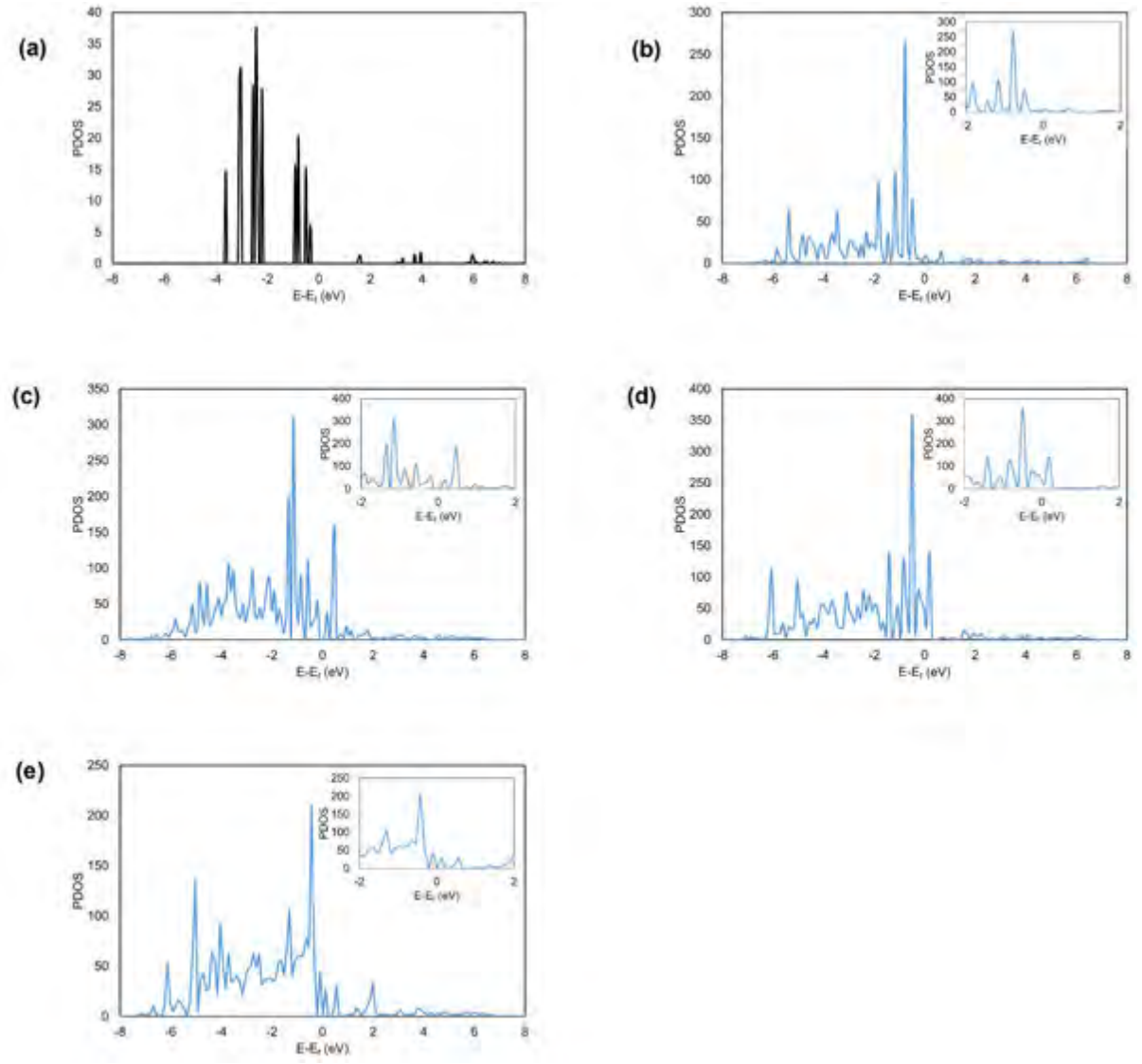


Figure 4.11: PDOS for the Pt 5d states; (a) free unsupported $Pt_{38}$ cluster, (b) $Pt_{38}$ on pristine graphene, (c) $Pt_{38}$ on monovacancy graphene, (d) $Pt_{38}$ on OH functionalised graphene and (e) $Pt_{38}$ on COOH functionalised graphene. The energy scale is reference to the Fermi level. Inserts show zoomed view of PDOS around Fermi level.

The PDOS of the OH functionalised graphene is similar to that of pristine graphene around the Fermi level with the Dirac shape but with a doublet peak at the Fermi level (see Figure 4.10 (c)). Post adsorption of the $Pt_{38}$ cluster on OH functionalised graphene, the doublet peak at the Fermi level disappears with appearance of new peaks around the Fermi level (energy range -2 to +2 eV) with the Dirac cone no longer visible. It is interesting to note that the number of states on carbon atoms at the Fermi level is the highest for OH functionalised graphene with the $Pt_{38}$ cluster adsorbed. The appearance of new states and changes to the PDOS of carbon around the Fermi level in conjunction with the changes in the PDOS of Pt 5d states of the $Pt_{38}$ cluster (see Figure 4.11 (d)) are indicative of hybridization between C 2p states and

Pt 5d states. The overlap of hybridized states between the C 2p and Pt 5d states leads to formation of bonds between the $Pt_{38}$ cluster and the OH functionalised graphene support.

The PDOS of the COOH functionalised graphene carbon atoms post adsorption of the $Pt_{38}$ cluster (see Figure 4.10 (d)) shows that the distribution of states below the Fermi level is similar to that obtained upon adsorption of the $Pt_{38}$ cluster on pristine and monovacancy defective graphene. The adsorption of the $Pt_{38}$ cluster on COOH functionalised graphene shows the appearance of distinct, unoccupied states on the carbon atoms below the Fermi level. The PDOS for the Pt 5d states of the $Pt_{38}$ cluster supported on COOH functionalised graphene (see Figure 4.11 (e)) shows a strong smearing of the states below the Fermi level with a predominance of states at energies less than 1-2 eV below the Fermi energy. The changes to the PDOS spectrum post adsorption of the $Pt_{38}$ cluster and the localised charge redistribution in the contact region is indicative of orbital interaction between the carbon 2p states and the Pt 5d states leading to covalent bonding between the $Pt_{38}$ cluster and the support.

An analysis was also performed to assess the reactivity of the $Pt_{38}$ cluster supported on the different support materials. Ruban et al. (1997) identified three main parameters as reactivity indicators for metals, viz. the d-band centre ($\varepsilon_d$), the d-band filling ($f_d$) and the coupling matrix element ($V_{ads}$) between the adsorbate states and the metal d-states. Other reactivity indicators which are considered to affect the metal reactivity to a lesser extent are the d-band width ($w_d$) and the d-band shape. The d-band centre has been identified as an important parameter characterising the ability of the d-electrons to form bonds with adsorbates (Ruban et al., 1997).

In the present study we use the reactivity parameters: d-band centre, d-band filling and the d-band width to assess the reactivity of the $Pt_{38}$ cluster supported on the different supports. The reactivity parameters are calculated for the entire $Pt_{38}$ cluster, for the facet interacting directly with the support and for the opposite facet to the one interacting with the support which is exposed to the gas phase reactants. The reactivity parameters are calculated to asses if the reactivity of the entire $Pt_{38}$ cluster relative to the free standing $Pt_{38}$ cluster is different, and for the different facets to access whether the effect of the support affects only the facet in contact with the support or extends to facets distant from the support.

The reactivity parameters of the $Pt_{38}$ cluster on the different supports is calculated using the following relations (Hensley et al., 2014):

$$\varepsilon_d = \frac{\int_{-\infty}^{\infty} N(E)EdE}{\int_{-\infty}^{\infty} N(E)dE} \tag{4.5}$$

$$w_d = \sqrt{\frac{\int_{-\infty}^{\infty} N(E)E^2 dE}{\int_{-\infty}^{\infty} N(E)dE}} \tag{4.6}$$

$$N_{states} = \int_{-\infty}^{\infty} N(E)dE \tag{4.7}$$

$$N_{occupied\ states} = \int_{-\infty}^{Ef} N(E)dE \tag{4.8}$$

$$f_d = \frac{N_{occpied\ states}}{N_{states}} \tag{4.9}$$

where $N(E)$ is the valence d-band density of states, and $E$ is the valence d-band energy. The energy intervals used for the integration is 0.11 eV with 300 points used.

The calculated electronic parameters of the $Pt_{38}$ cluster obtained in the present study presented in Table 4.6 compare well with previous calculations of the free standing $Pt_{38}$ cluster by Jennings et al. (2012). They calculated a d-band centre of -2.02 eV, Fermi level of -4.950 eV, and a d-band width of 2.72 eV for the $Pt_{38}$ cluster using the GGA-PW91 functional and ultrasoft pseudopotentials. The difference between the results of the present study and those of Jennings et al. (2012) might be ascribed to the use of different pseudopotential implementations. The difference in d-band energy of the square (100)-like facet and the hexagonal (111)-like facet in the present study is 0.29 eV, this difference in d-band centre energy is of the same order of magnitude predicted by Ruban et al. (1997) for the difference between the fcc (111) and fcc (100) facets of platinum. Ruban et al. (1997) calculated the d-band centre energy for the Pt (111) facet to be -2.25 eV whilst in the present study the d-band centre for the hexagonal (111) like facet is -2.21 eV which is close to the d-band centre of the iso-structural extended Pt (111). In a more recent study by Kitchin et al. (2004) the d-band centre for extended Pt (111) was calculated to be -2.44 eV.

From Table 4.6 it can be observed that there is a downward shift to more negative energy values of the d-band centre of the entire $Pt_{38}$ cluster relative to the free standing $Pt_{38}$ cluster d-band centre upon adsorption on the different supports. The extent of downshift of the d-band centre is as follows: OH functionalised graphene (0.33 eV) > COOH functionalised graphene (0.23 eV) > monovacancy defective graphene (0.18 eV) > pristine graphene (0.11 eV). The downshift of the d-band centre on all the supports and the varying degree of downshift of the d-band centre relative to the free standing $Pt_{38}$ cluster indicates bonding of the $Pt_{38}$ cluster with the support through the d-band. Furthermore, the downshift of the d-band centre upon adsorption correlates linearly with the binding energy, except for adsorption of the $Pt_{38}$ cluster on graphene with a monovacancy defect.

Table 4.6: Calculated Fermi level, d-band centre relative to Fermi level, d-band filling and d-band width for the $Pt_{38}$ cluster adsorbed on the different supports.

| | $\varepsilon_F$ (eV) | $\varepsilon_d - \varepsilon_F$ (eV) | $f_d$ | $w_d$ (eV) |
|---|---|---|---|---|
| **$Pt_{38}$ free standing cluster** | | | | |
| overall cluster | -4.00 | -1.96 | 0.98 | 2.56 |
| square facet | -4.00 | -1.92 | 0.97 | 2.56 |
| hexagonal facet | -4.00 | -2.21 | 0.98 | 2.92 |
| **$Pt_{38}$ on pristine graphene** | | | | |
| overall cluster | -2.22 | -2.07 | 0.92 | 3.05 |
| interacting facet (square) | -2.22 | -2.27 | 0.90 | 3.40 |
| opposite facet (square) | -2.22 | -1.51 | 0.88 | 2.35 |
| **$Pt_{38}$ on monovacancy graphene** | | | | |
| overall cluster | -2.21 | -2.14 | 0.77 | 3.26 |
| interacting facet (hexagonal) | -2.21 | -2.53 | 0.83 | 3.78 |
| opposite facet (hexagonal) | -2.21 | -1.93 | 0.84 | 2.85 |
| **$Pt_{38}$ on OH functionalised graphene** | | | | |
| overall cluster | -2.14 | -2.29 | 0.92 | 3.30 |
| interacting facet (square) | 2.14 | -2.42 | 0.90 | 3.47 |
| opposite facet (square) | 2.14 | -2.09 | 0.89 | 3.05 |
| **$Pt_{38}$ on COOH functionalised graphene** | | | | |
| overall cluster | -3.22 | -2.19 | 0.90 | 3.22 |
| interacting facet (hexagonal) | -3.22 | -2.13 | 0.92 | 3.11 |
| opposite facet (hexagonal) | -3.22 | -2.08 | 0.91 | 3.04 |

Comparing the $Pt_{38}$ cluster adsorbed on pristine and on monovacancy graphene indicates that the d-band centre for the $Pt_{38}$ cluster on monovacancy graphene is only 0.07 eV more negative than on pristine graphene, despite the strong binding energy on monovacancy graphene. A similar observation has been made by Fampiou & Ramasubramaniam (2012) for the adsorption of a $Pt_{13}$ cluster on pristine and monovacancy graphene with the d-band centre on monovacancy defective graphene being more negative by 0.06 eV. The minor shift of d-band centre upon $Pt_{38}$ cluster adsorption on monovacancy graphene relative to adsorption on pristine graphene might suggest that the stronger binding energy on monovacancy graphene is not only due to interaction of the metal d-band with carbon atoms, but rather due to a stabilisation of the monovacancy defect on graphene.

The d-band filling does not vary when the $Pt_{38}$ cluster is adsorbed on the various supports indicating almost ideal filling. It is interesting to note that the free standing $Pt_{38}$ cluster shows higher than ideal d-band filling (0.93 (Kitchin et al., 2004)) indicating a shift of the s vs d-band energy as a function of size. However, the d-band filling of the $Pt_{38}$ cluster adsorbed on monovacancy defective graphene is significantly lower. A net electron transfer from the $Pt_{38}$ cluster to the monovacancy defective graphene is observed, hence it can be concluded that electrons from the d-band were transferred to the support. Despite the smaller d-band centre shift of the entire $Pt_{38}$ cluster adsorbed on monovacancy defective graphene, the significantly lower degree of d-band filling indicates depopulation at the top of the d-band. The d-states at the top of the d-band are antibonding states which are destabilising in nature, therefore the depopulation of the states at the top of the d-band contribute to the stabilisation of the adsorbed system of the $Pt_{38}$ cluster on monovacancy graphene. It is further noted that a change in the degree of filling of the d-band is observed for the facets in direct contact with the support and the opposite facet which may imply electron transfer from the entire $Pt_{38}$ cluster.

An important aspect in the reactivity of the supported $Pt_{38}$ clusters is the d-band centre of the facets accessible to reactants in the gas phase. Here we examine the reactivity in terms of the d-band centre of the facet opposite the facet interacting with the support. The d-band centre of the opposite facet is typically shifted towards higher energies in comparison to the d-band centre of the hexagonal facet on the bare $Pt_{38}$ cluster.

The most favourable interaction with $Pt_{38}$ on monovacancy defective graphene is through its hexagonal facet. The d-band centre of the interacting facet of the $Pt_{38}$ cluster on graphene containing a monovacancy of -2.53 eV is more negative than the d-band centre of the Pt (111) surface (-2.44 eV). This result is consistent with the results of Fampiou & Ramasubramaniam (2012) who calculated a d-band centre of a $Pt_{13}$ cluster adsorbed on graphene containing a monovacancy lower than that of the Pt (111) surface. An upward shift of the centre of the d-band is observed for the opposite hexagonal facet by ca. 0.28 eV, a rather modest shift in the d-band centre in comparison to the shift obtained when binding to pristine graphene, despite the strong binding of $Pt_{38}$ to this support. This implies that the shift in reactivity obtained over this strongly binding support material will be less than the shift in reactivity obtained when binding $Pt_{38}$ to pristine graphene.

The most favourable interaction of $Pt_{38}$ with pristine graphene is through its square facet. The d-band energy of the opposite square facet is shifted 0.41 eV up relative to the d-band centre of a square facet of the unsupported $Pt_{38}$ cluster, and is 0.70 eV higher than that on a

hexagonal facet. This implies a significant change in the reactivity of the cluster even when depositing on the weakly interacting pristine graphene.

Rather modest shifts in the d-band centre are obtained upon adsorbing $Pt_{38}$ on OH functionalised graphene and COOH functionalised graphene. The d-band centre for the $Pt_{38}$ cluster facet interacting with OH functionalised graphene is calculated to be -2.42 eV which is very close to the d-band centre of -2.44 eV for the Pt (111) surface. A downward shift in the d-band centre on the opposite square facet relative to the d-band centre in a square facet on the unsupported $Pt_{38}$ cluster was obtained (-0.17 eV; the d-band centre on this square facet is still higher than the d-band centre on a hexagonal facet on the unsupported $Pt_{38}$ cluster by 0.12 eV). An upward shift in the d-band centre on the opposite facet of the same magnitude (0.13 eV) was obtained for adsorption of $Pt_{38}$ on COOH functionalised graphene, where the platinum cluster in its most favourable configuration interacts through a hexagonal facet with the support. This implies that the reactivity of $Pt_{38}$ adsorbed on OH or COOH functionalised graphene has a larger resemblance with the reactivity of the unsupported $Pt_{38}$ cluster than $Pt_{38}$ adsorbed on either pristine graphene or graphene containing a monovacancy.

On all the support materials but OH functionalised graphene, there is an upward shift of the d-band centre of the opposite facet relative to the d-band centre of the same facet of the free standing $Pt_{38}$ cluster. For the $Pt_{38}$ cluster adsorbed on OH functionalised graphene, there is a downward shift of 0.17 eV of the opposite square facet relative to the d-band centre of the square facet of the free standing $Pt_{38}$ cluster. The implication of the downward shift of the d-band centre of the opposite facet of the $Pt_{38}$ cluster adsorbed on OH functionalised graphene is that the square facet will be less reactive (bind adsorbates less strongly) compared to the reactivity of the square facet in the free standing $Pt_{38}$ cluster. Furtheron, the reactivity of the $Pt_{38}$ cluster supported on OH functionalised graphene is expected to the different to that of the $Pt_{38}$ cluster supported on COOH functionalised graphene due to the opposite shift in d-band centre of the opposite facets.

On all the different supports the d-band centre of the facet in contact with the support is downshifted more than that of the opposite facet exposed to adsorbate molecules, relative to the d-band centre of the same facet for the free unsupported $Pt_{38}$ cluster. Moreover, on all supports but monovacancy graphene there is a slightly lower d-band filling of the order of 0.02 for the opposite facet relative to the facet in contact with the support. This implies that there is slightly less d-electrons available to form bonds on the opposite facet than on the facet in contact with the support, thus a difference in reactivity between the facet in contact with the support and the opposite facet can be expected.

A correlation between the d-band centre and the d-band width can be deduced from the data reported in Table 4.6. The d-band centre and the d-band width move in the same direction, as the d-band centre becomes more negative the d-band width becomes wider, i.e. more positive. The implication is that the d-band width and the d-band centre are not independent variables.

## 4.4 Conclusions

The binding energy of the $Pt_{38}$ cluster on the different supports follow the order: monovacancy graphene > OH functionalised graphene > COOH functionalised graphene > pristine graphene. The stable binding energy of the $Pt_{38}$ cluster on monovacancy graphene is primarily due to the stabilisation of the monovacancy site by charge donation from the $Pt_{38}$ cluster to the support. The higher binding energy of the $Pt_{38}$ cluster on OH and COOH functionalised graphene indicates that even when the monovacancy site on graphene is occupied by the functional groups, the binding of the $Pt_{38}$ cluster is enhanced relative to binding on pristine graphene. The binding energy of the $Pt_{38}$ cluster on OH and COOH functionalised graphene is linearly correlated to the change in d-band centre of the adsorbed $Pt_{38}$ cluster.

The relative energy trends of the binding energy (i.e. stability ranking on the different supports) obtained without the inclusion of van der Waals interactions is maintained with the inclusion of van der Waals interactions. Inclusion of van der Waals interactions results in the correct sign of the binding energy on pristine graphene which is calculated to be endothermic with the GGA-PW91 functional. On other supports, e.g. OH functionalised graphene and monovacancy graphene a slightly different geometry with different bond lengths is predicted by vdW DFT methods compared to the standard GGA-PW91 calculations. Despite some discrepancies, in general the van der Waals DFT method (vdW-OptPBE) predicts similar geometries to the PW91 functional.

The functional groups on graphene (either as hydroxyl or as carboxylic acid) act as anchoring sites of the $Pt_{38}$ cluster, not through direct interaction with the functional group but indirectly by modifying the electronic properties of the carbon atoms in the vicinity of the functional group. The $Pt_{38}$-cluster then binds strongly to the modified carbon atoms in the vicinity of the functional group. The functional groups also modify differently the electronic properties of the supported $Pt_{38}$-cluster hence the reactivity of the supported cluster maybe modified relative to that of the free standing cluster. The effect of the functional group is not localised only to the atoms of the facet in contact with the support but also affects the entire cluster and the opposite facet not in contact with the support. This is manifested by the change in d-band centre of the

entire cluster, the interacting facet and the opposite facet relative to the d-band centres in the free unsupported $Pt_{38}$ cluster. The shift of the d-band centre of the $Pt_{38}$ cluster supported on OH and COOH functionalised graphene is rather small in comparison to the shifts obtained for the $Pt_{38}$ cluster supported on pristine graphene or graphene containing a monovacancy. This implies that the reactivity towards adsorbate molecules when supported on OH and COOH functionalised graphene is expected to bear greater resemblance to reactivity of the free standing $Pt_{38}$ cluster.

# 4.5 References

Amft, M., Sanyal, B., Eriksson, O. & Skorodumova, N.V. (2011) Small gold clusters on graphene, their mobility and clustering: a DFT study. *J. Phys. Condens. Matter* **23**, 205301-205310.

Bader, R.F.W. (1991) A quantum theory of molecular structure and its applications. *Chem. Rev.* **91**, 893-928.

Balasubramaniam, K. & Burghard, M. (2005) Chemically functionalized carbon nanotubes. *Small* **1**, 180-192.

Blöchl, P.E. (1994) Projector augmented-wave method. *Phys. Rev. B* **50**, 17953-17979.

Bučko, T., Lebégue, S., Hafner, J. & Ángyán, J.G. (2013) Tkatchenko-Scheffler van der Waals correction method with and without self-consistent screening applied to solids. *Phys. Rev. B* **87**, 064110-064125.

Burgess, R., Buono, C., Davies, P.R., Davies, R.J., Legge, T., Lai, A., Lewis, R., Morgan, D.J., Robinson, N. & Willock, D.J. (2015) The functionalisation of graphite surfaces with nitric acid: identification of functional groups and their effect on gold deposition. *J. Catal.* **323**, 10-18.

Chen, J., Hamou, M.A., Hu, H., Chen, Y., Rao, A.M., Eklund, P.C. & Haddon, R.C. (1998) Solution properties of single-walled carbon nanotube'. *Science* **282**, 95-98.

Chutia, A., Hamada, I. & Tokuyama, M. (2014) A theoretical insight on the interaction between Pt nanoparticles and hydroxylated graphene nanoflakes. *Surf. Sci.* **628**, 116-125.

Coleman, V.A., Knut, R., Karis, O., Grennberg, H., Jansson, U., Quinlan, R., Holloway, B.C., Sanyal, B. & Eriksson, O. (2008) Defect formation in graphene nanosheets by acid treatment: an x-ray absorption spectroscopy and density functional theory study. *J. Phys. D: Appl. Phys.* 41, 062001-062005.

Denis, P.A. & Iribarne, F. (2013) Comparative study of defect reactivity in graphene. *J. Phys. Chem.* C **117**, 19048-19055.

Dion, M., Rydberg, H., Schröder, E., Langreth, D.C. & Lundqvist, B.I. (2004) Van der Waals density functional for general geometries. *Phys. Rev. Lett.* **92**, 246401-246405.

Edwards, J.K., Freakly, S.J., Carley, A.F., Kiely, C.J. & Hutchings, G.J. (2014) Strategies for designing supported gold-palladium bimetallic catalysts for the direct synthesis of hydrogen peroxide. *Acc. Chem. Res*. **47**, 845-854.

Fampiou, I. & Ramasubramaniam, A. (2012) Binding of Pt nanoclusters to point defects in graphene: adsorption, morphology, and electronic structure. *J. Phys. Chem. C* **116**, 6543-6555.

Fampiou, I. & Ramasubramaniam, A. (2013) CO adsorption on defective graphene-supported $Pt_{13}$ nanoclusters. *J. Phys. Chem. C* **117**, 19927-19933.

Fuentes-Cabrera, M., Baskes, M.I., Melechko, A.V. & Simpson, M.L. (2008) Bridge structure for the graphene/ Ni (111) system: A first principles study. *Phys. Rev. B* **77**, 035405-035410.

Gao, W., Xiao, P., Henkelman, G., Liechtl, K.M. & Huang, R. (2014) Interfacial adhesion between graphene and silicon dioxide by density functional theory with van der Waals corrections. *J. Phys. D: Appl. Phys*. **47**, 255301-255307.

Giovannetti, G., Khomyakov, P.A., Brocks, G., Karpan, V.M., van den Brink, J. & Kelly, P.J. (2008) Doping graphene with metal contents. *Phys. Rev. Lett*. **101**, 026803-026807.

Henkelman, G., Arnaldsson, A. & Jónsson, H. (2006) A fast and robust algorithm for Bader decomposition of charge density. *Comput. Mater. Sci*. **36**, 354-360.

Hensley, A.J.R., Wang, Y. & McEwen, J.S. (2014) Adsorption of phenol on Fe(110) and Pd(111) from first principles. *Surf. Sci*. **630**, 244-253.

Jennings, P.C., Pollet, B.G. & Johnston, R.L. (2012) Electronic properties of Pt-Ti nanoalloys and the effect on reactivity for use in PEMFCs. *J. Phys. Chem. C.* **116**, 15241-15250.

Kitchin, J.R., Nørskov, J.K., Barteau, M.A. & Chen, J.G. (2004) Modification of the surface electronic and chemical properties of Pt (111) by subsurface 3d transition metals. *J. Chem. Phys.* **120**, 10240-10246.

Klimeš, J., Bowler, D.R. & Michaelides, A. (2010) Chemical accuracy for the van der Waals density functional. *J. Phys.: Condens. Matter* **22**, 022201-022206.

Klimeš, J. & Michaelides, A. (2012) Perspective: Advances and challenges in treating van der Waals dispersion forces in density functional theory. *J. Chem. Phys*. **137**, 120901-120913.

Kong, K., Choi, Y., Ryu, B.H., Lee, J.O. & Chang, H. (2006) Investigation of metal/carbon-related materials for fuel cell applications by electronic structure calculations. *Mater. Sci. Eng. C* **26**, 1207-1210.

Kou, R., Shao, P., Wang, D., Engelhard, M.H., Kwak, J.H., Wang, J., Viswanathan, V.V., Wang, C., Lin, Y., Wang, Y., Aksay, I.A. & Lin, J. (2009) Enhanced activity and stability of Pt catalysts on functionalized graphene sheets for electrocatalytic oxygen reduction. *Electrochem. Commun*. **11**, 954-957.

Kou, R., Shao, Y., Mei, D., Nie, Z., Wang, D., Wang, C., Viswanathan, V.V., Park, S., Aksay, I.A., Lin, Y., Wang, Y. & Liu, J. (2011) Stabilization of electrocatalytic metal nanoparticles at metal-metal oxide-graphene triple junction point. *J. Am. Chem. Soc.* **133**, 2541-2547.

Kresse, G. & Furthmüller, J. (1996a) Efficiency of ab-initio total energy calculations for metals and semiconductors using a plane-wave basis set. *Comput. Mater. Sci*. **6**, 15-50.

Kresse, G. & Furthmüller, J. (1996b) Efficient iterative schemes for ab-initio total-energy calculations using a plane wave basis set. *Phys. Rev. B* **54**, 11169-11186.

Kresse, G. & Jourbert, D. (1999) From ultrasoft pseudopotentials to the projector augmented-wave method. *Phys. Rev. B* **59**, 1758-1775.

Kresse, G. & Hafner, J. (1994) Ab initio molecular-dynamics simulation of the liquid-metal-amorphous-semi-conductor transition on germanium. *Phys. Rev. B* **49**, 14251-14269.

Kresse, G. & Hafner, J. (1993) Ab initio molecular dynamics for liquid metals. *Phys. Rev. B* **47**, 558-561.

Kuznetsova, A., Popova, I., Yates Jr., J.T., Bronikowski, M.J., Huffman, C.B., Liu, J., Smalley, R.E., Hwu, H. & Chen, J.G. (2001) Oxygen-containing functional groups on single-wall carbon

nanotubes: NEXAFS and vibrational spectroscopic studies. *J. Am. Chem. Soc*. **123**, 10699-10704.

Lide, D.R. CRC Handbook of Chemistry and Physics, 85th ed., CRC Press, 2004.

Lim, D.H. & Wilcox, J. (2011) DFT-based study on oxygen adsorption on defective graphene-supported Pt nanoparticles. *J. Phys. Chem. C* **115**, 22742-22747.

Maiti, A. & Ricca, A. (2004) Metal-nanotube interactions-binding energies and wetting properties. *Chem. Phys. Lett*. **395**, 7-11.

Methfessel, M. & Paxton, A.T. (1989) High precision sampling for Brillouin-zone integration in metals. *Phys. Rev. B* **40**, 3616-3621.

Monkhorst, H.J. & Pack, J.D. (1976) Special points for Brillouin-zone integrations. *Phys. Rev. B* **13**, 5188-5192.

Okamoto, Y. (2006) Density – functional calculations of icosahedral $M_{13}$ (M=Pt and Au) clusters on graphene sheets and flakes. *Chem. Phys. Lett*. **420**, 382-386.

Okazaki-Maeda, K., Morikawa, Y., Tanaka, S. & Kohyama, M. (2010). Structures of Pt clusters on graphene by first-principles calculations. *Surf. Sci.* **604**, 144-154.

Paz-Borbón, L.O., Johnston, R.L., Barcaro, G. & Fortunelli, A. (2008) Structural motifs, mixing, and segregation effects in 38-atom binary clusters. *J. Chem. Phys*. **128**, 134517-134529.

Perdew, J.P., Chevary, J.A., Vosko, S.H., Jackson, K.A., Pederson, M.R., Singh, D.J. & Fiolhais, C. (1992) Atoms, molecules, solids, and surfaces: applications of the generalized gradient approximation for exchange and correlation. *Phys. Rev. B* **46**, 6671-6686.

Prado-Burguete, C., Linares-Solano, A., Rodríguez-Reinoso, F. & Salinas-Martínez de Lecea, C. (1989) The effect of oxygen surface groups of the support on platinum dispersion in Pt/Carbon catalysts. *J. Catal.* **115**, 98-106.

Preobrajenski, A.B., Ling Ng, M., Vinogradov, A.S. & Mårtensson, N. (2008) Controlling graphene corrugation on lattice-mismatched substrates. *Phys. Rev. B* **78**, 073401-073406.

Ruban, A., Hammer, B., Stolze, P., Skriver, H.L. & Nørskov, J.K. (1997) Surface electronic structure and reactivity of transition and noble metals. *J. Mol. Catal. A. Chem* **115**, 421-429.

Rubeš, M., Kysilka, J., Nachtigall, P. & Bludskỳ. (2010) DFT/CC investigation of physical adsorption on a graphite (0001) surface*. Phys. Chem. Chem. Phys*. **12**, 6438-6444.

Rodríguez-Reinoso, F., Rodríguez-Ramos, I., Moreno-Castilla, C., Guerrero-Ruiz, A. & López-González, J.D. (1986) Platinum catalysts supported on activated carbon. *J. Catal.* **99**, 171-183.

Román-Pérez, G. & Soler, J.M. (2009) Efficient implementation of a van der Waals density functional: application to double-wall carbon nanotubes. *Phys. Rev. Lett.* **103**, 096102-096106.

Sanville, E., Kenny, S.D., Smith, R. & Henkelman, G. (2007) Improved grid-based algorithm for Bader charge allocation. *J. Comput. Chem*. **28**, 899-908.

Schneip, H.C., Li, J., McAllister, M.J., Sai, H., Herera-Alonso, M., Adamson, D.H., Prud'homme, R.K., Car, R., Saville, D.A. & Aksay, I.A. (2006) Functionalized single graphene sheets derived from splitting graphite oxide. *J. Phys. Chem. B* **110**, 8535-8539.

Shao, Y., Liu, J., Wang, Y. & Liu, Y. (2009) Novel catalyst support materials for PEM fuel cells: current status and future prospects. *J. Mater. Chem.* **19**: 46-59.

Subrahmanyam, K., Manna, A.K., Pati, S.K. & Rao, C.N.R. (2010) A study of graphene decorated with metal nanoparticles. *Chem. Phys. Lett*. **497**, 70-75.

Sutter, P., Sadowski, J.T. & Sutter, E. (2009) Graphene on Pt (111): growth and substrate interaction. *Phys. Rev. B* **80**, 245411-245421.

Tang, W., Sanville, E. & Henkelman, G. (2009) A grid-based Bader analysis algorithm without lattice bias. *J. Phys.: Condens. Matter* **21**, 084204-084211.

Thonhauser, T., Cooper, V.R., Li, S., Puzder, A., Hyldgaard, P. & Langreth, D.C. (2007) Van der Waals density functional: self-consistent potential and the nature of the van der Waals bond. *Phys. Rev. B* **76**, 125112-125123.

Tkatchenko, A., DiStasio Jr., R.A., Car, R. & Scheffler, M. (2012) Accurate and efficient method for many-body van der Waals interactions. *Phys. Rev. Lett*. **108**, 236402-236407.

Tonigold, K. & Groß, A. (2010) Adsorption of small aromatic molecules on the (111) surfaces of noble metals: A density functional theory study with Semiempirical corrections for dispersion effects. *J. Chem. Phys*. **132**, 224701-224711.

Vanin, M., Mortensen, J.J., Kelkkanen, A.K., Garcia-Lastra, J.M., Thygesen, K.S. & Jacobsen, K.W. (2010) Graphene on metals: A van der Waals density functional study. *Phys. Rev. B* **81**, 081408-081412.

Vedala, H., Sorescu, D.C., Kotchey, G.P. & Star, A. (2011) Chemical sensitivity of graphene edges decorated with metal nanoparticles. *Nano Lett*. **11**, 2342-2347.

Wissler, M. (2006) Graphite and carbon powders for electrochemical applications. *J. Power Sources* **156**, 142-150.

# Chapter 5: $Pt_{32}Pd_6$ cluster interaction with pristine and functionalised graphene

## 5.1 Introduction

Bimetallic alloys can display superior catalytic activity compared to their monometallic counter parts, e.g. a Pd-Au/C catalyst shows superior activity for $H_2O_2$ synthesis in comparison to the monometallic Au/C and Pd/C catalysts (Edwards et al., 2014). The Pd-Pt/C bimetallic catalyst shows higher oxygen reduction reaction (ORR) activity and an improved durability than either monometallic Pt/C or Pd/C catalysts (Kakade et al., 2012). The superior catalytic activity and durability of the bimetallic catalyst over the monometallic catalyst is desirable. Smaller quantities of the noble metal can be utilised in catalysts which utilises expensive noble metals like Pt without losing catalytic performance. The present chapter will focus on the bimetallic Pt-Pd catalyst modelled as a $Pt_{32}Pd_6$ cluster.

Edwards et al. (2014) observed a higher catalytic activity of the Pd-Au bimetallic alloy supported on acid pretreated carbon compared to the activity of the same bimetallic Pd-Au alloy supported on the acid non-pretreated carbon support for the production of $H_2O_2$. It was concluded that the acid pretreatment step does not only act as a cleaning step but also has an effect on the activity of the supported Pd-Au bimetallic alloy catalyst (Edwards et al., 2014). However, no explanation was provided on the origin of the enhanced activity on the acid pretreated support carbon supported catalyst. Burgess et al. (2015) showed that pretreatment of the carbon support with acid ($HNO_3$) results in addition of OH and COOH functional groups to the support. It is hypothesized that these functional groups may have led to activity difference between the Pd-Au supported on acid pretreated carbon and the Pt-Au supported on non-pretreated carbon. Therefore, it is expected that the presence of OH and COOH groups on the carbon support may also affect the physical characteristics of the Pt-Pd alloy supported on the acid pretreated carbon supports. The changed physical characteristics of the Pt-Pd alloy may affect its catalytic properties.

The chemical arrangement of alloy constituents in a free standing nanoparticle and a supported bimetallic nanoparticle can be different. The difference in arrangement can be due to preferential binding of one of the alloy constituent at the substrate-support interface (van

der Oetelaar et al., 2003). It has been shown through DFT studies that a $Pd_mAu_n$ cluster (m + n = 7) is anchored to pristine graphene preferentially with 3 Pd atoms interacting with the support as opposed to interaction with Au atoms (Yuan et al., 2014). This was ascribed to Pd interacting much stronger with pristine graphene than Au atoms.

In the present chapter we investigate whether the chemical ordering of the $Pt_{32}Pd_6$ cluster supported on OH and COOH functionalised graphene is altered relative to arrangement in the free standing $Pt_{32}Pd_6$ cluster. From chapter 3 it was established that the preferred arrangement of the free standing $Pt_{32}Pd_6$ cluster is where Pd atoms occupy the centre of the hexagonal facet on the surface mixed with Pt atoms. Arrangements in which Pd was segregated to either a square or hexagonal facet were found to be least stable than the mixed arrangement with Pd at the centre of the hexagonal facet. The core shell arrangement with all 6 Pd atoms in the core is the least preferred arrangement of the free standing $Pt_{32}Pd_6$ cluster.

## 5.2 Methodology

### 5.2.1 Definition of facets of the $Pt_{32}Pd_6$ cluster

The optimised lowest energy structure (highly exothermic excess energy) of the $Pt_{32}Pd_6$ cluster obtained in chapter 3 is used as the model for the Pt-Pd alloy nanoparticle. The optimised $Pt_{32}Pd_6$ cluster can be described by 5 unique facets as shown in Figure 5.1.
The unique facets are defined as follows:
**Facet A**: square facet, consisting of 4 Pt atoms, surrounded by 4 hexagonal facets each containing a central Pd atom.
**Facet B**: square facet, consisting of 4 Pt atoms, surrounded by 4 hexagonal facets, 2 of which contain a central Pd atom.
**Facet C**: hexagonal facet, consisting of a central Pd atom, surrounded by 3 identical hexagonal facets each containing a central Pd atom.
**Facet D**: hexagonal facet, consisting of a central Pd atom, surrounded by 3 hexagonal facets, 2 of which do not contain a central Pd atom.
**Facet E**: hexagonal facet, consisting only of Pt atoms, surrounded by 3 hexagonal facets, 2 of which consists of a central Pd atom.

The optimised bare supports from chapter 4 are used for pristine graphene, OH and COOH functionalised graphene. To investigate the interaction of the $Pt_{32}Pd_6$ cluster with the different supports, a similar approach to the one for the $Pt_{38}$ cluster interaction with the supports is

adopted. The approach of the cluster to the support is probed only for approach through the facets and not through corner or edge atoms.

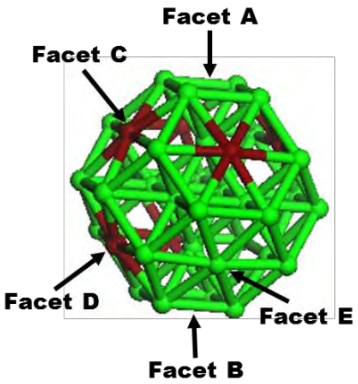


Figure 5.1: Labelling of the unique facets of the $Pt_{32}Pd_6$ cluster.

A detailed description of the procedure followed for the adsorption geometries to determine the facet of interaction of the $Pt_{32}Pd_6$ cluster with pristine and functionalised graphene supports is presented in *Appendix C1*. Similarly, the procedure for investigating rearrangement of the $Pt_{32}Pd_6$ cluster supported on the functionalised graphene supports is presented in *Appendix C2*.

### 5.2.2 Computational method

The calculations were performed using the Vienna ab initio simulation package VASP (Kresse & Hafner, 1993; Kresse & Hafner, 1994; Kresse & Furthmüller, 1996a; Kresse & Furthmüller, 1996b). To first investigate the facet of interaction of the cluster with the support, the Generalised Gradient Approximation GGA-PW91 functional (Perdew et al., 1992) was used for the exchange-correlation energy. Once the lowest energy adsorption geometries are identified at the standard DFT GGA level, the two lowest energy adsorption geometries were reoptimised by incorporating the van der Waals correction using the vdW-TS-SCS method (Tkatchenko et al., 2012; Bučko et al., 2013) and the vdW-OptPBE method (Dion et al., 2004; Thonhauser et al., 2007; Romàn-Pérez & Soler, 2009; Klimeš et al., 2010) as implemented in VASP. The electron-ion interactions were described by the projector augmented wave (PAW) method (Blöchl, 1994; Kresse & Jourbert, 1999) pseudopotentials. A plane wave basis set cut-off energy of 400 eV was used for the calculations. The method of Methfessel-Paxton (Methfessel & Paxton, 1989) smearing was employed with a smearing width $\sigma = 0.05$ eV.

For adsorption calculations of the $Pt_{32}Pd_6$ cluster on pristine graphene and OH functionalised graphene, a (6 × 6) unit cell of graphene was used. For adsorption on COOH functionalised

graphene a (7 × 7) unit cell was utilised due to the bulkier COOH group. From chapter 4 it was established that using bigger unit cells does not alter the binding energies by more than 0.12 eV, hence the calculations were performed using the small unit cells. A vacuum region of 25 Å was utilised to avoid spurious interactions between periodic images. Owing to the size of the unit cell, for geometry optimisation calculations the Brillouin zone was sampled at the single Γ-point in k-space. Similarly, from chapter 4 it was established that using a finer k-point grid of (5 × 5 × 1) only affects the calculated binding energies by 0.10 eV, hence for the binding of the $Pt_{32}Pd_6$ cluster the single Γ-point in k-space was utilised for geometry optimisation. Geometry optimisation calculations were performed for the adsorption calculations, with an electronic convergence criterion of energies below $10^{-5}$ eV and forces below 0.03 eV/Å on the unconstrained atoms. During the geometry optimisation all the atoms of the support and the $Pt_{32}Pd_6$ cluster were allowed to relax to the lowest energy state. The dipole correction was applied in the z-direction as implemented within the VASP code to correct for any induced dipoles which may have resulted during adsorption of the $Pt_{32}Pd_6$ cluster.

The binding energy and the formation energy were used to assess the interaction of the $Pt_{32}Pd_6$ cluster with the different supports. The binding energy of the $Pt_{32}Pd_6$ cluster to the different supports was calculated using the relation:

$$E_{bind} = E_{Pt_{32}Pd_6+\ support} - E_{support} - E_{Pt_{32}Pd_6} \quad (5.1)$$

Where $E_{Pt_{32}Pd_6+\ support}$ is the energy of the optimised support with the $Pt_{32}Pd_6$ cluster bound to it, $E_{support}$ is the energy of the optimised support without any $Pt_{32}Pd_6$ cluster adsorbed, $E_{support}$ will be the energy of pristine graphene, OH and COOH functionalised graphene depending on the considered support. $E_{Pt_{32}Pd_6}$ is the energy of the free standing optimised $Pt_{32}Pd_6$ cluster. A positive binding energy indicates unfavourable interaction whilst a negative binding energy indicates favourable interaction.

The formation energy was calculated relative to the free standing $Pd_{38}$ and $Pt_{38}$ clusters.

$$E_{form} = E_{Pt_{32}Pd_6+\ support} - E_{support} - \frac{6}{38}E_{Pd_{38}} - \frac{32}{38}E_{Pt_{38}} \quad (5.2)$$

Where $E_{Pd_{38}}$ is the energy of the optimised free standing $Pd_{38}$ cluster, and $E_{Pt_{38}}$ is the energy of the optimised free standing $Pt_{38}$ cluster.

We define the reference structure as the geometry in which the facet of approach of the $Pt_{32}Pd_6$ cluster to the functionalised graphene (i.e. OH and COOH) has a highly exothermic binding energy. To assess whether the rearranged structure is more stable (i.e. lower in energy) compared to the reference structure, the segregation energy is calculated. A positive segregation energy indicates that rearrangement to the rearranged structure is not preferred

over the reference structure, whereas a negative segregation energy indicates that the rearranged structure is more stable (i.e. lower in energy) relative to the reference structure.

$$E_{seg} = E_i - E_{ref} \quad (5.3)$$

Where $E_i$ is the total energy of the rearranged structure on the support and $E_{ref}$ is the total energy of the reference structure.

To gain further insights into the interaction of the $Pt_{32}Pd_6$ cluster with the different supports, electronic structure analysis calculations were performed. The electronic structure analysis includes PDOS analysis, Bader charge analysis, charge density difference analysis and d-band analysis. For electronic structure analysis calculations, a finer Monkhorst Pack (Monkhorst & Pack, 1976) k-point grid of (6 × 6 × 1) was utilised to sample the Brillouin zone. A single point energy calculation was performed on the lowest energy adsorption structures obtained from geometry optimisation calculations for electronic analysis calculations. The d-band analysis (d-band centre, d-band filling and d-band width) was performed using the method described in chapter 4 (section 4.3.6).

The charge density difference was determined from the relation:

$$\Delta\rho = \rho_{Pt_{32}Pd_6+\ support} - \rho_{support} - \rho_{Pt_{32}Pd_6} \quad (5.4)$$

Where $\rho_{Pt_{32}Pd_6+\ support}$ is the charge density of the optimised support with the $Pt_{32}Pd_6$ cluster adsorbed, $\rho_{support}$ is the charge density of the support without the $Pt_{32}Pd_6$ cluster in the same position as in the optimised geometry with the adsorbed $Pt_{32}Pd_6$ cluster and $\rho_{Pt_{32}Pd_6}$ is the charge density of the $Pt_{32}Pd_6$ cluster in the same position as in the optimised geometry with the support.

For carbon, oxygen and hydrogen atoms of the support, the atom resolved change in Bader charge determined using Bader charge partitioning method (Bader, 1991; Henkelman et al., 2006; Sanville et al., 2007; Tang et al., 2009) was calculated from:

$$\Delta q = q_{Pt_{32}Pd_6+\ support} - q_{support} \quad (5.5)$$

Where $q_{Pt_{32}Pd_6+\ support}$ is the atom resolved Bader charge on carbon, oxygen and hydrogen atoms of the optimised geometry (with the support and the $Pt_{32}Pd_6$ cluster adsorbed), $q_{support}$ is the atom resolved Bader charge on corresponding carbon, oxygen and hydrogen atoms of the support without the $Pt_{32}Pd_6$ cluster in the same position as in the optimised geometry. The atom resolved change in Bader charge on Pt and Pd atoms of the $Pt_{32}Pd_6$ cluster upon adsorption is calculated in a similar way to how the charge on the atoms of the support is calculated.

$$\Delta q = q_{Pt_{32}Pd_6+support} - q_{Pt_{32}Pd_6} \quad (5.6)$$

Where $q_{Pt_{32}Pd_6+support}$ is the atom resolved Bader charge on Pt and Pd atoms in the optimised geometry and $q_{Pt_{32}Pd_6}$ is the atom resolved Bader charge on corresponding Pt and Pd atoms of the $Pt_{32}Pd_6$ cluster without the support in the same position as in the optimised geometry.

## 5.3 Results and Discussion

### 5.3.1 $Pt_{32}Pd_6$ interaction with pristine graphene

#### *5.3.1.1 Adsorption structures of the $Pt_{32}Pd_6$ cluster on pristine graphene*

The optimised adsorption geometries of the $Pt_{32}Pd_6$ cluster interaction with pristine graphene are shown in Figure 5.2. The calculated binding and formation energies with the GGA-PW91 functional are endothermic.

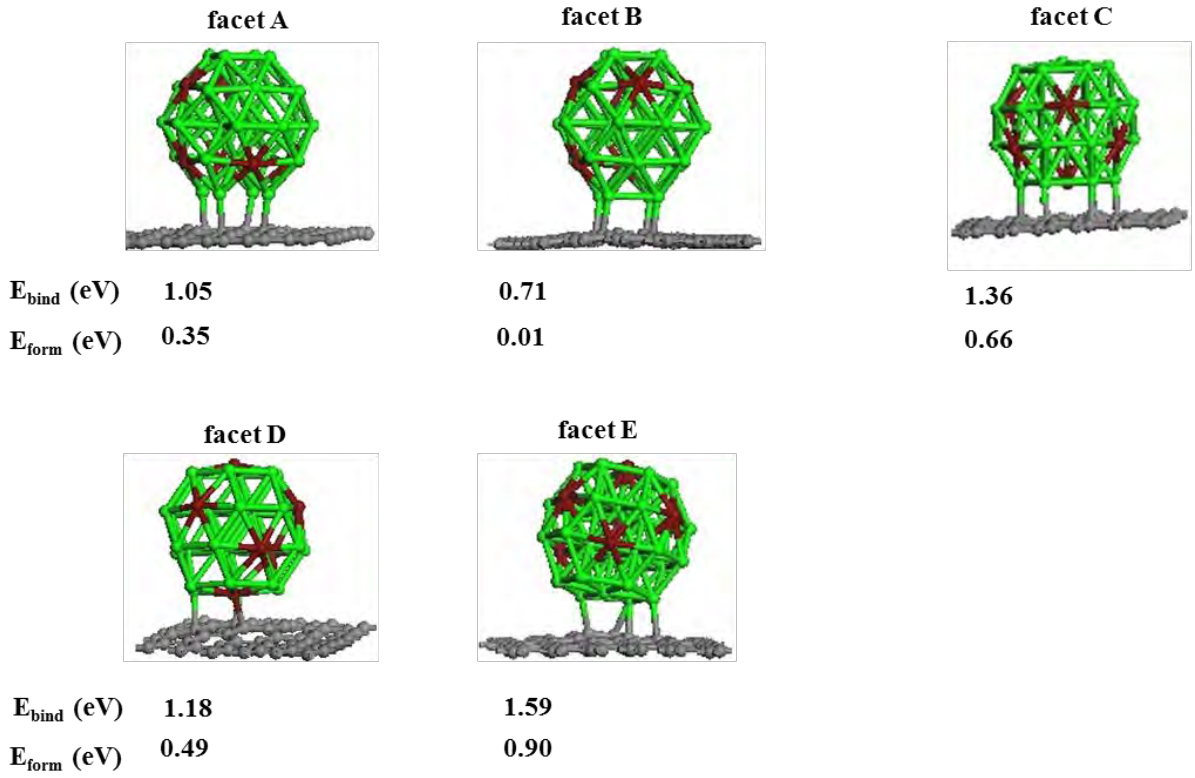


Figure 5.2: Optimised structures of the $Pt_{32}Pd_6$ cluster interaction with pristine graphene through the 5 unique facets of the cluster. The calculated energies are obtained using the GGA-PW91 functional.

The square facet approach structures through facet A and facet B have the least endothermic binding energies. The binding and formation energies of the approach through facet A and

facet B were recalculated by including van der Waals interactions, the results for the inclusion of the van der Waals interactions are presented in *Appendix C3*. Exothermic binding energies of -2.61 eV and -3.20 eV for facet A and facet B respectively were obtained using the vdW-OptPBE functional. Metal-graphene interactions are dominated by weak dispersion forces (Fuentes-Cabrera et al., 2008; Vanin et al., 2010) GGA-DFT does not include non-local correlation effects to describe these dispersion effects (Vanin et al., 2010), hence the positive binding and formation energies obtained with the GGA-PW91 functional.

The discussion on the results of the interaction of the $Pt_{32}Pd_6$ cluster with pristine graphene is based on the PW91 functional results, comparison of the geometry between the PW91 functional and vdW-OptPBE functional is deferred to *Appendix C*. The binding energy trend for the different facets of the $Pt_{32}Pd_6$ cluster can be rationalised by comparing the d-band centre of the 5 unique facets of the cluster. The unique facets have different d-band centres (see Table 5.1) which affect the interaction of the cluster with the pristine graphene support. The d-band centres calculated in Table 5.1 indicates that the d-band centre is highly dependent on the local environment of the facet, e.g. facets A and B are both Pt only facets but have different d-band centres. Facet A is a square Pt only facet with 4 neighbouring Pd atoms occupying the centre of hexagonal facets, whilst facet B is also a Pt only square facet with 2 neighbouring Pd atoms occupying the centre of hexagonal facets. Similarly, facets C and D are both hexagonal facets with central Pd atoms but different d-band centres. Facet C is a hexagonal facet with a central Pd atom with 3 neighbouring Pd atoms occupying the centre of hexagonal facets, whereas facet D is a hexagonal facet with a central Pd atom with a single Pd atom neighbour occupying the centre of the hexagonal facet and 3 neighbouring hexagonal facets consisting of Pt atoms only.

The d-band centre of the square (-1.92 eV) and hexagonal (-2.21 eV) facets of the $Pt_{38}$ cluster are more negative than the d-band centre of the square (facets A and B) and hexagonal facet (facet E) of the $Pt_{32}Pd_6$ cluster consisting of Pt atoms only. Interaction of the $Pt_{32}Pd_6$ cluster through the Pt only hexagonal facet (i.e. facet E) with pristine graphene results in a binding energy of 1.59 eV which is 0.28 eV more endothermic than the hexagonal facet interaction of the $Pt_{38}$ cluster with pristine graphene. For the square facets, the binding energy for the $Pt_{38}$ cluster interacting with pristine graphene through the square facet is 0.14 eV. The binding energy is more stable than the binding energies of 1.05 eV and 0.71 eV for the $Pt_{32}Pd_6$ cluster interacting with pristine graphene through facets A and B respectively. Thus, the binding of the $Pt_{32}Pd_6$ cluster to pristine graphene is less favourable to binding of the $Pt_{38}$ cluster to pristine graphene. Part of the difference in binding might be attributed to the upshifted d-band centre of the facets of the $Pt_{32}Pd_6$ cluster compared to those of the $Pt_{38}$ cluster.

Table 5.1: d-band centre relative to the Fermi level of the 5 unique facets of the $Pt_{32}Pd_6$ cluster.

| **Facet of $Pt_{32}Pd_6$ cluster** | **d-band centre $\varepsilon_d - \varepsilon_f$ (eV)** |
|---|---|
| Facet A | -1.73 |
| Facet B | -1.89 |
| Facet C | -1.84 |
| Facet D | -1.74 |
| Facet E | -1.82 |

There is no clear correlation between the d-band centre of the facet of the $Pt_{32}Pd_6$ cluster interacting with pristine graphene and the binding energy (see Figure 5.3).

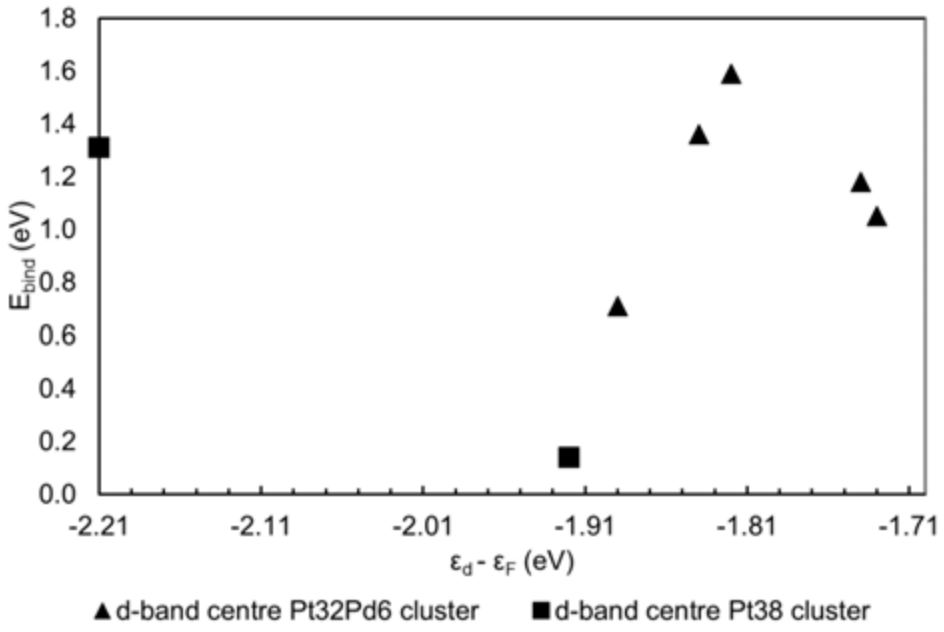


Figure 5.3: Binding energy dependency on relative d-band centre of interacting facet of the $Pt_{32}Pd_6$ and $Pt_{38}$ cluster adsorbed onto pristine graphene.

The binding energy of the $Pt_{32}Pd_6$ cluster does not only depend on the d-band centre of the facet interacting with the pristine graphene support, but also on the local environment surrounding the interacting facet. For a square facet of the $Pt_{32}Pd_6$ cluster interacting with pristine graphene, the local environment of the facet affects its binding energy to the support. Facet A has as neighbours 4 Pd atoms occupying the centre of hexagonal facets, whilst facet B has 2 neighbouring Pd atoms at the centre of hexagonal facets. Facet B with 2 neighbouring Pd atoms has a 0.34 eV less endothermic binding energy than facet A. A similar stabilising effect is observed for the hexagonal facets with a central Pd atom. Facet C has 3 neighbouring Pd atoms and has a 0.18 eV more endothermic binding energy than facet D which has 1 neighbouring Pd atom at the centre of the hexagonal facet. Thus, the content of Pd in the local

environment surrounding the facet in contact with the support affects the binding strength of the $Pt_{32}Pd_6$ cluster to the support.

The Pt-Pt bond distance of the interacting facet and opposite facet for the $Pt_{32}Pd_6$ cluster interacting with the pristine graphene through facets A and B were compared with the bond lengths of the same facets of the free standing $Pt_{32}Pd_6$ cluster. The comparison of the bond lengths of the supported and the free standing $Pt_{32}Pd_6$ cluster was done to assess the effect of interaction with the support on the geometry of the $Pt_{32}Pd_6$ cluster. From chapter 3 (Table 3.3) for the free standing $Pt_{32}Pd_6$ cluster, facet A is rectangular with side lengths 2.64 Å and 2.66 Å. Facet B is also rectangular with side lengths 2.65 Å and 2.70 Å. From Table 5.2 it is observed that upon adsorption through either facet A or facet B, the interacting facet loses its rectangular shape since the 4 Pt-Pt bond distances are not equivalent.

Table 5.2: Optimised parameters for geometric structures of the $Pt_{32}Pd_6$ cluster adsorbed on pristine graphene.

| | **Facet A** | **Facet B** |
|---|---|---|
| **$E_{bind}$ (eV)** | | |
| GGA-PW91 | 1.05 | 0.71 |
| $d_{Pt\text{-}Pt}$ [1], Å | | |
| | 2.95 | 2.83 |
| | 2.87 | 2.81 |
| | 2.96 | 2.86 |
| | 3.01 | 3.05 |
| $d_{Pt\text{-}Pt}$ [2], Å | | |
| | 2.69 | 2.67 |
| | 2.68 | 2.66 |
| | 2.70 | 2.67 |
| | 2.68 | 2.67 |
| $d_{Pt\text{-}C}$ , Å | | |
| | 2.22 | 2.22 |
| | 2.21 | 2.21 |
| | 2.25 | 2.20 |
| | 2.24 | 2.21 |

[1]Pt-Pt distance of the facet closest to graphene

[2] Pt-Pt distance of the facet opposite to the one interacting with the graphene

The Pt-Pt bond lengths of the interacting facets are elongated relative to the Pt-Pt bond lengths of the free standing $Pt_{32}Pd_6$ cluster. The opposite facets to the ones interacting with the support also lose their rectangular shape. The extent of Pt-Pt bond elongation for the opposite facets

relative to the Pt-Pt bond lengths in the free standing $Pt_{32}Pd_6$ cluster is lower than the extent of elongation for the interacting facet.

Some of the calculated Pt-C distances (see Table 5.2) are shorter for approach through facet B which also correlate with the least endothermic binding energy (i.e. more favourable interaction) of facet B compared to facet A.

*5.3.1.2 Electronic structure analysis*

Electronic structure analysis was performed for the $Pt_{32}Pd_6$ clustering interacting through facet B with pristine graphene since this is the lowest energy structure. The charge density difference plot in Figure 5.4 indicates that most of the charge redistribution occurs in the contact region between the cluster and the support. The charge redistribution in the contact region is indicative of bond formation between the cluster and the support. This is similar to the results obtained for the interaction of the $Pt_{38}$ cluster with pristine graphene shown in chapter 4.

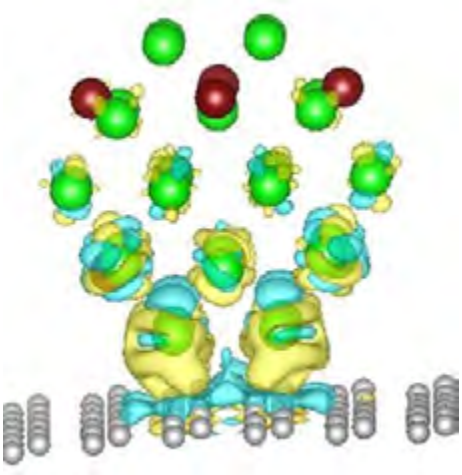

Figure 5.4: Charge density difference for the $Pt_{32}Pd_6$ cluster adsorbed on pristine graphene through facet B. Isosurface level at 0.0025e/ $Å^3$. Key: blue isosurface corresponds to charge depletion and yellow isosurface corresponds to charge accumulation.

The Bader charge analysis provides the atom-resolved charge which can be used to quantify change in charge during adsorption. The Bader charge analysis indicates that there is overall charge transfer of 0.05 e from pristine graphene to the $Pt_{32}Pd_6$ cluster upon adsorption. This amount of charge transfer is not significant, indicating that interaction of the $Pt_{32}Pd_6$ cluster is not dominated by charge transfer. Rather, interaction of the $Pt_{32}Pd_6$ cluster with the pristine graphene support is dominated by charge redistribution within the $Pt_{32}Pd_6$ cluster and the pristine graphene support. Despite the insignificant overall charge transfer, the four Pt atoms

of the square facet interacting with the support lose a total combined charge of 0.52 e upon interaction with the pristine graphene support. However, the overall net charge transfer is calculated to be charge donation of 0.05 e from support to the cluster, this is indicative of charge redistribution from the other atoms of the $Pt_{32}Pd_6$ cluster and the pristine graphene support which are not in the contact region. Charge redistribution by atoms not in the contact region of both the cluster and the pristine graphene has been observed for the $Pt_{38}$ cluster on pristine graphene (see chapter 4) and in a previous DFT study of $Pt_4$ cluster interaction with OH edge decorated graphene (Chutia et al., 2014).

The projected density of states analysis was calculated for carbon atoms of the support in the contact region, and for the entire $Pt_{32}Pd_6$ cluster. The PDOS analysis was to provide insight into electronic structure changes upon adsorption. The PDOS was projected onto C 2p states for carbon atoms of the support and Pt 5d and Pd 4d states for the $Pt_{32}Pd_6$.

Prior to adsorption of the $Pt_{32}Pd_6$ cluster on the pristine graphene support, the PDOS of the carbon atoms show only a very limited number of states around the Fermi level (see Figure 5.5 (a)). Post adsorption of the $Pt_{32}Pd_6$ cluster on the support, the PDOS of the carbon atoms shows a number of small peaks around the Fermi level as shown in Figure 5.5 (a). The appearance of the small peaks at the Fermi level post adsorption is indicative of the formation of bonds between the C 2p states and the Pt 5d-states of the square facet interacting with the support.

The PDOS of the free standing $Pt_{32}Pd_6$ cluster shown in Figure 5.5 (b) is discrete-like with occupied states at the Fermi level. Post adsorption of the $Pt_{32}Pd_6$ cluster on the pristine graphene support, the PDOS is transformed to a continuous profile exhibiting metallic characteristics. This is further indication of the strong interaction between the Pt-5d states and the C 2p states of the support.

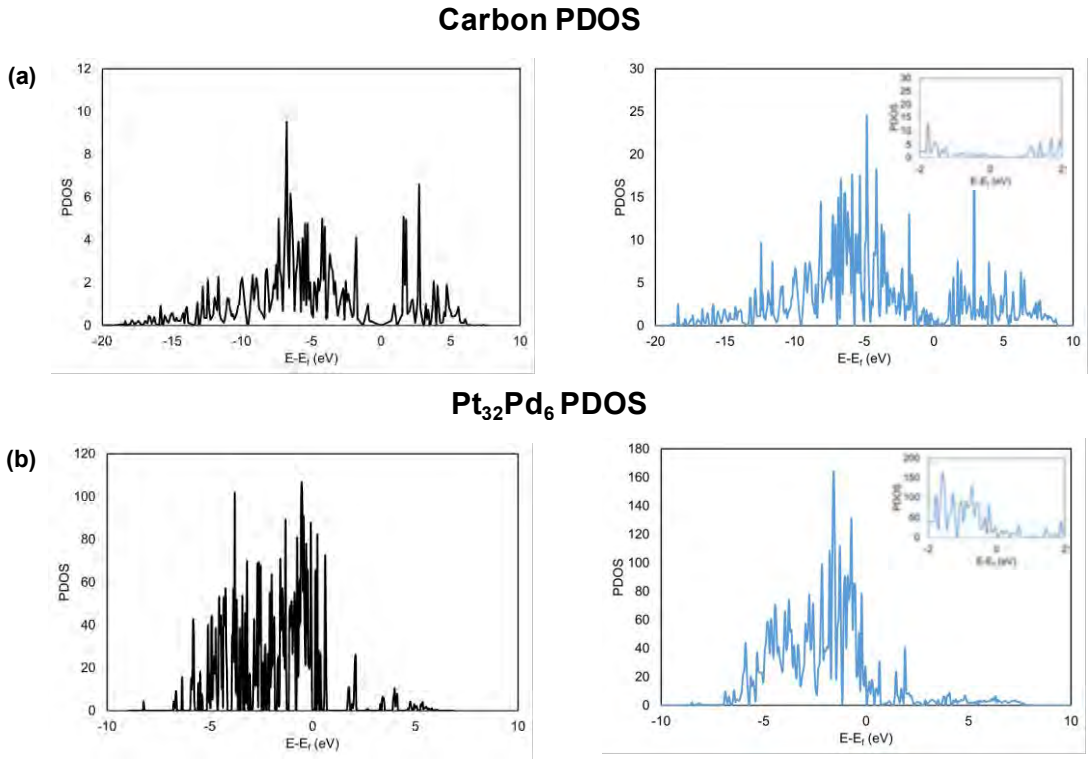


Figure 5.5: PDOS of the carbon, Pt and Pd atoms: (a) PDOS of carbon atoms of pristine graphene before adsorption (black curve) and after adsorption (blue curve), and (b) PDOS of $Pt_{32}Pd_6$ before (black curve) and after adsorption through facet B (blue curve). The energy scale is relative to the Fermi level. Inserts show zoomed view around the Fermi level.

d-band analysis calculations were performed to assess the reactivity of the supported $Pt_{32}Pd_6$ cluster by determining the d-band centre, d-band width and d-band filling and comparing them to those of the free standing $Pt_{32}Pd_6$ cluster.

The interaction of the $Pt_{32}Pd_6$ cluster with the pristine graphene support result in a downward shift of the d-band centre of the entire $Pt_{32}Pd_6$ cluster of 0.25 eV relative to the d-band centre of the free standing $Pt_{32}Pd_6$ cluster (see Table 5.3). The downshift of the d-band centre indicates that the $Pt_{32}Pd_6$ cluster interacts with the pristine graphene support through the d-band. In addition, there is a downshift of the d-band centre of the interacting and opposite facets of the $Pt_{32}Pd_6$ cluster upon interaction with the pristine graphene support. The downshift of the d-band centre relative to the d-band centre of the free standing $Pt_{32}Pd_6$ cluster for the interacting and opposite facets are 0.45 eV and 0.22 eV respectively.

The shift in d-band centre of the interacting facet and the opposite facet indicates that the interaction of the $Pt_{32}Pd_6$ cluster with the pristine graphene support is not limited only to the interacting facet but affects the entire $Pt_{32}Pd_6$ cluster. The extent of downshift of the d-band

centre is higher for the interacting facet than the opposite facet since the interacting facet is directly in contact with the pristine graphene support.

Table 5.3: Calculated d-band centre relative to the Fermi level, d-band filling and d-band width of the $Pt_{32}Pd_6$ cluster interacting with pristine graphene.

| | $\varepsilon_d - \varepsilon_f$ (eV) | $f_d$ | $w_d$ (eV) |
|---|---|---|---|
| **$Pt_{32}Pd_6$ free standing cluster** | | | |
| overall cluster | -1.82 | 0.88 | 2.84 |
| facet A | -1.73 | 0.88 | 2.73 |
| facet B | -1.89 | 0.87 | 2.73 |
| **$Pt_{32}Pd_6$ interacting through facet B with pristine graphene** | | | |
| overall cluster | -2.07 | 0.89 | 3.23 |
| interacting facet (facet B) | -2.34 | 0.88 | 3.61 |
| opposite facet (facet A) | -1.95 | 0.89 | 3.06 |

Of importance in supported catalysts is the reactivity of the facets available to reactants. To assess the reactivity of facets available to reactants, the change in the d-band centre of the opposite facet to the one interacting with the support is used as an indicator of the reactivity of the facets available to the reactants. The downshift of 0.22 eV for the opposite facet relative to the d-band centre of the same facet in the free standing $Pt_{32}Pd_6$ cluster indicates that the reactivity of the supported $Pt_{32}Pd_6$ cluster will be different to that of the unsupported free standing cluster. For the $Pt_{32}Pd_6$ cluster on pristine graphene, weaker binding of adsorbates on the opposite facet can be expected compared to the free unsupported $Pt_{32}Pd_6$ cluster. This is due to the downward shift of 0.22 eV of the d-band centre of the opposite facet. The difference in d-band centre between the fcc(111) and fcc(100) surfaces of Pt has been calculated to be of the order of 0.20 eV (Ruban et al., 1997). The downshift of 0.22 eV of the opposite facet is of the same order of magnitude as the difference between fcc(100) and fcc(111) facets of Pt which have different reactivity. Hence, the of the supported $Pt_{32}Pd_6$ cluster is expected to differ from the free standing $Pt_{32}Pd_6$ cluster.

## 5.3.2 $Pt_{32}Pd_6$ interaction with OH functionalised graphene

### *5.3.2.1 Adsorption structures of the $Pt_{32}Pd_6$ cluster on OH functionalised graphene*

The optimised adsorption geometries of the $Pt_{32}Pd_6$ cluster interacting with OH functionalised graphene are presented in Figure 5.6. All calculated binding energies on OH functionalised

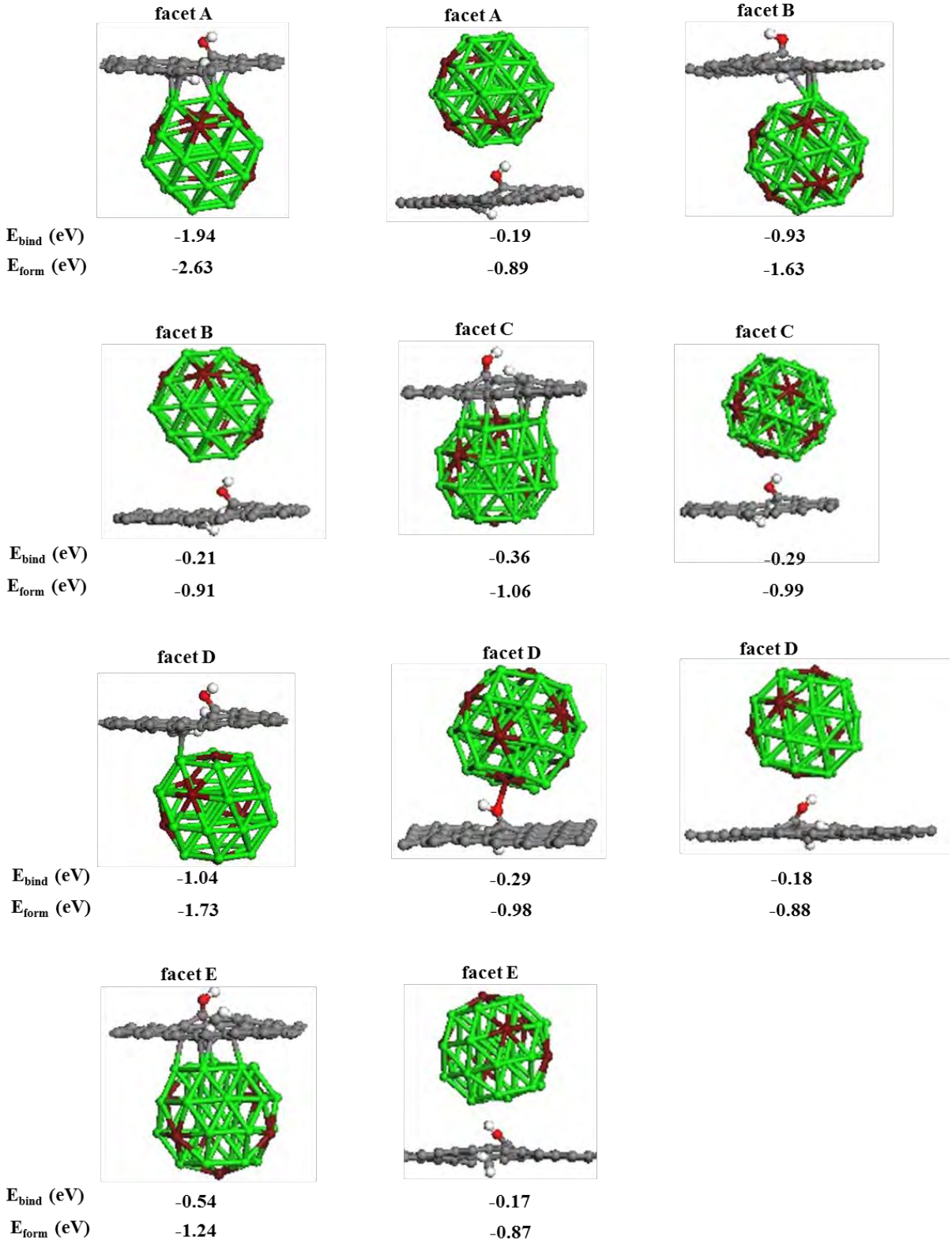


Figure 5.6: Optimised adsorption geometries of the $Pt_{32}Pd_6$ cluster interacting with OH functionalised graphene through the different facets of approach. The calculated energies are obtained using the GGA-PW91 functional.

graphene are exothermic. This indicates that the presence of the OH group stabilises adsorption of the cluster to the support relative to adsorption on pristine graphene, where binding energies are endothermic.

For all the different approaches through each of the unique facets the underneath/bottom approach adsorption geometries have more exothermic binding energies than the ontop geometries (see Figure 5.7). This suggests that binding from underneath leads to stronger interaction between the cluster and the modified carbon atoms around the functional group. For ontop approach, the cluster interacts with the support via direct interaction with the functional group. For ontop adsorption geometries, the variation of the binding energy for the unique facets is small and is hardly dependent on the d-band centre of the facet interacting with the support.

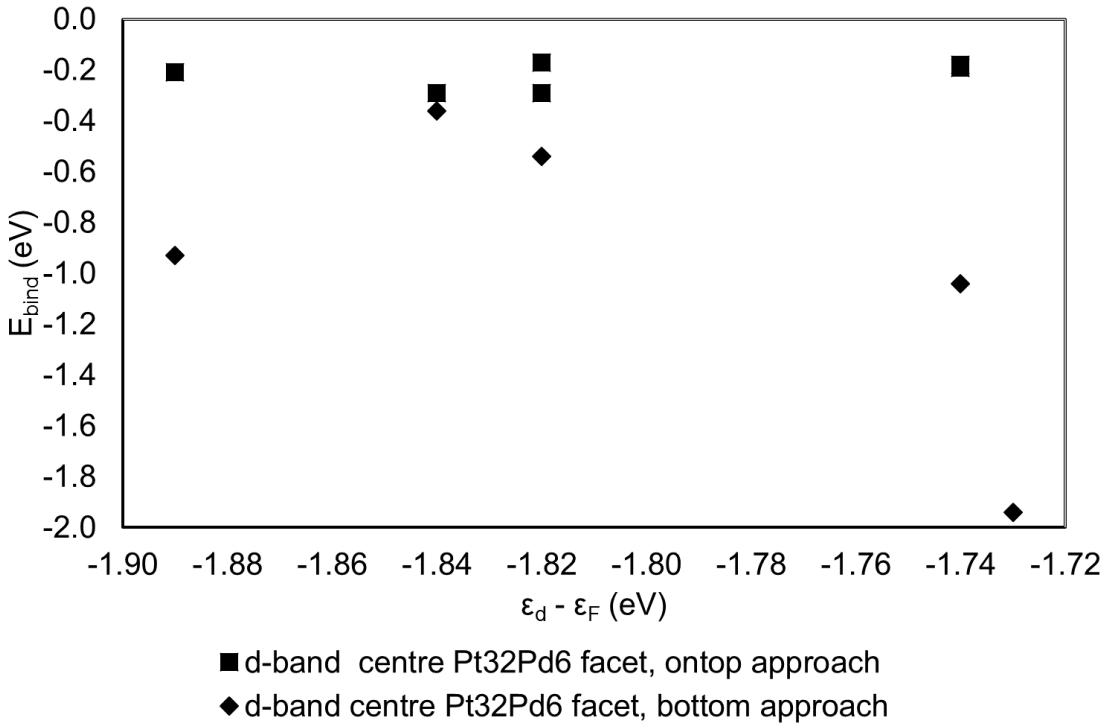


Figure 5.7: Variation of the binding energy of the $Pt_{32}Pd_6$ cluster with the d-band centre of the interacting facet of the $Pt_{32}Pd_6$ cluster adsorbed on OH functionalised graphene support.

There is no clear trend between the binding energy and the d-band centre for the underneath approach geometries. However, the highly exothermic binding energy of -1.94 eV for approach through facet A which has the least negative d-band centre of -1.73 eV. The second most exothermic binding energies are for facet D and facet B with the least exothermic binding energy being that for facet C.

Comparison of facet D and facet E, which are both hexagonal facets consisting of Pt atoms with the difference being the central Pd atom on facet D, indicates that the central Pd atom leads to an upward shift of 0.08 eV of the d-band centre relative to that of facet E. The result of the upward shift of the d-band centre is a 0.50 eV more exothermic binding energy of facet D than facet E.

The facet of approach of the $Pt_{32}Pd_6$ cluster which results in the most exothermic binding and formation energy on OH functionalised graphene support is the underneath approach through facet A with binding energy of -1.94 eV and formation energy of -2.63 eV. This adsorption geometry is used as the reference to calculate the segregation energy for the rearranged structures of the $Pt_{32}Pd_6$ cluster adsorbed on OH functionalised graphene. The rearranged structures are constructed from the same adsorption geometry as the reference structure, i.e. underneath approach through a square facet with the position of the Pt and Pd atoms varied within the $Pt_{32}Pd_6$ cluster relative to the arrangement in the reference structure.

The lowest energy adsorption geometries (i.e. highly exothermic binding energies) which are underneath approach through facet A and facet D were re-optimised by including the van der Waals interaction. The corresponding calculated binding energies are -3.35 eV and -2.99 eV calculated with the vdW-OptPBE functional. The results indicate that stability ranking is not altered by including dispersion effects, though the difference in energy between the two structures using the vdW-OptPBE functional is only 0.36 eV compared to the PW91 difference of 0.90 eV.

The bond lengths of the interacting and opposite facet of the $Pt_{32}Pd_6$ cluster for underneath approach through facet A and facet D on OH functionalised graphene were calculated to assess structural changes to the cluster upon adsorption to the support. Similar to adsorption of the $Pt_{38}$ cluster on OH functionalised graphene (Chapter 4 section 4.4.4), there is distortion of the graphene structure in the vicinity of the OH group upon adsorption of the $Pt_{32}Pd_6$ cluster. This is in contrast to what is observed for the $Pt_{32}Pd_6$ cluster adsorbed on pristine graphene, where there is almost no structural distortion of graphene in the contact region.

The calculated Pt-Pt bond lengths for the interacting facet for underneath approach through facet A indicates bond elongation, with different 4 Pt-Pt bond lengths (see Table 5.4) relative to the rectangular facet of the free standing $Pt_{32}Pd_6$ cluster with side lengths 2.66 Å and 2.64 Å. Minimal bond elongation is observed on the opposite facet relative to the bond lengths of the opposite facet in the free standing unsupported $Pt_{32}Pd_6$ cluster.

For the underneath approach through facet D, the opposite facet is facet C. The extent of Pt-Pt and Pt-Pd bond elongation is higher in the interacting facet (see Table 5.4) relative to the free standing unsupported $Pt_{32}Pd_6$ cluster (see Table 3.3 facet D). There is also bond elongation of the Pt-Pt side lengths and Pt-Pd diagonal bond lengths of the opposite facet relative to the bond lengths of this facet in the free standing unsupported $Pt_{32}Pd_6$ cluster (see Table 3.3 facet C).

Table 5.4: Optimised parameters for geometric structures of the $Pt_{32}Pd_6$ cluster adsorbed on OH functionalised graphene.

| | **Facet A underneath** | **Facet D underneath** | |
|---|---|---|---|
| **$E_{bind}$ (eV)** | | | |
| GGA-PW91 | -1.94 | -1.04 | |
| | | | |
| | | Side length | Diagonal length |
| $d_{Pt\text{-}Pt}$ [1], Å | 3.45 | 2.80 | 2.83 |
| $d_{Pd\text{-}Pt}$ [1], Å | 2.96 | 2.72 | 2.76 |
| | 2.87 | 2.72 | 2.70 |
| | 3.22 | 2.74 | 2.74 |
| | | 2.89 | 2.88 |
| | | 2.81 | 2.81 |
| | | | |
| | | Side length | Diagonal length |
| $d_{Pt\text{-}Pt}$ [2], Å | 2.64 | 2.71 | 2.75 |
| $d_{Pd\text{-}Pt}$ [2], Å | 2.66 | 2.65 | 2.73 |
| | 2.67 | 2.70 | 2.72 |
| | 2.66 | 2.66 | 2.75 |
| | | 2.72 | 2.74 |
| | | 2.65 | 2.75 |
| | | | |
| | 2.20 | 2.15 | |
| | 2.23 | 2.34 | |
| $d_{Pt\text{-}C}$ , Å | 2.16 | 2.31 | |
| | 2.26 | 2.35 | |
| | 2.15 | 2.41 | |
| | 2.32 | 2.37 | |
| | | | |

[1]Pt-Pt and Pd-Pt distance of the facet closest to OH functionalised graphene

[2] Pt-Pt and Pd-Pt distance of the facet opposite to the one interacting with the OH functionalised graphene

The calculated Pt-C bond lengths for approach through facet A are shorter than the bond lengths for approach through facet D. The shorter Pt-C bond lengths for approach through facet A correlates with the more exothermic binding energy of facet A compared to the longer Pt-C and less exothermic binding energy for approach through facet D.

#### *5.3.2.2 Rearrangement of the $Pt_{32}Pd_6$ cluster on OH functionalised graphene*

The optimised structures for the rearrangements of the $Pt_{32}Pd_6$ cluster supported on OH functionalised graphene considered in the present study are shown in Figure 5.8. The $Pt_{32}Pd_6$ cluster arrangement in the reference structure (arrangement of the $Pt_{32}Pd_6$ cluster in Figure 5.6 with $E_{bind}$ = -1.94 eV) is the lowest energy (highly exothermic excess energy) arrangement in the free standing unsupported $Pt_{32}Pd_6$ cluster. All possible rearrangements of the $Pt_{32}Pd_6$ cluster on OH functionalised graphene investigated were found to be higher in energy (less exothermic excess energy) than the reference structure $Pt_{32}Pd_6$ arrangement, see Appendix B1 Figure B.1 and B.2 for the free standing unsupported $Pt_{32}Pd_6$ stability ranking of the different arrangements of the $Pt_{32}Pd_6$ cluster.

The binding energy is not the descriptor to consider for assessing stability on the support since the free standing unsupported $Pt_{32}Pd_6$ cluster energies are different. The high energy clusters (i.e. least stable) free standing $Pt_{32}Pd_6$ clusters are expected to have higher propensity for binding to the support hence more exothermic binding energies. Yuan et al. (2014) made a similar observation for the calculations on Pd-Au clusters on pristine graphene where high energy free standing clusters had higher exothermic binding energies than the low energy free standing clusters.

The segregation energy is the best descriptor for stability of the rearranged supported $Pt_{32}Pd_6$ clusters. Calculation of the segregation energy makes use of absolute energies of the reference state and the rearranged states without referencing to any free standing unsupported $Pt_{32}Pd_6$ cluster energy or energy of the support. The calculated segregation energy and the difference in energy between the free standing $Pt_{32}Pd_6$ clusters with different arrangements and the lowest energy free standing $Pt_{32}Pd_6$ cluster arrangement are not equal (see Appendix B). The segregation energy can be thought of as consisting of two contributors. The first contributor is the energy to transform from the lowest energy $Pt_{32}Pd_6$ cluster arrangement to the rearranged structure in the free standing unsupported $Pt_{32}Pd_6$ cluster. The

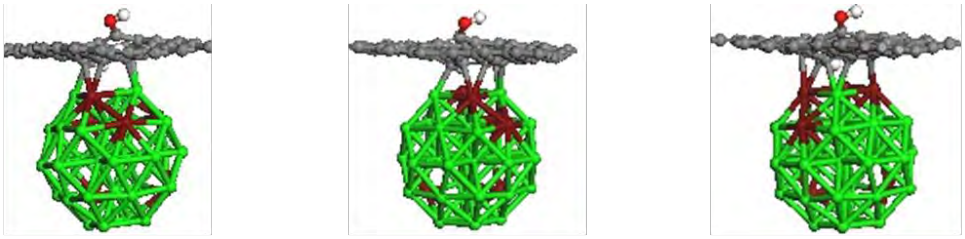

| | | | |
|---|---|---|---|
| $E_{bind}$ (eV) | -2.21 | -2.01 | -1.84 |
| $E_{form}$ (eV) | -2.44 | -2.41 | -2.23 |
| $E_{seg}$ (eV) | 0.20 | 0.22 | 0.40 |

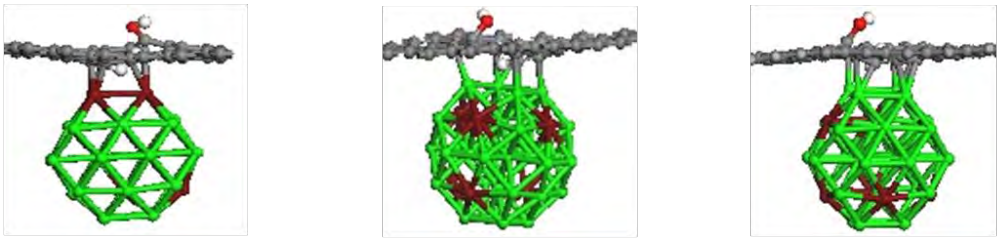

| | | | |
|---|---|---|---|
| $E_{bind}$ (eV) | -1.75 | -1.55 | -1.54 |
| $E_{form}$ (eV) | -2.14 | -2.17 | -2.21 |
| $E_{seg}$ (eV) | 0.50 | 0.46 | 0.42 |

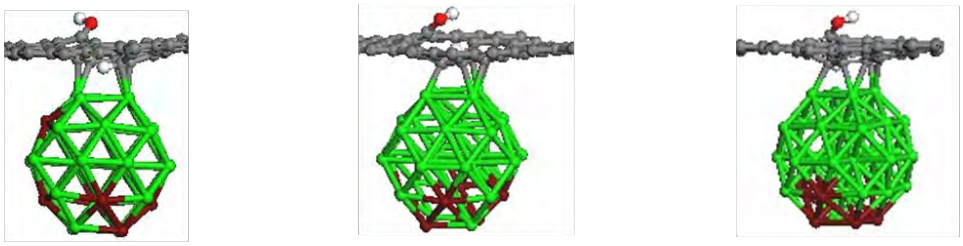

| | | | |
|---|---|---|---|
| $E_{bind}$ (eV) | -2.00 | -1.91 | -1.84 |
| $E_{form}$ (eV) | -2.44 | -2.30 | -2.20 |
| $E_{seg}$ (eV) | 0.19 | 0.33 | 0.43 |

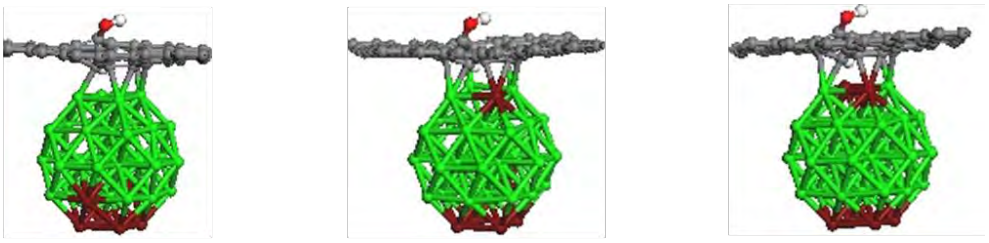

| | | | |
|---|---|---|---|
| $E_{bind}$ (eV) | -1.75 | -1.61 | -1.79 |
| $E_{form}$ (eV) | -2.06 | -1.98 | -2.23 |
| $E_{seg}$ (eV) | 0.55 | 0.65 | 0.40 |

Figure 5.8: Optimised structures for the rearrangement of the $Pt_{32}Pd_6$ cluster interaction with OH functionalised graphene. Calculated energies are obtained using the GGA-PW91 functional.

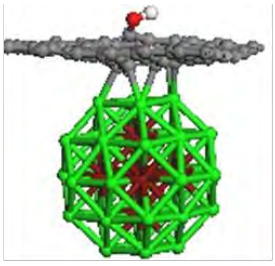
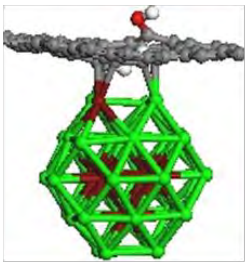
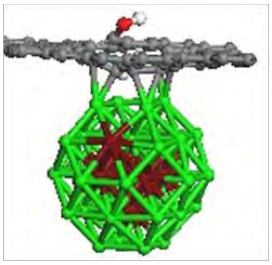

| | | | |
|---|---|---|---|
| $E_{bind}$ (eV) | -1.99 | -1.95 | -2.00 |
| $E_{form}$ (eV) | -1.16 | -1.30 | -1.23 |
| $E_{seg}$ (eV) | 1.47 | 1.34 | 1.41 |

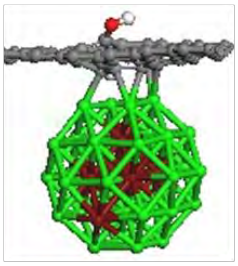
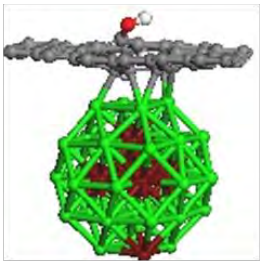
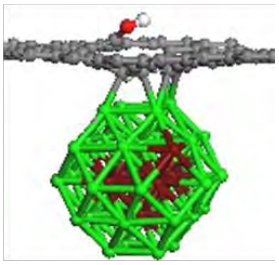

| | | | |
|---|---|---|---|
| $E_{bind}$ (eV) | -1.99 | -2.03 | -1.90 |
| $E_{form}$ (eV) | -1.22 | -1.38 | -1.27 |
| $E_{seg}$ (eV) | 1.41 | 1.25 | 1.36 |

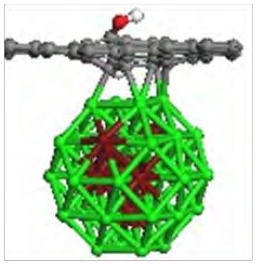
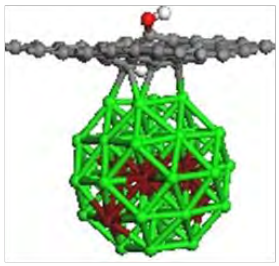
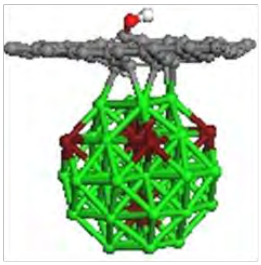

| | | | |
|---|---|---|---|
| $E_{bind}$ (eV) | -2.01 | -1.97 | -1.91 |
| $E_{form}$ (eV) | -1.33 | -1.24 | -1.90 |
| $E_{seg}$ (eV) | 1.30 | 1.40 | 0.73 |

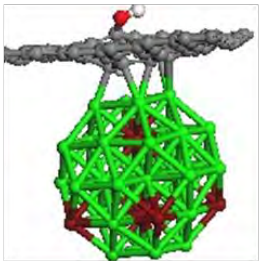
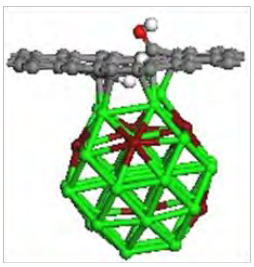

| | | |
|---|---|---|
| $E_{bind}$ (eV) | -2.00 | -1.94 |
| $E_{form}$ (eV) | -1.99 | -2.63 |
| $E_{seg}$ (eV) | 0.64 | 0.00 |

Figure 5.8 continued: Optimised structures for the rearrangement of the $Pt_{32}Pd_6$ cluster interaction with OH functionalised graphene. Calculated energies are obtained using the GGA-PW91 functional.

second contributor is the effect of the support, if the support did not have any effect the segregation energy would be equal to the difference in energy to transform from the lowest energy $Pt_{32}Pd_6$ arrangement to the rearranged structure in the free standing unsupported $Pt_{32}Pd_6$ cluster.

Rearranged structures in which the number of anchoring Pd atoms (Pd atoms on the facet in contact with the support) increases leads to a decrease in the binding energy of the cluster and an increase in the segregation energy (see first four adsorption geometries at the top of Figure 5.8). This indicates that the rearranged structures with Pd on the facet interacting with the support are energetically less favourable compared to the reference structure. As the concentration of Pd atoms increases on the interacting facet, the d-band centre of the facet resembles that of pure Pd. Pd has a different d-band centre to Pt: Pd(111) d-band centre = -1.83 eV vs Pt(111) d-band centre = -2.25 eV (Ruban et al., 1997). Thus, it is expected that the Pt(100)-like facet will interact differently to the Pd(100)-like facet with OH functionalised graphene, hence the different binding and segregation energies as the concentration of Pd on the interacting facet increases.

Arrangements in which anchoring atoms are Pt atoms only, with Pd atoms segregating to the bottom half of the cluster (see structures 8-10 counted from the top in Figure 5.8) also have positive segregation energies. These type of arrangements have the top half of the cluster closer to the support, consisting of Pt atoms only without nearby Pd atoms hence they are expected to have properties more like those of pure Pt clusters.

The extreme case of rearranged structures with core shell arrangement with all Pd atoms in the core and Pt atoms on the shell has the highly endothermic segregation energy of 1.47 eV on OH functionalised graphene (see Figure 5.8 continued top left geometry). The perfect core shell free standing unsupported $Pt_{32}Pd_6$ cluster is the least energetically preferred arrangement with a highly endothermic excess energy. In addition, arrangements in which Pd atoms segregate to the surface whilst the rest of the Pd atoms remain in the core (see structures 2-7 counted from the top in Figure 5.8 continued) have endothermic segregation energies in excess of 1 eV. Moreover, the free standing unsupported $Pt_{32}Pd_6$ cluster arrangements of the cluster with Pd segregating to the surface while the rest are in the core region are energetically unfavourable with positive excess energies (see Appendix B). The positive excess energy for the free standing $Pt_{32}Pd_6$ cluster arrangements with Pd distributed between the interior and the exterior sites, and the endothermic segregation energy in excess of 1 eV for these supported $Pt_{32}Pd_6$ clusters on OH functionalised graphene, indicate the preference of Pd to be on the surface mixed with Pt rather than being in the interior.

Based on the investigated possible rearrangements of the $Pt_{32}Pd_6$ cluster supported on OH functionalised graphene in the present study, it is concluded that the preferred ordering of the $Pt_{32}Pd_6$ cluster in the free standing unsupported $Pt_{32}Pd_6$ cluster is not altered on the OH functionalised graphene supported $Pt_{32}Pd_6$ cluster. Stated differently, there is no thermodynamic driving force for the rearrangement of the $Pt_{32}Pd_6$ cluster supported on OH functionalised graphene, it retains the same arrangement as the one of the free standing $Pt_{32}Pd_6$ cluster. Under reaction conditions we expect the reference structure (i.e. underneath approach through facet A) to be the dominant arrangement of the $Pt_{32}Pd_6$ cluster on OH functionalised graphene compared to the rearranged forms.

*5.3.2.3 Electronic structure analysis*

The charge density difference plot was calculated for the adsorption geometry with the most exothermic formation energy on OH functionalised graphene, which is the underneath approach through facet A interacting with the support. Similar to adsorption of the $Pt_{32}Pd_6$ cluster on pristine graphene, adsorption of the $Pt_{32}Pd_6$ cluster on OH functionalised graphene through interaction with facet A results in charge redistribution within the contact region between the cluster and support. The charge redistribution in the contact region is indicative of covalent bond formation between cluster and support. Interaction between the $Pt_{32}Pd_6$ cluster and OH functionalised graphene results in charge redistribution within the $Pt_{32}Pd_6$ cluster, with Pt atoms interacting with the support undergoing higher extent of redistribution than the rest of the atoms of the $Pt_{32}Pd_6$ cluster (see Figure 5.9).

At the isosurface level at which the charge density difference plot is calculated, the charge redistribution to the OH functional group is insignificant compared to charge redistribution from carbon atoms in the contact region between the support and the $Pt_{32}Pd_6$ cluster. Therefore, the OH functional group modifies the electronic properties of the carbon atoms in the contact region without directly contributing to the net charge redistribution.

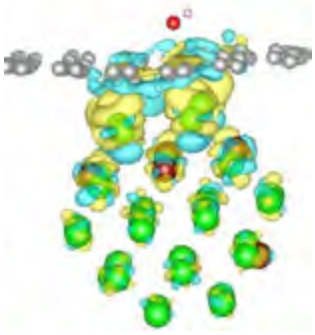

Figure 5.9: Charge density difference for the $Pt_{32}Pd_6$ cluster adsorbed on OH functionalised graphene. Isosurface level at 0.0025e/ $Å^3$. Key: blue isosurface corresponds to charge depletion and yellow isosurface corresponds to charge accumulation.

The Bader charge analysis was performed on the lowest energy adsorption structure in which the $Pt_{32}Pd_6$ cluster interacts via facet A through the underneath approach. The calculated overall charge transfer for the reference structure is a net charge transfer of 0.08 e to the $Pt_{32}Pd_6$ cluster from the support. The overall charge transfer to the $Pt_{32}Pd_6$ cluster is rather small. Hence, the interaction of the $Pt_{32}Pd_6$ cluster with OH functionalised graphene is dominated by charge redistribution within the cluster and the support. Despite the small amount of overall charge transfer to the $Pt_{32}Pd_6$ cluster, there is significant amount of charge loss (0.49 e) from Pt atoms of the facet interacting with the support similar to the observation for adsorption of the $Pt_{32}Pd_6$ cluster on pristine graphene.

The Bader charge analysis was also performed to gain insight of the relation between the segregation energy and the amount of charge transfer from the anchoring atoms. This analysis was limited to the rearranged structures where the Pd atoms rearranged to become anchoring atoms on the facet of in contact with the support (i.e. 4 top adsorption geometries in Figure 5.8). An increase in the number of anchoring Pd atoms on the square facet interacting with the OH functionalised graphene support result in an increase of both the segregation energy and the charge loss from the anchoring Pd atoms (see Figure 5.10). Interestingly, the total charge loss of 0.26 e for four anchoring Pd atoms is lower than the total charge loss of 0.49 e from four anchoring Pt atoms (i.e. underneath approach through facet A). The difference in charge transfer might originate from better orbital interaction between Pt 5d states and carbon atoms of OH functionalised graphene compared to interaction between carbon atoms of OH functionalised graphene and Pd 4d states. The better interaction between Pt 5d states compared to Pd 4d states may result in enhanced charge transfer.

The d-band centre of the square facet interacting with the support resembles pure Pd(100)-like facet as the concentration of Pd atoms on the square facet increases. Therefore, the reactivity and ability of charge transfer between the $Pt_{32}Pd_6$ cluster and OH functionalised graphene is expected to be different due to the different d-band centre of the pure Pt(100)-like facet and Pd(100)-like facet.

The weak interaction between the $Pt_{32}Pd_6$ cluster with Pd atoms as anchoring atoms with the OH functionalised graphene support results in a small amount of charge transfer from the anchoring Pd atoms. The consequence of the small quantity of charge transfer from the anchoring Pd atoms is a positive segregation energy.

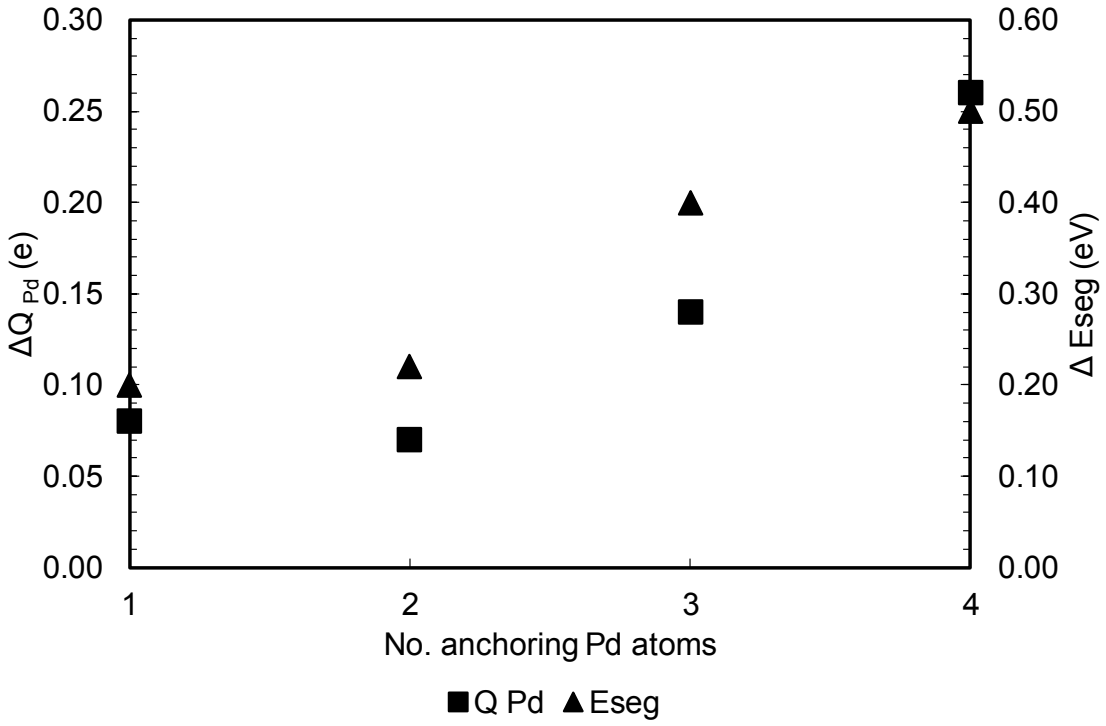


Figure 5.10: Net charge transfer from anchoring Pd atoms dependency on the number of anchoring Pd atoms on primary axis and the segregation energy dependency on the anchoring Pd atoms on the secondary axis for the rearranged $Pt_{32}Pd_6$ cluster (rearranged structures with Pd segregating to the square facet interacting with the support) on OH functionalised graphene.

The PDOS analysis was performed only for the underneath approach of the $Pt_{32}Pd_6$ cluster interacting through facet A to the OH functionalised graphene support. The PDOS of carbon atoms of OH functionalised graphene post adsorption of the $Pt_{32}Pd_6$ cluster is characterised by appearance of new states around the Fermi level (see Figure 5.11 (a)). Pre adsorption of the $Pt_{32}Pd_6$ cluster, the PDOS of the carbon atoms of OH functionalised graphene consists of two small peaks at the Fermi level with the inverted cone at the Fermi level.

The PDOS of the $Pt_{32}Pd_6$ cluster is transformed from a discrete-like PDOS to a continuous PDOS upon adsorption on the OH functionalised graphene support (see Figure 5.11 (b)). The appearance of new peaks in the PDOS of carbon atoms of the support around the Fermi level and the modified PDOS of the $Pt_{32}Pd_6$ cluster post adsorption are indicative of orbital interaction between C 2p states and d states of the $Pt_{32}Pd_6$ cluster.

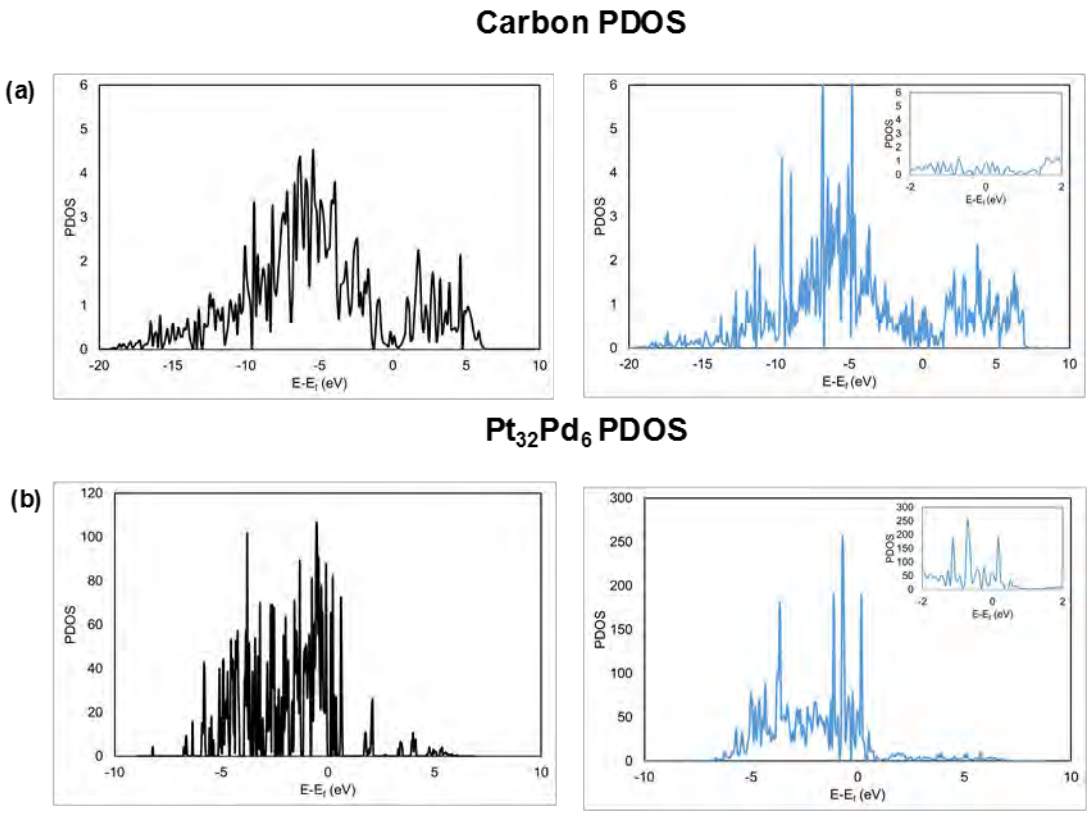


Figure 5.11: PDOS of the carbon atoms of OH functionalised graphene, Pt and Pd atoms: (a) PDOS of carbon atoms of OH functionalised graphene before adsorption (black curve) and after adsorption (blue curve), and (b) PDOS of $Pt_{32}Pd_6$ before (black curve) and after adsorption through facet A (blue curve). The energy scale is relative to the Fermi level. Inserts show zoomed view around the Fermi level.

The d-band centre, d-band width and the d-band filling for the interacting facet and opposite facet for the underneath approach of the $Pt_{32}Pd_6$ cluster interacting through facet A with the OH functionalised graphene was considered for the assessment of reactivity of the supported $Pt_{32}Pd_6$ cluster.

Upon interaction of the $Pt_{32}Pd_6$ cluster with the OH functionalised graphene support, there is downward shift of 0.21 eV of the d-band centre of the entire cluster relative to the d-band centre of the free standing $Pt_{32}Pd_6$ cluster (see Table 5.5). The shift in d-band centre of the entire cluster indicates that the cluster interacts with the cluster via the d-band.

Table 5.5: Calculated d-band centre relative to Fermi level, d-band filling and d-band width for the $Pt_{32}Pd_6$ cluster interacting with OH functionalised graphene.

| | $\varepsilon_d - \varepsilon_F$ (eV) | $f_d$ | $w_d$ (eV) |
|---|---|---|---|
| **$Pt_{32}Pd_6$ free standing cluster** | | | |
| overall cluster | -1.82 | 0.88 | 2.84 |
| facet A | -1.73 | 0.88 | 2.73 |
| facet B | -1.89 | 0.87 | 2.73 |
| **$Pt_{32}Pd_6$ interacting through facet A with OH functionalised graphene** | | | |
| overall cluster | -2.03 | 0.85 | 3.09 |
| interacting facet (facet A) | -2.14 | 0.86 | 3.34 |
| opposite facet (facet B) | -1.96 | 0.85 | 2.96 |

There is a downward shift in d-band centre of both the interacting and the opposite facet for the $Pt_{32}Pd_6$ cluster supported on OH functionalised graphene relative to the d-band centre of the same facets in the free standing unsupported $Pt_{32}Pd_6$ cluster. For the interacting facet the downshift of the d-band centre is 0.41 eV and for the opposite facet 0.07 eV. The higher extent of the downshift of the d-band centre of the interacting facet is due to contact between the facet and the support. In addition, the shift in d-band centre for both the interacting and opposite facets indicate that the effect of the interaction of the cluster and support is not localised to the contact region but extends to the facets not directly interacting with the OH functionalised graphene support.

The d-band centre of the opposite facet is important as it indicates the reactivity of the facets available to reactants. The small d-band centre shift of 0.07 eV of the opposite facet relative to the d-band centre of the same facet in the free standing $Pt_{32}Pd_6$ cluster indicates that the reactivity of the supported $Pt_{32}Pd_6$ cluster is expected to resemble that of the free standing $Pt_{32}Pd_6$ cluster. Despite the small downward shift in d-band centre of the opposite facet, the difference in d-band centre between the interacting and opposite facet for the supported $Pt_{32}Pd_6$ cluster is 0.34 eV which is higher than the difference of 0.16 eV in the free standing $Pt_{32}Pd_6$ cluster. Therefore, the difference in d-band centre between the interacting and opposite facet may result in a different reactivity between the OH functionalised graphene supported $Pt_{32}Pd_6$ cluster and the free standing unsupported $Pt_{32}Pd_6$ cluster.

## 5.3.3 $Pt_{32}Pd_6$ interaction with COOH functionalised graphene

### *5.3.3.1 Adsorption structures of the $Pt_{32}Pd_6$ cluster on COOH functionalised graphene*

All the investigated structures of the $Pt_{32}Pd_6$ cluster interacting with the COOH functionalised graphene support have negative binding energies calculated with the GGA-PW91 functional (see Figure 5.12). The negative binding energies indicate that adsorption of the $Pt_{32}Pd_6$ cluster on the COOH functionalised graphene support is favoured unlike binding on pristine graphene. Unlike on the OH functionalised graphene support, on COOH functionalised graphene the most stable adsorption geometry is for the $Pt_{32}Pd_6$ cluster approach from the ontop position interacting through facet B, labelled facet B(2) with a binding energy of -1.11 eV (see Figure 5.12). The adsorption geometry is such that the COOH group is located to the side of the approaching $Pt_{32}Pd_6$ cluster, with the O of the carbonyl (CO) of the COOH group a distance of 2.85 Å from the central Pt atom of the hexagonal facet closest to the COOH group.

From Figure 5.13, it is observed that for facets A (d band centre = -1.73 eV) and C (d band centre = -1.84 eV) the binding energy for the bottom approach is more exothermic than for the ontop configurations. Whilst, for facets D and facet B(2) the atop approach is more stable than the bottom approach. For both facet D and facet B(2) ontop approaches, the $Pt_{32}Pd_6$ cluster is positioned to the side of the COOH functional group resulting in direct interaction between the hexagonal facet of the cluster and the COOH functional group of the support. From Figure 5.13 there is no clear correlation between the d-band centre of the interacting facet of the $Pt_{32}Pd_6$ cluster and the binding energy. The same observation was made for $Pt_{32}Pd_6$ on OH functionalised graphene.

Comparison of the binding energies for structures labelled facet A(2), facet B(2) and facet B(3) in Figure 5.12, indicates that the surrounding environment to the square facet interacting with the support is important in determining the binding energy. The structure labelled facet A(2) has a square facet interacting with the support, with 4 Pd atom neighbours, and one of the Pd atoms bonded to O of the carbonyl (CO) of the COOH functional group. Structures B(2) and B(3) are identical square facets interacting with the support, with 2 Pd atom neighbours. The difference between structure B(2) and B(3) is that for B(3) one of the Pd neighbour atom is bonded directly to O of the carbonyl (CO) of the COOH functional group. For B(2) it is a Pt atom bonded directly to O of the carbonyl (CO) of the COOH functional group. The latter arrangement results in stabilisation of 0.33 eV in the binding energy relative to the former arrangement. The reason for this is, in the latter arrangement the hexagonal facet closest to the COOH group consists only of Pt atoms. Thus, the d-band centre of this facet is different to

that of the hexagonal facet which has a central Pd atom. Therefore, based on the difference in d-band centre of the facet closest to the COOH group in both cases, i.e. B(2) and B(3) the two facets will interact differently with the COOH group.

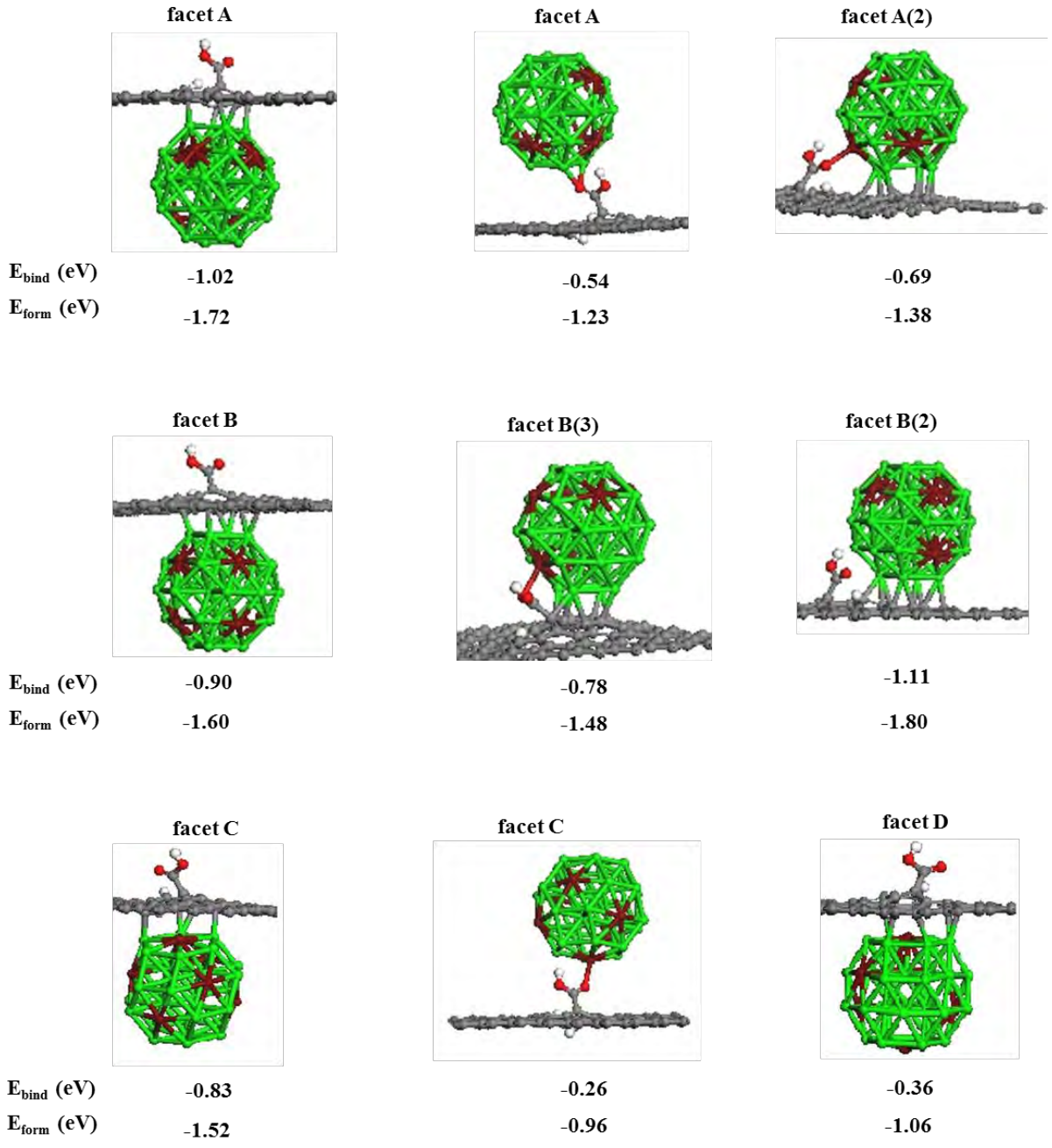


Figure 5.12: Optimised structures of the $Pt_{32}Pd_6$ cluster interaction with COOH functionalised graphene through the 5 unique facets of the cluster. Calculated energies are obtained using the GGA-PW91 functional.

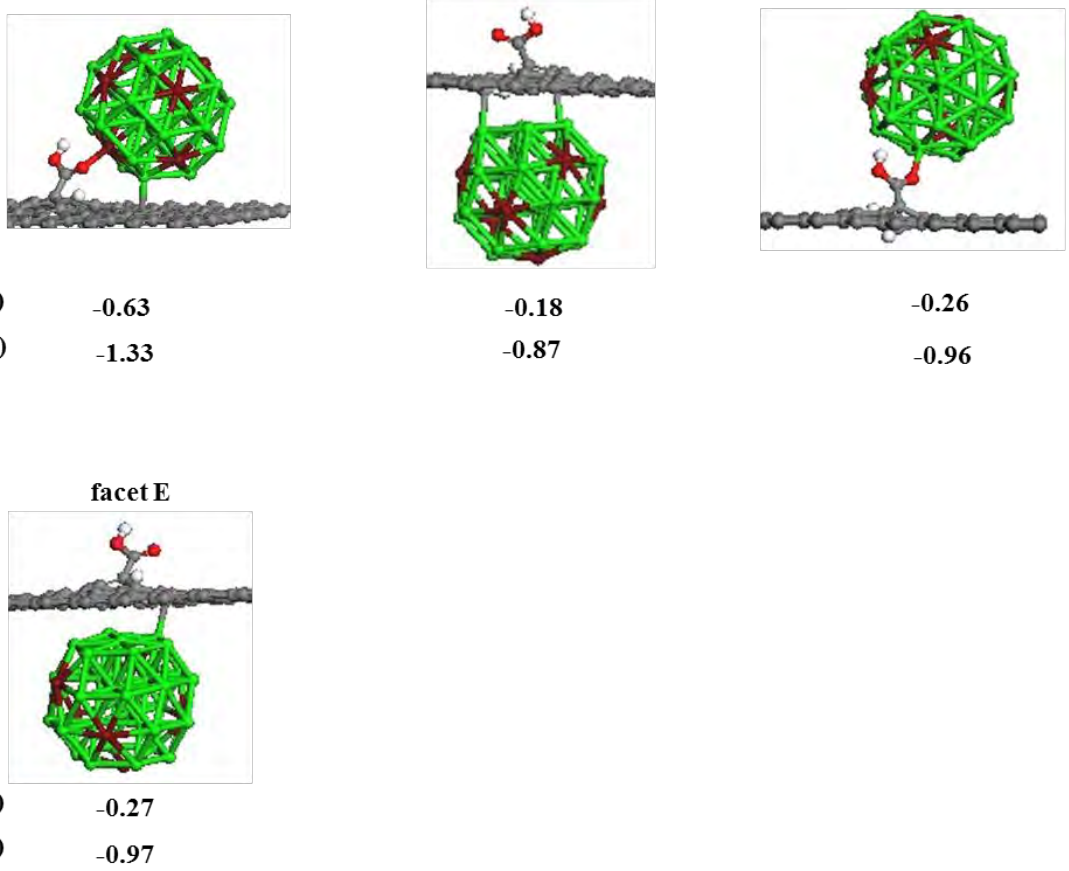


Figure 5.12 continued: Optimised structures for the $Pt_{32}Pd_6$ cluster interaction with COOH functionalised graphene through the 5 unique facets of the cluster. Calculated energies are obtained using the GGA-PW91 functional.

The binding energy for the structure labelled facet A(2) is 0.09 eV less exothermic than that for the structure labelled facet B(3). The opposite trend is observed for the underneath approach structures, underneath approach through facet A has a binding energy which is 0.12 eV more exothermic than underneath approach through facet B. Comparison of underneath approach via the hexagonal facets, i.e. facet C, facet D and facet E indicates that the hexagonal facet with a central Pd atom binds stronger to the support than facet E which consist only of Pt atoms. The central Pd atom at the centre of a hexagonal facet consisting of Pt atoms result in a change of the d-band centre of -0.02 eV for facet C and -0.08 eV for facet D to the d-band centre of a hexagonal facet consisting only of Pt atoms. The different d-band centre result in more favourable interaction of the hexagonal facet with a central Pd atom (i.e. facet C and facet D) than the Pt only hexagonal facet (i.e. facet E).

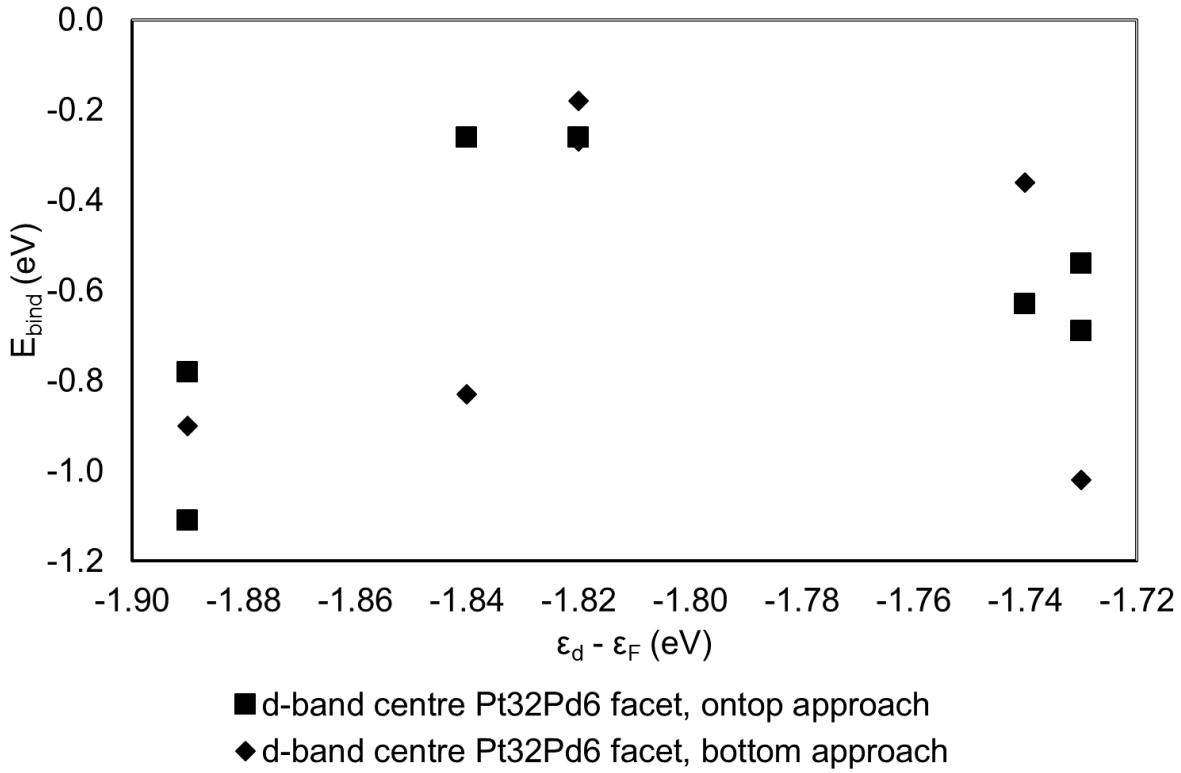


Figure 5.13: Variation of the binding energy of the $Pt_{32}Pd_6$ cluster with the d-band centre of the interacting facet of the $Pt_{32}Pd_6$ cluster adsorbed on COOH functionalised graphene support.

The bond lengths of the interacting and opposite facets of the $Pt_{32}Pd_6$ cluster are calculated for the two most stable adsorption geometries, i.e. facet B(2) and underneath approach through facet A. There is bond elongation on the interacting facet in both geometries. The interacting facet losses the rectangular shape it possesses for the free standing $Pt_{32}Pd_6$ cluster (See Table 5.6). The extent of bond elongation on the opposite facet is small compared to the interacting facet for both the low energy adsorption geometries.

Generally the calculated Pt-C bond distances for the underneath approach through facet A are shorter than those of the ontop approach structure labelled facet B(2). This is despite the stronger binding for facet B(2) structure compared to underneath approach through facet A.

Table 5.6: Optimised parameters for geometric structures of the $Pt_{32}Pd_6$ cluster adsorbed onto COOH functionalised graphene.

| | **Facet B(2)** | **Facet A (underneath)** |
|---|---|---|
| **$E_{bind}$ (eV)** | | |
| GGA-PW91 | -1.11 | -1.02 |
| $d_{Pt\text{-}Pt}$ [1], Å | | |
| | 2.93 | 2.85 |
| | 2.84 | 2.93 |
| | 2.93 | 2.80 |
| | 2.91 | 3.03 |
| $d_{Pt\text{-}Pt}$ [2], Å | | |
| | 2.69 | 2.70 |
| | 2.70 | 2.70 |
| | 2.69 | 2.70 |
| | 2.68 | 2.66 |
| $d_{Pt\text{-}C}$, Å | | |
| | 2.26 | 2.18 |
| | 2.25 | 2.15 |
| | 2.30 | 2.33 |
| | 2.39 | 3.03 |

[1]Pt-Pt distance of the facet closest to COOH functionalised graphene

[2] Pt-Pt distance of the facet opposite to the one interacting with COOH functionalised graphene

### *5.3.3.2 Rearrangement of the $Pt_{32}Pd_6$ cluster on COOH functionalised graphene*

The adsorption structure labelled facet B(2) in Figure 5.12 is taken as reference for calculating the segregation energy of rearranged structures of the $Pt_{32}Pd_6$ cluster supported on COOH functionalised graphene. The investigated rearranged structures of the $Pt_{32}Pd_6$ cluster supported on COOH functionalised graphene are presented in Figure 5.14. Similar to rearrangement on OH functionalised graphene, the rearranged structure with perfect core shell arrangement with all Pd atoms in the core is the least energetically preferred arrangement with an endothermic segregation energy of 1.29 eV. Arrangements in which surface concentration of Pd increases with remaining Pd atoms in the core, have less endothermic segregation energies compared to the perfect core shell arrangement. This indicates that Pd atoms prefers to be on the surface than to be in the core region. The preferred tendency of Pd to be on the surface is observed both for the free standing $Pt_{32}Pd_6$ cluster and the $Pt_{32}Pd_6$ cluster supported on OH and COOH functionalised graphene.

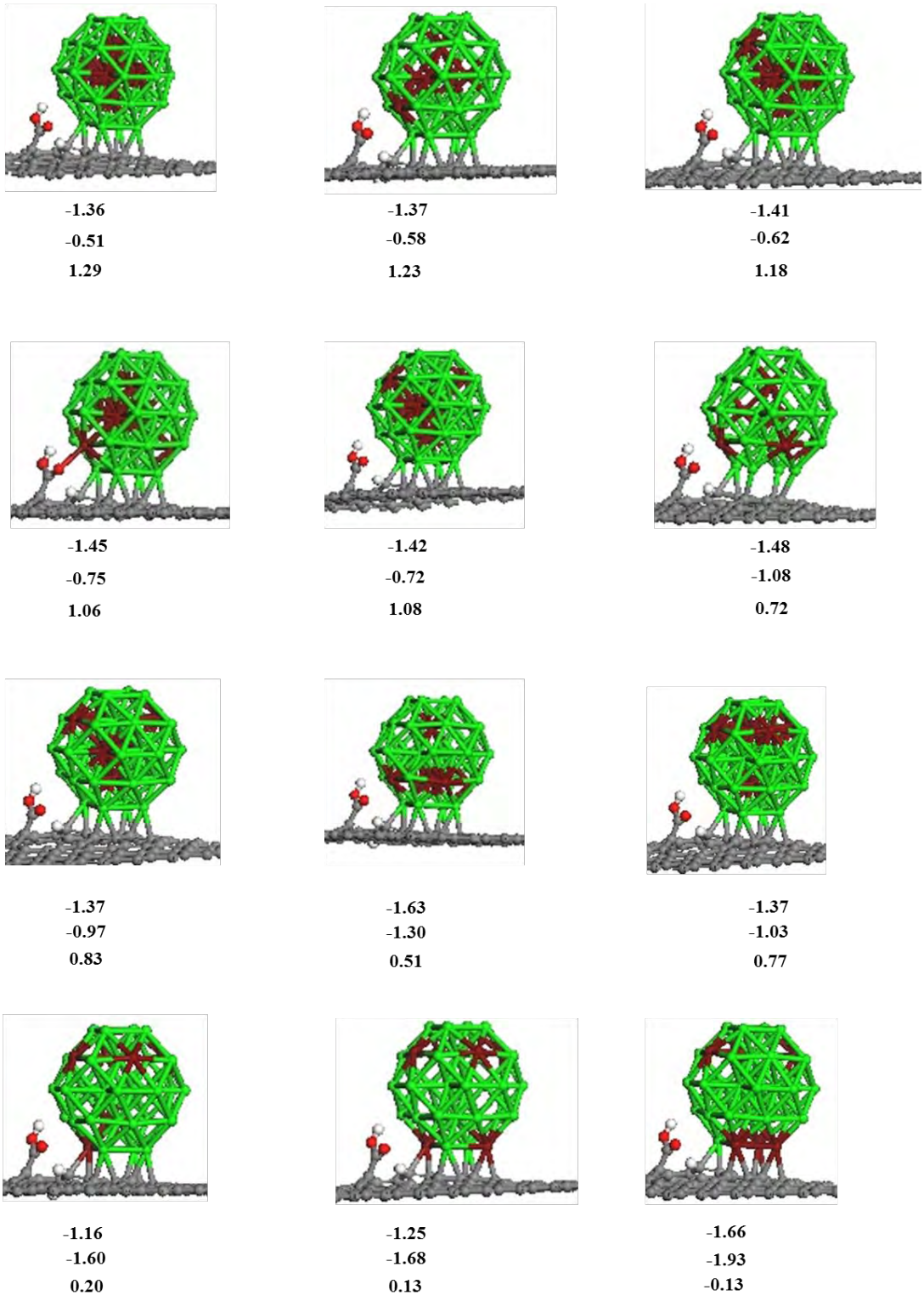


Figure 5.14: Optimised structures for the rearrangement of the $Pt_{32}Pd_6$ cluster interaction with COOH functionalised graphene. Calculated energies are obtained with the GGA-PW91 functional.

Rearranged structures in which more than two Pd atoms are on the surface, and at the centre of the hexagonal facet with the rest in the core region, have low endothermic segregation energies which decrease further with increase in surface Pd concentration (see Figure 5.14).

Rearranged structures with 3 and 4 Pd atoms on the surface and in the lower half of the cluster (see structures 6 and 8 counted from the top in Figure 5.14) closer to the support, have lower segregation (least endothermic) energies than the same arrangements but with Pd atoms in the top half of the cluster furthest from the support (see structures 7 and 9 counted from the top in Figure 5.14).

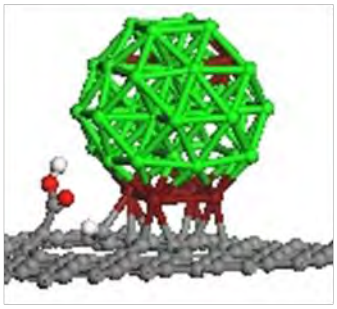

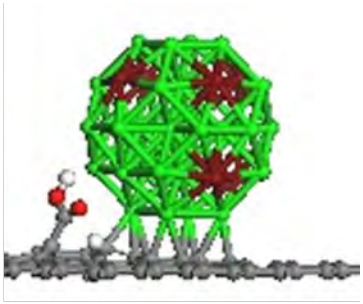

| | | |
|---|---|---|
| $E_{bind}$ (eV) | -1.47 | -1.11 |
| $E_{form}$ (eV) | -1.82 | -1.80 |
| $E_{seg}$ (eV) | -0.01 | 0.00 |

Figure 5.14 continued: Optimised structures for the rearrangement of the $Pt_{32}Pd_6$ cluster interaction with COOH functionalised graphene. Calculated energies are obtained with the GGA-PW91 functional.

The arrangement with 3 Pd atoms in the lower half of the cluster, closest to the support, has a segregation energy which is 0.11 eV less endothermic than the arrangement with 3 Pd atoms in the top half of the cluster furthest from the support. Similarly, the arrangement with 4 Pd atoms in the lower half of the cluster has a segregation energy less endothermic by 0.26 eV compared to the corresponding arrangement with 4 Pd atoms in the top half of the cluster Therefore, increase in Pd concentration on the half closest to the support has a stabilising effect on the binding energy of the $Pt_{32}Pd_6$ cluster on COOH functionalised graphene. The carbon atoms of the COOH functionalised graphene support tend to bind Pd atoms stronger than Pt atoms, hence having a higher concentration of Pd atoms in the lower half of the cluster closest to the support has a stabilising effect. This is supported by discussion to follow next, where it is observed that as Pd concentration increases on the interacting facet the stability of the adsorbed $Pt_{32}Pd_6$ cluster increases.

Rearranged structures in which all Pd atoms are located on the surface have low endothermic segregation energies less than 0.20 eV. Increasing the number of Pd atoms anchoring the cluster to the support (i.e. Pd atoms on interacting facet) result in arrangements which are lower in energy (more stable) than the reference structure.

The rearranged structure with 3 anchoring Pd atoms has an exothermic segregation energy of -0.13 eV. This is indication that this arrangement is lower in energy than the reference structure. The difference in energy between the free standing reference structure $Pt_{32}Pd_6$ arrangement and the free standing rearranged structure (with 3 Pd atoms occupying a square facet of the $Pt_{32}Pd_6$ cluster) is 0.43 eV. On COOH functionalised graphene the rearranged structure with the 3 Pd atoms anchoring the cluster to the support is 0.13 eV lower in energy than the reference structure. The $Pt_{32}Pd_6$ cluster in the rearranged form with a segregation energy of -0.13 eV is located to the side of the COOH group like the reference structure. The difference is that in the rearranged structure the distance between the central Pt atom on the hexagonal facet and the O of the carbonyl (CO) of the COOH group is 3.16 Å compared to a distance of 2.85 Å for the reference structure. The difference in stability between the free standing clusters and the supported clusters indicates that interaction of the cluster with the support has an effect on the stability and arrangement of the supported $Pt_{32}Pd_6$ clusters. plays The structure with 4 anchoring Pd atoms has a segregation energy of -0.01 eV. This indicates that this arrangement is degenerate with the reference structure arrangement and will be present in equal proportions with the reference structure arrangement under equilibrium conditions.

Therefore, on COOH functionalised graphene there is a thermodynamic driving force for rearrangement of the $Pt_{32}Pd_6$ cluster to other lower energy arrangements with different ordering of the Pt and Pd atoms within the equilibrated $Pt_{32}Pd_6$ cluster. Thus, under equilibrium reaction conditions, on COOH functionalised graphene we would expect to find the reference structure arrangement of the $Pt_{32}Pd_6$ cluster, together with the rearranged forms of the $Pt_{32}Pd_6$ cluster with 3 and 4 Pd atoms anchoring structures coexisting. The rearranged structure with 3 Pd atoms anchoring is expected to be the dominant form of the $Pt_{32}Pd_6$ cluster on COOH functionalised graphene. This arrangement has Pd atoms segregated towards the cluster-support interface, thereby exposing a higher concentration of Pt atoms on the surface.

#### *5.3.3.3 Electronic structure analysis*

The charge density difference analysis was performed on the reference geometry (geometry labelled facet B(2) in Figure 5.12). Majority of charge redistribution occurs in the contact region between the $Pt_{32}Pd_6$ cluster and the COOH functionalised graphene support. This is indicative of bond formation between anchoring Pt atoms of the cluster and the support. There is also charge redistribution to atoms of the $Pt_{32}Pd_6$ cluster not in the contact region, though the extent of charge redistribution to these atoms is smaller than for atoms in the contact region. There is charge redistribution on the COOH group upon adsorption of the $Pt_{32}Pd_6$ cluster on COOH

functionalised graphene. This result is the opposite to that on OH functionalised graphene where there was no visible charge redistribution on the OH functional group.

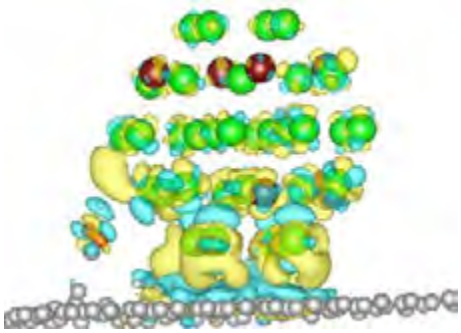

Figure 5.15: Charge density difference for the $Pt_{32}Pd_6$ cluster adsorbed on COOH functionalised graphene. Isosurface level at 0.0025e/ $Å^3$. Key: blue isosurface corresponds to charge depletion and yellow isosurface corresponds to charge accumulation.

The overall charge transfer calculated from the Bader analysis is a small charge transfer of 0.06 e from the support to the $Pt_{32}Pd_6$ cluster. This amount of charge transfer is too small to be of any significance, hence the interaction of the $Pt_{32}Pd_6$ cluster with COOH functionalised graphene is dominated by charge redistribution within the $Pt_{32}Pd_6$ cluster and support rather than by charge transfer. Despite a small overall charge transfer upon adsorption of the $Pt_{32}Pd_6$ cluster on COOH functionalised graphene, there is charge loss from Pt atoms of the square facet interacting with the support of 0.47 e. This indicates charge contribution by other atoms of the $Pt_{32}Pd_6$ cluster and atoms of the support which are not in the contact region.

The Bader charge on atoms of the square facet interacting with the support was calculated for the rearranged structures with increasing concentration of Pd atoms. As the number of Pd atoms increase on the square facet interacting with the support, the quantity of charge loss from Pd atoms increases (see Figure 5.16). It is further observed from Figure 5. that as the number of anchoring Pd atoms increases, the segregation energy decreases and goes through a minimum at $E_{seg}$ = -0.13 eV when 3 Pd atoms are anchoring the particle to the support.

Interestingly, the rearranged structure with 4 anchoring Pd atoms has a total charge loss of 0.42 e from anchoring atoms. The total charge loss of 0.42 e is only 0.05 e less than the total charge loss of 0.47 e of the 4 anchoring Pt atoms of the reference structure. On the contrary, the similar arrangement on OH functionalised graphene result in a total charge loss of 0.26 e from anchoring Pd atoms while for the reference structure there is total charge loss of 0.49 e from the 4 anchoring Pt atoms.

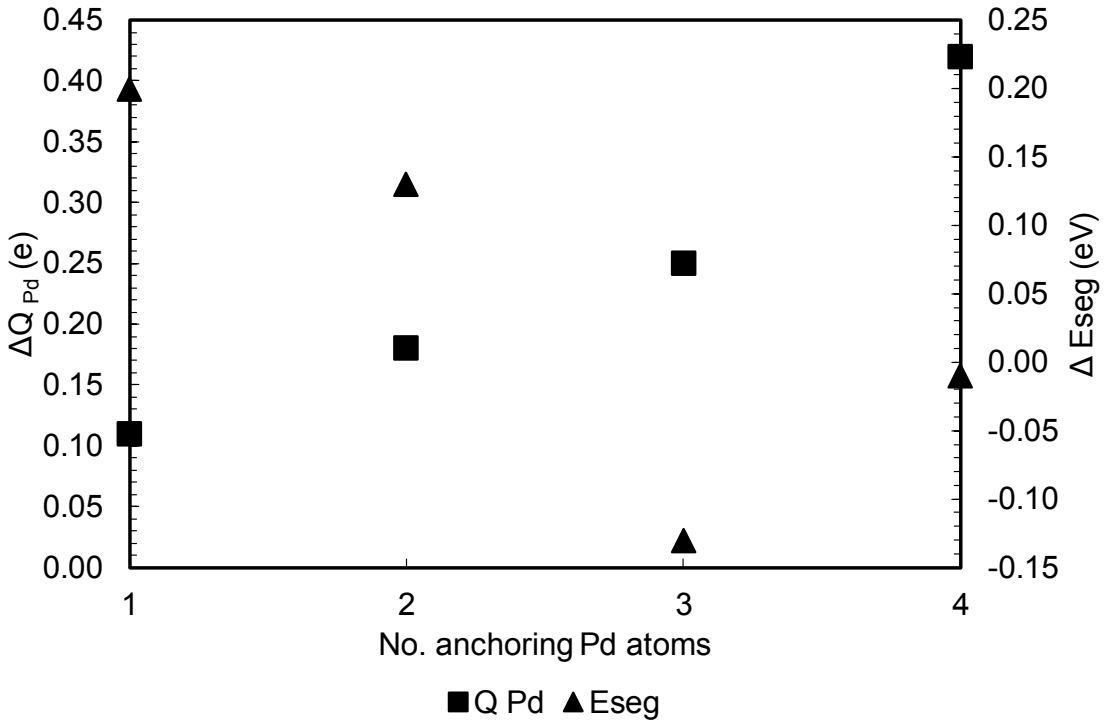


Figure 5.16: Net charge transfer from anchoring Pd atoms as a function of the number of anchoring Pd atoms on the primary axis and the segregation energy as a function of the anchoring Pd atoms on secondary axis for the rearranged $Pt_{32}Pd_6$ cluster (rearranged structures with Pd segregating to the square facet interacting with the support) on COOH functionalised graphene.

The lower charge loss from the anchoring Pd atoms on OH functionalised graphene results in endothermic segregation energies, whereas the higher charge loss on COOH functionalised graphene relative to OH functionalised graphene results in exothermic segregation energies. Therefore, COOH functionalisation results in higher charge loss from anchoring Pd atoms than OH functionalisation. Better orbital interaction between Pd 4d states than Pt 5d states with carbon atoms of the COOH functionalised graphene may lead to enhanced charge transfer between anchoring Pd atoms on the COOH functionalised graphene support. The opposite occurs on OH functionalised graphene where there is higher charge transfer between anchoring Pt atoms and the OH functionalised graphene support.

PDOS analysis was performed on the rearranged structure with 3 Pd atoms anchoring the $Pt_{32}Pd_6$ cluster to the support with a segregation energy of -0.13 eV. This arrangement is the lowest energy arrangement of the $Pt_{32}Pd_6$ cluster on COOH functionalised graphene.

Comparison of the carbon PDOS of the COOH functionalised graphene pre and post adsorption of the $Pt_{32}Pd_6$ cluster in Figure 5.17 (a) indicates that the two sharp peaks at the Fermi level pre adsorption are reduced in intensity post adsorption. The PDOS of the $Pt_{32}Pd_6$ cluster adsorbed on COOH functionalised graphene depicted in Figure 5.17 (b) indicates that

the PDOS is transformed upon adsorption. The PDOS of the $Pt_{32}Pd_6$ cluster is discrete-like with occupied states at the Fermi level for the bare cluster. Post adsorption the PDOS is well defined and continuous though still rather discrete-like at energies (0 – 2 eV) above the Fermi level. The changes to carbon PDOS and PDOS of the $Pt_{32}Pd_6$ cluster post adsorption are indicative of formation of bonds between the COOH functionalised graphene support and the $Pt_{32}Pd_6$ cluster.

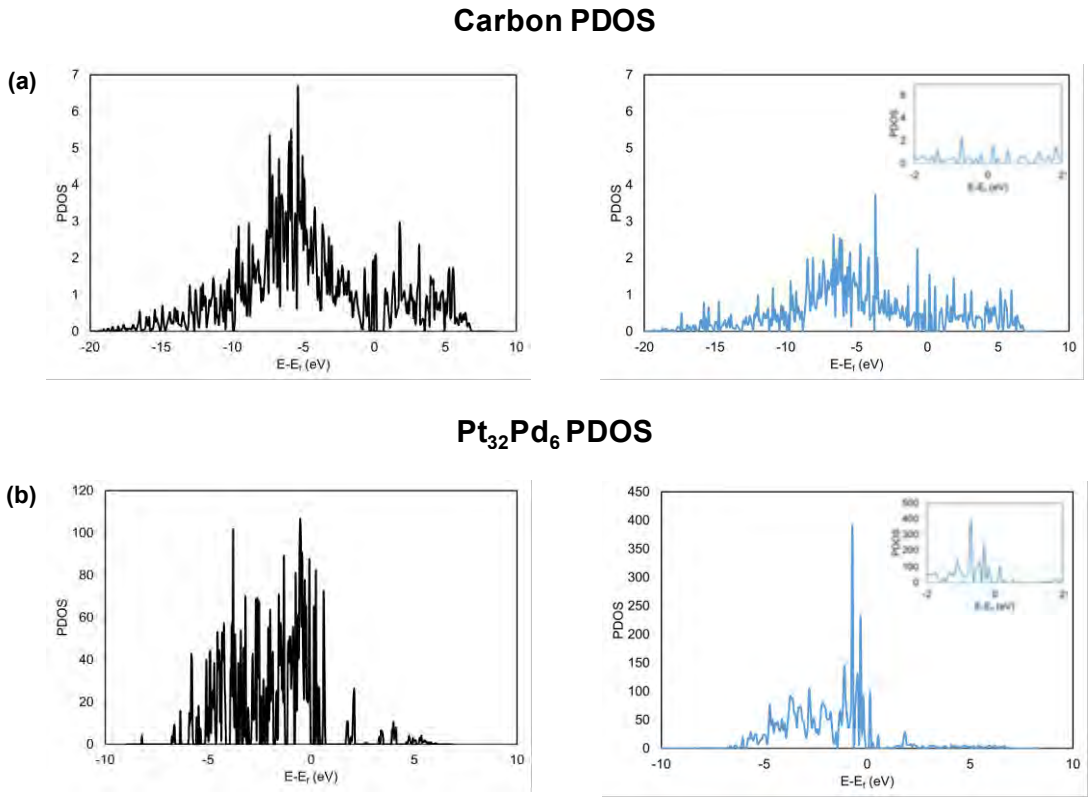


Figure 5.17: PDOS of the carbon, Pt and Pd atoms: (a) PDOS of carbon atoms of COOH functionalised graphene before adsorption (black curve) and after adsorption (blue curve), and (b) PDOS of $Pt_{32}Pd_6$ before (black curve) and after adsorption (blue curve). The energy scale is relative to the Fermi level. Inserts show zoomed view around the Fermi level.

To assess the reactivity and changes of the d-band of the supported $Pt_{32}Pd_6$ cluster in comparison to the free standing $Pt_{32}Pd_6$ cluster, the rearranged structure with 3 Pd atoms anchoring the cluster to the support was considered. The d-band centre, d-band width and d-band filling for the entire $Pt_{32}Pd_6$ cluster and for the interacting and opposite facets were determined. The free standing $Pt_{32}Pd_6$ cluster for the considered adsorption geometry has a different arrangement to the lowest energy free standing $Pt_{32}Pd_6$ cluster. Therefore, the d-band properties of the free standing $Pt_{32}Pd_6$ cluster for the rearranged cluster is different to that used for adsorption on pristine and OH functionalised graphene. However, for the free standing $Pt_{32}Pd_6$ cluster, the rearranged cluster in not the most stable arrangement.

Table 5.7: Calculated d-band centre relative to the Fermi level, d-band filling and d-band width for the $Pt_{32}Pd_6$ cluster interacting with COOH functionalised graphene.

| | $\varepsilon_d - \varepsilon_F$ (eV) | $f_d$ | $w_d$ (eV) |
|---|---|---|---|
| **$Pt_{32}Pd_6$ free standing cluster (rearranged)** | | | |
| overall cluster | -1.82 | 0.89 | 2.75 |
| interacting facet (square facet with 3 Pd atoms) | -1.53 | 0.90 | 2.13 |
| opposite facet (square facet with 4 Pt atoms) | -1.95 | 0.88 | 2.85 |
| **$Pt_{32}Pd_6$ interacting through square facet with 3 Pd atoms with COOH functionalised graphene** | | | |
| overall cluster | -1.99 | 0.91 | 2.93 |
| interacting facet (square facet with 3 Pd atoms) | -2.00 | 0.90 | 2.96 |
| opposite facet (square facet with 4 Pt atoms) | -1.90 | 0.92 | 2.77 |

The $Pt_{32}Pd_6$ cluster interacts through the d-band with the COOH functionalised graphene support results in 0.17 eV downward shift of the d-band centre of the entire cluster relative to the d-band centre of the free standing $Pt_{32}Pd_6$ cluster (see Table 5.7). The effect of the interaction between the $Pt_{32}Pd_6$ cluster and the COOH functionalised graphene support is not only limited to the contact region since there is shift of the d-band centre of the interacting and the opposite facets. The extent of d-band centre shift of 0.47 eV for the interacting facet is higher than for the opposite facet (0.05 eV). The small shift in d-band centre of the opposite facet of 0.05 eV relative to the d-band centre of the same facet in the free standing $Pt_{32}Pd_6$ cluster suggests that the reactivity of the supported $Pt_{32}Pd_6$ cluster will bear resemblance to that of the free unsupported $Pt_{32}Pd_6$ cluster. However, the free standing $Pt_{32}Pd_6$ cluster has a different arrangement to that of the rearranged $Pt_{32}Pd_6$ cluster on COOH functionalised graphene. The free standing $Pt_{32}Pd_6$ cluster is such that Pd and Pt atoms are mixed on the surface with Pd situated at the centre of the hexagonal facet. On the COOH functionalised graphene support Pd atoms of the $Pt_{32}Pd_6$ cluster segregate towards the cluster-support interface thereby exposing more Pt atoms on the surface. Therefore, the difference in arrangement between the COOH functionalised graphene supported $Pt_{32}Pd_6$ cluster and the free standing $Pt_{32}Pd_6$ cluster is expected to lead to a difference in reactivity between the supported and unsupported $Pt_{32}Pd_6$ cluster.

In the free standing $Pt_{32}Pd_6$ cluster the d-band centre of square facets consisting of Pt atoms only is -1.82 eV and -1.89 eV, whilst on the rearranged $Pt_{32}Pd_6$ cluster the d-band centre of a square facet consisting of Pt atoms only is -1.95 eV. The difference in d-band centre of the square facets suggests a different reactivity between the free standing $Pt_{32}Pd_6$ cluster and the rearranged $Pt_{32}Pd_6$ cluster supported on COOH functionalised graphene.

### 5.3.4 Comparison of OH and COOH functionalised graphene

The binding energy of the $Pt_{32}Pd_6$ cluster is stabilised on functionalised graphene compared to adsorption on pristine graphene. Binding on OH functionalised graphene is more stable at -1.94 eV compared to COOH functionalisation with a binding energy of -1.47 eV. The binding energy on pristine graphene is endothermic at 0.71 eV calculated with the GGA–PW91 functional.

The most stable adsorption on OH functionalised graphene is when the $Pt_{32}Pd_6$ cluster approaches from below the functional group (i.e. the graphene sheet is between the OH functional group and the $Pt_{32}Pd_6$ cluster). Conversely, the most stable adsorption configuration on COOH functionalised graphene is where the $Pt_{32}Pd_6$ cluster is positioned to the side of the COOH functional group, approaching from the side of the graphene bearing the COOH functional group. On OH functionalised graphene the binding energies in which the $Pt_{32}Pd_6$ cluster approaches from below the functional group (i.e. the graphene sheet is between the functional group and the $Pt_{32}Pd_6$ cluster) have exothermic binding energies than when the $Pt_{32}Pd_6$ cluster is directly interacting with the functional group.

For adsorption on OH functionalised graphene the lowest energy structure has arrangement of the $Pt_{32}Pd_6$ cluster identical to the lowest energy arrangement (highly exothermic excess energy) of the free standing $Pt_{32}Pd_6$ cluster. Investigated rearrangements of the $Pt_{32}Pd_6$ cluster on OH functionalised graphene resulted in positive segregation energies. On the contrary, on COOH functionalised graphene the supported $Pt_{32}Pd_6$ cluster can rearrange to other arrangements of the $Pt_{32}Pd_6$ cluster which were otherwise not stable for the free standing $Pt_{32}Pd_6$ cluster. In addition, on COOH functionalised graphene the lowest energy arrangements are where Pd atoms are segregated towards the cluster-support interface thereby exposing more Pt atoms on the surface of the cluster. Increasing Pd concentration to more than two Pd atoms on the square facet interacting with the COOH functionalised

graphene support leads to stabilised interaction between the $Pt_{32}Pd_6$ cluster and COOH functionalised graphene resulting in highly exothermic formation energies.

On both OH and COOH functionalised graphene the net charge transfer from the support to the $Pt_{32}Pd_6$ cluster is small and insignificant. Hence, interaction of the $Pt_{32}Pd_6$ cluster with the functionalised and pristine graphene supports is not dominated by charge transfer but by charge redistribution within the $Pt_{32}Pd_6$ cluster and the support. The extent of charge redistribution within the $Pt_{32}Pd_6$ cluster is higher for the case of COOH functionalised graphene than for OH functionalised and pristine graphene.

Despite the insignificant overall charge transfer, there is charge loss from the atoms of the interacting facet on both OH and COOH functionalised graphene supports. A higher amount of charge loss from Pd atoms on the interacting facet is calculated on COOH functionalised graphene than on OH functionalised graphene. The higher charge loss from anchoring Pd atoms on COOH functionalised graphene correlates with negative segregation energies and highly exothermic formation energies of the supported $Pt_{32}Pd_6$ cluster. Therefore, it can be postulated that COOH functionalisation modifies the electronic properties of the carbon atoms in the vicinity of the functional group different to OH functionalisation. The difference in electronic modification is manifested by a higher charge loss from the Pd atoms on the interacting facet on COOH functionalised graphene than on OH functionalised graphene.

On both OH and COOH functionalised graphene, new peaks appear at and around the Fermi level in the PDOS of the carbon atoms of the functionalised supports. In addition, there is a corresponding change to the PDOS of the $Pt_{32}Pd_6$ cluster which is transformed from discrete to continuous. The changes to the PDOS of the carbon atoms of the support and the $Pt_{32}Pd_6$ cluster indicates that there is bond formation between the carbon 2p states of the support and the $Pt_{32}Pd_6$ cluster d states.

For $Pt_{32}Pd_6$ cluster interaction with OH and COOH functionalised graphene, the cluster interacts through the d-band with the support resulting in shift of the d-band centre of the supported $Pt_{32}Pd_6$ cluster relative to the d-band centre of the free standing $Pt_{32}Pd_6$ cluster. The d-band centre downshift is 0.21 eV on OH functionalised graphene, 0.17 eV on COOH functionalised graphene and 0.25 eV on pristine graphene. On functionalised graphene (i.e. OH and COOH functionalised) the d-band centre of the supported $Pt_{32}Pd_6$ cluster correlates with the binding energy of the $Pt_{32}Pd_6$ cluster.

On both OH and COOH functionalised graphene supports, the effect of the interaction between the cluster and support is not localised to the contact region only, but affects the entire $Pt_{32}Pd_6$ cluster. There is a shift in the d-band centre of the interacting and opposite facet indicating the non-localised effect. The extent of d-band centre downshift is higher for the interacting facet than the opposite facet. For the interacting facets the downshifts of the d-band centre are 0.41 eV and 0.47 eV for OH and COOH functionalised graphene respectively. The corresponding d-band centre shifts of the opposite facets are 0.07 eV downshift on OH functionalised graphene and an upward shift of 0.05 eV on COOH functionalised graphene. The reactivity of the $Pt_{32}Pd_6$ cluster supported on OH functionalised graphene is expected to resemble that of the free standing $Pt_{32}Pd_6$ cluster due to the small shift in d-band centre of the opposite facet relative to the d-band centre of the same facet in the free standing $Pt_{32}Pd_6$. In contrast, a different reactivity of the $Pt_{32}Pd_6$ cluster supported on COOH functionalised graphene is expected relative to the activity of the free standing $Pt_{32}Pd_6$ cluster despite the small upward shift in d-band centre of 0.05 eV. This is because on COOH functionalised graphene the $Pt_{32}Pd_6$ cluster adopts a different arrangement to the lowest energy free standing $Pt_{32}Pd_6$ cluster arrangement. The arrangement on the COOH functionalised graphene exposes more Pt atoms on the surface (Pd is segregated towards the cluster-support interface), and the facets exposed have a different atomic composition to those of the free standing $Pt_{32}Pd_6$ cluster.

## 5.4 Conclusions

Functionalisation of graphene with OH and COOH enhances and stabilises the bonding of the $Pt_{32}Pd_6$ cluster on the graphene support relative to bonding on pristine graphene. The binding is enhanced more on OH functionalised graphene than COOH functionalised graphene.

On OH functionalised graphene the $Pt_{32}Pd_6$ cluster adopts the same arrangement as the lowest energy arrangement of the free standing $Pt_{32}Pd_6$ cluster. The Pd atoms mix with the Pt atoms on the surface and occupy the centre of the hexagonal facets. The $Pt_{32}Pd_6$ cluster is anchored to the OH functionalised graphene support by Pt atoms. Conversely, on COOH functionalised graphene the $Pt_{32}Pd_6$ cluster rearranges from the ordering in the free standing $Pt_{32}Pd_6$ cluster. Pd atoms are segregated towards the cluster-support interface on COOH functionalised graphene, thereby exposing more Pt atoms on the surface. In the free standing $Pt_{32}Pd_6$ cluster the rearranged form with Pd atoms segregated to one square facet is not energetically stable.

On both OH and COOH functionalised graphene there is change to the PDOS of the carbon atoms of the support in the contact region and the PDOS of the supported $Pt_{32}Pd_6$ cluster. The changes to the PDOS indicates formation of metal-carbon bonds due to orbital interaction between the carbon 2p states and the $Pt_{32}Pd_6$ d states. Interaction of the $Pt_{32}Pd_6$ cluster with pristine and functionalised graphene is characterised by charge redistribution within the $Pt_{32}Pd_6$ cluster and the support and not by charge transfer to or from the support.

On OH functionalised graphene the reactivity of the supported $Pt_{32}Pd_6$ cluster is expected to resemble that of the free standing $Pt_{32}Pd_6$ cluster due to a small downward shift of the d-band centre of the opposite facet relative to that of the free standing $Pt_{32}Pd_6$ cluster. On COOH functionalised graphene a different reactivity of the supported $Pt_{32}Pd_6$ cluster to the free standing $Pt_{32}Pd_6$ cluster is expected, due to a different arrangement of the supported $Pt_{32}Pd_6$ cluster compared to the free standing $Pt_{32}Pd_6$ cluster.

For the COOH functionalised graphene supported $Pt_{32}Pd_6$ cluster, more Pt atoms are exposed on the facets of the cluster that are available for interaction with adsorbate molecules. In addition, different facets, with different d-band centres, are present on the $Pt_{32}Pd_6$ cluster supported on COOH functionalised graphene compared to the facets of the free standing $Pt_{32}Pd_6$ cluster. This implies difference in the reactivity of the $Pt_{32}Pd_6$ cluster on COOH functionalised graphene compared to the free standing $Pt_{32}Pd_6$ cluster. The reactivity of the $Pt_{32}Pd_6$ cluster supported on pristine graphene is expected to the different to that of the free standing $Pt_{32}Pd_6$ cluster. This is due to a higher downshift of the d-band centre of the opposite facet for the supported cluster relative to the d-band centre of the same facet in the free standing $Pt_{32}Pd_6$ cluster. The higher extent of d-band centre shift of the opposite facet on pristine graphene indicates weaker binding of adsorbates on the opposite facet relative to adsorption on the same facet of the free standing $Pt_{32}Pd_6$ cluster.

# 5.6 References

Bader, R.F.W. (1991) A quantum theory of molecular structure and its applications. *Chem. Rev.* **91**, 893-928.

Blöchl, P.E. (1994) Projector augmented-wave method. *Phys. Rev. B* **50**, 17953-17979.

Bučko, T., Lebégue, S., Hafner, J. & Ángyán, J.G. (2013) Tkatchenko-Scheffler van der Waals correction method with and without self-consistent screening applied to solids. *Phys. Rev. B* **87**, 064110-064125.

Burgess, R., Buono, C., Davies, P.R., Davies, R.J., Legge, T., Lai, A., Lewis, R., Morgan, D.J., Robinson, N. & Willock, D.J. (2015) The functionalisation of graphite surfaces with nitric acid: identification of functional groups and their effect on gold deposition. *J. Catal.* **323**, 10-18.

Chutia, A., Hamada, I. & Tokuyama, M. (2014) A theoretical insight on the interaction between Pt nanoparticles and hydroxylated graphene nanoflakes. *Surf. Sci.* **628**, 116-125.

Dion, M., Rydberg, H., Schröder, E., Langreth, D.C. & Lundqvist, B.I.(2004) Van der Waals density functional for general geometries. *Phys. Rev. Lett.* **92**, 246401-246405.

Edwards, J.K., Freakly, S.J., Carley, A.F., Kiely, C.J. & Hutchings, G.J. (2014) Strategies for designing supported gold-palladium bimetallic catalysts for the direct synthesis of hydrogen peroxide. *Acc. Chem. Res*. **47**, 845-854.

Fuentes-Cabrera, M., Baskes, M.I., Melechko, A.V. & Simpson, M.L. (2008) Bridge structure for the graphene/ Ni (111) system: A first principles study. *Phys. Rev. B* **77**, 035405-035410.

Henkelman, G., Arnaldsson, A. & Jónsson, H. (2006) A fast and robust algorithm for Bader decomposition of charge density. *Comput. Mater. Sci*. **36**, 354-360.

Kakade, B.A., Tamaki, T., Ohashi, H. & Yamaguehi, T. (2012) Highly active bimetallic PdPt and CoPt nanocrystals for methanol electro-oxidation. *J. Phys. Chem. C* **116**, 7464-7470.

Klimeš, J., Bowler, D.R. & Michaelides, A. (2010) Chemical accuracy for the van der Waals density functional. *J. Phys.: Condens. Matter* **22**, 022201-022206.

Kresse, G. & Furthmüller, J. (1996a) Efficiency of ab-initio total energy calculations for metals and semiconductors using a plane-wave basis set. *Comput. Mater. Sci*. **6**, 15-50.

Kresse, G. & Furthmüller, J. (1996b) Efficient iterative schemes for ab-initio total-energy calculations using a plane wave basis set. *Phys. Rev. B* **54**, 11169-11186.

Kresse, G. & Jourbert, D. (1999) From ultrasoft pseudopotentials to the projector augmented-wave method. *Phys. Rev. B* **59**, 1758-1775.

Kresse, G. & Hafner, J. (1994) Ab initio molecular-dynamics simulation of the liquid-metal-amorphous-semi-conductor transition on germanium. *Phys. Rev. B* **49**, 14251-14269.

Kresse, G. & Hafner, J. (1993) Ab initio molecular dynamics for liquid metals. *Phys. Rev. B* **47**, 558-561.

Methfessel, M. & Paxton, A.T. (1989) High precision sampling for Brillouin-zone integration in metals. *Phys. Rev. B* **40**, 3616-3621.

Monkhorst, H.J. & Pack, J.D. (1976) Special points for Brillouin-zone integrations. *Phys. Rev. B* **13**: 5188-5192.

Perdew, J.P., Chevary, J.A., Vosko, S.H., Jackson, K.A., Pederson, M.R., Singh, D.J. & Fiolhais, C. (1992) Atoms, molecules, solids, and surfaces: applications of the generalized gradient approximation for exchange and correlation. *Phys. Rev. B* **46**, 6671-6686.

Román-Pérez, G. & Soler, J.M. (2009) Efficient implementation of a van der Waals density functional: application to double-wall carbon nanotubes. *Phys. Rev. Lett.* **103**, 096102-096106.

Ruban, A., Hammer, B., Stolze, P., Skriver, H.L. & Nørskov, J.K. (1997) Surface electronic structure and reactivity of transition and noble metals. *J. Mol. Catal. A. Chem* **115**, 421-429.

Sanville, E., Kenny, S.D., Smith, R. & Henkelman, G. (2007) Improved grid-based algorithm for Bader charge allocation. *J. Comput. Chem*. **28**, 899-908.

Tang, W., Sanville, E. & Henkelman, G. (2009) A grid-based Bader analysis algorithm without lattice bias. *J. Phys.: Condens. Matter* **21**, 084204-084211.

Tkatchenko, A., DiStasio Jr., R.A., Car, R. & Scheffler, M. (2012) Accurate and efficient method for many-body van der Waals interactions. *Phys. Rev. Lett*. **108**, 236402-236407.

Thonhauser, T., Cooper, V.R., Li, S., Puzder, A., Hyldgaard, P. & Langreth, D.C. (2007) Van der Waals density functional: self-consistent potential and the nature of the van der Waals bond. *Phys. Rev. B* **76**, 125112-125123.

van der Oetelaar, L.C.A., Nooij, O.W., Oerlemans, S., Denier van der Gon, A.W., Brongersma, H.H., Lefferts, L., Roosenbrand, A.G. & van Veen, J.A.R. (1998) Surface segregation in supported Pd-Pt nanoclusters and alloys. *J. Phys. Chem. B* **102**, 3445-3455.

Vanin, M., Mortensen, J.J., Kelkkanen, A.K., Garcia-Lastra, J.M., Thygesen, K.S. & Jacobsen, K.W. (2010) Graphene on metals: A van der Waals density functional study. *Phys. Rev. B* **81**, 081408-081412.

Yuan, D.W., Liu, C. & Liu, Z.R. (2014) Structures and catalytic properties of $Pd_mAu_n$ (m+n =7) bimetallic clusters supported on graphene by first-principles studies. *Phys. Lett. A* **378**, 408-415.

# Chapter 6: $Pt_{38}$ cluster interaction with $TiO_2$(110) surfaces

## 6.1 Introduction

$TiO_2$ has various applications ranging from being used as a pigment, photocatalyst, gas sensor, electronic device and as support material in heterogeneous catalysis (Diebold, 2003). Of special interest to the present study is the use of $TiO_2$ as support material for metal nanoparticles. In the present study we focus on the Pt-$TiO_2$ system owing to its use in various catalytic systems: $NO_X$ reduction catalyst (Chen et al., 2012), electrocatalyst for fuel cells (Marković et al., 2001), photocatalyst (Campbell, 2012) and many more catalytic reactions. Furthermore, the Pt/$TiO_2$ system is considered a prototype system for strong-metal-support-interactions (Tauster, 1987), hence insight of the interaction between metal nanoparticles and transition metal oxide supports can be gained by studying the Pt/$TiO_2$ system. The properties of $TiO_2$ which make it an ideal support material are its high mechanical stability, high thermal stability, resistant to corrosive environments both oxidative or reductive (Huang et al., 2009), and relative abundance (Orita, 2010).

$TiO_2$ consists of three main crystal forms: viz. rutile, anatase and brookite, although other phases have been observed (Diebold, 2003). The rutile phase is the stable phase in the bulk whilst the anatase phase is the stable phase for nanoparticles (Zhang & Banfield, 1998). In the present study the main focus will be on the rutile phase. The (110) facet is the lowest energy facet for rutile $TiO_2$ (Jones & Hockey, 1971a; Jones & Hockey, 1971b; Diebold, 2003). We seek to understand interaction of metal nanoparticles with the rutile $TiO_2$(110) surface. Therefore, knowledge of the surface is important to understand its interaction with deposited metal particles. The rutile $TiO_2$(110) surface is used as a model surface to gain insight into metal oxide surface properties owing to the ease with which this surface can be prepared and its relative availability (Diebold, 2003; Ganduglia-Pirovano et al., 2007).

## 6.2 Rutile $TiO_2$(110) surface

Figure 6.1 shows the surface slab of rutile $TiO_2$(110) together with the label of the different types of surface oxygen atoms and surface titanium atoms. A layer on the $TiO_2$(110) surface consist of a tri-atomic layer (-O-Ti-O-) comprising a row of titanium atoms which have oxygen

atoms above and below. Therefore, for the $TiO_2$(110) surface slab, a four-layer slab consists of four tri-atomic layers of (-O-Ti-O-). The surface consists of two different types of oxygen atoms: the surface oxygen atoms labelled $O_{3c}$ which have three nearest neighbours like in the bulk crystal of rutile $TiO_2$, and $O_{2c}$ oxygen atoms which are protruding on the surface and have coordination number of two and are termed bridging oxygen atoms. Two types of surface titanium atoms are present on the surface: the $Ti_{6c}$ atoms which are bridged by the $O_{2c}$ oxygen atoms and have a coordination number of 6 like in the bulk structure of $TiO_2$, and $Ti_{5c}$ atoms which have coordination number of 5.

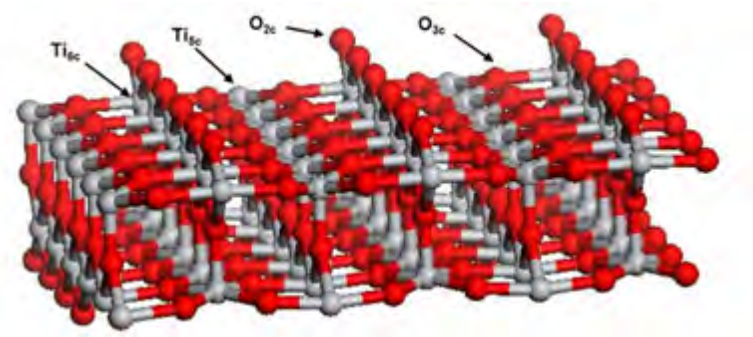


Figure 6.1: Rutile $TiO_2$(110) bilayer surface slab with the different surface oxygen and titanium atoms labelled.

The reactivity of the rutile $TiO_2$(110) surface depends on the surface composition. It follows that deposition of metal nanoparticles on the $TiO_2$(110) surface will depend on composition of the surface. Scanning tunnelling microscopy (STM) studies have revealed that the surface of rutile $TiO_2$(110) can consist of point defects in the form of surface oxygen bridge monovacancies and surface hydroxyl groups (Diebold, 2003). Other point defects which have been observed on other metal oxides surfaces include surface oxygen bridge divacancies, kinks, corners and steps (Rieboldt et al., 2014a). The surface defects are known to determine the surface chemistry, reactivity and nucleation of metal particles on the oxide surface (Diebold, 2003; Ganduglia-Pirovano et al., 2007; Ammal & Heyden, 2010; Diebold et al., 2010).

## 6.3 Electronic structure of rutile $TiO_2$(110) surface

Standard generalised gradient approximations (GGA) functionals are known to underestimate the band gap of bulk rutile $TiO_2$. The experimental band gap is 3.0 eV and the prediction from GGA functionals is around 1.80 eV (Perron et al., 2007). The underestimation of the band gap by GGA functionals is due to the well documented shortfalls of standard GGA functionals to correctly describe strongly correlated systems such as found in metal oxides where the

electrons are localised. The approximation of exact exchange within the standard GGA methods lead to self-interaction error, where electron delocalisation is predicted in states which are localised leading to the wrong prediction of the electronic and geometric structure (Morgan & Watson, 2007).

The PDOS spectrum of bulk rutile $TiO_2$ and rutile stoichiometric $TiO_2$(110) surface are the same with no features in the band gap between the conduction band and the valence band (Henrich & Kurtz, 1981). A partially reduced rutile $TiO_2$(110) surface which has missing surface oxygen bridge atoms has a different electronic structure to the stoichiometric rutile $TiO_2$(110) surface. Experimental investigations show that the electronic structure of the partially reduced rutile $TiO_2$(110) surface is characterised by appearance of a small state approximately 0.8 eV below the conduction band (Henrich et al., 1976; Tait & Kasowski, 1979). The band gap state is due to charge left behind when the bridging surface oxygen atoms are removed and the charge is localised on Ti atoms next to the vacancy site (Henrich et al., 1976; Tait & Kasowski, 1979; Di Valentin et al., 2006; Morgan & Watson, 2007; Calzado et al., 2008). Standard GGA functionals do not predict presence of the defect state in the band gap of the partially reduced rutile $TiO_2$(110) surface as observed experimentally. Instead GGA calculations indicate that the electrons occupy the bottom of the conduction band with charge delocalised over subsurface Ti atoms (Morgan & Watson, 2007). The over delocalisation of the excess charge left behind by the bridging surface oxygen atoms is a result of self-interaction error of standard GGA functionals (Morgan & Watson, 2009).

In order to improve on the GGA prediction of the electronic structure of the partially reduced rutile $TiO_2$(110) surface, different options have been investigated. The different options include; hybrid functionals which incorporate a certain fraction of exact exchange from Hartree Fock (Di Valentin et al., 2006; Shibuya et al., 2012), and DFT+ U methods which includes the U term to compensate for deficiencies of standard DFT (Morgan & Watson, 2007; Calzado et al., 2008; Morgan & Watson, 2009; Chrétien & Metiu, 2011). The hybrid functionals and the DFT+U method predict existence of the defect state in the band gap of the partially reduced rutile $TiO_2$(110) surface in agreement with experimental measurements. However, the computational cost of including exact exchange from Hartree Fock in hybrid functionals is high, whereas the DFT+U method comes at no additional computational cost compared to standard GGA DFT (Morgan & Watson, 2009). Morgan & Watson (2009) investigated the effect of the U parameter in the DFT+U method in predicting the appearance of the defect state in the band gap of partially reduced rutile $TiO_2$(110) surface, and a U value lying in the range 4.2 eV < U < 6 eV was determined to result in appearance of the defect state in the band gap.

# 6.4 Interaction of metal nanoparticles with rutile $TiO_2$(110) surface

## 6.4.1 Experimental studies

A comparative study has been conducted to compare the size of Pt clusters deposited on stoichiometric $TiO_2$(110) surface, partially reduced $TiO_2$(110) surface, hydroxylated, i.e. surface OH groups on $TiO_2$(110) surface and oxidised, i.e. O adatoms on $TiO_2$(110) surface (Rieboldt et al., 2014a). It was observed that the Pt cluster size was comparable on all surfaces except on the hydroxylated surface where the Pt cluster size was larger (Rieboldt et al., 2014a). The sintering behaviour on the different surfaces was investigated and it was found that the highest cluster growth was observed on the stoichiometric and hydroxylated $TiO_2$(110) surfaces, with the least Pt cluster growth size observed on the oxidised $TiO_2$(110) surface (Rieboldt et al., 2014a).

## 6.4.2 DFT studies

DFT studies on Pt cluster interaction with $TiO_2$ are either standard DFT or DFT + U calculations. Figure 6.2 shows a plot of the binding energy of Pt clusters on the stoichiometric and partially reduced $TiO_2$(110) surfaces. Depending on the method used, i.e. standard DFT or DFT + U, the binding energy, geometry and electronic structure can be different. Binding on partially reduced $TiO_2$(110) is stronger than binding on stoichiometric $TiO_2$(110). On the partially reduced $TiO_2$(110) surface formation of Pt-Ti bonds at the vacancy site between the Pt cluster atoms and Ti atoms at the vacancy site are important in determining the binding energy (Jiang et al., 2012).

For cluster sizes $n < 6$, the preferred arrangement of the cluster adsorbed on $TiO_2$ supports is a flat planar structure, and for $n > 7$ the preferred arrangement is a 3 dimensional structure (Chrétien & Metiu, 2007a; Chrétien & Metiu, 2007b; Jiang et al., 2012). The 3 dimensional structures do not result in maximum contact with the support compared to flat planar small clusters where all atoms of the cluster bind to the support. Therefore, the increase in binding energy for larger 3 dimensional clusters is less.

The binding energy of small Pt clusters to $TiO_2$ surfaces is determined by Pt-O and Pt-Ti bonds on the surface atoms (Ammal & Heyden, 2011; Çakir & Gülseren, 2012; Jiang et al., 2012; Rieboldt et al., 2014b). Binding of Pt clusters to the stoichiometric and partially reduced

$TiO_2$(110) surfaces is accompanied by small charge transfer in the order of 0.50 e for $Pt_n$ clusters (n = 1-8) (Chrétien & Metiu, 2007a; Chrétien & Metiu, 2007b: Ammal & Heyden, 2011; Jiang et al., 2012; Çakir & Gülseren, 2012). Formation of Pt-O and Pt-Ti bonds upon adsorption of $Pt_n$ (n = 4-8) on stoichiometric $TiO_2$(110) surface was deduced from charge accumulation along these bonds (Jiang et al., 2012). Charge polarisation at the cluster-support interface was also observed upon adsorption of small $Pt_n$ clusters by Jiang et al. (2012).

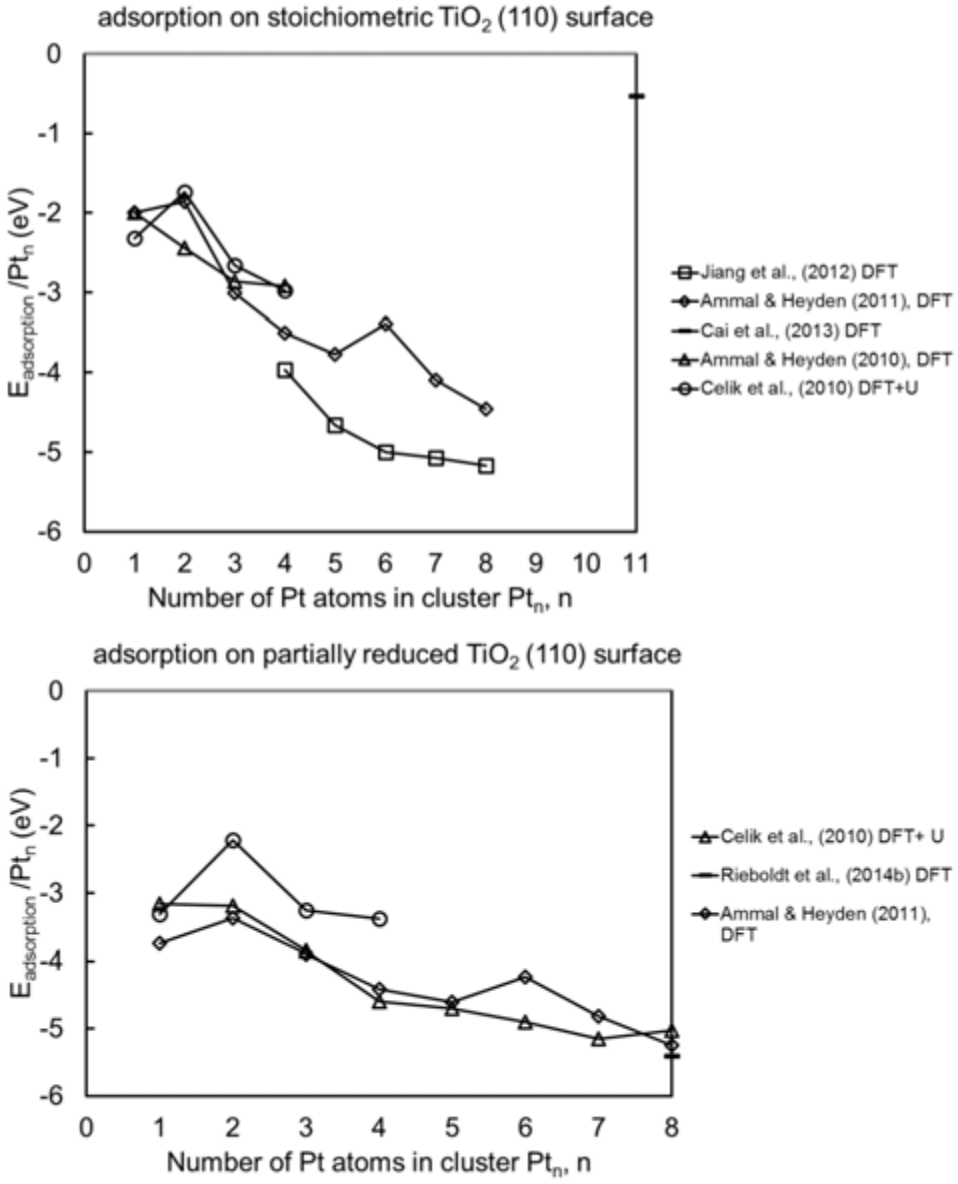


Figure 6.2: Calculated adsorption energies of $Pt_n$ clusters on stoichiometric and partially reduced $TiO_2$(110) surfaces. The method used for determination of the adsorption energy for each reference are included.

## 6.5 Aims and Objectives

Most studies on the interaction of Pt clusters with rutile $TiO_2$ surfaces have been limited to small clusters of ca. 8 atoms. In the present chapter the interaction of rutile $TiO_2$ surfaces with a larger 38 atom cluster (ca. 1mn particle) will be considered. The aim of the present chapter is to investigate binding of the $Pt_{38}$ cluster to the stoichiometric, partially reduced and hydroxylated rutile $TiO_2$(110) surfaces. In addition, the effect of the different surfaces on the reactivity of the supported $Pt_{38}$ cluster will be investigated.

## 6.6 Methodology

### 6.6.1 Structural models

The Pt particle is modelled as a 38 atom truncated octahedron cluster, the cluster consists of square (100)-like facets and hexagonal (111)-like facets. The rutile $TiO_2$(110) surface is represented by a (6 × 3) unit cell periodic slab consisting of 4 tri-atomic layers. The bulk rutile $TiO_2$ and the (110) surface optimisation results are presented in Appendix D. The optimised bulk lattice parameter of; a = 4.604 Å and c = 2.954 Å (c/a = 0.642) obtained for U = 0 eV are used for the adsorption calculations. The optimised lattice parameters in the present study are similar to those obtained in previous studies (Ammal & Heyden, 2011; Jiang et al., 2012; Çakir & Gülseren, 2012) and comparable to the experimentally measured values, a = 4.59 Å and c = 2.96 Å (c/a = 0.645) (Burdett et al., 1987).The stoichiometric or perfect rutile $TiO_2$(110) surface is obtained by cleaving the optimised bulk rutile $TiO_2$ along the(110) plane resulting in a slab with a stoichiometric ratio of Ti to O of 1:2. To model the partially reduced rutile $TiO_2$(110) surface with a bridging oxygen monovacancy, the central $O_{2c}$ oxygen atom of the stoichiometric $TiO_2$(110) was removed. Removal of the central bridging oxygen atom in the (6 × 3) unit cell results in a concentration of (1/18) ML or 0.06 ML of the oxygen vacancies. This concentration is similar to experimentally observed surface oxygen bridge vacancies of 0.04 ML – 0.06 ML on $Ar^+$ sputter cleaned $TiO_2$(110) surfaces for STM studies (Bonanni et al., 2012) and 0.08 ML (Rieboldt et al., 2014b). To model the hydroxylated surface with OH groups, hydrogen atoms were added to the two central bridging oxygen atoms of the stoichiometric $TiO_2$(110) surface. Three different arrangements of the two OH groups were investigated; the investigated arrangements are shown in Figure 6.3. The lowest energy structure out of the three investigated was then used for adsorption studies of the $Pt_{38}$ cluster.

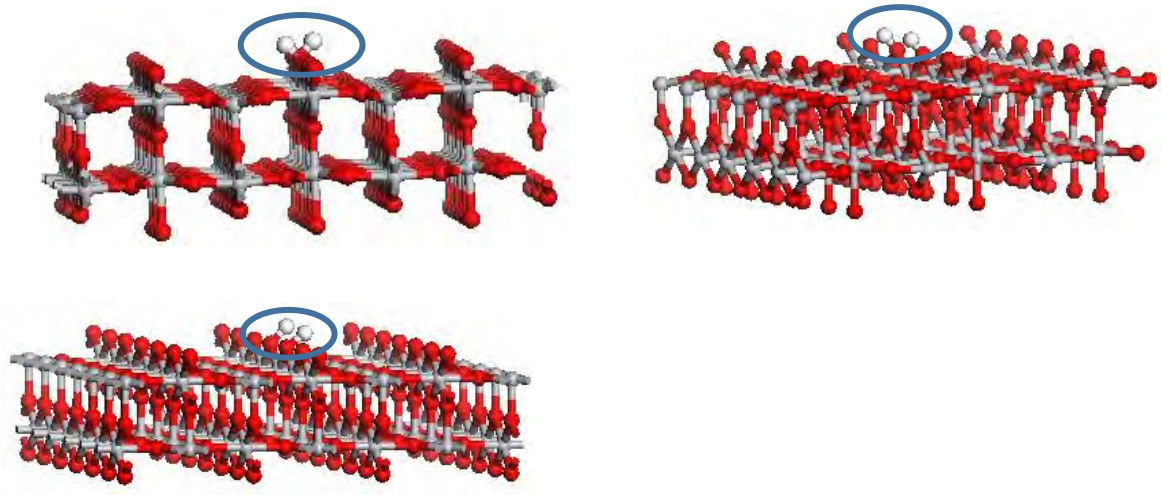

Figure 6.3: Structure for the three investigated arrangements of the OH on the hydroxylated $TiO_2$(110) surface.

To investigate interaction of the $Pt_{38}$ cluster with the different $TiO_2$(110) surfaces, approach of the cluster to the support through the square and hexagonal facets was considered. Owing to the large size of unit cell utilised and taking guidance from previous calculations on small $Pt_n$ clusters and the fact that metal atoms prefer to bind atop oxygen atoms of metal oxides (Matveev et al., 1999; Yulikov et al., 2006), to study adsorption of the $Pt_{38}$ cluster on the support only the metal ontop position geometries were investigated. For the metal ontop position the metal atoms of the facet interacting with the support are placed on average 2.10 Å above the bridging ($O_{2c}$) oxygen atoms.

## 6.6.2 Computational method

The Vienna ab initio simulation package VASP (Kresse & Hafner, 1993; Kresse & Hafner, 1994; Kresse & Furthmüller, 1996a; Kresse & Furthmüller, 1996b) was utilised for the calculations. Spin polarised calculations were performed. The generalised gradient approximation GGA PW91 functional (Perdew et al., 1992) was used for the exchange correlation energy. The GGA method was augmented with the + U term in the so called DFT + U method using Dudarev's approach (Dudarev et al., 1998) as implemented in the VASP code. The DFT +U method corrects for over delocalisation by standard GGA methods for the description of metal oxides. U term of U = 4.5 eV was applied to the Ti 3d states. For choice of the U parameter see Appendix D. The electron-ion interactions are described by the projector augmented wave (PAW) method (Blöchl, 1994; Kresse & Jourbert, 1999) pseudopotentials. The plane wave basis set cut-off energy was set at 400 eV. Gaussian smearing (Fu & Ho, 1983; Elsässer et al., 1994) was utilised with a smearing width σ = 0.01 eV.

For adsorption calculations a (6 × 3) periodic unit cell slab consisting of 4 tri-atomic layers was utilised, with the bottom two tri-atomic layers fixed at the bulk optimised positions. The top two tri-atomic layers together with the $Pt_{38}$ cluster were allowed to relax during the geometry optimisation calculations. The convergence criterion for the geometry optimisation calculations was an electronic convergence criterion of energies below $10^{-5}$ eV and forces below 0.03 eV/Å on unconstrained atoms. Adsorption was performed on only one side of the slab, with the dipole correction implemented within the VASP code applied in the z-direction to correct for any induced dipole which may arise as a result of cluster adsorption. The vacuum region was set at 25 Å to avoid spurious interactions between periodic images. Owing to the large unit cell size used, for geometry optimisation calculations the Brillouin zone sampling was sampled at the single Γ-point in k-space.

The binding energy (equivalent to the adsorption energy) of the $Pt_{38}$ cluster to the different $TiO_2$(110) surfaces was calculated from the relation:

$$E_{bind} = E_{Pt_{38}+\ support} - E_{support} - E_{Pt_{38}} \quad (6.1)$$

where $E_{Pt_{38}+\ support}$ is the energy of the optimised support with the $Pt_{38}$ cluster bound to it, $E_{support}$ is the energy of the optimised support without any $Pt_{38}$ cluster adsorbed, $E_{support}$ will be the energy of stoichiometric $TiO_2$(110) surface, partially reduced $TiO_2$(110) with monovacancy bridging oxygen atom and hydroxylated $TiO_2$(110) surface. $E_{Pt_{38}}$ is the energy of the free standing unsupported optimised $Pt_{38}$ cluster.

To gain further insight into the interaction of the $Pt_{38}$ cluster with the different supports, PDOS analysis were performed. Change in Bader charge analysis using Bader charge partitioning method (Bader, 1991; Henkelman et al., 2006; Sanville et al., 2007; Tang et al., 2009) and electron density difference plot analysis were also performed to assess charge transfer during adsorption of the $Pt_{38}$ cluster to the support. Single point energy calculations on the optimised structures were performed for electronic analysis calculations. For the PDOS, Bader and charge density difference plot analysis a Monkhorst Pack (Monkhorst & Pack, 1976) k-point grid of (2 × 3 × 1) was utilised to sample the Brillouin zone. The charge density difference was determined from the relation:

$$\Delta\rho = \rho_{Pt_{38}+\ support} - \rho_{support} - \rho_{Pt_{38}} \quad (6.2)$$

Where $\rho_{Pt_{38}+support}$ is the charge density of the optimised support with the $Pt_{38}$ cluster adsorbed, $\rho_{support}$ is the charge density of the support without the $Pt_{38}$ cluster in the same position as in the optimised geometry and $\rho_{Pt_{38}}$ is the charge density of the $Pt_{38}$ cluster in the same position as in the optimised geometry.

For Ti, O and H atoms, the atom resolved change in Bader charge upon adsorption is calculated from:

$$\Delta q = q_{Pt_{38}+\ support} - q_{support} \quad (6.3)$$

Where $q_{Pt_{38}+\ support}$ is the atom resolved Bader charge on Ti, O and H atoms in the optimised geometry with the support and the $Pt_{38}$ cluster adsorbed, $q_{support}$ is the atom resolved Bader charge on the corresponding Ti, O and H atoms of the support without the $Pt_{38}$ cluster in the same position as in the optimised geometry. The atom resolved change in Bader charge on Pt atoms of the $Pt_{38}$ cluster upon adsorption is calculated in a similar way to how charge on Ti, O and H atoms is calculated.

$$\Delta q = q_{Pt_{38}+\ support} - q_{Pt_{38}} \quad (6.4)$$

Where $q_{Pt_{38}+support}$ is the atom resolved Bader charge on Pt atoms in the optimised geometry with the support and the $Pt_{38}$ cluster adsorbed and $q_{Pt_{38}}$ is the atom resolved Bader charge on the corresponding Pt atoms of the $Pt_{38}$ cluster without the support in the same position as in the optimised geometry.

## 6.7 Results and Discussion

Of the three investigated arrangements of the OH's on the hydroxylated $TiO_2$(110) surface, the arrangement with the two OH's pointing in opposite directions was found to be the lowest energy arrangement by about 0.03 eV. The hydroxylated $TiO_2$(110) surface is proposed to be a result of water dissociation at a vacancy site on the partially reduced $TiO_2$(110) surface (Brookes et al., 2001). In the present study the dissociative adsorption energy of water on the partially reduced $TiO_2$(110) surface resulting in the hydroxylated $TiO_2$(110) surface is calculated to be -3.64 eV. The highly exothermic dissociative adsorption energy of water indicates that dissociation of water at the vacancy site of the partially reduced $TiO_2$(110) site is energetically feasible.

### 6.7.1 $Pt_{38}$ interaction with stoichiometric $TiO_2$(110)

Approach through the square facet of the $Pt_{38}$ cluster binds stronger by 0.29 eV than the hexagonal facet on the stoichiometric $TiO_2$(110) surface. The most stable binding energy of the $Pt_{38}$ cluster on the stoichiometric $TiO_2$(110) surface of -2.73 eV obtained in the present study is less exothermic than the calculated adsorption energy for smaller $Pt_n$ (n = 1-8) clusters (Ammal & Heyden, 2011; Jiang et al., 2012; Çakir & Gülseren, 2012; Rieboldt et al., 2014).

For smaller $Pt_n$ (n = 1-6) clusters the preferred arrangement of the free standing clusters is a planar 2 dimensional structure which result in maximum contact between cluster atoms and the support hence the higher binding energy. Whereas, for larger cluster sizes the free standing clusters adopt 3 dimensional structures, thus contact to the support is through a few atoms of the 3 dimensional structure and not the entire atoms of the cluster resulting in lower binding energies.

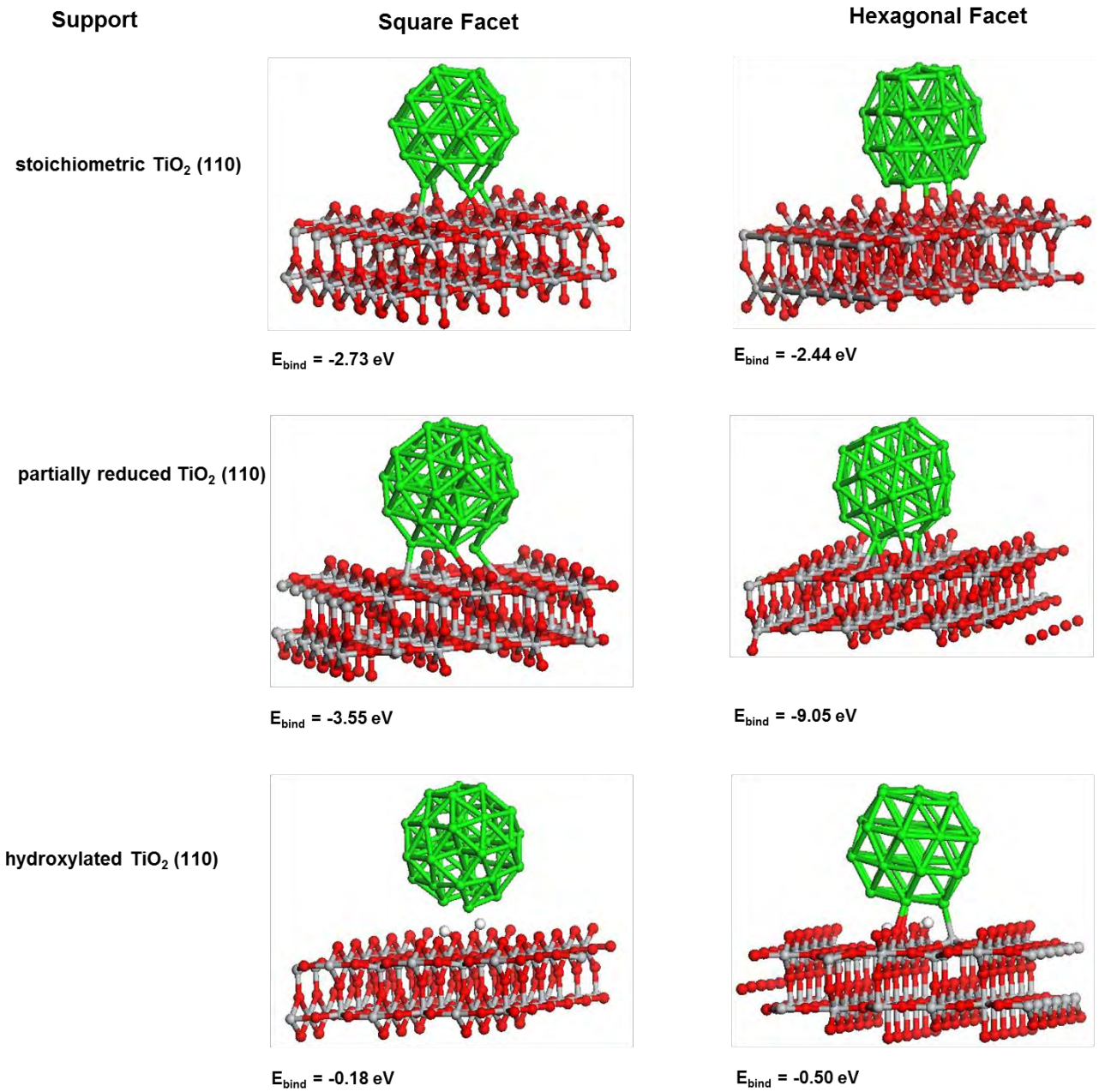


Figure 6.4: Optimised structures of the $Pt_{38}$ cluster on different $TiO_2$(110) surface: stoichiometric, partially reduced $TiO_2$ with monovacancy bridging oxygen atom and hydroxylated $TiO_2$.

Approach of the $Pt_{38}$ cluster through the square facet results in distortion of the support around the contact region. This is manifested by one of the Ti atoms bonded to the Pt atom of the interacting facet being elevated out of plane by 0.54 Å. A similar observation of distortion of the support upon adsorption of small $Pt_n$ (n =1-8) on the stoichiometric $TiO_2$(110) surface was made by Jiang et al. (2012).

The calculated Pt-$O_{2c}$ bond lengths for the hexagonal facet approach of the $Pt_{38}$ cluster adsorbed on the stoichiometric $TiO_2$(110) surface are slightly shorter than those calculated for the square facet approach (see Table 6.1). Comparison of Pt-$Ti_{5c}$ bond lengths for both square and hexagonal facet approaches indicate that the Pt-$Ti_{5c}$ bond lengths for the square facet approach are shorter than those for the hexagonal facet approach. This implies that for the hexagonal facet approach, bonding between Pt atoms of the interacting facet and Ti atoms of the support is weak. The higher exothermic binding energy of the square facet approach despite the slightly longer Pt-$O_{2c}$ bond lengths further strengthen the suggestion that shorter Pt-$Ti_{5c}$ bond lengths for this approach are stronger than those for the hexagonal facet approach.

Stronger Pt-Ti bonds for the square facet approach is indicated by structural distortion of the support around the contact region where a titanium atom is displaced out of plane towards the approaching cluster. Thus the number of Pt-O bonds together with Pt-Ti bonds enhances the binding of the $Pt_{38}$ cluster to the support in agreement with suggestions in previous studies for smaller $Pt_n$ (n = 1-8) clusters (Ammal & Heyden, 2011; Jiang et al., 2012). Adsorption of the $Pt_{38}$ cluster via both the square and the hexagonal facet results in structural distortion of the facet of the cluster interacting with the support. Comparison of calculated bond lengths of both interacting and opposite facets of the $Pt_{38}$ cluster (see Table 6.1) with the optimised bond lengths of the corresponding facets for the unsupported $Pt_{38}$ cluster indicates that there is bond elongation of the Pt-Pt bond lengths upon adsorption.

For the free standing $Pt_{38}$ cluster the square facet has bond lengths of 2.70 Å whereas the bond lengths for the hexagonal facet are side lengths of 2.65 Å and diagonal bond lengths of 2.70 Å. The extent of bond elongation for the interacting facet is higher for approach through the square facet than approach through the hexagonal facet. For both the hexagonal and square facet approaches the bond lengths of the opposite facet are similar to the optimised bond lengths of the same facets of the free standing $Pt_{38}$ cluster. This indicates that there is less structural distortion on the opposite facet. Therefore, interaction of the $Pt_{38}$ cluster with the stoichiometric $TiO_2$(110) surface does not stretch the Pt-Pt bond lengths of the cluster to

the same extent. There is less stretching of the Pt-Pt bond lengths on the opposite facet compared to the interacting facet.

Table 6.1: Optimised parameters for geometric structures of $Pt_{38}$ adsorbed on different $TiO_2$(110) surface. Side length corresponds to corner to corner length while diagonal length corresponds to corner to central Pt atom on hexagonal facet.

| | **Stoichiometric** | | | **Partially reduced** | | | **Hydroxylated** | | |
|---|---|---|---|---|---|---|---|---|---|
| Interacting Pt facet | Square | Hexagonal | | Square | Hexagonal | | Square | Hexagonal | |
| $E_{bind}$, (eV) | -2.73 | -2.44 | | -3.55 | -9.05 | | -0.18 | -0.50 | |
| | | | | | | | | | |
| $d_{Pt-Pt}$ [1], Å | | **side** | **diagonal** | | **side** | **diagonal** | | **side** | **diagonal** |
| | 2.79 | 2.79 | 2.73 | 2.73 | 2.74 | 2.72 | 2.71 | 2.72 | 2.75 |
| | 3.01 | 2.82 | 2.71 | 2.81 | 2.68 | 2.72 | 2.84 | 2.90 | 2.77 |
| | 3.32 | 2.66 | 2.81 | 3.15 | 2.71 | 2.93 | 2.70 | 2.69 | 2.77 |
| | 2.77 | 2.81 | 2.75 | 2.72 | 2.62 | 2.80 | 2.68 | 2.80 | 2.74 |
| | | 2.79 | 2.75 | | 2.72 | 2.90 | | 2.71 | 2.78 |
| | | 2.69 | 2.81 | | 2.70 | 3.00 | | 2.71 | 2.75 |
| | | | | | | | | | |
| $d_{Pt-Pt}$ [2], Å | | **side** | **diagonal** | | **side** | **diagonal** | | **side** | **diagonal** |
| | | | | | | | | | |
| | 2.70 | 2.65 | 2.70 | 2.71 | 2.63 | 2.66 | 2.69 | 2.65 | 2.69 |
| | 2.68 | 2.69 | 2.70 | 2.69 | 2.70 | 2.70 | 2.69 | 2.71 | 2.69 |
| | 2.68 | 2.64 | 2.71 | 2.68 | 2.63 | 2.71 | 2.69 | 2.63 | 2.71 |
| | 2.70 | 2.71 | 2.69 | 2.70 | 2.69 | 2.66 | 2.69 | 2.73 | 2.69 |
| | | 2.64 | 2.68 | | 2.63 | 2.70 | | 2.65 | 2.65 |
| | | 2.68 | 2.71 | | 2.70 | 2.70 | | 2.67 | 2.74 |
| | | | | | | | | | |
| $d_{Pt-O_{2c}}$, Å | 2.08 | 2.03 | | 2.02 | 1.97 | | 3.17 | 2.11 | |
| | 2.07 | 2.00 | | 2.05 | 1.97 | | 2.26 | 2.15 | |
| | 2.10 | 2.01 | | | | | | 2.41 | |
| | | | | | | | | | |
| | | | | | | | | | |
| | | | | | | | | | |
| $d_{Pt-Ti_{5c}}$, Å | 2.82 | 4.05 | | 2.56 | 2.79 | | | 2.55 | |
| | 2.50 | 3.80 | | 2.80 | 2.86 | | | | |
| | | 3.91 | | | 2.84 | | | | |
| | | 3.82 | | | **2.68** | | | | |
| | | 3.70 | | | **2.70** | | | | |
| | | | | | | | | | |
| | | | | | | | | | |
| $d_{Pt-O_{3c}}$, Å | | | | | 2.17 | 2.20 | | | |
| | | | | | | | | | |
| $d_{Pt-H}$, Å | | | | | | | 2.54 | 2.43 | |
| | | | | | | | 2.45 | 2.39 | |
| | | | | | | | | | |
| $d_{O-H}$, Å | | | | | | | 1.00 | 1.00 | |
| | | | | | | | 0.99 | 0.98 | |

[1]Pt-Pt distance in the facet closest to the support

[2] Pt-Pt distance in facet opposite and furthest to the one interacting with the support

## 6.7.2 $Pt_{38}$ interaction with partially reduced $TiO_2$(110)

On the partially reduced $TiO_2$(110) surface, approach of the $Pt_{38}$ cluster through the hexagonal facet binds stronger than the square facet by 5.50 eV. The calculated binding energies of the $Pt_{38}$ cluster on the partially reduced $TiO_2$(110) surface are more exothermic than those calculated on the stoichiometric $TiO_2$(110) surface for both the hexagonal and square facet approach. The monovacancy defect enhances adsorption of the $Pt_{38}$ cluster on the support compared to adsorption on the defect free stoichiometric $TiO_2$(110) surface. This result is consistent with previous studies on smaller $Pt_n$ (n = 1-8) clusters (Çelik et al., 2010; Ammal & Heyden, 2011; Çakir & Gülseren, 2012; Rieboldt et al., 2014).

The enhanced binding energy of -9.05 eV for the hexagonal facet approach of the $Pt_{38}$ cluster on the partially reduced $TiO_2$(110) surface is attributed to formation of Pt-Ti bonds at the vacancy site. Figure 6.5 indicates the central Pt atom of the interacting hexagonal facet; it is observed that this central Pt atom is positioned as if it occupies the lattice site of the missing oxygen bridge atom. The bond lengths of the central Pt atom and the Ti atoms at the vacancy site are 2.68 Å and 2.70 Å. Timperman et al. (2010a) concluded from XRD and XPS measurements that the was formation of Pt-Ti bonds at the interface between the support and Pt nanoparticles for the Pt on $TiO_2$ catalyst. Pt-Ti bonds were confirmed by shifts in the XPS spectra of Ti and Pt atoms (Timperman et al., 2010a). The formation of the partial alloy (Pt-Ti) was confirmed by a shortened lattice parameter for the Pt supported on $TiO_2$, the shorter lattice parameter was of the same magnitude as the lattice parameter of the Pt-Ti alloy. Furtheron, the compressed lattice parameter of Pt supported on $TiO_2$ was attributed to Pt being drawn into the structure of the $TiO_2$ support, this is consistent with the observation of the present study where the central Pt atom of the interacting hexagonal facet occupies the vacancy site on the surface of the partially reduced $TiO_2$(110) surface.

The adsorption geometry of the $Pt_{38}$ cluster approach through the hexagonal facet is in a tilted configuration (see Figures 6.4 and 6.5), which maximises contact between the $Pt_{38}$ cluster and the support. In addition, the adsorption geometry is such that the central Pt atom on the hexagonal facet interacting with the support occupies the site of the vacant surface oxygen bridge atom (see Figure 6.5). This Pt atom is bonded to Ti atoms at the vacancy site which have missing bonds due to the surface oxygen bridge vacancy. This type of adsorption geometry has been observed for small size $Pt_n$ (n = 1-8) clusters (Çelik et al., 2010; Ammal & Heyden, 2011; Çakir & Gülseren, 2012; Rieboldt et al., 2014). For the square facet approach of the $Pt_{38}$ cluster there is no bonding of Pt atoms to Ti atoms with missing bonds at the vacancy site. Similar to adsorption on the stoichiometric $TiO_2$(110) surface, binding to the

partially reduced $TiO_2$(110) surface results in structural distortion of the support in the contact region. The result of which is one of the Ti atoms bonded to a Pt atom is elevated out of plane by 0.30 Å towards the approaching cluster.

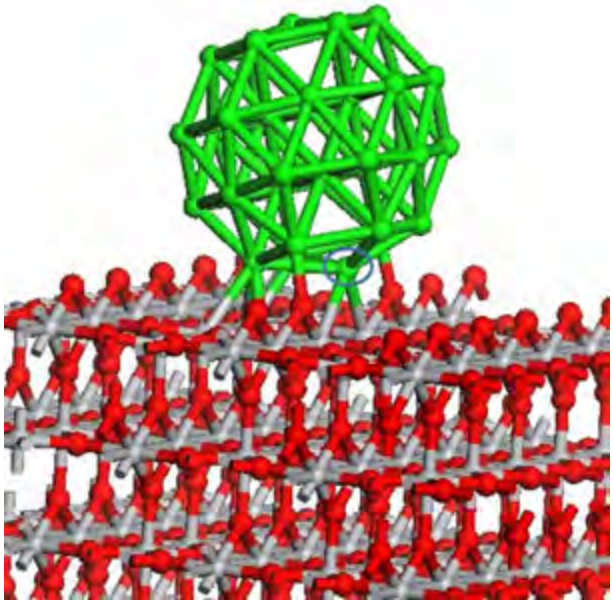

Figure 6.5: Central Pt atom of the hexagonal facet circled indicating bonds formed at the vacancy site for the $Pt_{38}$ cluster adsorbed on the partially reduced $TiO_2$(110) surface.

The enhanced binding energy of the hexagonal facet compared to the square facet on the partially reduced $TiO_2$(110) surface is due to higher contact area between the interacting hexagonal facet and the support than the interacting square facet. As a consequence of the higher contact for the hexagonal facet approach structure, the are more Pt-$Ti_{5C}$ bonds formed for the hexagonal facet approach than for the square facet approach. It is thus concluded that the higher the contact area between the cluster and the support, the higher possibility of Pt-Ti bonds being formed which have a stabilising effect on the binding of the cluster to the $TiO_2$ support.

The calculated Pt-$O_{2c}$ bond lengths for the hexagonal facet approach are slightly shorter than those for the square facet approach (see Table 6.1). Moreover, there is also bonding to in-plane surface oxygen atoms resulting in Pt-$O_{3c}$ bonds (bond lengths 2.17 Å and 2.20 Å) for the hexagonal facet approach of the $Pt_{38}$ cluster. Pt-$O_{3c}$ bonds are not present for the square facet approach of the $Pt_{38}$ cluster. The number of Pt atoms bonded to surface $Ti_{5c}$ atoms resulting in formation of Pt-$Ti_{5c}$ bonds is higher for the hexagonal facet approach than the square facet approach. Moreover, there is formation of Pt-$Ti_{5C}$ bonds at the vacancy site for the hexagonal facet approach which are not present for the square facet approach. Thus the number of Pt-O and Pt-Ti bonds is higher for the hexagonal facet approach than the square

facet approach. This suggests stronger $Pt_{38}$ cluster interaction with the support while approaching the support through the hexagonal facet compared to the square facet. The tilted configuration of the $Pt_{38}$ cluster on partially reduced $TiO_2$(110) surface results in shorter Pt-$O_{2C}$ bonds (1.97 Å) than on other $TiO_2$(110) surface and thus also contribute to enhanced binding of the hexagonal facet approach of $Pt_{38}$ on partially reduced $TiO_2$(110) surface.

Comparison of bond lengths of the interacting and the opposite facet with corresponding bond lengths of the optimised free standing $Pt_{38}$ cluster was done. There is bond elongation and distortion of the interacting facet upon adsorption of the $Pt_{38}$ cluster on the partially reduced $TiO_2$(110) surface. The extent of bond elongation on the interacting facet is higher for the hexagonal facet approach on the partially reduced $TiO_2$(110) surface than on the stoichiometric $TiO_2$(110) surface. Similar to adsorption on the stoichiometric $TiO_2$(110) surface, for both hexagonal and square facet approaches the bond lengths on the opposite facets are similar to the bond lengths in the free standing $Pt_{38}$ cluster. This indicates less distortion on the opposite facet.

### 6.7.3 $Pt_{38}$ interaction with hydroxylated $TiO_2$(110)

On the hydroxylated surface the binding energy of the $Pt_{38}$ cluster for both the hexagonal and the square facet approach are weakly exothermic compared to binding on the stoichiometric and the partially reduced $TiO_2$(110) surface. This suggests the rutile $TiO_2$(110) surface should be dehydrogenated prior to depositing metal nanoparticles. A destabilising effect on the binding energy of small $Pt_n$ (Cai et al., 2013; Rieboldt et al., 2014) and $Au_n$ (Matthey et al., 2007) clusters on the hydroxylated $TiO_2$(110) surface has been observed previously. For approach of the cluster to the stoichiometric and partially reduced $TiO_2$(110) surfaces through the square facet, the binding energy of the cluster is more stable than on hydroxylated $TiO_2$(110): stoichiometric $TiO_2$(110) more stable by 2.55 eV and partially reduced $TiO_2$(110) more stable by 3.37 eV. Similarly, for the hexagonal facet approach binding on stoichiometric $TiO_2$(110) and partially reduced $TiO_2$(110) surface is more stable than on hydroxylated $TiO_2$(110) by 1.94 eV and 8.55 eV respectively. The implication of higher stability of the $Pt_{38}$ cluster on the stoichiometric and partially reduced $TiO_2$(110) surfaces is that deposition of the $Pt_{38}$ cluster on the hydroxylated $TiO_2$(110) surface will lead to dehydroxylation of the surface. The dehydroxylation process is expected to result in $Pt_{38}$ deposited partially reduced $TiO_2$(110) surface since it is the most stable adsorption state.

The most stable binding energy of -0.50 eV for the $Pt_{38}$ cluster in the present study is more exothermic than the calculated binding energy of -0.11 eV for a $Pt_{11}$ cluster (Cai et al., 2013) and less exothermic than –4.52 eV calculated for a $Pt_8$ cluster (Rieboldt et al., 2014b). The difference in binding energy between the study by Cai et al. (2013) and Rieboldt et al. (2014b) may originate from the different pseudopotentials and thickness of $TiO_2$ slab. Cai et al. (2013) utilises ultrasoft pseudopotentials, RPBE functional and a two tri-layer thick $TiO_2$(110) slab whilst Rieboldt et al. (2014b) utilises projector augmented wave pseudopotentials, PBE functional and a four tri-layer thick $TiO_2$(110) slab. There is minimal contact between the $Pt_{38}$ cluster and the hydroxylated $TiO_2$(110) surface in the present study hence the weak binding energy of -0.50 eV, whereas for the small $Pt_8$ cluster on hydroxylated $TiO_2$(110) surface in the study by Rieboldt et al. (2014b) the cluster adopts a two dimensional geometry which results in maximum contact between the $Pt_{38}$ cluster and hydroxylated support.

The adsorption structure for approach through the hexagonal facet is slightly tilted to allow for maximisation of contact between the cluster and the support (see Figure 6.4). For approach through the square facet the adsorption structure is such that the cluster is interacting weakly with the support as can be inferred from the calculated Pt-O and Pt-Ti bond lengths reported in Table 6.1. As observed for adsorption on the stoichiometric and partially reduced $TiO_2$(110) surfaces, there is structural distortion of the support in the contact region resulting in 0.57 Å elevation out of plane relative to the (110) surface towards the approaching $Pt_{38}$ cluster for the Ti bonded to a Pt atom of the interacting facet (see Figure 6.4). For approach through the hexagonal facet, one Pt atom of the facet is bonded to a surface Ti atom with a Pt-Ti bond of 2.55 Å whilst for approach through the square facet there is not such formation of Pt-Ti bonds since the two closest Pt atoms to the surface have Pt-Ti bond lengths of 4.66 Å and 4.30 Å. This further strengthens the observation that the number of Pt-Ti bonds is vital in stabilising the binding of the $Pt_{38}$ cluster to the support.

The calculated Pt-$O_{2c}$ bond lengths for the square facet approach are longer than those calculated for the hexagonal facet approach (see Table 6.1). Interestingly the calculated Pt-$O_{2c}$ bond lengths for both the hexagonal (2.11 Å, 2.15 Å and 2.41 Å) and the square facet (3.17 Å and 2.26 Å) approach on the hydroxylated $TiO_2$(110) surface are longer than those calculated on the most stable adsorption structures on stoichiometric (2.08 Å, 2.07 Å and 2.10 Å) and the partially reduced $TiO_2$(110) (1.97 Å). This may imply that the Pt-O bonds on the hydroxylated $TiO_2$(110) surface are weaker than those on the stoichiometric and the partially reduced $TiO_2$ (110) surface hence resulting in a weaker binding energy on the hydroxylated $TiO_2$(110) surface. The calculated Pt-H bond lengths are longer than 2.10 Å which is the longest calculated Pt-$O_{2c}$ bond length on the partially reduced and stoichiometric $TiO_2$(110)

surfaces. This indicates that the cluster is optimised a distance further away from the surface on the hydroxylated $TiO_2$(110) surface. The calculated O-H bond distances for both the hexagonal and square facet approach are similar to the O-H bond distance in the optimised hydroxylated support. This shows that the interaction between the $Pt_{38}$ cluster and the hydroxylated support does not alter the O-H bond lengths of the surface OH groups.

For both hexagonal and square facet approaches there is bond elongation on the interacting facet bond lengths albeit of a lesser extent compared to that on the stoichiometric and partially reduced $TiO_2$(110) surfaces. This is further evidence of the weak interaction between the hydroxylated support and the $Pt_{38}$ cluster. Similarly, for both the square and hexagonal facet approach the bond lengths on the opposite facet are not changed relative to those of the optimised free standing $Pt_{38}$ cluster.

## 6.7.4 Electronic structure analysis

Electronic structure analysis calculations were performed on the lowest energy adsorption structure on each support, i.e. square facet approach on the stoichiometric $TiO_2$(110) surface and hexagonal facet approach on both the partially reduced and hydroxylated $TiO_2$(110) surfaces.

### 6.7.4.1 Charge density difference

On all the different $TiO_2$(110) surfaces, there is charge redistribution in the contact region between the $Pt_{38}$ cluster and the support (see Figure 6.6). The charge redistribution is indicative of the formation of strong bonds between the support and the $Pt_{38}$ cluster. This conclusion is consistent with previous studies for the adsorption of a $Pt_4$ cluster on the stoichiometric $TiO_2$(110) surface (Ammal & Heyden, 2011; Jiang et al., 2012). On the stoichiometric and hydroxylated $TiO_2$(110) surfaces the bulk of the charge redistribution is localised within the contact region with minimal charge redistribution to the rest of the cluster. On the contrary, for the $Pt_{38}$ cluster adsorbed on the partially reduced $TiO_2$(110) surface, charge loss from the rest of the atoms of the $Pt_{38}$ cluster is greater than for the case on the other supports.

On all the different supports there is charge accumulation along the Pt-$Ti_{5c}$ bonds as represented by the yellow isosurface. This observation is consistent with previous results on

smaller Pt clusters (Ammal & Heyden, 2011; Jiang et al., 2012). The accumulation of charge along the Pt-Ti bonds from the charge density difference plots is indicative of formation of Pt-Ti bonds. This is in agreement with experimental observations of the formation of Pt-Ti bonds for Pt supported on $TiO_2$ catalyst (Timperman et al., 2010a; Vogel et al., 2010: Timperman et al., 2010b Lewera et al., 2011).

From the zoomed view of the charge density difference plot of the $Pt_{38}$ cluster on partially reduced $TiO_2$(110) surface (see Figure 6.7) it is observed that there is charge accumulation around the central Pt atom of the interacting hexagonal facet. This is further indication of the formation of Pt-Ti bonds between the central Pt atom of the interacting hexagonal facet and the Ti atoms at the vacancy site on the surface. Formation of Pt-Ti bonds at the vacancy site stabilises the binding energy for the hexagonal facet approach of the $Pt_{38}$ cluster on partially reduced $TiO_2$(110) surface.

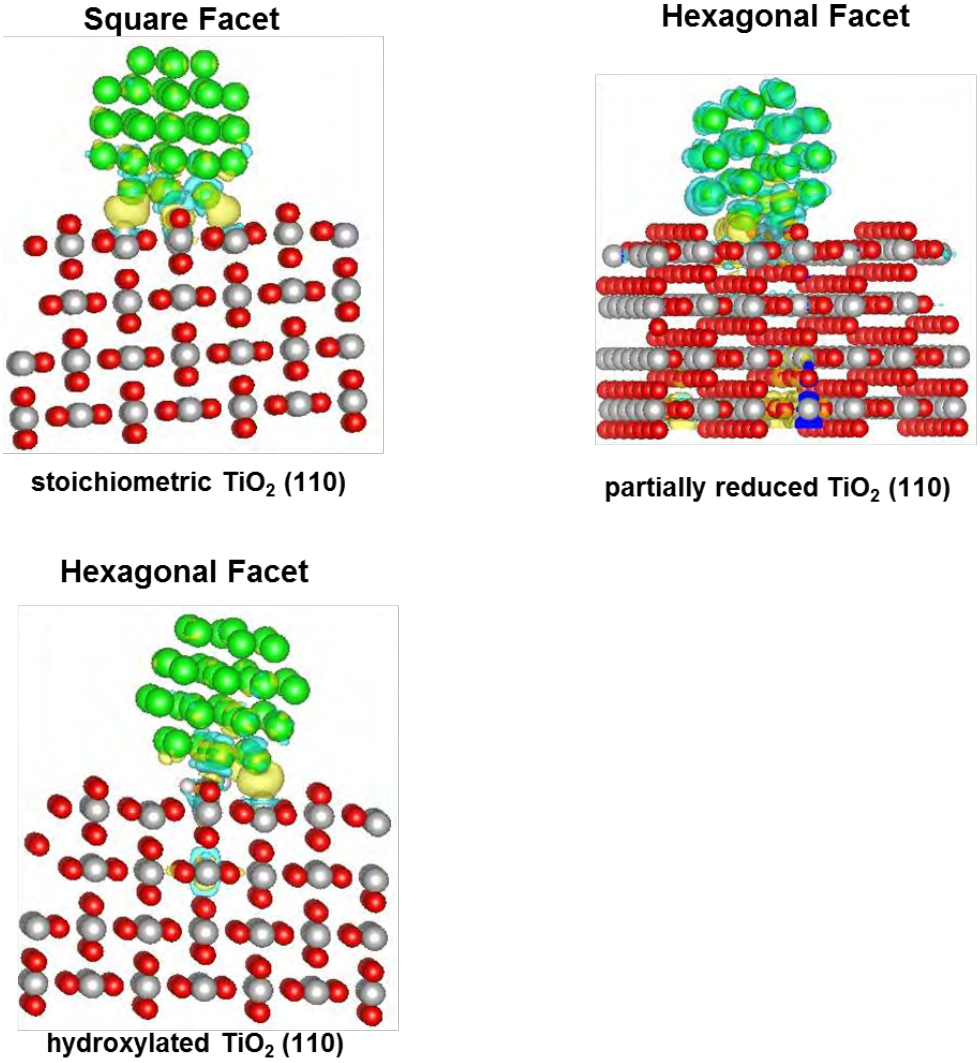


Figure 6.6: Charge density difference plots on lowest energy adsorption structures: $Pt_{38}$ on stoichiometric $TiO_2$(110), $Pt_{38}$ on partially reduced $TiO_2$(110) and $Pt_{38}$ on hydroxylated $TiO_2$(110).

Isosurface at 0.0025 e/ Å$^3$. Isosurface key: blue colour represents charge depletion and yellow colour represent charge accumulation.

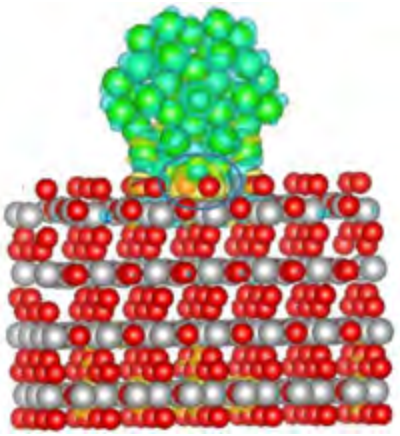

Figure 6.7: Charge accumulation at the vacancy site indicating formation of Pt-Ti bonds at the vacancy site for the $Pt_{38}$ cluster adsorbed on the partially reduced $TiO_2$(110) surface.

### 6.7.4.2 Bader charge analysis

Table 6.2 summarises the net charge transfer upon adsorption of the $Pt_{38}$ cluster on the different $TiO_2$(110) surfaces.

Table 6.2: Change in the charge on the platinum cluster (Δq overall) and on the facet facing the support (Δq interacting facet) based on Bader charge analysis.

| Substrate | Binding energy (eV) | Δq overall (e) | Δ q interacting facet (e) |
|---|---|---|---|
| stoichiometric $TiO_2$ (110) | -2.73 | -0.25 | -0.25 |
| partially reduced $TiO_2$ (110) | -9.05 | -6.20 | -0.75 |
| hydroxylated $TiO_2$ (110) | -0.50 | -0.22 | -0.15 |

The Bader charge analysis of the partially reduced $TiO_2$(110) surface indicates that the Ti atoms adjacent to the oxygen vacancy site have a positive charge of 2.67 e, this result is in agreement with a previous study by Morgan & Watson (2009) where the charge due to the defect peak on partially reduced $TiO_2$(110) was found localised on adjacent Ti atoms to the vacancy site with a formal charge of $Ti^{3+}$.

On all the different supports there is overall net charge transfer from the $Pt_{38}$ cluster to the support. The highest quantity of charge transfer is for the $Pt_{38}$ cluster adsorbed on the partially reduced $TiO_2$(110) surface. The net charge transfer of 0.25 e and 0.22 e transferred from the

$Pt_{38}$ cluster adsorbed on the stoichiometric and the hydroxylated $TiO_2$(110) surfaces respectively is lower than the charge transfer from smaller $Pt_n$ (n = 1-8) clusters which is in the order of 0.50 e (Çelik et al., 2010; Ammal & Heden, 2011; Jiang et al., 2012). This indicates that on the stoichiometric and hydroxylated $TiO_2$(110) surfaces net charge transfer does not increase with cluster size. This is because as cluster size increases there fewer atoms in contact with the support compared to smaller clusters.

On the partially reduced $TiO_2$(110) surface the net charge transfer of 6.20 e from the $Pt_{38}$ cluster is higher than the charge loss calculated in previous studies for smaller $Pt_n$ (n = 1-8) clusters (Çelik et al., 2010; Ammal & Heden, 2011). The higher quantity of charge transfer for the $Pt_{38}$ cluster adsorbed on the partially reduced $TiO_2$(110) surface is indication that there might be overall true charge transfer from the cluster to the support to stabilise the vacancy site which has missing bonds. The small charge transfer for adsorption of the $Pt_{38}$ cluster on stoichiometric and hydroxylated $TiO_2$(110) surfaces suggests that electron redistribution upon adsorption is dominant over true electron transfer.

The atom-resolved change in Bader charge analysis indicates that on all the different supports Ti atoms bonded to Pt atoms donate charge upon adsorption. Similarly, on all supports there is an overall net charge loss from the interacting facet of the cluster. However, the atom-resolved Bader charge partitioning for the atoms of the interacting facet indicate that not all Pt atoms of the facet donate or lose charge. On the stoichiometric $TiO_2$(110) surface the Pt atom forming the shortest Pt-$Ti_{5c}$ bond (2.50 Å) gains charge of 0.31 e. For adsorption on the partially reduced $TiO_2$(110) surface, all Pt atoms of the interacting facet of the $Pt_{38}$ cluster except the central Pt atom on the hexagonal facet interacting with the support lose total combined charge of 0.99 e. The central Pt atom on the interacting hexagonal facet, which occupies the vacant site on the surface and is bonded to two Ti atoms at the vacant site gains charge of 0.25 e. Jiang et al. (2012) observed overall charge transfer to small $Pt_n$ clusters (n = 1-4) on partially reduced $TiO_2$(110), whilst for larger cluster $Pt_n$ sizes (n = 5-8) there was overall charge loss from the cluster with charge transferred only to the single atom occupying the vacancy site on the surface.

On the hydroxylated $TiO_2$(110) surface there is polarisation of the hexagonal facet interacting with the support. The 3 Pt atoms aligned and bonding to the central bridge row of oxygen atoms bearing the two OH's lose a combined total charge of 0.61 e. The Pt atoms at the end of the hexagonal facet bonding to the surface $Ti_{5c}$ atoms gain total combined charge of 0.41 e, whist the Pt atoms at the end of the hexagonal facet which is furthest away from the surface and not bonding to the surface gain total combined charge of 0.05 e.

The extent of charge redistribution to the opposite facet not directly interacting with the support varies with the support. On the stoichiometric $TiO_2$(110) surface the total net charge gain on the opposite facet is 0.10 e despite an overall charge loss from the $Pt_{38}$ cluster. This indicates polarisation of the adsorbed cluster with different charge on the interacting facet and opposite facet. On the hydroxylated $TiO_2$(110) surface there is no net overall charge transfer to or from the opposite facet. The combined total charge loss from the opposite facet for the $Pt_{38}$ cluster adsorbed on the partially reduced $TiO_2$(110) surface is 1.17 e indicating no polarisation between the interacting and opposite facet. Thus, the effect of the cluster-support interaction on charge transfer appears localised on the hydroxylated $TiO_2$(110) surface whilst the effect is not localised on the partially reduced and stoichiometric $TiO_2$(110) surfaces. On the stoichiometric and partially reduced $TiO_2$(110) surfaces there is substantial charge loss from the opposite facet not directly interacting with the support.

The quantity of charge transfer to the surface oxygen atoms bonded to the $Pt_{38}$ cluster also varies with the $TiO_2$(110) surface. On the stoichiometric $TiO_2$(110) surface all the $O_{2c}$ atoms bonded to Pt atoms gain charge with a combined total charge of 0.29 e. On the partially reduced $TiO_2$(110) surface both the $O_{2c}$ and the $O_{3c}$ surface oxygen atoms bonded to the $Pt_{38}$ cluster lose charge with a combined total charge loss of 0.10 e. For adsorption onto the hydroxylated $TiO_2$(110) surface one of the OH bonded to the $Pt_{38}$ cluster lose 0.01 e and the other OH bonded to the cluster gain 0.02 e. The other surface O bridge atom in the same row with the two OH's and bonded to the $Pt_{38}$ cluster gain 0.06 e of charge. The smaller quantity of charge transfer to the oxygen atoms on the hydroxylated $TiO_2$(110) surface can be attributed to the fact that the cluster is optimised to a distance further away from the surface relative to the Pt-$O_{2c}$ bond distances on the other surfaces. This means that contact between the $Pt_{38}$ cluster and the hydroxylated support is minimal thereby affecting charge transfer between the cluster and the hydroxylated $TiO_2$(110) surface.

A correlation exists between the binding energy of the $Pt_{38}$ cluster and the net charge transfer from the interacting facet of the $Pt_{38}$ cluster, higher charge loss from the interacting facet corresponds to highly exothermic binding energy.

### 6.7.4.3 PDOS analysis

The PDOS analysis was performed to gain further insight into changes to the electronic structure of the support and the $Pt_{38}$ cluster upon adsorption. The density of states for the support material was projected onto the valance s states for hydrogen atoms, p states for the oxygen atoms and 3d states for titanium atoms. For the $Pt_{38}$ cluster the density of states was projected onto the valence 5d states. The PDOS of the support and the $Pt_{38}$ cluster before and after adsorption of the $Pt_{38}$ cluster on the support are compared in order to identify changes brought about by the adsorption process.

The PDOS of the stoichiometric $TiO_2$(110) surface consists of a band gap of 2.10 eV with no states in the band gap (See Figure 6.8 a) The PDOS profile and the band gap are similar to previous studies where a band gap of 2.01 eV was calculated (Çelik et al., 2010; Zhang & Alexandrova, 2011; Zhang et al., 2015). After adsorption of the $Pt_{38}$ cluster on the stoichiometric $TiO_2$(110) surface the PDOS profile of the support retains similar features to the PDOS before adsorption except that the band gap has narrowed down to approximately 1.50 eV. A similar band gap narrowing of the stoichiometric $TiO_2$(110) surface has been observed upon adsorption of small $Pt_n$ (n = 1-4) clusters (Çelik et al., 2010) and small $Pd_n$ (n = 1-4) clusters (Zhang & Alexandrova, 2011). Thus the interaction of the $Pt_{38}$ cluster with the stoichiometric $TiO_2$(110) results in a reduced band gap of the support, and consequently the support induces new states in the Pt 5d PDOS of the $Pt_{38}$ cluster (see Figure 6.9 b). The changes to the PDOS of the support together with the concomitant changes to the PDOS of the $Pt_{38}$ cluster are indicative of bond formation between the cluster and support.

The PDOS of the partially reduced $TiO_2$(110) surface consists of a peak in the band gap located approximately 0.8 eV below the conduction band (see Figure 6.8 b) consistent with previous studies (Morgan & Watson, 2007; Calzado et al., 2008; Çelik et al., 2010; Zhang et al., 2015). Upon adsorption of the $Pt_{38}$ cluster, the PDOS of the partially reduced $TiO_2$(110) surface resembles the PDOS before adsorption except that the peak in the band gap disappears. The band gap remains identical to before adsorption at 1.6 eV. For smaller $Pt_n$ (n = 1-4) clusters (Çelik et al., 2010) a reduction in band gap dependent on cluster size was observed for adsorption on the partially reduced $TiO_2$(110) surface.

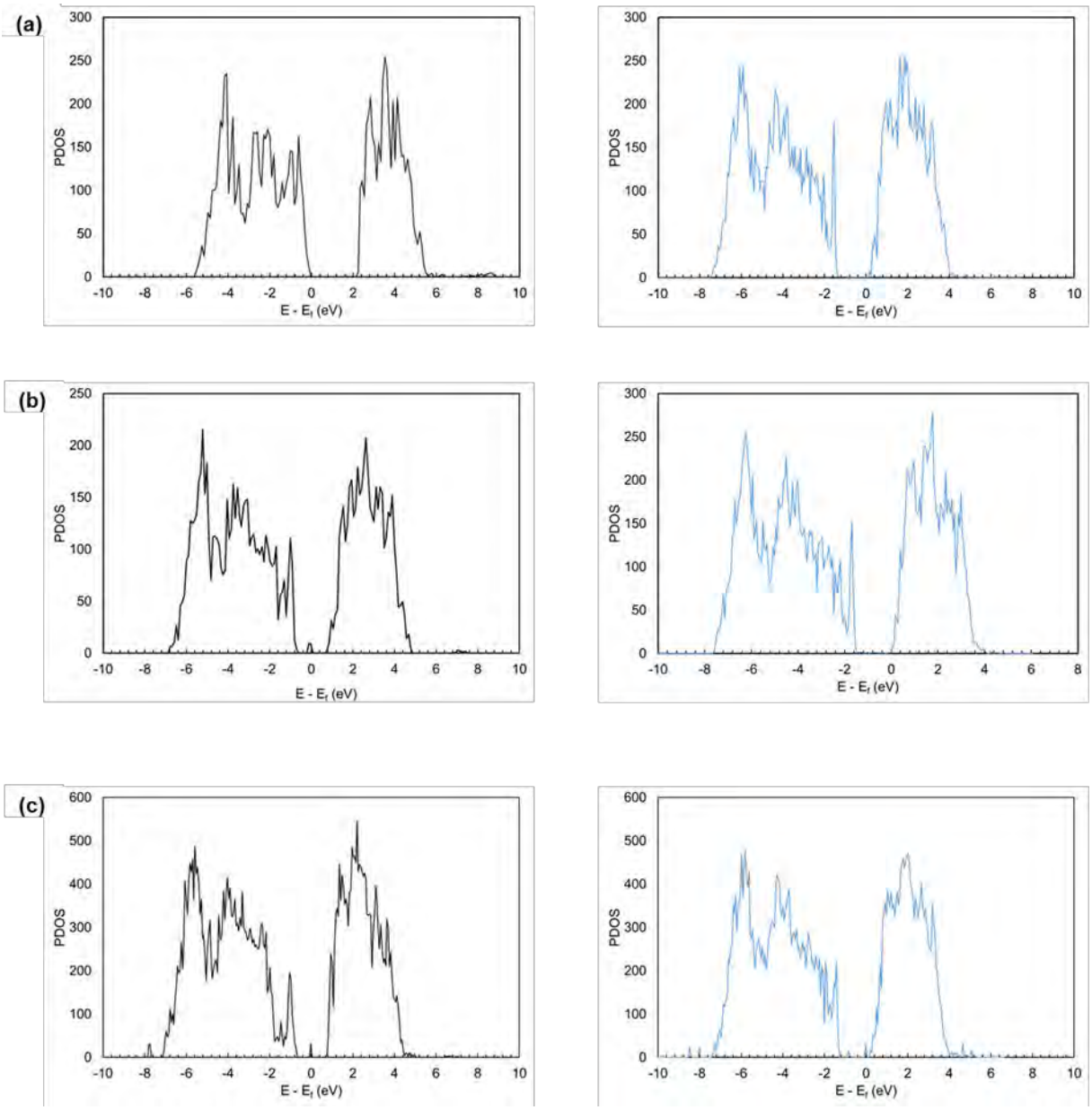


Figure 6.8: PDOS for the support material before adsorption (left) and after adsorption (right) of: (a) stoichiometric $TiO_2$(110) surface, (b) partially reduced $TiO_2$(110) surface and (c) hydroxylated $TiO_2$ (110) surface. The energy scale is relative to the Fermi level.

The $Pt_{38}$ cluster adsorbate on the partially reduced $TiO_2$(110) surface results in the disappearance of the peak in the band gap, and concomitantly the Pt 5d PDOS of the $Pt_{38}$ cluster consists of new states which were not present before adsorption (see Figure 6.9 c). Changes to both the PDOS of the support and the $Pt_{38}$ cluster indicates orbital interaction between the cluster and support leading to formation of strong bonds between the cluster and support.

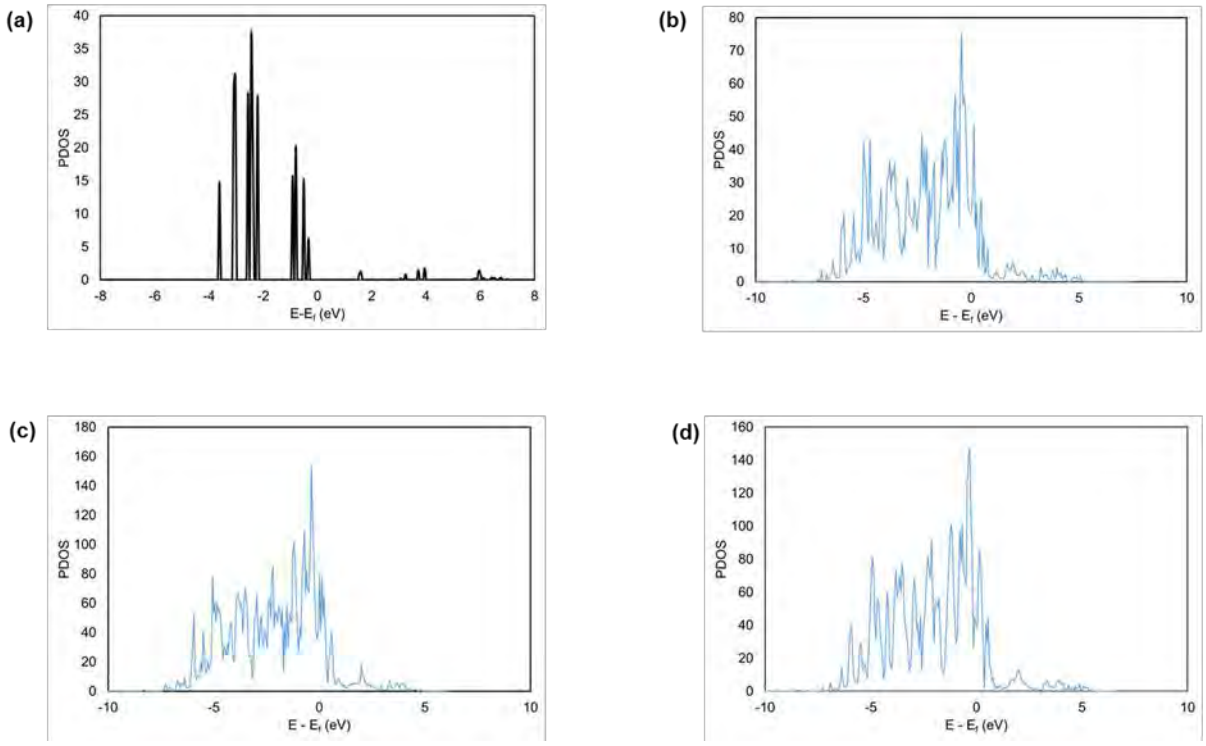


Figure 6.9: PDOS of the Pt 5d states: (a) unsupported $Pt_{38}$ cluster, (b) $Pt_{38}$ on stoichiometric $TiO_2$(110), (c) $Pt_{38}$ on partially reduced $TiO_2$(110) and (d) $Pt_{38}$ on hydroxylated $TiO_2$(110). The energy scale is relative to the Fermi level.

The free support of hydroxylated $TiO_2$(110) surface consists of a band gap of 1.6 eV with a peak in the band gap which is located at the Fermi level similar to the PDOS of the partially reduced $TiO_2$(110) surface. In previous calculations a peak has been observed in the band gap of the hydroxylated $TiO_2$(110) surface (Di Valentin & Pacchioni, 2006; Mao et al., 2013; Zhang et al., 2015). After adsorption of the $Pt_{38}$ cluster on the hydroxylated $TiO_2$(110) surface, the PDOS of the support retains similar features to before adsorption with some changes occurring in the band gap. The band gap is still 1.6 eV but now consists of two peaks, there is a peak at the bottom of the conduction band with reduced intensity relative to the peak at the Fermi level for the bare support and a smaller peak appears 0.4 eV above the bottom of the valence band. The appearance of the new peaks and reduction of peak intensity within the band gap of the support together with the new states in the PDOS of the $Pt_{38}$ cluster (see Figure 6.9 d) are indicative of bond formation between cluster and support.

Adsorption of the $Pt_{38}$ cluster on the different $TiO_2$(110) surfaces results in transformation of the PDOS of the $Pt_{38}$ cluster from discrete to continuous (see Figure 6.9). A continuous PDOS with a continuous d-band is characteristic of metallic properties, hence the adsorbed $Pt_{38}$ cluster on the different $TiO_2$(110) surfaces have metallic characteristics. On the contrary, for

smaller $Pt_n$ (n =1-4) clusters, adsorption of the clusters does not result in metallisation of the cluster as the PDOS of the clusters remain discrete (Çelik et al., 2010).

#### 6.7.4.4 d-band centre analysis

In the present study the d-band centre, d-band width and the d-band filling are the reactivity descriptors used to assess the effect of the interaction of the $Pt_{38}$ cluster with the different support materials. Similar to analysis for charge density difference, Bader and PDOS analysis for the reactivity descriptors is performed only for the lowest energy structures on the various surfaces.

There is a downward shift in the d-band centre of the $Pt_{38}$ cluster upon adsorption on the different supports relative to the d-band centre of the free standing $Pt_{38}$ cluster (see Table 6.3). The downward shift of the d-band centre upon adsorption indicates that the $Pt_{38}$ cluster interacts with the support through the d-band. The extent of shift of the d-band centre is dependent on the surface composition and follows the order: partially reduced $TiO_2$(110) (0.15 eV) > stoichiometric $TiO_2$(110) (0.10 eV) > hydroxylated $TiO_2$(110) (0.05 eV). A linear correlation exists between the binding energy and the shift in the d-band centre of the entire $Pt_{38}$ cluster bonded to the different supports. Despite the highly exothermic binding energy of the $Pt_{38}$ cluster on the partially reduced $TiO_2$(110) surface relative to adsorption on the other surfaces, the difference in d-band centre shift between the three is modest. The modest shift in d-band centre indicates that the highly exothermic binding energy on the partially reduced $TiO_2$(110) surface is not only due to the stronger interaction through the d-band but is also due to stabilisation of the high energy surface monovacancy.

The d-band filling is identical for the $Pt_{38}$ cluster adsorbed onto the different surfaces indicating almost ideal filling, the ideal d-band filling in Pt is 0.93 (Kitchin et al., 2004). The d-band filling for the free standing $Pt_{38}$ cluster is higher than the ideal filling indicating a shift of the s-band energy versus the d-band energy as a function of Pt particle size.

On all supports there is a shift in d-band centre for the entire $Pt_{38}$ cluster, the facet interacting with the support and the opposite facet relative to the d-band centre of the free standing $Pt_{38}$ cluster. The shifts indicate that the effect of the interaction between the support and the cluster is not localised only to the facet interacting with the support but affects the entire $Pt_{38}$ cluster. On all supports but the hydroxylated $TiO_2$(110) support, the d-band centre of the interacting

facet of the $Pt_{38}$ cluster is typically shifted to more negative energies relative to the d-band centre of the same facet in the free standing $Pt_{38}$ cluster.

Table 6.3: Calculated d-band centre relative to Fermi level, d-band width and the d-band filling for the $Pt_{38}$ cluster, the interacting and the opposite facet on the different $TiO_2$(110) supports.

| | $E_{ads}$ (eV) | $\varepsilon_d - \varepsilon_F$ (eV) | $f_d$ | $w_d$ (eV) |
|---|---|---|---|---|
| **$Pt_{38}$ free unsupported** | | | | |
| overall cluster | | -1.96 | 0.98 | 2.56 |
| square facet | | -1.92 | 0.97 | 2.56 |
| hexagonal facet | | -2.21 | 0.98 | 2.92 |
| **$Pt_{38}$ on stoichiometric $TiO_2$(110)** | | | | |
| overall cluster | -2.73 | -2.06 | 0.87 | 2.94 |
| interacting facet (square) | | -2.17 | 0.86 | 3.13 |
| opposite facet (square) | | -1.90 | 0.87 | 2.70 |
| **$Pt_{38}$ on partially reduced $TiO_2$(110)** | | | | |
| overall cluster | -9.05 | -2.11 | 0.87 | 2.97 |
| Interacting facet (hexagonal) | | -2.25 | 0.87 | 3.15 |
| opposite facet (hexagonal) | | -1.90 | 0.87 | 2.70 |
| **$Pt_{38}$ on hydroxylated $TiO_2$(110)** | | | | |
| overall cluster | -0.50 | -2.01 | 0.86 | 2.91 |
| interacting facet (hexagonal) | | -1.97 | 0.87 | 2.86 |
| opposite facet (hexagonal) | | -1.85 | 0.87 | 2.71 |

Of vital importance to the reactivity of the supported $Pt_{38}$ cluster is the reactivity of the facets of the cluster which are available and exposed to reactants. This is assessed by shift in the d-band centre of the opposite facet since this facet is taken as a representative of exposed facets to adsorbate molecules. Interestingly the same d-band centre of -1.90 eV is calculated for the opposite facet of the $Pt_{38}$ cluster adsorbed onto the stoichiometric and the partially reduced $TiO_2$(110) surfaces. The extent of d-band centre upward shift of the opposite facet follows the order: hydroxylated $TiO_2$(110) (0.35 eV) > partially reduced $TiO_2$(110) (0.31 eV) > stoichiometric $TiO_2$(110) (0.02 eV). There is a small upward shift of 0.02 eV of the d-band centre of the opposite facet of the $Pt_{38}$ cluster adsorbed on the stoichiometric $TiO_2$(110) relative to the free standing $Pt_{38}$ cluster d-band centre of the square facet. The small shift in d-band

centre indicates that the reactivity of the free unsupported $Pt_{38}$ cluster will be identical to the reactivity of a $Pt_{38}$ cluster (approach through the square facet) supported on the stoichiometric $TiO_2$(110) surface.

The higher extent of shift of the d-band centre towards more positive energies for the opposite hexagonal facets of the $Pt_{38}$ cluster adsorbed on the partially reduced and hydroxylated $TiO_2$(110) surfaces indicate different reactivity towards adsorbate molecules of the supported $Pt_{38}$ cluster to that of the free unsupported $Pt_{38}$ cluster. The binding of adsorbate molecules with the opposite facet of the $Pt_{38}$ cluster adsorbed on the partially reduced and hydroxylated $TiO_2$(110) surfaces is expected to be weaker than on the free standing unsupported $Pt_{38}$ cluster. The reactivity of the $Pt_{38}$ cluster adsorbed onto the partially reduced and hydroxylated $TiO_2$(110) surfaces is expected to be identical due to the similar shift in d-band centre of the opposite facet compared to the d-band centre of the same facet in the free standing $Pt_{38}$ cluster.

## 6.8 Conclusions

The binding energy of the $Pt_{38}$ cluster on the different surfaces follows the order: partially reduced $TiO_2$(110) > stoichiometric $TiO_2$(110) > hydroxylated $TiO_2$(110). The surface hydroxyl groups on the hydroxylated $TiO_2$(110) surface have a destabilising effect on the binding energy of the $Pt_{38}$ cluster. Deposition of the $Pt_{38}$ cluster on the hydroxylated $TiO_2$(110) is expected to result in dehydrogenation of the surface forming the highly stable $Pt_{38}$ cluster bound on the partially reduced $TiO_2$(110) surface. A surface oxygen bridge vacancy site on the partially reduced $TiO_2$(110) has a stabilising effect on the binding energy of the $Pt_{38}$ cluster on the rutile $TiO_2$(110) surface. The binding energy of the $Pt_{38}$ cluster on the partially reduced $TiO_2$(110) is stabilised through stabilisation of the vacancy through interaction with the cluster by electron donation, formation of Pt-Ti bonds at the vacancy site and formation of Pt-O bonds between the $Pt_{38}$ cluster and the in-plane oxygen atoms ($O_{3C}$) on the surface. Maximisation of the Pt-Ti surface bonds has a stabilising effect on the binding energy of the $Pt_{38}$ cluster on the $TiO_2$(110) surfaces.

The electronic structure of the $Pt_{38}$ cluster is affected upon interaction with the different supports, and the changed electronic structure also affects the reactivity of the supported $Pt_{38}$ cluster. The effect of the cluster-support interaction is not localised but extends to the entire $Pt_{38}$ cluster. This is manifested by changes to the d-band centre of the entire $Pt_{38}$ cluster, the interacting facet and the opposite facet to the one interacting with the support relative to the

d-band centre of the free standing $Pt_{38}$ cluster. The binding energy of the $Pt_{38}$ cluster on the different supports was found to correlate with the change in the d-band centre of the adsorbed $Pt_{38}$ cluster. In addition, the binding energy was found to also correlate with the net amount of charge transfer from interacting facet of the $Pt_{38}$ cluster.

The reactivity of the $Pt_{38}$ cluster supported on the stoichiometric $TiO_2$(110) surface towards adsorbate molecules is expected to bear similar resemblance to that of the unsupported $Pt_{38}$ cluster. This is due to the identical d-band centre of the opposite facet on the stoichiometric $TiO_2$(110) surface with the d-band centre of the same facet of the unsupported $Pt_{38}$ cluster. The reactivity of the $Pt_{38}$ cluster supported on the partially reduced and hydroxylated $TiO_2$(110) surfaces is expected to be different to that of the unsupported $Pt_{38}$ cluster. This is due to the similar change in d-band centre of the opposite facet of the $Pt_{38}$ cluster adsorbed on the two surfaces relative to the d-band centre of the same facet in the free standing $Pt_{38}$ cluster. On both supports the d-band centre of the opposite facet is shifted upward towards positive energy values.

## 6.9 References

Ammal, S.C. & Heyden, A. (2010) Modeling the noble metal / $TiO_2$ (110) interface with hybrid DFT functionals: A periodic electrostatic embedded cluster model study. *J. Chem. Phys.* **133**, 164703-164718.

Ammal, S.C. & Heyden, A. (2011) Nature of $Pt_n/TiO_2$ (110) interface under water-gas shift reaction conditions: A constrained ab initio thermodynamics study. *J. Phys. Chem. C*. **115**, 19246-19259.

Bader, R.F.W. (1991) A quantum theory of molecular structure and its applications. *Chem. Rev.* **91**, 893-928.

Bikondoa, O., Pang, C.L., Ithuin, R., Muryn, C.A., Onishi, H. & Thornton, G. (2006) Direct visualization of defect-mediated dissociation of water on $TiO_2$ (110). *Nat. Mater*. **5**, 189-192.

Blöchl, P.E. (1994) Projector augmented-wave method. *Phys. Rev. B* **50**, 17953-17979.

Bonanni, S., Aït-Mansour, K., Brune, H. & Harbich, W. (2011) Overcoming the strong metal-support interaction state: CO oxidation on $TiO_2$ (110)-supported Pt nanoclusters. *ACS Catal.* **1**, 385-389.

Bonanni, S., Aït-Mansour, K., Harbich, W. & Brune, H. (2012) Effect of the $TiO_2$ reduction state on the catalytic CO oxidation on deposited size-selected Pt clusters. *J. Am. Chem. Soc*. **134**, 3445-3450.

Brookes, I.M., Muryn, C.A.& Thornton, G. (2001) Imaging water dissociation on $TiO_2$ (110). *Phys. Rev. Lett.* **87**, 266103-266107.

Bruix, A., Rodriguez, J.A., Ramírez, P.J., Senanayake, S.D., Evans, J., Park, J.B., Stacchiola, D., Liu, P., Hrbek, J. & Illas, F. (2012) A new type of strong metal-support interaction and the production of $H_2$ through the transformation of water on $Pt/CeO_2$ (111) and $Pt/CeO_x/TiO_2$ (110) catalysts. J. Am. Chem. Soc. **134**, 8968-8974.

Burdett, K., Hughbanks, T., Miller, G.J., Richardson Jr., J.W. & Smith, J.V. (1987) Structural-electronic relationships in inorganic solids: powder neutron diffraction studies of the rutile and anatase polymorphs of titanium dioxide at 15 and 295 K. *J. Am. Chem. Soc.* **109**, 3639-3646.

Cai, Q., Wang, X. & Wang, J.G. (2013) Distinction between supported Au and Pt catalysts for CO oxidation: insights from DFT study. *J. Phys. Chem. C* **117**, 21331-21336.

Çakir, D. & Gülseren, O. (2012) Adsorption of Pt and bimetallic PtAu clusters on the partially reduced rutile (110) $TiO_2$ surface: A first-principles study. *J. Phys. Chem. C* **116**, 5735-5746.

Calzado, C.J., Hernández, N.C. & Sanz, J.F. (2008) Effect of on-site coulomb repulsion term U on the band-gap states of the reduced rutile (110) $TiO_2$ surface. *Phys. Rev. B* **77**, 045118-045128.

Campbell, C.T. (2012) Electronic pertubations. *Nat. Chem.* **4**, 597-598.

Çelik, V., Ünal, H., Mete, E. & Ellialtioğlu, Ş. (2010) Theoretical analysis of small Pt particles on rutile $TiO_2$ (110) surfaces. *Phys. Rev. B* **82**, 205113-205125.

Chen, J., Lim, B., Lee, E.P. & Xia, Y. (2009) Shape-controlled synthesis of platinum nanocrystals for catalytic and electrocatalytic applications. *Nano Today* **4**, 81-95.

Chrétien, S. & Metiu, H. (2007a) Density functional study of the interaction between small Au clusters, $Au_n$ (n=1-7) and the rutile $TiO_2$ surface. II. Adsorption on a partially reduced surface. *J. Chem. Phys*. **127**, 244708-244723.

Chrétien, S. & Metiu, H. (2007b) Density functional study of the interaction between small Au clusters, Au n (n = 1-7) and the rutile $TiO_2$ surface. I. Adsorption on the stoichiometric surface. *J. Chem. Phys*. **127**, 084704-084713.

Chrétien, S. & Metiu, H. (2011) Electronic structure of partially reduced rutile $TiO_2$ (110) surface: where are the unpaired electrons located?. *J. Phys. Chem. C* **115**, 4696-4705.

Diebold, U. (2003) The surface science of titanium dioxide. *Surf. Sci. Reports* **48**, 53-229.

Diebold, U., Li, S.C. & Schmid, M. (2010) Oxide surface science. *Annu. Rev. Phys. Chem*. **61**, 129-148.

Di Valentin, C. & Pacchioni, G. (2006) Electronic structure of defect states in hydroxylated and reduced rutile $TiO_2$ (110) surface. *Phys. Rev. Lett*. **97**, 166803-166807.

Dudarev, S.L., Botton, G.A., Savrasov, S.Y., Humphreys, C.J. & Sutton, A.P. (1998) Electron-energy-loss spectra and the structural stability of nickel oxide: An LSDA + U study. *Phys. Rev. B* **57**, 1505-1509.

Elsässer, C., Fähnle, M., Chan, C.T. & Ho, K.M. (1994) Density-functional energies and forces with Gaussian-broadened fractional occupations. *Phys. Rev. B* **49**, 13975-13978.

Fu, C.L. & Ho, K.M. (1983) First-principles calculation of the equilibrium ground-state properties of transition metals: Applications to Nb and Mo. *Phys. Rev. B* **28**, 5480-5486.

Epling, W.S., Peden, C.H.F., Henderson, M.A. & Diebold, U. (1998) Evidence for oxygen adatoms on $TiO_2$ (110) resulting from $O_2$ dissociation at vacancy sites. *Surf. Sci*. **412/413,** 333-343.

Ganduglia-Pirovana, M., Hofmann, A. & Sauer, J. (2007) Oxygen vacancies in transition metal and rare earth oxides: current state of understanding and remaining challenges. *Surf. Sci. Reports* **62**, 219-270.

Henkelman, G., Arnaldsson, A. & Jónsson, H. (2006) A fast and robust algorithm for Bader decomposition of charge density. *Comput. Mater. Sci*. **36**, 354-360.

Henrich, V.E. & Kurtz, R.L. (1981) Surface electronic structure of $TiO_2$: Atomic geometry, ligand coordination, and the effect of adsorbed hydrogen. *Phys. Rev. B* **23**, 6280-6287.

Henrich, V.E., Dresselhaus, G. & Zeiger, H.J. (1976) Observation of two-dimensional phases associated with defect states on the surface of $TiO_2$. *Phys. Rev. Lett*. **36**, 1335-1338.

Huang, S.Y., Gausen, P., Park, S. & Popov, B.N. (2009) Development of a titanium dioxide-supported platinum catalyst with ultrahigh stability for polymer electrolyte membrane fuel cell applications. *J. of Am. Chem. Soc.* **131**, 13898-13899.

Jiang, D., Overbury, S.H. & Dai, S. (2012) Structures and energetics of Pt clusters on $TiO_2$: interplay between metal-metal bonds and metal-oxygen bonds. *J. Phys. Chem. C* **116**, 21880-21885.

Jones, P. & Hockey, J.A. (1971a) Infra-red studies of rutile surfaces Part I. *Trans. Faraday Soc.* **67**, 2669-2678.

Jones, P. & Hockey, J.A. (1971b) Infra-red studies of rutile surfaces- Part 2- hydroxylation, hydration and structure of rutile surfaces. *Trans. Faraday Soc*. **67**, 2679-2678.

Kitchin, J.R., Nørskov, J.K., Barteau, M.A. & Chen, J.G. (2004) Modification of the surface electronic and chemical properties of Pt (111) by subsurface 3d transition metals. *J. Chem. Phys.* **120**, 10240-10246.

Kresse, G. & Furthmüller, J. (1996a) Efficiency of ab-initio total energy calculations for metals and semiconductors using a plane-wave basis set. *Comput. Mater. Sci*. **6**, 15-50.

Kresse, G. & Furthmüller, J. (1996b) Efficient iterative schemes for ab-initio total-energy calculations using a plane wave basis set. *Phys. Rev. B* **54**, 11169-11186.

Kresse, G. & Jourbert, D. (1999) From ultrasoft pseudopotentials to the projector augmented-wave method. *Phys. Rev. B* **59**, 1758-1775.

Kresse, G. & Hafner, J. (1994) Ab initio molecular-dynamics simulation of the liquid-metal-amorphous-semi-conductor transition on germanium. *Phys. Rev. B* **49**, 14251-14269.

Kresse, G. & Hafner, J. (1993) Ab initio molecular dynamics for liquid metals. *Phys. Rev. B* **47**, 558-561.

Lewera, A., Timperman, L., Roguska, A. & Alonso-Vante, N. (2011) Metal-support interactions between nanosized Pt and metal oxides ($WO_3$ and $TiO_2$) studied using X-ray photoelectron spectroscopy. *J. Phys. Chem. C* **115**, 20153-20159.

Mao, X., Lang, X., Wang, Z., Hao, Q., Wen, B., Ren, Z., Dai, D., Zhou, C., Liu, L. & Yang, X. (2013) Band-gap states of $TiO_2$(110): major contribution from surface defects. *Phys. Chem. Lett.* **4**, 3839-3844.

Marković, N.M., Schmidt, T.J., Stamenkovíc, V. & Ross, P.N. (2001) Oxygen reduction reaction on Pt and Pt bimetallic surfaces: a selective review. *Fuel Cells* **1**,105-116.

Matthey, D., Wang, J.G., Wendt, S., Matthiesen, J., Schaub, R., Laegsgaard, E., Hammer, B. & Besenbacher, F. (2007) Enhanced bonding of gold nanoparticles on oxidized $TiO_2$ (110). *Science* **315**, 1692-1696.

Matveev, A.V., Neyman, K.M., Yudamov, I.V. & Rösch, N. (1999) Adsorption of transition metal atoms on oxygen vacancies and regular sites of the MgO(001) surface. *Surf. Sci.* **426**, 123-139.

Monkhorst, H.J. & Pack, J.D. (1976) Special points for Brillouin-zone integrations. *Phys. Rev. B* **13**, 5188-5192.

Morgan, B. & Watson, G.W. (2007) A DFT+U description of oxygen vacancies at the $TiO_2$ rutile (110) surface. *Surf. Sci*. **601**, 5034-5041.

Morgan, B.J. & Watson, G.W. (2007) A DFT+U description of oxygen vacancies at the $TiO_2$ rutile (110) surface. *Surf. Sci.* **601**, 5034-5041.

Morgan, B.J. & Watson, G.W. (2009) A density functional theory + U study of oxygen vacancy formation of the (110), (100), (101), and (001) surfaces of rutile $TiO_2$. *J. Phys. Chem. C* **113**, 7322-7328.

Orita, N. (2010) Generalised gradient approximation + U study for metallization mechanism of Niobium-doped anatase titanium dioxide. *Jpn. J. Appl. Phys*. **9**, 055801-055806.

Perdew, J.P., Chevary, J.A., Vosko, S.H., Jackson, K.A., Pederson, M.R., Singh, D.J. & Fiolhais, C. (1992) Atoms, molecules, solids, and surfaces: applications of the generalized gradient approximation for exchange and correlation. *Phys. Rev. B* **46**, 6671-6686.

Perron, H., Domain, C., Roques, J., Drot, R., Simoni, E. & Catalette, H. (2007) Optimisation of accurate rutile $TiO_2$ (110), (100), (101), (101) and (001) surface models from periodic DFT calculations. *Theor. Chem. Acc.* **117**, 565-574.

Rashkeev, S.N., Lupini, A.R. & Overbury, S.H. (2007) Role of the nanoscale in catalytic CO oxidation by supported Au and Pt nanostructures. *Phys. Rev. B* **76**, 035438-035446.

Rieboldt, F., Helveg, S., Bechstein, R., Lammich, L., Besenbacher, F., Lauristsen, J.V. & Wendt, S. (2014a) Formation and sintering of Pt nanoparticles on vicinal rutile $TiO_2$ surfaces. *Phys. Chem. Chem. Phys*. **16**, 21289-21299.

Rieboldt, F., Vilhelmsen, L.B., Koust, S., Lauritsen, J.V., Helveg, S., Lammich, L., Besenbacher, F., Hammer, B. & Wendt, S. (2014b) Nucleation and growth of Pt nanoparticles on reduced and oxidized rutile $TiO_2$ (110). *J. Chem. Phys*. **141**, 214702-214711.

Sanville, E., Kenny, S.D., Smith, R. & Henkelman, G. (2007) Improved grid-based algorithm for Bader charge allocation. *J. Comput. Chem*. **28**, 899-908.

Schaub, R., Thostrup, P., Lopez, N., Laegsgaard, E., Stensgaard, I., Nørskov, J.K. & Besenbacher, F. (2001) Oxygen vacancies as active sites for water dissociation on rutile $TiO_2$ (110). *Phys. Rev. Lett*. **87**, 266104-266105.

Shibuya, T., Yasuoka, K., Mirbt, S. & Sanyal, B. (2012) A systematic study of polarons due to oxygen vacancy formation at the rutile $TiO_2$ (110) surface by GGA + U and HSE06 methods. *J. Phys.: Condens. Matter* **24**, 435504-435512.

Tait, R.H. & Kasowski, R.V. (1979) Ultraviolet photoemission and low-energy electron diffraction studies of $TiO_2$ (rutile) (001) and (110) surfaces. *Phys. Rev. B* **20**, 5178-5191.

Tang, W., Sanville, E. & Henkelman, G. (2009) A grid-based Bader analysis algorithm without lattice bias. *J. Phys.: Condens. Matter* **21**, 084204-084211.

Tauster, S.J. (1987) Strong metal-support interactions. *Acc. Chem. Res*. **20**, 389-394.

Timperman, L., Lewera, A., Vogel, W. & Alonso-Vante, N. (2010a) Nanostructured platinum becomes alloyed at oxide-composite substrate. *Electrochem. Commun*. **12**, 1772-1775.

Timperman, L., Feng, Y.J., Vogel, W. & Alonso-Vante, N. (2010b) Substrate effect on oxygen reduction electrocatalysis. *Electrochim. Acta* **55**, 7558-7563.

Vogel, W., Timperman, L. & Alonso-Vante, N. (2010) Probing metal substrate interaction of Pt nanoparticles: structural XRD analysis and oxygen reduction reaction. *Appl. Catal., A: General* **377**, 167-173.

Yulikov, M., Sterrer, M., Heyde, M., Rust, H.P., Risse, T., Freund, H.J., Pacchiani, G. & Scagnelli, A. (2006) Binding of single gold atoms on thin MgO(001) films. *Phys. Rev. Lett.* **96**, 146804-146808.

Zhang, D., Yang, M. & Dong, S. (2015) Improving the photocatalytic activity of $TiO_2$ through reduction*. RCS Adv.* **5**, 35661-35666.

Zhang, H. & Banfield, J.F. (1998) Thermodynamic analysis of phase stability on nanocrystalline titania. *J. Mater. Chem* **8**, 2073-2076

# Chapter 7: $Pt_{32}Pd_6$ cluster interaction with Nb-doped $TiO_2$(110) surfaces

## 7.1 Introduction

$TiO_2$ has recently emerged as an alternative support to the preferred carbon support for application in polymer electrolyte fuel cells (PEFC's). The properties of $TiO_2$ which makes it desirable for application in PEFC's are its resistance to corrosion, high mechanical strength and stability (Huang et al., 2010; Wang et al., 2013). Despite its resistance to corrosion and strong stability which are essential features for a durable electrocatalyst support, pure $TiO_2$ is a semiconductor with low conductivity at room temperature. The low conductivity of pure $TiO_2$ is not a desirable quality of an electrocatalyst support since it will result in low performance of the electrocatalyst due to resistance to electron flow through the support. For PEFC application a corrosion resistant and electrically conducting support material is desirable, so that electron conduction is not impeded and thus the electrochemical reactions occurring on the catalytically active material are not affected (Park & Seol, 2007).

Different strategies exist to improve the electrical conductivity of $TiO_2$ such that it can be used as an electrocatalyst support. The conductivity of $TiO_2$ can be improved by partially reducing the oxide to form sub-stoichiometric oxides with high conductivity. The sub-stoichiometric oxides have higher conductivities but are not stable under fuel cell operating conditions since they are oxidised back to the stoichiometric $TiO_2$ which is semiconducting (Chavellier et al., 2012). Other ways of improving the conductivity of $TiO_2$ is through doping with either n-type or p-type dopants (Morris et al., 2000). Doping is considered the preferred method to improve the conductivity of $TiO_2$, because it does not result in changes to the structure of the oxide (Bernasik et al., 1993; Arbiol et al., 2002). n-Type dopants introduces charge to the structure, common n-type dopants for $TiO_2$ are Nb and Ta. p-Type dopants result in electron holes or deficiencies, e.g. doping with Fe, Co and Ni (Dunnill et al., 2012). $TiO_2$ can also be doped with non-metals such as carbon, fluorine, nitrogen and sulphur (Dunnill et al., 2012). A desirable doping element for $TiO_2$ should be acid and corrosion resistant and not leach for application in PEFC's (Chevalier et al., 2012).

Nb is used as an n-type dopant for $TiO_2$. Niobium (Nb) n-type doping is preferred for $TiO_2$ since the ionic size of $Ti^{4+}$ (0.68 Å) and $Nb^{5+}$ (0.70 Å) are similar hence substituting a Nb atom for a Ti atom in the crystal structure of $TiO_2$ is not expected to affect the crystal structure of the oxide (Bernasik et al., 1993; Arbiol et al., 2002; Huang et al., 2010; Wang et al., 2013).

## 7.2 Electronic structure of Nb-doped $TiO_2$

Experimental measurements through X-ray photoelectron spectroscopy (XPS) indicate that Nb can be incorporated into the crystal structure of $TiO_2$ such that Nb occupies close to 50 % of the lattice sites of Ti *(*Gao, 1999; Morris et al., 2000; Huang et al., 2010). A low level of doping or substitution of Nb for Ti in the crystal structure of $TiO_2$ is desirable to minimise metal to metal (Nb-Nb) interaction within the crystal structure (Morris et al., 2000). Experimental measurements of the electronic structure of bulk Nb-doped $TiO_2$ indicates that Nb incorporation results in the appearance of a defect peak within the band gap of the $TiO_2$ (Morris et al., 2000). The defect peak is the source of conductivity of doped $TiO_2$ (Morris et al., 2000).

DFT calculations have been carried out to investigate the electronic structure of Nb-doped $TiO_2$. Using standard DFT, Morgan & Watson (2009) observed that the extra charge introduced by Nb doping is predicted to be located at the bottom of the conduction band. By incorporating the + U term to the DFT calculations in the DFT+U method, Morgan & Watson (2009) were able to show that the extra charge from Nb dopant atoms result in appearance of a defect peak within the band gap of $TiO_2$. The defect peak was separated from the conduction band for both anatase and rutile $TiO_2$.

Two different approaches are used for implementation of the DFT+U method to describe the electronic structure of Nb-doped $TiO_2$. One approach by Morgan & Watson (2009) is to perform spin-polarised calculations with the U term applied to Ti d-states only. Morgan & Watson (2009) concluded that applying or not applying the U term to Nb d-states have little effect on the results. The approach of Morgan & Watson (2009) result in the correct description of the electronic structure of Nb-doped anatase and rutile $TiO_2$ which is consistent with experimental measurements. The range of U values which results in the electronic structure consistent with experimental measurements is 4 eV < U < 6 eV. The second approach by Orita (2010) is to apply the U parameter to both Ti and Nb d-states without performing spin-polarised calculations. The result of the second approach is the prediction that Nb doped rutile $TiO_2$ is metallic which is not consistent with experimental observations which shows that Nb-doped

rutile $TiO_2$ is semi-conducting. The second approach uses higher values of U to open up the band gap to match the experimentally observed band gap of $TiO_2$.

## 7.3 Nb-doped $TiO_2$ as catalyst support in polymer electrolyte fuel cells

Nb-doped $TiO_2$ supported Pt nanoparticles have been tested for activity and durability for application in PEFC (Park & Seol, 2007; *Huang et al.,* 2010; Chevallier et al., 2012; Wang et al., 2013; Valenzuela et al., 2013). The Nb-doped $TiO_2$ supported catalyst was found to have higher oxygen reduction reaction (ORR) activity and higher durability than the Pt/C catalyst. Huang et al. (2010) observed that Nb-doped anatase $TiO_2$ has low conductivity compared to Nb-doped rutile $TiO_2$. Huang et al. (2010) observed that 25 atomic % Nb doping of rutile $TiO_2$ resulted in high ORR activity and high durability compared to Pt/C catalyst. Other authors have also observed a high ORR activity and durability upon doping with different Nb content: 5 at. % Nb by Chevallier et al. (2012), 5 at. % Nb by Valenzuela et al. (2013), 10 at. % Nb by Liu et al. (2014) and 10 at. % by Park & Seol (2007).

The aim of the present chapter is to investigate how the $Pt_{32}Pd_6$ cluster interacts with the Nb-doped partially reduced $TiO_2$(110) surface, whether it is through Pd atoms as anchoring or Pt atoms as anchoring. Interaction with Pd atoms as anchoring atoms corresponds to preferential segregation of Pd atoms towards the cluster-support interface. The Nb dopant atoms can be positioned either on the surface, second or third layers of the partially reduced $TiO_2$(110) surface. The effect of the position of Nb dopant atoms on the preferred interaction of the $Pt_{32}Pd_6$ cluster (i.e. either Pd atoms or Pt atoms anchoring) with the Nb-doped partially reduced $TiO_2$(110) surface will be explored.

## 7.4 Methodology

### 7.4.1 Structural models

#### *7.4.1.1 Model of Nb-doped partially reduced $TiO_2$(110) surface*

The Nb-doped partially reduced $TiO_2$(110) surface was built from the optimised 4 tri-atomic layer thick partially reduced $TiO_2$(110) surface slab. To construct the 12.5 at. % Nb-doped partially reduced $TiO_2$(110) surface, 1 Ti atom from the 8 Ti sites in the (1×1) unit cell of a 4

tri-atomic layer of partially reduced $TiO_2$(110) surface slab was substituted for by a Nb atom. The three different models of the Nb-doped partially reduced $TiO_2$(110) surface considered are the surface segregated model, subsurface segregated model and the bulk model. The three different surface slab models considered were based on the experimental observation by Sheppard et al. (2012) where processing conditions, i.e. temperature and oxygen partial pressure were found to have an influence on whether Nb accumulates or is depleted from the surface and near surface region. Some synthesis methods of Nb doped $TiO_2$ involve annealing in an oxygen reduced atmosphere (Orita, 2010), or post annealing under pure $H_2$ atmosphere to activate the Nb dopant atoms (Yamada et al., 2008). The annealing conditions can thus affect location of Nb dopant atoms within the host structure of $TiO_2$.

For the surface segregated model, the Nb dopant atoms were located in the surface layer of the partially reduced $TiO_2$(110) surface. For the subsurface segregated model, the Nb dopant atoms were located in the second tri-atomic layer of the 4 tri-atomic layer thick partially reduced $TiO_2$(110) surface slab. For the bulk model the Nb dopant atoms were located in the third tri-atomic layer of the 4 tri-atomic layer thick partially reduced $TiO_2$(110) surface slab. For all three different models the top two tri-atomic layers of the partially reduced $TiO_2$(110) surface were relaxed while the bottom two tri-atomic layers are fixed at the bulk optimised atomic positions.

In the real system, Nb-doped $TiO_2$ is a solid solution. Therefore, Nb atoms are expected to be found arranged randomly or in orderly form within the crystal structure and not in layer form as assumed in the present study. The method of placing Nb dopant atoms in layered form in the present study follows a similar method used in a previous study by Tripković et al. (2012). The present study aims to investigate the effect of the presence of Nb within the structure of the partially reduced $TiO_2$(110) surface on the binding of the cluster. It is not the aim to locate the precise location of Nb within the crystal structure of $TiO_2$. Thus the layered approach for Nb location in the present study is to provide a first approximation to get insight into the role of Nb atoms within the partially reduced $TiO_2$(110) surface.

#### *7.4.1.2 $Pt_{32}Pd_6$ cluster approach to Nb-doped partially reduced $TiO_2$(110)*

Preliminary investigations of the interaction of the $Pt_{32}Pd_6$ cluster with the stoichiometric Nb-doped $TiO_2$(110) and Nb-doped partially reduced $TiO_2$(110) surface revealed that binding of the $Pt_{32}Pd_6$ cluster is more stable on the Nb-doped partially reduced $TiO_2$(110) surface. Results of the preliminary investigation are presented in Appendix E.1. Moreover, the preliminary investigation revealed that there is 0.03 eV energy difference between the most

stable facet of approach (i.e. square facet B) and the second most stable facet of approach (hexagonal facet E) on Nb-doped partially reduced $TiO_2$(110) surface. Hence, binding through facet B and facet E result in equivalent binding energies indicating that adsorption through the two facets (i.e. facet B and E) is the preferred facets of binding of the $Pt_{32}Pd_6$ cluster to the support.

The arrangements of the $Pt_{32}Pd_6$ cluster approach with the Nb-doped partially reduced $TiO_2$(110) surface are shown in Figure 7.1. The hexagonal facet is the facet with of approach of the $Pt_{32}Pd_6$ cluster to the support. The hexagonal facet is chosen since it allows for maximum number of Pd atoms to interact with the support and thus represent Pd segregated towards the cluster-support interface. The Pt atoms anchoring structure represent the case where Pt atoms are preferentially segregated towards the cluster-support interface. Similarly, the Pd atoms anchoring structure represent the case where Pd atoms are segregated towards the cluster-support interface.

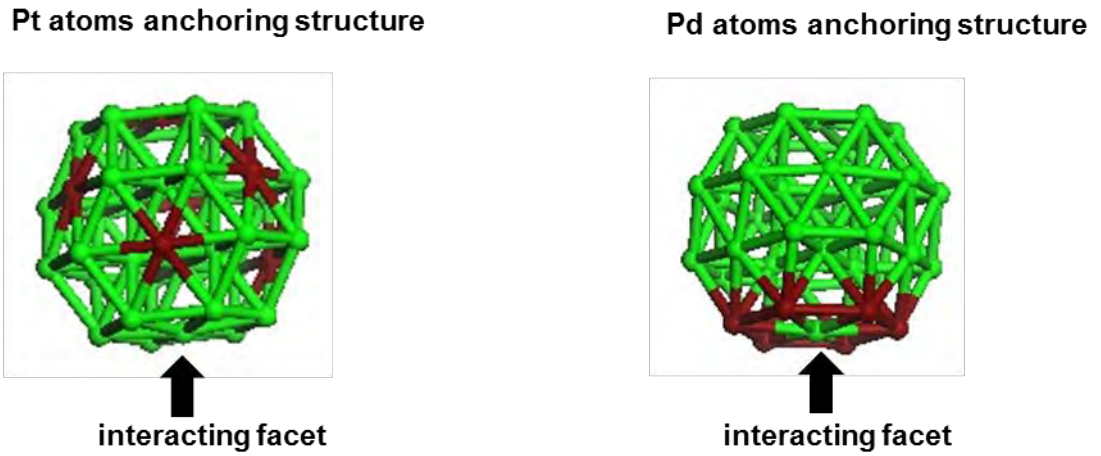


Figure 7.1: Pt atoms anchoring structure and Pd atoms anchoring structure of the $Pt_{32}Pd_6$ cluster with the interacting facets indicated.

Approach of the $Pt_{32}Pd_6$ cluster interacting with the support through either the Pt atoms only facet (Pt atoms anchoring structure) or the Pd atoms anchoring facet (Pd atoms anchoring structure) was investigated on the Nb-doped partially reduced $TiO_2$(110) surface. The effect of the position of Nb dopant atoms within the structure of the partially reduced $TiO_2$(110) surface on the interaction with the $Pt_{32}Pd_6$ cluster was investigated by considering the following:

1. partially reduced $TiO_2$(110) surface with no Nb.
2. partially reduced $TiO_2$(110) surface with Nb located in the surface layer of the partially reduced $TiO_2$(110) surface slab.

3. partially reduced $TiO_2$(110) surface with Nb located in the second layer counted from the top of the partially reduced $TiO_2$(110) surface slab.
4. partially reduced $TiO_2$(110) surface with Nb located in the third layer counted from the top of the partially reduced $TiO_2$(110) surface slab.

### 7.4.2 Computational methodology

The Vienna ab initio simulation package VASP (Kresse & Hafner, 1993; Kresse & Hafner, 1994; Kresse & Furthmüller, 1996a; Kresse & Furthmüller, 1996b) was utilised for the calculations. Spin polarised calculations were performed. The generalised gradient approximation GGA PW91 functional (Perdew et al., 1992) was used for exchange correlation energy. The GGA method was augmented with the + U term in the so called DFT + U method utilising Dudarev's approach (Dudarev et al., 1998) as implemented in the VASP code. DFT + U corrects for over delocalisation by standard GGA methods for the description of metal oxides. U term of U = 4.5 eV was applied to Ti 3d states. For choice of the U term see Appendix D. The electron-ion interactions are described by the projector augmented wave (PAW) method (Blöchl, 1994; Kresse & Jourbert, 1999) pseudopotentials. The plane wave basis set cut-off energy was set at 400 eV. Gaussian smearing (Fu & Ho, 1983; Elsässer et al., 1994) was utilised with a smearing width σ = 0.01eV.

For adsorption calculations a *p*(6 × 3) periodic unit cell slab consisting of 4 tri-atomic layers was utilised, with the bottom two tri-atomic layers fixed at the bulk optimised positions. The top two tri-atomic layers together with the $Pt_{32}Pd_6$ cluster were allowed to relax during the geometry optimisation calculations. The convergence criterion for the geometry optimisation calculations was an electronic convergence criterion of energies below $10^{-5}$ eV and forces below 0.03 eV/Å on unconstrained atoms. Adsorption was performed on only one side of the slab, with the dipole correction implemented within the VASP code applied in the z-direction to correct for any induced dipole which may arise upon adsorption of the cluster. The vacuum region was set at 25 Å to avoid spurious interactions between periodic images. Owing to the big unit cell size used, for the geometry optimisation calculations the Brillouin zone sampling was sampled at the single Γ-point in k-space.

The binding energy (equivalent to the adsorption energy) of the $Pt_{32}Pd_6$ cluster to the $TiO_2$ support was calculated from the relation:

$$E_{bind} = E_{Pt_{32}Pd_6 + support} - E_{support} - E_{Pt_{32}Pd_6} \quad (7.1)$$

Where $E_{Pt_{32}Pd_6+support}$ is the energy of the optimised support (i.e. Nb-doped partially reduced $TiO_2$(110)) with the $Pt_{32}Pd_6$ cluster bound to it, $E_{support}$ is the energy of the optimised support (i.e. Nb-doped partially reduced $TiO_2$(110)) without the $Pt_{32}Pd_6$ cluster adsorbed, and $E_{Pt_{32}Pd_6}$ is the energy of the optimised free unsupported $Pt_{32}Pd_6$ cluster.

The formation energy was also considered to determine the stability of the bimetallic cluster on the support. The formation energy was calculated relative to the optimised free standing $Pd_{38}$ and $Pt_{38}$ clusters.

$$E_{form} = E_{Pt_{32}Pd_6+support} - E_{support} - \frac{6}{38}E_{Pd_{38}} - \frac{32}{38}E_{Pt_{38}} \quad (7.2)$$

Where $E_{Pt_{32}Pd_6+support}$ and $E_{support}$ have the same meaning as above in equation 7.1, $E_{Pd_{38}}$ is the energy of the optimised unsupported $Pd_{38}$ cluster and $E_{Pt_{38}}$ is the energy of the optimised unsupported $Pt_{38}$ cluster.

The segregation energy is also used to assess if the rearranged structures are lower in energy than the reference structure with the same arrangement as the free standing $Pt_{32}Pd_6$ cluster. The adsorption geometry with free unsupported $Pt_{32}Pd_6$ cluster arrangement which has the highly exothermic formation energy is taken as the reference structure in order to calculate the segregation energy from the relation:

$$E_{seg} = E_i - E_{ref} \quad (7.3)$$

Where $E_i$ is the total energy of the rearranged structure on the support and $E_{ref}$ is the total energy of the adsorption structure with arrangement of the lowest energy structure of the unsupported $Pt_{32}Pd_6$ cluster (with the highly exothermic excess energy).

To gain further insight into the interaction of the $Pt_{32}Pd_6$ cluster with the different supports, PDOS analysis was performed. Change in Bader charge analysis using the Bader charge partitioning method (Bader, 1991; Henkelman et al., 2006; Sanville et al., 2007; Tang et al., 2009) and electron density difference plot analysis were also performed to assess charge transfer during adsorption of the $Pt_{32}Pd_6$ cluster to the support. For the PDOS, Bader and charge density difference plot analysis a Monkhorst Pack (Monkhorst & Pack, 1976) k-point grid of (2 × 3 × 1) was utilised to sample the Brillouin zone. Charge density difference was determined from the relation:

$$\Delta\rho = \rho_{Pt_{32}Pd_6+support} - \rho_{support} - \rho_{Pt_{32}Pd_6} \quad (7.4)$$

Where $\rho_{Pt_{32}Pd_6+support}$ is the charge density of the optimised support with the $Pt_{32}Pd_6$ cluster adsorbed, $\rho_{support}$ is the charge density of the support without the $Pt_{32}Pd_6$ cluster in the same position as in the optimised geometry and $\rho_{Pt_{32}Pd_6}$ is the charge density of the $Pt_{32}Pd_6$ cluster in the same position as in the optimised geometry with the support.

For Ti, Nb and O atoms, the atom resolved change in Bader charge upon adsorption is calculated from:

$$\Delta q = q_{Pt_{32}Pd_6 + support} - q_{support} \quad (7.5)$$

Where $q_{Pt_{32}Pd_6 + support}$ is the atom resolved Bader charge on Ti, Nb and O atoms in the optimised geometry with the support and the $Pt_{32}Pd_6$ cluster adsorbed, $q_{support}$ is the atom resolved Bader charge on the corresponding Ti, Nb and O atoms of the support without the $Pt_{32}Pd_6$ cluster in the same position as in the optimised geometry. The atom resolved change in Bader charge on Pt and Pd atoms of the $Pt_{32}Pd_6$ cluster upon adsorption is calculated in a similar way to how charge on Ti, Nb and O atoms is calculated.

$$\Delta q = q_{Pt_{32}Pd_6 + support} - q_{Pt_{32}Pd_6} \quad (7.6)$$

Where $q_{Pt_{32}Pd_6 + support}$ is the atom resolved Bader charge on Pt and Pd atoms in the optimised geometry with the support and the $Pt_{32}Pd_6$ cluster adsorbed and $q_{Pt_{32}Pd_6}$ is the atom resolved Bader charge on the corresponding Pt and Pd atoms of the $Pt_{32}Pd_6$ cluster without the support in the same position as in the optimised geometry.

## 7.5 Results and discussion

### 7.5.1 Interaction of $Pt_{32}Pd_6$ cluster with Nb-doped partially reduced $TiO_2$(110) surface

The optimised structures of adsorption geometries of the $Pt_{32}Pd_6$ cluster on the support with different location of Nb atoms together with the calculated energies are presented in Figure 7.2. The calculated bond lengths for the adsorption structures as a function of Nb location are presented in Table 7.1.

A plot of formation energy for both interactions through Pt anchoring and Pd anchoring atoms indicates that the formation energy varies with position of the Nb atoms within the partially reduced $TiO_2$(110) surface slab (see Figure 7.3). The presence of Nb atoms within the partially reduced $TiO_2$(110) surface slab enhances binding of the $Pt_{32}Pd_6$ cluster on the support material. The binding and formation energies of the $Pt_{32}Pd_6$ cluster on the Nb-doped partially reduced $TiO_2$(110) surface are more exothermic than on the partially reduced $TiO_2$(110) surface.

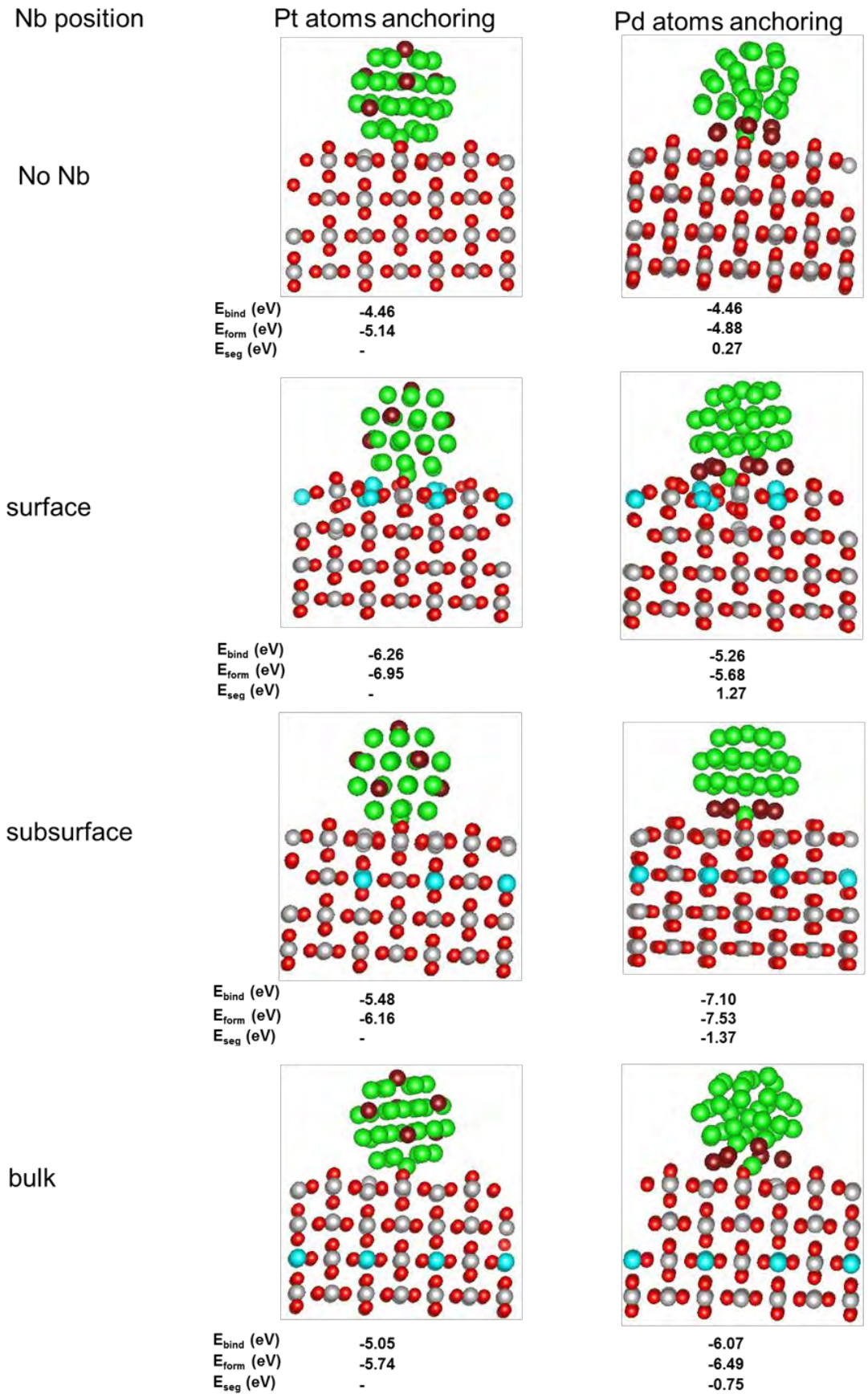


Figure 7.2: Adsorption structures for the $Pt_{32}Pd_6$ cluster with different anchoring facets as a function of the Nb position on the bulk model of partially reduced Nb-doped $TiO_2$(110). Key: red spheres represent oxygen atoms, grey spheres Ti atoms, light blue Nb atoms, green Pt atoms and maroon Pd atoms.

Table 7.1*:* Optimised bond lengths of the $Pt_{32}Pd_6$ cluster with approach via the anchoring Pt and anchoring Pd atom structures on the different Nb-doped partially reduced $TiO_2$(110) surface model.

| **No Nb** | | **Nb 1st layer** | | **Nb 2nd layer** | | **Nb 3rd layer** | |
|---|---|---|---|---|---|---|---|
| Pt anchoring | Pd anchoring | Pt anchoring | Pd anchoring | Pt anchoring | Pd anchoring | Pt anchoring | Pd anchoring |
| **Interacting facet** | | **Interacting facet** | | **Interacting facet** | | **Interacting facet** | |
| Side length | | Side length | | Side length | | Side length | |
| $d_{Pt-Pt}$ , Å | $d_{Pd-Pd}$ , Å | $d_{Pt-Pt}$ , Å | $d_{Pd-Pd}$ , Å | $d_{Pt-Pt}$ , Å | $d_{Pd-Pd}$ , Å | $d_{Pt-Pt}$ , Å | $d_{Pd-Pd}$ , Å |
| 2.66 | 2.86 | 2.99 | 3.78 | 2.88 | 3.14 | 2.68 | 3.27 |
| 2.66 | 2.81 | 2.74 | 2.70 | 2.70 | 2.73 | 2.61 | 2.89 |
| 2.68 | 2.78 | 2.73 | 4.57 | 2.71 | 2.78 | 2.84 | 2.89 |
| 3.04 | 3.70 | 2.71 | 3.32 | 2.69 | 2.72 | 2.74 | 2.85 |
| 2.67 | 3.70 | 2.76 | 2.90 | 2.64 | 2.78 | 2.79 | 4.61 |
| 2.76 | 2.79 | 2.74 | 2.74 | 2.80 | 2.77 | 2.74 | 2.83 |
| Diagonal length | | Diagonal length | | Diagonal length | | Diagonal length | |
| $d_{Pt-Pt}$ , Å | $d_{Pt-Pd}$ , Å | $d_{Pt-Pt}$ , Å | $d_{Pt-Pd}$ , Å | $d_{Pt-Pt}$ , Å | $d_{Pt-Pd}$ , Å | $d_{Pt-Pt}$ , Å | $d_{Pt-Pd}$ , Å |
| 2.85 | 2.88 | 2.74 | 2.79 | 2.63 | 2.80 | 2.78 | 2.85 |
| 2.76 | 2.85 | 2.70 | 2.97 | 2.69 | 2.83 | 2.90 | 2.80 |
| 2.80 | 2.66 | 2.69 | 3.95 | 2.64 | 2.95 | 2.97 | 2.88 |
| 2.76 | 2.97 | 3.10 | 3.29 | 2.94 | 2.83 | 2.87 | 3.65 |
| 3.08 | 4.37 | 2.77 | 2.76 | 3.23 | 2.84 | 2.97 | 4.31 |
| 2.68 | 2.75 | 3.66 | 2.87 | 2.70 | 2.95 | 2.89 | 3.82 |
| **Opposite facet** | | **Opposite facet** | | **Opposite facet** | | **Opposite facet** | |
| Side length | | Side length | | Side length | | Side length | |
| $d_{Pt-Pt}$ , Å | $d_{Pt-Pt}$ , Å | $d_{Pt-Pt}$ , Å | $d_{Pt-Pt}$ , Å | $d_{Pt-Pt}$ , Å | $d_{Pt-Pt}$ , Å | $d_{Pt-Pt}$ , Å | $d_{Pt-Pt}$ , Å |
| 2.58 | 2.68 | 2.68 | 2.63 | 2.66 | 2.68 | 2.59 | 2.66 |
| 2.65 | 2.68 | 2.60 | 2.67 | 2.61 | 2.68 | 2.76 | 2.66 |
| 2.59 | 2.72 | 2.67 | 2.62 | 2.67 | 2.64 | 2.60 | 2.67 |
| 2.65 | 2.68 | 2.60 | 2.63 | 2.60 | 2.72 | 2.71 | 2.69 |
| 2.58 | 2.66 | 2.69 | 2.64 | 2.68 | 2.65 | 2.59 | 2.71 |
| 2.65 | 2.68 | 2.62 | 2.70 | 2.60 | 2.68 | 2.71 | 2.66 |
| Diagonal length | | Diagonal length | | Diagonal length | | Diagonal length | |
| $d_{Pt-Pd}$ , Å | $d_{Pt-Pt}$ , Å | $d_{Pt-Pd}$ , Å | $d_{Pt-Pt}$ , Å | $d_{Pt-Pd}$ , Å | $d_{Pt-Pt}$ , Å | $d_{Pt-Pd}$ , Å | $d_{Pt-Pt}$ , Å |
| 2.76 | 2.60 | 2.73 | 2.68 | 2.76 | 2.68 | 2.86 | 2.65 |
| 2.79 | 2.68 | 2.74 | 2.67 | 2.73 | 2.68 | 2.85 | 2.59 |
| 2.78 | 2.66 | 2.74 | 2.65 | 2.79 | 2.70 | 2.79 | 2.71 |
| 2.75 | 2.60 | 2.68 | 2.64 | 2.75 | 2.69 | 2.77 | 2.60 |
| 2.73 | 2.66 | 2.73 | 2.67 | 2.73 | 2.70 | 2.76 | 2.66 |
| 2.76 | 2.75 | 2.75 | 2.65 | 2.76 | 2.69 | 2.78 | 2.69 |
| $d_{Pt-Ti_{5C}}$ , Å | $d_{Pd-Ti_{5C}}$ , Å | $d_{Pt-Nb_{5C}}$ , Å | $d_{Pd-Nb_{5C}}$ , Å | $d_{Pt-Ti_{5C}}$ , Å | $d_{Pd-Ti_{5C}}$ , Å | $d_{Pt-Ti_{5C}}$ , Å | $d_{Pd-Ti_{5C}}$ , Å |
| 2.61, 2.55 | 2.72, 3.04 | 2.42,2.42,2.52 | 2.52,2.57,2.53 | 2.61,2.74,2.70 | 2.53, 2.56 | 2.37 | 2.53, 2.74 |
| **2.72**, **2.70** [A] | **2.72, 2.53** [B] | 2.46,**2.65,2.91** [D] | 2.78,**2.64,2.64** [E] | 2.66,**2.61,3.02** [E] | **2.77, 2.73** [F] | **2.56, 2.93** [G] | **2.51, 2.56** [H] |
| $d_{Pt-O_{2C}}$ , Å | $d_{Pd-O_{2C}}$ , Å | $d_{Pt-O_{2C}}$ , Å | $d_{Pd-O_{2C}}$ , Å | $d_{Pt-O_{2C}}$ , Å | $d_{Pd-O_{2C}}$ , Å | $d_{Pt-O_{2C}}$ , Å | $d_{Pd-O_{2C}}$ , Å |
| 2.09, 2.14 | 2.16, 2.04 | 2.08, 2.10 | 2.19, 2.09 | 2.05, 1.98 | 2.23, 2.23 | 2.12, 2.12 | 2.16, 2.46 |
| 2.18 | **2.17, 2.18** [C] | | | | 2.16, 2.19 | | 2.19, 2.**23** [I] |

[A] Pt-$T_{i5C:}$ Pt –Ti bonds between the surface Ti atoms with missing bonds at the oxygen monovacancy site and Pt atoms.

[B] Pt-$T_{i5C}$: Pt –Ti bonds between the surface Ti atoms with missing bonds at the oxygen monovacancy site and Pt atoms.

[C] Pt-$O_{3C}$: Pt-$O_{3C}$ bonds between Pt atoms and the surface oxygen atoms with coordination number 3.

[D] Pt-$T_{i5C}$: Pt –Ti bonds between the surface Ti atoms with missing bonds at the oxygen monovacancy site and Pt atoms.

[E] Pt-$T_{i5C}$: Pt –Ti bonds between the surface Ti atoms with missing bonds at the oxygen monovacancy site and Pt atoms.

[F] Pt-$T_{i5C}$: Pt –Ti bonds between the surface Ti atoms with missing bonds at the oxygen monovacancy site and Pt atoms.

[G] Pt-$T_{i5C}$: Pt –Ti bonds between the surface Ti atoms with missing bonds at the oxygen monovacancy site and Pt atoms.

[H] Pt-$T_{i5C}$: Pt –Ti bonds between the surface Ti atoms with missing bonds at the oxygen monovacancy site and Pt atoms.

[I] Pd-$O_{3C}$: Pd-$O_{3C}$ bonds between Pd atoms and the surface oxygen atoms with coordination number 3.

For structures in which the $Pt_{32}Pd_6$ cluster is anchored to the support by Pt atoms, it can be seen in Figure 7.2 and Figure 7.3 that as Nb is positioned away from the surface layer and on layer 2 and 3 of the slab, the formation energy and the binding energy becomes less exothermic. The highly exothermic binding and formation energy are attained when Nb atoms are located in the surface layer for the Pt atoms anchoring structures. Conversely, for the structure in which the $Pt_{32}Pd_6$ cluster is anchored to the support through Pd atoms, the binding and formation energy becomes more negative as the Nb atoms are not positioned on the surface layer but are located on layers within the partially reduced $TiO_2$(110) surface slab. The highly exothermic binding and formation energy of the structure which has Pd atoms as anchoring atoms are obtained when Nb atoms are positioned in the second layer (subsurface segregated model) of the Nb-doped partially reduced $TiO_2$(110) surface slab.

It is also worth mentioning that with Nb dopant atoms not on the surface (i.e. occupies the 2$^{nd}$ and 3$^{rd}$ layers) the binding and formation energies of the structures in which the $Pt_{32}Pd_6$ cluster is anchored to the support through Pd atoms are more exothermic than those of the structures anchored by Pt atoms. The highly exothermic formation energies for Pd anchored structures compared to Pt anchored structures for Nb positioned below the surface layer indicates that the former arrangements are energetically more stable than the latter arrangements. This is the opposite of the observed stability of the free standing unsupported $Pt_{32}Pd_6$ cluster where the latter arrangement is more stable than the former arrangement.

The adsorption geometries for both Pt atoms anchoring and Pd atoms anchoring structures is such that the central Pt atom at the centre of the interacting hexagonal facet occupies the site of the vacant surface oxygen bridge atom on the surface as seen in Figure 7.2. When Nb atoms are on the surface layer of the partially reduced $TiO_2$(110) surface slab, there is reconstruction of the support upon adsorption of the $Pt_{32}Pd_6$ cluster (see Figure 7.2). Elevation of Nb atoms in the contact region when Nb is located in the surface of the partially reduced $TiO_2$(110) surface slab can be seen in Figure 7.2 and the calculated short Pt-Nb and Pd-Nb distances (see Table 7.1). The short Pt-Nb and Pd-Nb distances indicate the close proximity of the $Pt_{32}Pd_6$ cluster to the surface Nb atoms.

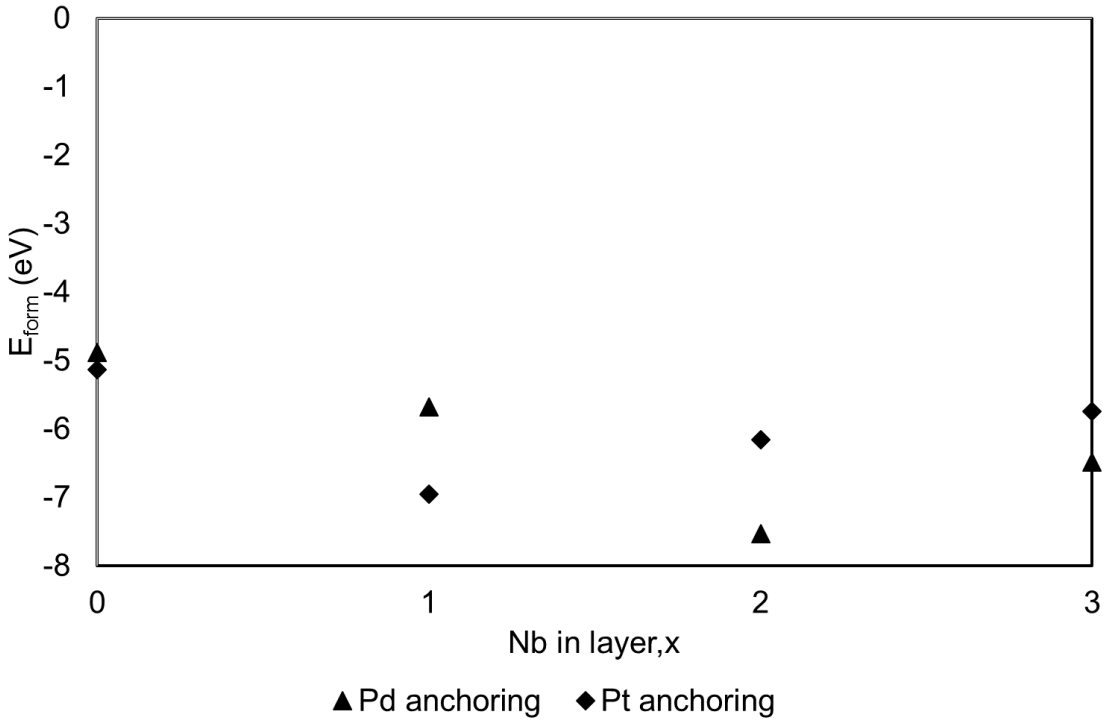


Figure 7.3: Variation of formation energy of the $Pt_{32}Pd_6$ cluster with position of Nb dopant atoms within the partially reduced $TiO_2$(110) surface.

From Figure 7.2 it is observed that there is visible distortion of the interacting facet of the $Pt_{32}Pd_6$ cluster interacting with the support through Pd atoms anchoring facet. There is no observable distortion of the interacting facet for the Pt atoms anchoring facet of the $Pt_{32}Pd_6$ cluster to the support. The extent of distortion of the interacting facet for the $Pt_{32}Pd_6$ cluster interacting through Pd atoms anchoring facet is corroborated by bond elongation of diagonal and side bond lengths of the interacting facet (see Table 7.1) compared to the bond lengths of the same facet of the free standing $Pt_{32}Pd_6$ cluster (see chapter 3, Table 3.2). The extent of bond elongation for the $Pt_{32}Pd_6$ cluster interacting with the support through Pt atoms anchoring facet is lower, this can be deduced by comparing the reported diagonal and side bond lengths

of the interacting facet (see Table 7.1) and the corresponding bond lengths of the same facet in the free standing $Pt_{32}Pd_6$ cluster (see chapter 3, Table 3.3).

Distortion of the interacting hexagonal facet is due to bond elongation of the diagonal and side bond lengths in order for bond formation to occur between the interacting facet and $Ti_{5c}$ atoms on the surface of the support. The $Ti_{5C}$ atoms are located adjacent to the central oxygen bridge row of oxygen atoms containing the vacant site on the surface of the partially reduced $TiO_2$(110) surface. Formation of Pt-Ti or Pd-Ti bonds stabilises binding of the $Pt_{32}Pd_6$ cluster on the partially reduced $TiO_2$(110) surface, hence maximisation of the formation of Pt-Ti or Pd-Ti bonds is vital.

The higher extent of bond distortion of the interacting hexagonal facet for the Pd atoms anchoring structure than the Pt atoms anchoring structure is probably due to the difference in orbital interaction between Pd 4d states and Pt 5d states with the states of the support. To achieve the same strength of interaction, it maybe that close proximity is needed for orbital interaction between Pd 4d states and the states of the support compared to Pt 5d states and the states of the support.

The segregation energy varies with location of Nb dopant atoms within the partially reduced $TiO_2$(110) surface (see Figure 7.4). In the absence of Nb dopant atoms, i.e. partially reduced $TiO_2$(110) surface the segregation energy is positive indicating that the preferred arrangement is when the cluster interacts with the support through the Pt atoms anchoring to the support. The segregation energy is more endothermic when Nb dopant atoms are located on the surface of the partially reduced $TiO_2$(110) surface. Positioning Nb dopant atoms away from the surface in the second and third layers of the partially reduced $TiO_2$(110) surface results in the $Pt_{32}Pd_6$ cluster interacting with the support through the Pd atoms as anchoring atoms being the preferred arrangement with exothermic segregation energies. The result of which is more Pt atoms are exposed on the surface of the $Pt_{32}Pd_6$ cluster and available for adsorbates to adsorb on. Therefore, depending on the location of Nb dopant atoms within the partially reduced $TiO_2$(110) surface slab, Nb position may alter the arrangement of the $Pt_{32}Pd_6$ cluster relative to the most stable arrangement of the free unsupported $Pt_{32}Pd_6$ cluster.

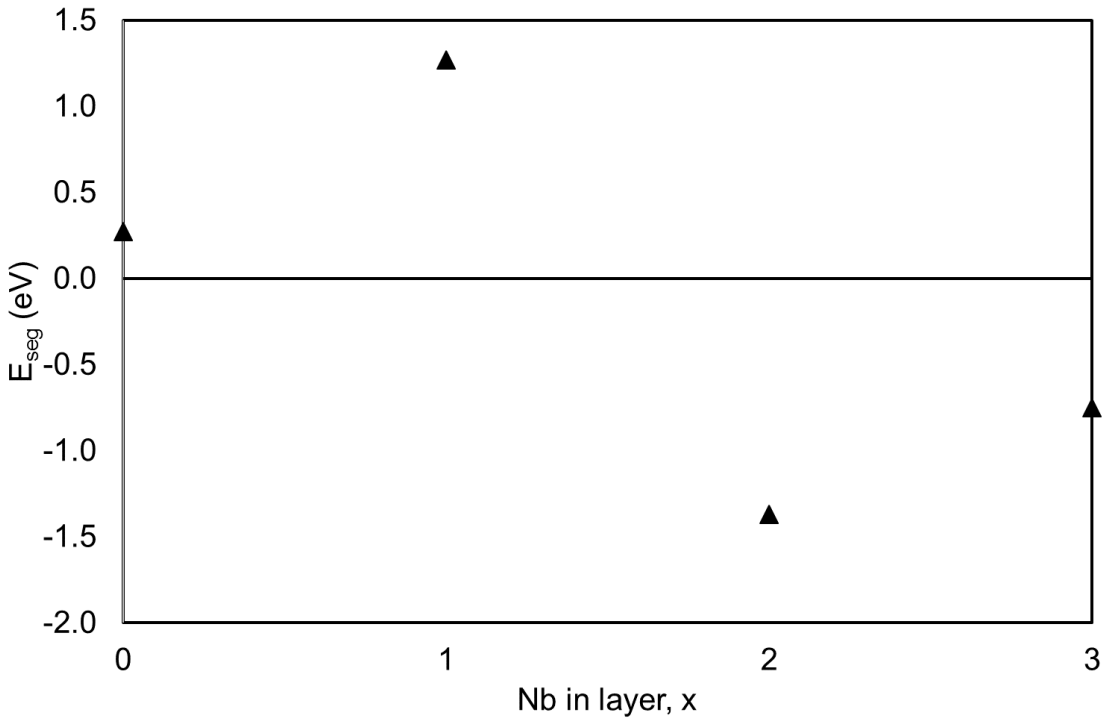


Figure 7.4: Variation of segregation energy with position of Nb dopant atoms within the partially reduced $TiO_2$(110) surface.

## 7.5.2 Electronic structure analysis

### 7.5.2.1 Charge density analysis

Variation of charge density difference with position of Nb atoms within the partially reduced $TiO_2$ (110) surface slab for the Pt atoms anchoring and Pd atoms anchoring structures is presented in Figure 7.5. The charge redistribution in the contact region between the $Pt_{32}Pd_6$ cluster and the support indicates formation of bonds between the cluster and the support. For both Pt atoms anchoring and Pd atoms anchoring structures there is observed charge accumulation (yellow isosurface) along Pt-Ti and Pd-Ti bonds. The charge accumulation is due to charge loss from Ti or Nb to Pd or Pt atoms bonded to surface $Ti_{5c}$ or $Nb_{5c}$ atoms. This result is consistent with previous studies where charge accumulation was observed along Pt-Ti bonds for adsorption of $Pt_2$ (Xia et al., 2015) and $Pt_{1\text{-}6}$ (Jiang et al., 2012) on rutile $TiO_2$(110) surfaces.

The amount of charge accumulation on the surface of the $Pt_{32}Pd_6$ cluster increases as Nb dopant atoms are positioned away from the surface layer (i.e. positioned in the 2$^{nd}$ and 3$^{rd}$ layer) of the partially reduced $TiO_2$(110) surface slab. The charge accumulation on the surface of the $Pt_{32}Pd_6$ cluster is visible from the increase in intensity of the yellow isosurface on the

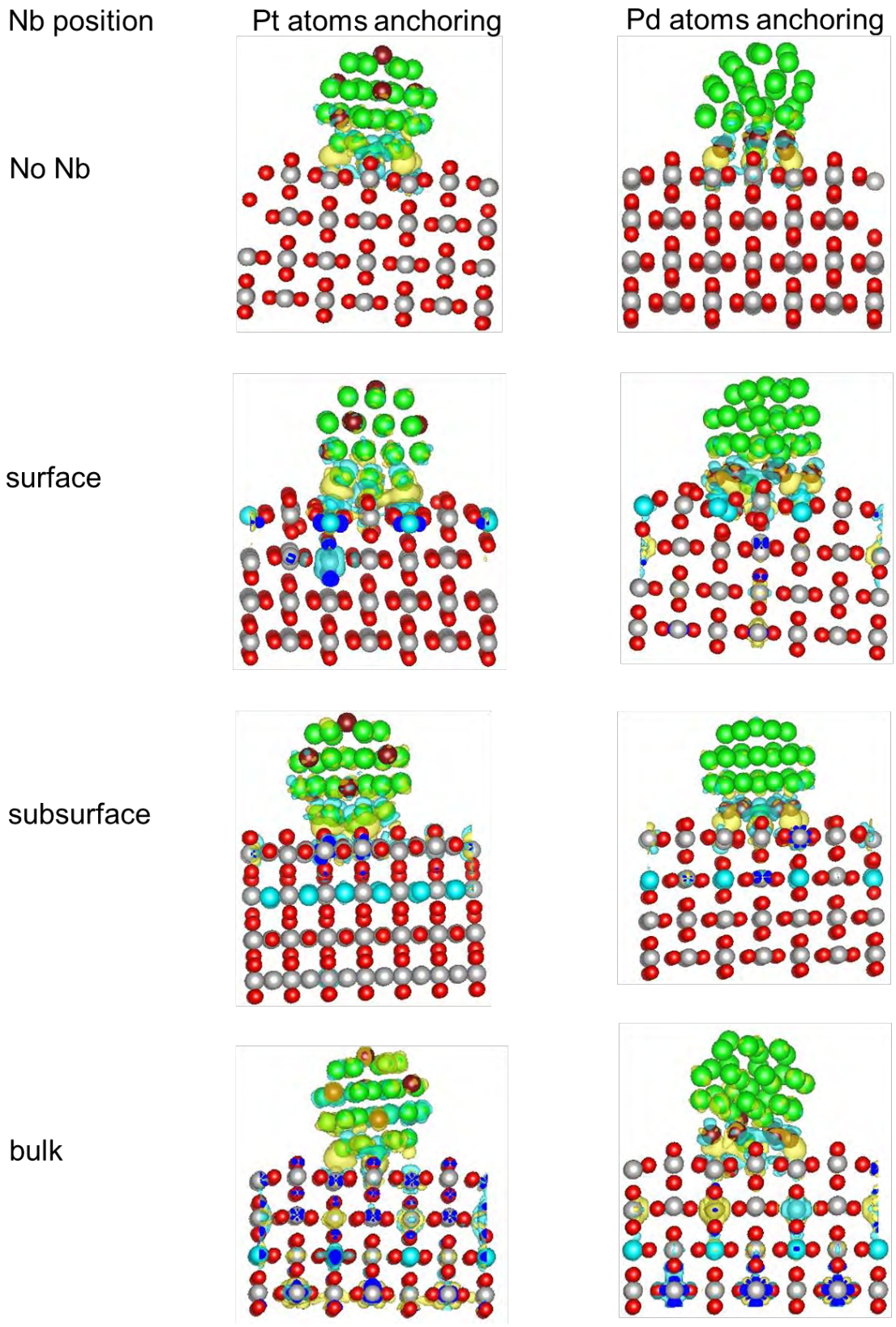


Figure 7.5: Variation of charge density difference with position of Nb atoms within the partially reduced $TiO_2$(110) surface. Isosurface level is at 0.0025 e/ Å$^3$. Key: blue isosurface represents charge depletion and yellow isosurface represents charge accumulation.

surface of the adsorbed cluster (see Figure 7.5). The extent of charge accumulation on the surface of the supported $Pt_{32}Pd_6$ cluster is higher on the Pt atoms anchoring structures than on the Pd atoms anchoring structures. This is probably due to different orbital interaction between Pt 5d states of the Pt atoms anchoring structures and Pd 4d states of the Pd atoms anchoring structures with the support. The difference in orbital interaction between Pt 5d states and Pd 4d states with the support may result in difference in charge transfer upon adsorption.

Location of Nb dopant atoms on the surface layer of the partially reduced $TiO_2$(110) surface slab results in charge redistribution from the second layer atoms for both the Pt and Pd atoms anchoring structures. Similarly, for Nb located in the third layer of the partially reduced $TiO_2$(110) surface slab, it can be seen from Figure 7.5 that for Pt atoms and Pd atoms anchoring structures there is charge redistribution from both the layer above and below the layer containing Nb atoms. This indicates that despite not being in direct contact with the $Pt_{32}Pd_6$ cluster the presence of Nb atoms within the partially reduced $TiO_2$(110) surface slab affects the charge transferred to the adsorbed $Pt_{32}Pd_6$ cluster.

#### 7.5.2.2 Bader charge analysis

The Bader charge partitioning method was employed to quantify the quantity of charge transfer upon adsorption of the $Pt_{32}Pd_6$ cluster on the different supports. For the bare Nb-doped partially reduced $TiO_2$(110) surface, the calculated Bader charge is a positive charge of 4.5 for the substitute Nb atoms and the adjacent Ti atoms to the substituted Nb atoms have a positive charge of 3. For both the Pt and Pd atoms anchoring structures there is overall net charge transfer from the support to the $Pt_{32}Pd_6$ cluster upon adsorption. The direction of net charge transfer from support to the cluster was obtained irrespective of the position of Nb atoms within the partially reduced $TiO_2$(110) surface slab. The presence of Nb atoms within the partially reduced $TiO_2$(110) surface slab results in an increased quantity of charge transfer to the $Pt_{32}Pd_6$ cluster compared to charge transfer from the undoped partially reduced $TiO_2$(110) surface. The difference in charge loss from the doped and undoped partially reduced $TiO_2$(110) surface is due to the difference in electronegativity between Ti (1.5) and Nb (1.6) atoms.

The quantity of charge transferred to the $Pt_{32}Pd_6$ cluster while interacting with the support via the Pd atoms as anchoring atoms is lower than the charge transferred when Pt atoms are anchoring (see Figure 7.6). The only exception to this trend is where Nb is situated in the third layer where charge transfer to the cluster is higher for the Pd atoms anchoring structure than the Pt anchoring structure. This trend will be explained later based on the data presented in

Figure 7.7. For Pt atoms anchoring structure the d-band centre of the interacting facet is -1.82 eV, whilst the corresponding d-band centre for the Pd atoms anchoring structure is -1.88 eV. The difference in d-band centre of the interacting facets can contribute to the observed difference in charge transfer between the two arrangements. The slightly different d-band centres indicate slightly different d-band properties for the two arrangements which imply they may interact differently with the support material.

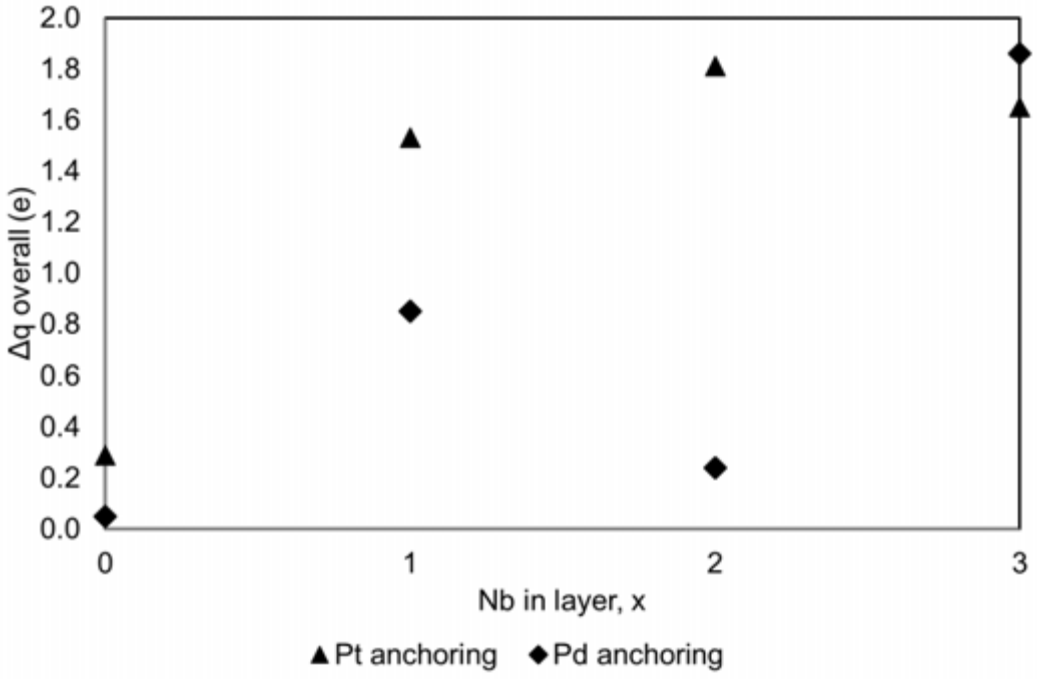


Figure 7.6: Variation of overall charge transfer to the $Pt_{32}Pd_6$ cluster with location of Nb atoms within the partially reduced $TiO_2$(110) surface.

The charge transferred when Nb atoms are located in the second layer is lower than for the case when Nb is on the surface for the Pd atoms anchoring structure. The lowest energy arrangement with the cluster interacting via the anchoring Pd atoms is obtained when Nb atoms are located in the second layer. This arrangement corresponds to the smallest amount of charge transfer from the Nb-doped partially reduced $TiO_2$(110) surface to the adsorbed $Pt_{32}Pd_6$ cluster.

In Figure 7.7 the net charge on Nb atoms for both the Pt atoms and Pd atoms anchoring structures is plotted as a function of the position of Nb atoms within the partially reduced $TiO_2$(110) surface slab. It is observed that the net charge on Nb atoms varies with the interacting facet. For the Pt atoms anchoring structure, there is net charge accumulation on Nb atoms situated in the surface layer, whereas for Nb atoms positioned in the second and third layers there is net charge loss from Nb atoms. The opposite trend is observed for the Pd

atoms anchoring structure, there is net charge loss from Nb atoms located in the surface layer. Positioning Nb atoms in the second layer results in no net charge transfer from Nb atoms and in the third layer there is net charge accumulation on Nb atoms.

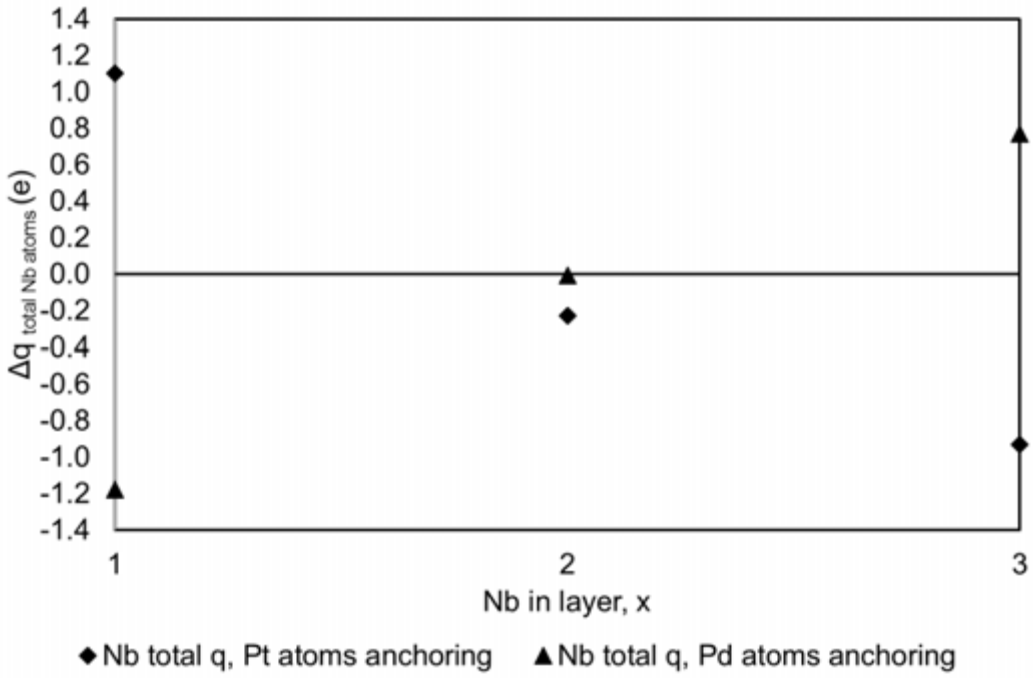


Figure 7.7: Net change in charge on Nb atoms in different positions, for Pt atoms and Pd atoms anchoring structures.

For Nb in the surface layer and third layer of the partially reduced $TiO_2$(110) surface slab, the magnitude of net charge on Nb atoms is similar and of opposite signs for both Pt atoms and Pd atoms anchoring structures. For Nb positioned in the second layer the magnitude of net charge on Nb atoms is higher for the Pt atoms anchoring structure compared to Pd atoms anchoring structure where there is zero net charge on Nb atoms.

The zero net charge on Nb atoms in the second layer of the partially reduced $TiO_2$(110) surface for interaction through the Pd atoms anchoring structure, coincides with the smallest amount of charge transfer to the adsorbed $Pt_{32}Pd_6$ cluster. The small overall charge transfer to the $Pt_{32}Pd_6$ cluster is as a result of no charge contribution by Nb atoms in the second layer of the partially reduced $TiO_2$(110) surface. The small overall charge transfer is of the same order of magnitude as that from the pure undoped partially reduced $TiO_2$(110) surface.

### 7.5.2.3 PDOS analysis

The PDOS analysis was performed to gain further insight into the change in the density of states of the support and the $Pt_{32}Pd_6$ cluster upon adsorption. The PDOS analysis was limited only to adsorption of the $Pt_{32}Pd_6$ cluster on the subsurface model (Nb in the second layer) of the Nb-doped partially $TiO_2$(110) surface. The rationale behind the choice of Nb in the second layer surface slab is it is on this surface model where the lowest energy arrangement of the $Pt_{32}Pd_6$ cluster (with the most exothermic segregation energy) was obtained. For the PDOS analysis both the Pt atoms anchoring geometry and Pd atoms anchoring geometry were considered. The total valence projected density of states was projected onto the oxygen 2p states, Ti 3d states and Nb 4d states. For the $Pt_{32}Pd_6$ cluster the density of states was projected onto valance 4d states for Pd and 5d states for Pt atoms.

The PDOS of the bare subsurface model of the partially reduced $TiO_2$(110) surface with Nb in the second layer consists of a band gap of approximately 1.6 eV with two peaks located within the band gap (see Figure 7.8 (a)). The band gap lies below the Fermi level. This result in consistent with the results obtained by Xia et al. (2015) where doping rutile $TiO_2$(110) with Nb was found to result in the band gap lying below the Fermi level. Morgan et al. (2009) calculated the PDOS of Nb-doped $TiO_2$ with 2 at. % Nb doping and it consisted of a peak in the band gap. The height of the peak in the band gap is dependent on the concentration of Nb dopant atoms (Morris et al., 2000). In the present study the band gap of Nb-doped partially reduced $TiO_2$(110) surface consists of two peaks, one peak is due to the presence of Nb dopant atoms and the other peak is due to the surface oxygen bridge vacancy.

Upon adsorption of the $Pt_{32}Pd_6$ cluster on the subsurface model of the Nb-doped partially reduced $TiO_2$(110) surface through interaction with Pt atoms as anchoring atoms, the PDOS of the support consists of one sharp peak at -0.90 eV and tiny peaks (around -0.20 eV) in the band gap as can be seen in Figure 7.9 (b). The appearance of tiny peaks and disappearance of the other sharp peak in the band gap indicates that upon adsorption of the $Pt_{32}Pd_6$ cluster to the support there is change to the electronic structure of both support and cluster. Concomitant changes to the PDOS of the support and cluster indicates formation of bonds between the cluster and support.

Post adsorption of the $Pt_{32}Pd_6$ cluster interacting with the support through Pd atoms, there is a small peak centred at -0.20 eV below the Fermi level with the peak at -0.90 eV joined to the valence band. A plot of the PDOS difference between the PDOS of the support post adsorption of the $Pt_{32}Pd_6$ cluster through Pd atoms anchoring and the bare facet in shown in Figure 7.8

(d). The PDOS difference indicates that post adsorption the are regions of gain and reduction in PDOS. Predominantly there is loss in PDOS in energies between 0 – 2 below the Fermi level, this region for the bare support consists of two sharp peaks. The two sharp peaks are diminished after adsorption of the $Pt_{32}Pd_6$ cluster on the support. Thus, interaction of the $Pt_{32}Pd_6$ cluster with the support through Pd atoms result in the support almost exhibiting metallic properties due to no band gap. The different PDOS profile of the support for the $Pt_{32}Pd_6$ cluster interacting with the support through Pt atoms anchoring and Pd atoms anchoring structures indicate a different change to the electronic properties of the support. Modification of the electronic properties of the support upon adsorption of the $Pt_{32}Pd_6$ cluster is dependent on the identity of the atoms (i.e. Pt or Pd) of the cluster directly in contact with the support.

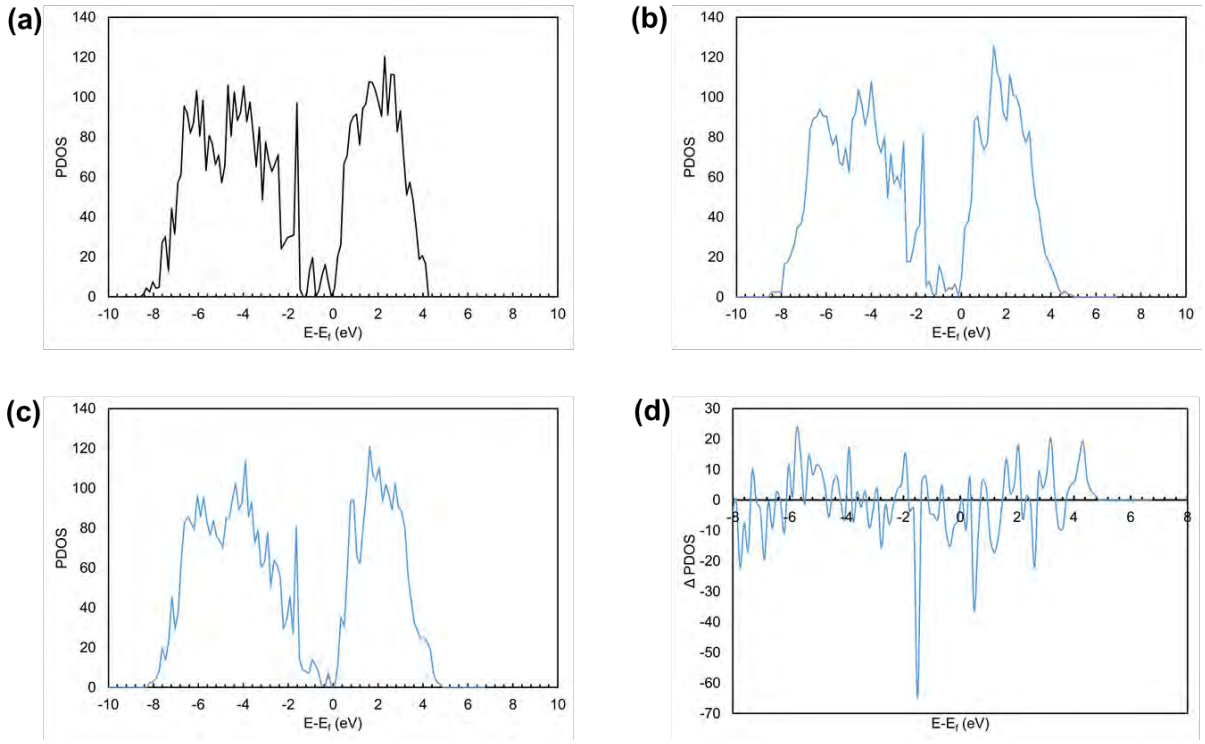


Figure 7.8: PDOS analysis for the Nb-doped partially reduced $TiO_2$(110) surface with Nb located in the second layer: (a) bare Nb-doped partially reduced $TiO_2$(110) surface, (b) Nb-doped partially reduced $TiO_2$(110) surface with the adsorbed $Pt_{32}Pd_6$ cluster interacting through Pt atoms and (c) Nb-doped partially reduced $TiO_2$(110) surface with the adsorbed $Pt_{32}Pd_6$ cluster interacting via the Pd atoms, (d) PDOS difference (c)-(a). The energy scale is relative to the Fermi level.

The PDOS of the $Pt_{32}Pd_6$ cluster is transformed from a discrete spectrum to a continuous distribution upon binding of the cluster to the support. Irrespective of arrangement of Pt and Pd atoms in the $Pt_{32}Pd_6$ cluster, and the atoms anchoring the cluster to the support, the PDOS of the cluster is transformed to a continuous spectrum which is characteristic of metallic properties (see Figure 7.9).

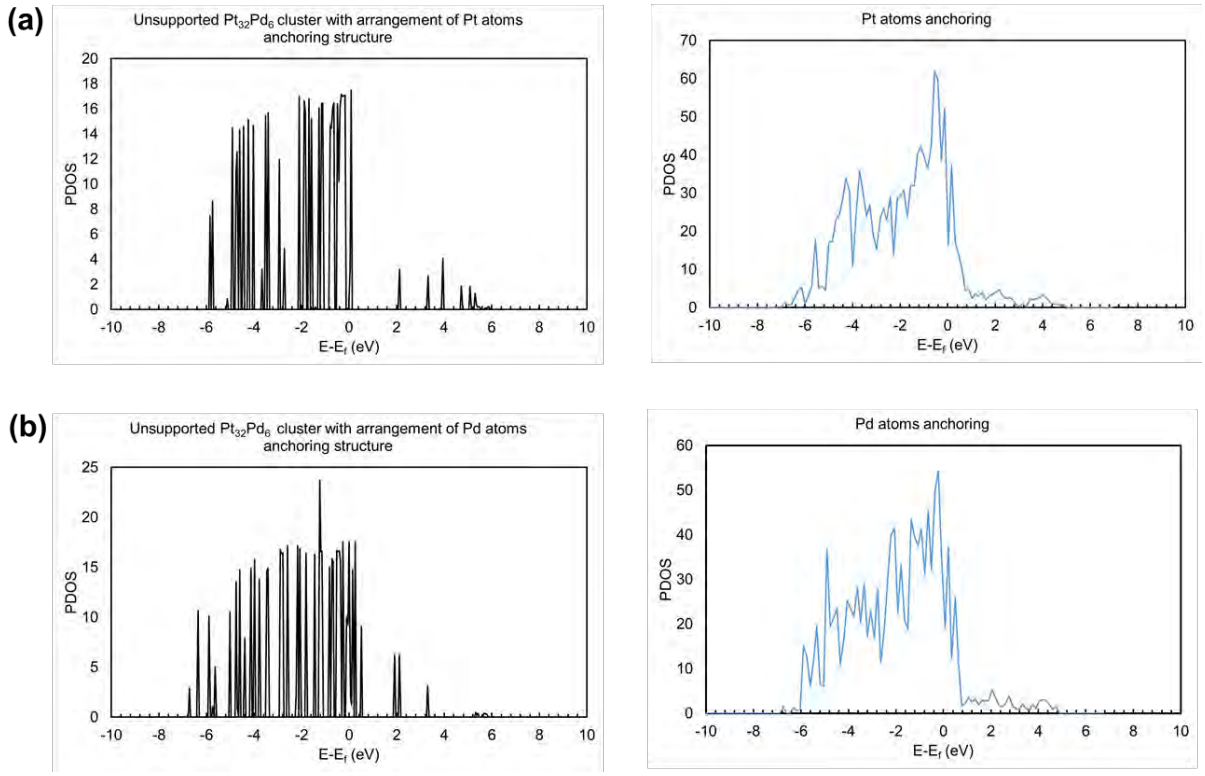


Figure 7.9: PDOS analysis of the $Pt_{32}Pd_6$ cluster: (a) $Pt_{32}Pd_6$ cluster adsorbed on Nb-doped partially reduced $TiO_2$(110) surface through Pt atoms as anchoring atoms and (b) $Pt_{32}Pd_6$ cluster adsorbed on Nb-doped partially reduced $TiO_2$(110) through Pd atoms as anchoring atoms. The graphs in black are for the unsupported $Pt_{32}Pd_6$ cluster and the blue graphs are for the $Pt_{32}Pd_6$ cluster after adsorption on the support. The energy scale is relative to the Fermi level.

### 7.5.2.4 d-band analysis

The d-band centre, d-band filling and the coupling matrix between the metal states and adsorbate states have been identified as reactivity descriptors for a metal to form bonds to adsorbates (Ruban et al., 1997). The d-band centre, d-band width and the d-band filling for the overall $Pt_{32}Pd_6$ cluster, the facet interacting with the support and the opposite facet to that interacting with the support were considered for analysis in the present chapter. The d-band centre, d-band filling and d-band width were calculated using the same methods presented in section 4.3.6.

The same geometries considered for PDOS analysis are also considered for analysis of reactivity. For supported nanoparticles the reactivity of the facets of the particle exposed and available to reactants is important. Therefore, to characterise the reactivity of facets available to reactants we consider the reactivity of the opposite facet to the one interacting with the

support as representative of the reactivity of other facets. Results for d-band analysis on the subsurface model of Nb-doped partially reduced $TiO_2$(110) surface are presented in Table 7.2.

Table 7.2: Calculated d-band centre relative to the Fermi level, d-band filling and d-band width for the $Pt_{32}Pd_6$ cluster adsorbed on the subsurface model (Nb located in second layer) of Nb-doped partially reduced $TiO_2$(110) surface.

| | $\varepsilon_d - \varepsilon_F$ (eV) | $f_d$ | $w_d$ (eV) |
|---|---|---|---|
| **Unsupported $Pt_{32}Pd_6$ cluster arrangement with Pt atoms anchoring arrangement** | | | |
| overall cluster | -1.82 | 0.93 | 2.73 |
| interacting facet | -1.89 | 0.95 | 2.68 |
| opposite facet | -1.73 | 0.96 | 2.46 |
| **Supported $Pt_{32}Pd_6$ cluster arrangement with Pt atoms anchoring** | | | |
| overall cluster | -1.91 | 0.85 | 2.78 |
| interacting facet | -2.06 | 0.86 | 2.95 |
| opposite facet | -1.73 | 0.84 | 2.54 |
| **Unsupported $Pt_{32}Pd_6$ cluster arrangement with Pd atoms anchoring arrangement** | | | |
| overall cluster | -1.88 | 0.88 | 2.73 |
| interacting facet | -1.70 | 0.91 | 2.40 |
| opposite facet | -1.94 | 0.89 | 2.74 |
| **Supported $Pt_{32}Pd_6$ cluster arrangement with Pd atoms anchoring** | | | |
| overall cluster | -1.92 | 0.85 | 2.81 |
| interacting facet | -1.69 | 0.88 | 2.44 |
| opposite facet | -1.89 | 0.85 | 2.76 |

The difference in d-band centre of 0.06 eV for the unsupported $Pt_{32}Pd_6$ cluster for the different arrangements, i.e. Pt atoms anchoring arrangement and Pd atoms anchoring arrangement indicate that the d-band centre is dependent on the arrangement of the alloy constituent elements. Thus, for the same bimetallic Pt-Pd alloy composition, the electronic properties and reactivity of the alloy can vary depending on the arrangement of alloy constituent elements.

Upon adsorption of the $Pt_{32}Pd_6$ cluster to the support through interaction with the Pt atoms anchoring and Pd atoms anchoring structure there is a small downward shift of the d-band centre of the overall cluster relative to that of the unsupported $Pt_{32}Pd_6$ cluster. The shift of the d-band centre of the overall cluster is: 0.09 eV for interaction through Pt atoms and 0.04 eV for interaction through Pd atoms. The small downshift of the d-band centre of the overall cluster upon adsorption on the support would suggest small changes to the d-band of the $Pt_{32}Pd_6$ cluster but the PDOS profile in Figure 7.9 indicates that there is substantial change to the d-band of the $Pt_{32}Pd_6$ cluster upon binding to the support. Thus, despite the small shift in d-band centre of the supported $Pt_{32}Pd_6$ cluster, the $Pt_{32}Pd_6$ cluster still interacts with the support through the d-band.

The change in d-band centre for the interacting facet for the $Pt_{32}Pd_6$ cluster interacting via Pt atoms is a downshift of 0.17 eV. The corresponding change in d-band centre for the interacting facet of the $Pt_{32}Pd_6$ cluster interacting with the support through Pd atoms is 0.01 eV (which for all intents and purposes can be regarded as equivalent to no change). The different change in d-band centre of the $Pt_{32}Pd_6$ cluster depending on the interacting facet indicates that interaction of the cluster with the support is dependent on the arrangement of Pt and Pd atoms within the $Pt_{32}Pd_6$ cluster. Interaction through Pd atoms as anchoring atoms leaves the d-band centre of the interacting facet almost unperturbed relative to the d-band centre of the same facet for the unsupported $Pt_{32}Pd_6$ cluster. Interaction through Pt atoms as anchoring atoms does perturb the d-band centre of the interacting facet relative to the d-band centre of the same facet for the unsupported $Pt_{32}Pd_6$ cluster.

Analysis of the d-band centre for the opposite facet to the one interacting with the support indicates that the d-band centre of the opposite facet for the $Pt_{32}Pd_6$ cluster interacting with the support through Pt atoms anchoring is virtually unchanged. Therefore, it can be expected that the reactivity of the $Pt_{32}Pd_6$ cluster which interacts through Pt atoms to the subsurface model of the Nb doped partially reduced $TiO_2$(110) will have similar reactivity to the unsupported $Pt_{32}Pd_6$ cluster with the same arrangement. This is due to the same d-band centre of the opposite facet for both the supported and unsupported $Pt_{32}Pd_6$ cluster with the arrangement of the Pt atoms anchoring structure. On the contrary, there is a small upward shift of 0.05 eV of the d-band centre of the opposite facet of the $Pt_{32}Pd_6$ cluster interacting with the support through Pd atoms as anchoring atoms. The upward shift of 0.05 eV of the d-band centre is small hence the supported cluster maybe expected to have similar reactivity to that of the unsupported $Pt_{32}Pd_6$ cluster.

The d-band filling of the supported $Pt_{32}Pd_6$ cluster is lower than the d-band filling for the unsupported $Pt_{32}Pd_6$ cluster for both different arrangements. This is despite overall charge transfer to the $Pt_{32}Pd_6$ cluster upon adsorption on the subsurface model of the Nb-doped partially reduced $TiO_2$(110) surface. The difference in d-band filling between the unsupported and the supported $Pt_{32}Pd_6$ cluster is higher for the Pt anchoring atoms structure, and this is probably due to the higher amount of charge transfer to the surface of the $Pt_{32}Pd_6$ cluster for this arrangement than for the Pd atoms anchoring structure.

## 7.6 Conclusions

Pd was found to segregate to the cluster-support interface depending on location of Nb atoms within the structure of the partially reduced $TiO_2$(110) surface. Positioning of Nb in the second and third layers of the 4 layer thick partially reduced $TiO_2$(110) surface slab result in a thermodynamic driving force for Pd segregation towards the cluster-support interface, thereby exposing a higher concentration of Pt atoms on the surface of the $Pt_{32}Pd_6$ cluster.

The binding energy of the $Pt_{32}Pd_6$ cluster to the support is enhanced on the Nb-doped partially reduced $TiO_2$(110) surface than on the partially reduced $TiO_2$(110) surface without Nb. The presence of Nb dopant atoms within the partially reduced $TiO_2$(110) surface results in enhanced charge transfer to the $Pt_{32}Pd_6$ cluster compared to charge transfer from the partially reduced $TiO_2$(110) surface. The quantity of charge transfer to the $Pt_{32}Pd_6$ cluster increases as Nb dopant atoms are positioned away from surface and are located in the 2$^{nd}$ and 3$^{rd}$ layers of the partially reduced $TiO_2$(110) surface.

The presence of the Nb atoms within the partially reduced $TiO_2$(110) surface changes the electronic structure of the partially reduced $TiO_2$(110) surface as evidenced by appearance of a peak in the band gap. Interaction of the $Pt_{32}Pd_6$ cluster with the Nb-doped partially reduced $TiO_2$(110) surface with Nb in the second layer result in the $Pt_{32}Pd_6$ cluster attaining metallic characteristics due to a continuous d-band.

From d-band analysis in the present chapter, it is observed that despite changing the d-band structure of the $Pt_{32}Pd_6$ cluster, interaction of the $Pt_{32}Pd_6$ cluster with the subsurface model of Nb-doped partially reduced $TiO_2$(110) surface is expected not to significantly change the reactivity of the supported $Pt_{32}Pd_6$ cluster. The reactivity of the supported $Pt_{32}Pd_6$ cluster is expected to resemble that of the unsupported $Pt_{32}Pd_6$ cluster due to the similar d-band centre of the opposite facet for both the supported and unsupported $Pt_{32}Pd_6$ cluster. However, due

to the thermodynamic driving force towards Pd segregation towards the cluster-support interface when Nb is positioned in the 2nd and 3rd layers of the partially reduced $TiO_2$(110) surface, it is expected that the supported $Pt_{32}Pd_6$ cluster may display different reactivity to the free standing $Pt_{32}Pd_6$ cluster. The difference in reactivity is expected to be due to a different arrangement of the free and supported $Pt_{32}Pd_6$ cluster. For the supported $Pt_{32}Pd_6$ cluster there is a higher concentration of Pt atoms exposed on the surface of the $Pt_{32}Pd_6$ cluster compared to the free standing $Pt_{32}Pd_6$ cluster. In addition, the d-band centre of the exposed facets of the $Pt_{32}Pd_6$ cluster supported on the Nb-doped partially reduced $TiO_2$(110) surface is different to those of the facets of the free standing $Pt_{32}Pd_6$ cluster. Thus, a difference in reactivity can be expected for the $Pt_{32}Pd_6$ cluster supported on the Nb-doped partially reduced $TiO_2$(110) compared to the free unsupported $Pt_{32}Pd_6$ cluster because of different adsorption strength of adsorbate molecules between the two.

# 7.7 References

Arbiol, J., Cerdá, J., Dezanneau, G., Cirera, A., Peiró, F., Cornet, A. & Morante, J.R. (2002) Effects of Nb doping on $TiO_2$ anatase-to-rutile phase transition. *J. Appl. Phys*. **92**, 853-861.

Bader, R.F.W. (1991) A quantum theory of molecular structure and its applications. *Chem. Rev.* **91**, 893-928.

Bernasik, A., Radecka, M., Rekas, M. & Sloma, M. (1993) Electrical properties of Cr- and Nb-doped $TiO_2$ thin films. *Appl. Surf. Sci.* **65**, 240-245.

Blöchl, P.E. (1994) Projector augmented-wave method. *Phys. Rev. B* **50**, 17953-17979.

Chevallier, L., Bauer, A., Cavaliere, S., Hui, R., Roziére, J. & Jones, D.J. (2012) Mesoporous nanostructured Nb-doped titanium dioxide microsphere catalyst supports for PEM fuel cell electrodes. *ACS Appl. Mater. Interfaces* **4**, 1752-1759.

Dudarev, S.L., Botton, G.A., Savrasov, S.Y., Humphreys, C.J. & Sutton, A.P. (1998) Electron-energy-loss spectra and the structural stability of nickel oxide: An LSDA + U study. *Phys. Rev. B* **57**,1505-1509.

Dunnill, C.W., Kafizas, A. & Parkin, I.P. (2012) CVD production of doped titanium dioxide thin films. *Chem. Vap. Deposition* **18**, 89-101.

Elsässer, C., Fähnle, M., Chan, C.T. and Ho, K.M. 1994. 'Density-functional energies and forces with Gaussian-broadened fractional occupations'. *Phys. Rev. B* 49: 13975-13978.

Fu, C.L. & Ho, K.M. (1983) First-principles calculation of the equilibrium ground-state properties of transition metals: Applications to Nb and Mo. *Phys. Rev. B* **28**, 5480-5486.

Gao, Y. (1999) In-situ IR and spectroscopic ellipsometric analysis of growth process and structural properties of $Ti_{1-x}Nb_xO_2$ thin films by metal-organic chemical vapor deposition. *Thin Solid Films* **346**, 73-81.

Han, Y., Zhang, M., Li., W. & Zhang, J. (2012) Effect and $TiO_2$ support on the structural and electronic properties of $Pd_mAg_n$ clusters: a first-principles study. *Phys. Chem. Chem. Phys*. **14**, 8683-8692.

Henkelman, G., Arnaldsson, A. & Jónsson, H. (2006) A fast and robust algorithm for Bader decomposition of charge density. *Comput. Mater. Sci*. **36**, 354-360.

Huang, S., Ganesan, P. & Popov, B.N. (2010) Electrocatalytic activity and stability of niobium-doped titanium oxide supported platinum catalyst for polymer electrolyte membrane fuel cells. *Appl. Catal. B: Environmental* **96**, 224-231.

Jiang, D., Overbury, S.H. & Dai, S. (2012) Structures and energetics of Pt clusters on $TiO_2$: interplay between metal-metal bonds and metal-oxygen bonds. *J. Phys. Chem. C* **116**, 21880-21885.

Kresse, G. & Furthmüller, J. (1996a) Efficiency of ab-initio total energy calculations for metals and semiconductors using a plane-wave basis set. *Comput. Mater. Sci*. **6**, 15-50.

Kresse, G. & Furthmüller, J. (1996b) Efficient iterative schemes for ab-initio total-energy calculations using a plane wave basis set. *Phys. Rev. B* **54**, 11169-11186.

Kresse, G. & Jourbert, D. (1999) From ultrasoft pseudopotentials to the projector augmented-wave method. *Phys. Rev. B* **59**, 1758-1775.

Kresse, G. & Hafner, J. (1994) Ab initio molecular-dynamics simulation of the liquid-metal-amorphous-semi-conductor transition on germanium. *Phys. Rev. B* **49**, 14251-14269.

Kresse, G. & Hafner, J. (1993) Ab initio molecular dynamics for liquid metals. *Phys. Rev. B* **47**, 558-561.

Liu, X., Wu, X. & Scott, K. (2014) Study of niobium and tantalum doped titania-supported Pt electrocatalysts for methanol oxidation and oxygen reduction reactions. *Catal. Sci. Technol*. **4**, 3891-3898.

Monkhorst, H.J. & Pack, J.D. (1976) Special points for Brillouin-zone integrations. *Phys. Rev. B* **13**, 5188-5192.

Morgan, B.J., Scanlon, D.O. & Watson, G.W. (2009) Small polarons in Nb- and Ta-doped rutile and anatase $TiO_2$. *J. Mater. Chem*. **19**, 5175-5178.

Morgan, B.J., Scanlon, D.O. & Watson, G.W. (2011) Comment on 'Generalized gradient approximation +U study for metallization mechanism of niobium-doped anatase titanium dioxide' [Jpn. J. Appl. Phys. 49 (2010) 055801]. *Jpn. J. Appl. Phys*. **50**, 069101-069103.

Morris, D., Dou, Y., Rebane, J., Mitchell, C.E.J., Egdell, R.G., Law, D.S.L., Vittadini, A. & Casarin, M. (2000) Photoemission and STM study of the electronic structure of Nb-doped $TiO_2$. *Phys. Rev. B* **61**, 13445-13457.

Orita, N. (2010) Generalised gradient approximation + U study for metallization mechanism of Niobium-doped anatase titanium dioxide. *Jpn. J. Appl. Phys*. **9**, 055801-055806.

Park, K. & Seol, K. (2007) Nb-$TiO_2$ supported Pt cathode catalyst for polymer electrolyte membrane fuel cells. *Electrochem. Commun*. **9**, 2256-2260.

Perdew, J.P., Chevary, J.A., Vosko, S.H., Jackson, K.A., Pederson, M.R., Singh, D.J. & Fiolhais, C. (1992) Atoms, molecules, solids, and surfaces: applications of the generalized gradient approximation for exchange and correlation. *Phys. Rev. B* **46**, 6671-6686.

Ruban, A., Hammer, B., Stolze, P., Skriver, H.L. & Nørskov, J.K. (1997) Surface electronic structure and reactivity of transition and noble metals. *J. Mol. Catal. A: Chemical* **115**, 421-429.

Sheppard, L.R., Dittrich, T. & Nowotny, M.K. (2012) The impact of niobium surface segregation on charge separation in niobium-doped titanium dioxide. *J. Phys. Chem. C* **116**, 20923-20929.

Sanville, E., Kenny, S.D., Smith, R. & Henkelman, G. (2007) Improved grid-based algorithm for Bader charge allocation. *J. Comput. Chem*. **28**, 899-908.

Tang, W., Sanville, E. & Henkelman, G. (2009) A grid-based Bader analysis algorithm without lattice bias. *J. Phys.: Condens. Matter* **21**, 084204-084211.

Tripković, V., Abild-Pedersen, F., Studt, F., Cerri, I., Nagami, T., Bligaard, T. & Rossmeisl, J. (2012) Metal oxide-supported platinum overlayers as proton-exchange membrane fuel cell cathodes. *ChemCatChem* **4**, 228-235.

Valenzuela, E., Ramos-Sanchez, V., Arista, A.A.L. & Savadogo, O. (2013) Nanostructured $TiO_2$ doped with Nb as a novel support for PEMFC. *Hindawi Publishing Corporation J. Mater*. : 1-6.

Wang, Y., Wilkinson, D.P., Guest, A., Neburchilov, V., Baker, R., Nan, F., Botton, G.A. & Zhang, J. (2013) Synthesis of Pd and Nb-doped $TiO_2$ composite supports and their corresponding Pt-Pd alloy catalysts by a two-step procedure for the oxygen reduction reaction. *J. Power Sources* **221**: 232-241.

Xia, X., Jones, G., Sarwar, M., Tang, Q., Harkness, I. & Thompsett, D. (2015) A DFT study of Pt layer deposition on catalyst supports of titanium oxide, nitride and carbide. *J. Mater. Chem. A* **3**, 24504-24511.

Yamada, N., Hitosugu, T., Hoang, N.L.H., Furubayashi, Y., Hirose, Y., Konuma, S., Shimada, T. & Hasegawa, T. (2008) Structural, electrical and optical properties of sputter-deposited Nb-doped $TiO_2$ (TNO) polycrystalline films. *Thin Solid Films* **516**, 5754-5757.

# Chapter 8: Comparison between graphene and $TiO_2$ based supports

In this chapter comparison is made between the $Pt_{38}$ cluster supported on graphene based supports (i.e. pristine, monovacancy defective, OH and COOH functionalised graphene) and $TiO_2$ based supports (stoichiometric, partially reduced and hydroxylated $TiO_2$(110) surfaces). A similar comparison is also made for the $Pt_{32}Pd_6$ cluster supported on graphene based supports and the Nb-doped partially reduced $TiO_2$(110) surface.

## 8.1 $Pt_{38}$ on graphene and $TiO_2$ supports

Table 8.1 summarises the major results obtained for the $Pt_{38}$ cluster supported on graphene based supports and $TiO_2$ based supports. The adsorption geometries of the $Pt_{38}$ cluster adsorbed on the various supports are presented in Figure 8.1.

Table 8.1: Summary of the binding energy, change in d-band centre relative to the Fermi level and metal-cluster bond lengths for the $Pt_{38}$ cluster adsorbed on graphene and $TiO_2$ supports. (for the $\Delta\ \varepsilon_d - \varepsilon_F$ results, negative change corresponds to a downshift and a positive change corresponds to an upward shift of the d-band centre)

| | **Graphene based supports** | | | | **$TiO_2$(110) based supports** | | |
|---|---|---|---|---|---|---|---|
| | pristine | monovacancy | OH functionalised | COOH functionalised | stoichiometric | Partially reduced | hydroxylated |
| Interacting facet | square | hexagonal | square | hexagonal | square | hexagonal | hexagonal |
| $E_{bind}$ (eV) | 0.14 | -6.67 | -1.64 | -1.43 | -2.73 | -9.05 | -0.50 |
| Overall cluster | | | | | | | |
| $\Delta\ \varepsilon_d - \varepsilon_F$ (eV) | -0.11 | -0.18 | -0.33 | -0.23 | -0.10 | -0.15 | -0.05 |
| Interacting facet | | | | | | | |
| $\Delta\ \varepsilon_d - \varepsilon_F$ (eV) | -0.35 | -0.32 | -0.50 | 0.06 | -0.25 | -0.04 | 0.24 |
| Opposite facet | | | | | | | |
| $\Delta\ \varepsilon_d - \varepsilon_F$ (eV) | 0.41 | 0.28 | -0.17 | 0.14 | 0.02 | 0.31 | 0.36 |
| Metal-cluster distances (Å) | | | | | | | |
| | **Pt-C** | **Pt-C** | **Pt-C** | **Pt-C** | **Pt-$O_{2C}$** | **Pt-$O_{2C}$** | **Pt-$O_{2C}$** |
| | 2.19 | 2.25, 2.26, | 2.17, 2.16 | 2.15, 2.20 | 2.07, 2.08 | 1.97, 2.17 | 2.11, 2.15 |
| | 2.20 | 2.29 | 2.24, 2.25 | 2.29 | 2.10 | 2.20 | 2.41 |
| | | | 2.26 | | | | |
| | | | | | **Pt-$Ti_{5C}$** | **Pt-$Ti_{5C}$** | **Pt-$Ti_{5C}$** |
| | | | | | 2.82, 2.50 | 2.68, 2.70 | 2.55 |
| | | | | | | 2.79, 2.84 | |
| | | | | | | 2.86 | |

The calculated change in d-band centre relative to the Fermi level in Table 8.1 is the difference in d-band centre for the supported $Pt_{38}$ cluster relative to the d-band centre of the free unsupported $Pt_{38}$ cluster.

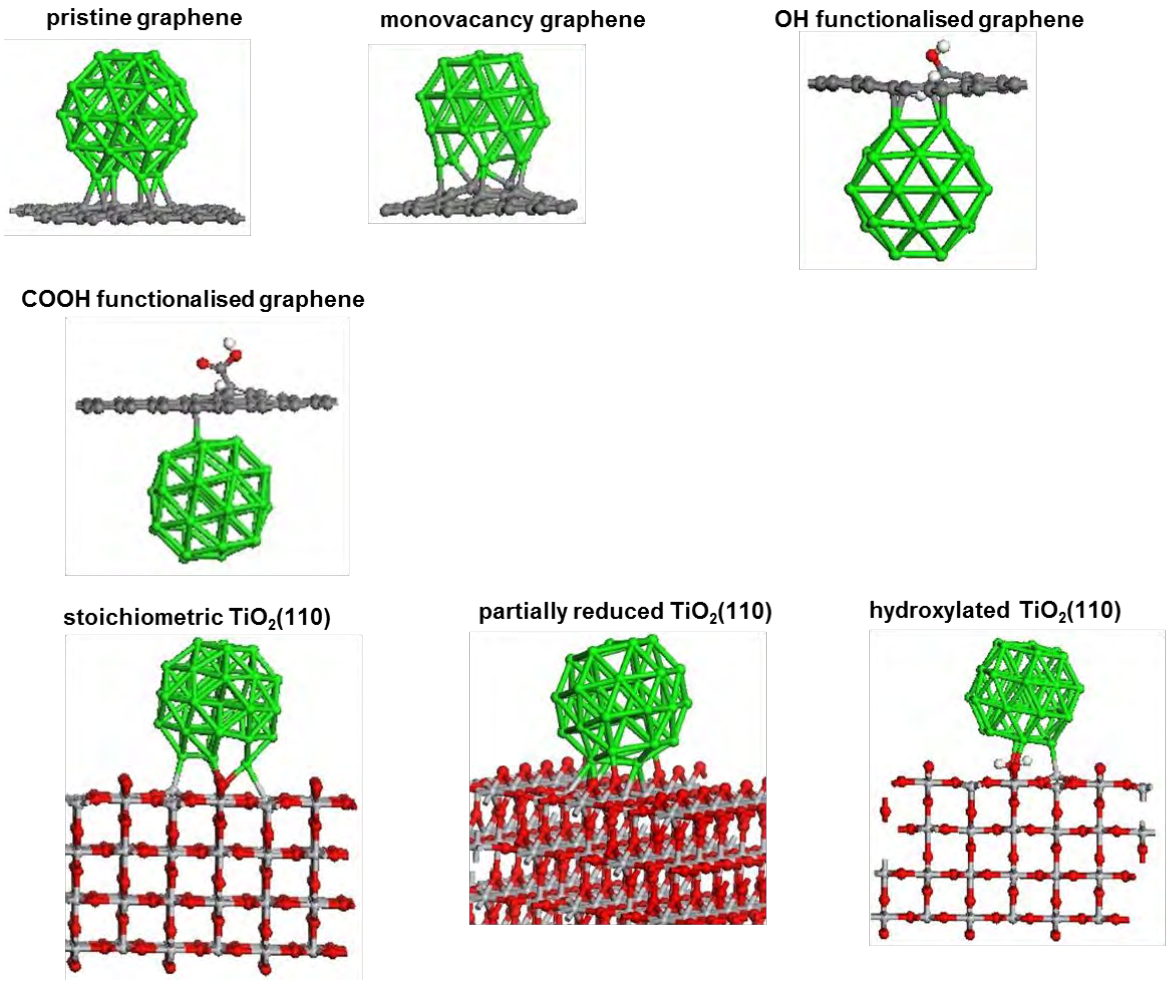


Figure 8.1: Adsorption geometry of the $Pt_{38}$ cluster adsorbed on the different graphene and $TiO_2$ supports.

The calculated binding energies (see Table 8.1) of the $Pt_{38}$ cluster on the graphene based supports follows the trend: monovacancy > OH functionalised graphene > COOH functionalised graphene > pristine graphene. The highly exothermic binding energies on the defect containing graphene indicates that the $Pt_{38}$ cluster is attached strongly to the support in the presence of defects than on pristine graphene. The weaker binding energy on pristine graphene imply likelihood of cluster detachment from the support whilst the enhanced binding on defect containing graphene imply less likelihood of cluster detachment from support compared to pristine graphene. The binding energies on $TiO_2(110)$ based supports follow the order: partially reduced $TiO_2(110)$ > stoichiometric $TiO_2(110)$ > hydroxylated $TiO_2(110)$. The hydrogen adatoms on the hydroxylated $TiO_2(110)$ result in weaker binding of the $Pt_{38}$ cluster to the support relative to adsorption on the stoichiometric $TiO_2(110)$ surface. The energy difference of -8.55 eV between $Pt_{38}$ on hydroxylated $TiO_2(110)$ and $Pt_{38}$ on partially reduced $TiO_2(110)$ imply that upon deposition of $Pt_{38}$ on hydroxylated $TiO_2(110)$ there will be dehydrogenation of the hydroxyl groups resulting in $Pt_{38}$ on partially reduced $TiO_2(110)$. The

calculated binding energies of the $Pt_{38}$ cluster on the $TiO_2$(110) surfaces except on hydroxylated $TiO_2$(110) are more exothermic than on graphene based supports. This indicates that the $Pt_{38}$ cluster is attached strongly to the stoichiometric and partially reduced $TiO_2$(110) surfaces than on pristine graphene, monovacancy graphene, OH and COOH functionalised graphene. The implication of which is the probability of particle detachment from the $TiO_2$ based supports is lower than on the graphene based supports.

It can be expected that the $Pt_{38}$ cluster will be located at the defect sites on graphene based supports as opposed to the defect free sites of the support. For the $Pt_{38}$ cluster to diffuse from a defect site to a defect free (i.e. pristine) site of the graphene support at least an activation energy greater than or equal to the difference in binding energy of the $Pt_{38}$ cluster at the defect site and on the defect free site has to be overcome. The difference in energy between the defect and defect free sites on graphene are as follows: monovacancy graphene (6.81 eV) > OH functionalised graphene (1.78 eV) > COOH functionalised graphene (1.57 eV). The minimum activation energies (which is equivalent to the difference in binding energy between the two sites) to be overcome for the diffusion of the $Pt_{38}$ cluster from a defect site to a defect free site on the graphene support are high and thus likely not feasible. Thus, the $Pt_{38}$ cluster is expected to be trapped at the monovacancy site and at the OH and COOH functional group sites. On the $TiO_2$(110) surfaces, the energy difference between a surface oxygen bridge vacancy site (i.e. partially reduced) and stoichiometric site of the support is 6.32 eV and the difference with the hydroxylated site is 2.23 eV. Hence, on the $TiO_2$(110) surfaces the $Pt_{38}$ cluster is expected to be located at the vacancy site as opposed to a defect free site (i.e. stoichiometric) or hydroxylated surface with hydrogen adatoms on the surface.

The facet of approach of the $Pt_{38}$ cluster to the support depends on the type of defect on graphene based supports whilst on $TiO_2$ based support the facet of approach is independent of the defect type. Pt-C bonds are less strong compared to the cohesive energy of Pt (Maiti & Ricca, 2004) meaning Pt-Pt bonds are stronger than Pt-C bonds, thus the preferred approach of the $Pt_{38}$ cluster to the pristine graphene support is the one which minimises Pt-C bonds. Approach of the $Pt_{38}$ cluster to pristine graphene through the square facet result in fewer Pt-C bonds than the hexagonal facet, hence the square facet binds stronger. On monovacancy graphene, the hexagonal facet is more stable than the square facet. The hexagonal facet approach result in stronger binding due to achieving maximum contact between the $Pt_{38}$ cluster and the dangling bonds at the vacancy site, thus resulting in a stable adsorption state.

On functionalised graphene, approach from underneath on the side not bearing the functional group is more stable than atop approach where there is direct bonding to the functional group.

For the bottom approach of the $Pt_{38}$ cluster, there is bonding to the modified carbon atoms around the attached functional group, this is absent for the atop approach. On OH functionalised graphene, the square facet approach of the $Pt_{38}$ cluster lead to the most stable adsorption state. On the contrary, on COOH functionalised graphene the hexagonal facet lead to the most stable adsorption state. From Figure 8.1 it can be observed that on COOH functionalised graphene the $Pt_{38}$ cluster is adsorbed in a tilted configuration, not all 7 atoms of the hexagonal facet are close to and bonding to the support.

Adsorption on $TiO_2$(110) based surfaces of $Pt_{4-6}$ clusters has been observed to be dependent on maximisation of Pt-O and Pt-Ti bonds on the surface (Jiang et al., 2012). On the partially reduced and hydroxylated $TiO_2$(110) surfaces the facet of approach of the $Pt_{38}$ cluster is the hexagonal facet which maximises formation of Pt-O and Pt-Ti bonds on the surface. The optimised geometries of the $Pt_{38}$ cluster on the partially reduced and hydroxylated $TiO_2$(110) surfaces have the $Pt_{38}$ cluster tilted in order to maximise contact with the support (see Figure 8.1). On the stoichiometric $TiO_2$(110) surface, approach through the square facet is the most stable adsorption state. From Figure 8.1 it is also observed that the $Pt_{38}$ cluster on the stoichiometric $TiO_2$(110) surface is tilted. The tilted configuration is to ensure that the $Pt_{38}$ cluster is closer to the surface Ti atoms to ensure formation of Pt-Ti bonds which stabilises binding of the cluster to the support.

In general, the $Pt_{38}$ cluster is optimised closer to the support on the $TiO_2$ based supports than on the graphene based supports. The Pt-$O_{2c}$ bond lengths calculated on the $TiO_2$ based supports are shorter than the Pt-C bond lengths calculated on the graphene based supports. The shorter distance of the $Pt_{38}$ cluster to the support on the $TiO_2$ based supports (excluding hydroxylated $TiO_2$(110)) correlates with stronger binding of the $Pt_{38}$ cluster to the $TiO_2$ supports compared to the graphene supports. In addition, the $Pt_{38}$ cluster on the $TiO_2$ based supports form bonds to more than one species, i.e. oxygen and titanium atoms whilst on the graphene based supports the $Pt_{38}$ cluster binds only to carbon atoms. Thus, the stronger binding on the $TiO_2$ based supports can be attributed to formation of more than one kind of bond at the interface (i.e. Pt-O and Pt-Ti) compared to Pt-C bonds on the graphene based supports.

OH and COOH functionalised graphene affects the electronic properties of the supported $Pt_{38}$ cluster differently. This is manifested by the different change in d-band centre of the entire cluster, interacting and opposite facets presented in Table 8.1. The binding of adsorbates (e.g. $O_2$, CO, $H_2$) to metal surfaces is known to be correlated to the d-band centre of the metal. Nørskov et al. (2009) state as a rule ‘‘the higher in energy the d-states relative to the Fermi level of a metal, the stronger the interaction with adsorbate states’’. This rule thus allows for

inferences to be drawn about the reactivity of metals towards adsorbate molecules by looking at shifts in the d-band centre of the metal. In addition, this analysis has been extended to the adsorption of molecules on clusters supported on graphene based supports and found to be applicable. Lim & Wilcox (2012) showed through DFT calculations that the adsorption strength of oxygen reduction reaction (ORR) intermediates (e.g. $O_2$, $O_2H$, OH and $H_2O$) on a $Pt_{13}$ cluster supported on monovacancy graphene were weaker compared to adsorption on the unsupported $Pt_{13}$ cluster due to shift of the d-band centre of the cluster to more negative values. Similarly, Kim et al. (2012) observed from DFT calculations that the adsorption energy of $H_2$, CO and OH on $Pt_{1,4,6}$ clusters supported on strained graphene were correlated to the d-band centre of the cluster, upward shift of the d-band centre of the cluster corresponded to stronger binding of the adsorbates whilst downward shift of the d-band centre correlated with weaker binding of the adsorbates. Therefore, in the present study the d-band centre change of the opposite facet to the one interacting with the support was used as descriptor of activity of the supported $Pt_{38}$ cluster. The opposite facet is used to assess reactivity of the supported cluster since this facet is considered to be representative of the facets of the cluster exposed and available to adsorbate molecules.

It can be expected that the reactivity of the $Pt_{38}$ cluster with adsorbate molecules will be different between the OH and COOH functionalised graphene supported cluster. This is due to different changes in d-band centre of the opposite facets on the two supports (see Table 8.1). The downward shift of 0.17 eV of the d-band centre of the opposite facet of the $Pt_{38}$ cluster on OH functionalised graphene is expected to weakly bind adsorbate molecules compared to adsorption on COOH functionalised graphene where there is an upward shift of 0.14 eV on the opposite facet of the $Pt_{38}$ cluster.

The stoichiometric $TiO_2$(110) surface is expected not to significantly alter the reactivity of the supported $Pt_{38}$ cluster due to a small upward shift of 0.02 eV of the d-band centre of the opposite facet. On the partially reduced and hydroxylated $TiO_2$(110) surfaces, the extent of upward shift of the d-band centre of the opposite facet (0.31 eV and 0.36 eV respectively) is higher than that obtained on OH functionalised (-0.17 eV) and COOH functionalised (0.14 eV) graphene supports. Therefore, adsorbate molecules are expected to bind stronger to the $Pt_{38}$ cluster supported on the partially and hydroxylated $TiO_2$(110) surfaces than on the $Pt_{38}$ cluster supported on OH and COOH functionalised graphene. It is worth noting that despite destabilisation of the binding of the $Pt_{38}$ cluster on the hydroxylated $TiO_2$(110) surface, the binding of adsorbate molecules on the $Pt_{38}$ cluster supported on the hydroxylated $TiO_2$(110) surface is expected to be identical to that of the $Pt_{38}$ cluster supported on the partially reduced

$TiO_2$(110) surface. This is due to similar shifts of the d-band centre of the opposite facet of the $Pt_{38}$ cluster supported on the partially reduced and hydroxylated $TiO_2$(110) surfaces.

The implications for catalyst support choice from the $Pt_{38}$ results are the following: By supporting the $Pt_{38}$ cluster on either OH or COOH functionalised graphene, different reactivity of the supported $Pt_{38}$ cluster may be obtained. The OH functionalised graphene offers enhanced binding of the $Pt_{38}$ cluster to the support compared to binding on COOH functionalised graphene. The implication of the enhanced binding is that the $Pt_{38}$ cluster is less likely to detach from the OH functionalised graphene support than on COOH functionalised graphene support. In turn binding on COOH functionalised graphene is enhanced compared to pristine graphene.

Catalyst poisons like CO are expected to bind stronger to the $Pt_{38}$ cluster supported on COOH functionalised graphene than on the $Pt_{38}$ cluster supported on OH functionalised graphene. Thus, supporting the $Pt_{38}$ cluster on OH functionalised graphene may result in less catalyst poisoning than supporting on COOH functionalised graphene, and in turn may also aid in improving the activity of the catalyst. Weaker binding of adsorbates on the OH functionalised graphene supported $Pt_{38}$ cluster maybe desirable in fine tuning the selectivity of the catalyst towards a desired product. The selectivity maybe different on the $Pt_{38}$ cluster supported on COOH functionalised graphene due to stronger binding of adsorbates on this support. Therefore, the choice between the OH and COOH functionalised graphene support will depend on the reaction catalysed.

Attachment of the $Pt_{38}$ cluster is enhanced more on the partially reduced and stoichiometric $TiO_2$(110) surfaces compared to pristine and functionalised graphene supports. By implication the detachment of the supported $Pt_{38}$ cluster is expected to be minimised and thus durability of the catalyst supported on the $TiO_2$ based supports is expected to be higher than for the graphene based supports. The defect free $TiO_2$(110) surface hardly changes the adsorption strength of adsorbates on the exposed facet of the $Pt_{38}$ cluster compared to the adsorption strength on the free standing $Pt_{38}$ cluster. The partially reduced $TiO_2$(110) surface offers enhanced attachment of the $Pt_{38}$ cluster to the support and subsequently result in stronger binding of adsorbates on the $Pt_{38}$ cluster adsorbed on the partially reduced $TiO_2$(110) surface. The stronger binding of adsorbates is due to the higher extent of upward shift of the d-band centre towards the Fermi level. The stronger binding of adsorbates on the $Pt_{38}$ cluster supported on the partially reduced $TiO_2$(110) surface imply higher chances of the catalyst being poisoned due to stronger binding of poison molecules to the cluster. Moreover, the

stronger binding may imply stronger binding of reaction intermediates which can either negatively or positively affect the activity and selectivity of the catalyst.

The hydroxylated $TiO_2$(110) surface is not desirable as support material for the $Pt_{38}$ cluster. The $Pt_{38}$ cluster is weakly bound on the hydroxylated $TiO_2$(110) surface which imply higher chances of particle detachment from the support, leading to a less durable catalyst. The choice between the graphene based and $TiO_2$ based supports will depend to a great extent on the reaction being catalysed.

## 8.2 $Pt_{32}Pd_6$ on graphene and $TiO_2$ supports

Table 8.2 summarises the major results obtained for the $Pt_{32}Pd_6$ cluster supported on graphene based supports and $TiO_2$ based supports. Figure 8.2 shows the adsorption geometries of the $Pt_{32}Pd_6$ cluster adsorbed on graphene based supports and the Nb-doped partially reduced $TiO_2$(110) support.

Table 8.2: Summary of the binding energy, change in d-band centre relative to the Fermi level and metal-cluster bond lengths for the $Pt_{32}Pd_6$ cluster adsorbed on the graphene and $TiO_2$ supports. (for the $\Delta\ \varepsilon_d - \varepsilon_F$ results, negative change corresponds to a downshift and a positive change corresponds to an upward shift of the d-band centre)

| | **Graphene based supports** | | | **$TiO_2$(110) based support** |
|---|---|---|---|---|
| | pristine | OH functionalised | COOH functionalised | Nb-doped partially reduced |
| Interacting facet | square | square | square | hexagonal |
| $E_{bind}$ (eV) | 0.71 | -1.94 | -1.66 | -7.10 |
| Overall cluster | | | | |
| $\Delta\ \varepsilon_d - \varepsilon_F$ (eV) | -0.25 | -0.21 | -0.17 | -0.04 |
| Interacting facet | | | | |
| $\Delta\ \varepsilon_d - \varepsilon_F$ (eV) | -0.61 | -0.41 | -0.47 | 0.01 |
| Opposite facet | | | | |
| $\Delta\ \varepsilon_d - \varepsilon_F$ (eV) | -0.06 | -0.07 | 0.05 | -0.16 |
| Metal-cluster distances (Å) | | | | |
| | **Pt-C** | **Pt-C** | **Pt-C** | **Pd-$O_{2C}$** |
| | 2.20 | 2.15, 2.16 | 2.25, 2.26 | 2.05, 1.98 |
| | 2.21 | 2.20, 2.23 | 2.30, 2.39 | |
| | 2.22 | 2.26, 2.32 | | **Pt-$Ti_{5C}$** |
| | | | | 2.53, 2.56 |
| | | | | **Pd-$Ti_{5C}$** |
| | | | | 2.77, 2.73 |
| | | | | |

Similar to adsorption of the $Pt_{38}$ cluster, binding of the $Pt_{32}Pd_6$ cluster is enhanced on OH and COOH functionalised graphene compared to binding on pristine graphene. The binding energy of the $Pt_{32}Pd_6$ cluster on the Nb-doped partially reduced $TiO_2$(110) surface is stronger than on OH and COOH functionalised graphene. The difference in binding energy of the $Pt_{32}Pd_6$ cluster adsorbed on OH and COOH functionalised graphene compared to binding on pristine graphene is 2.65 eV and 2.37 eV respectively. Thus, a minimum activation energy equivalent to the difference in energy between the functionalised site and the pristine graphene site would have to be overcome in order for the $Pt_{32}Pd_6$ cluster to diffuse from the functionalised site to the defect free site.

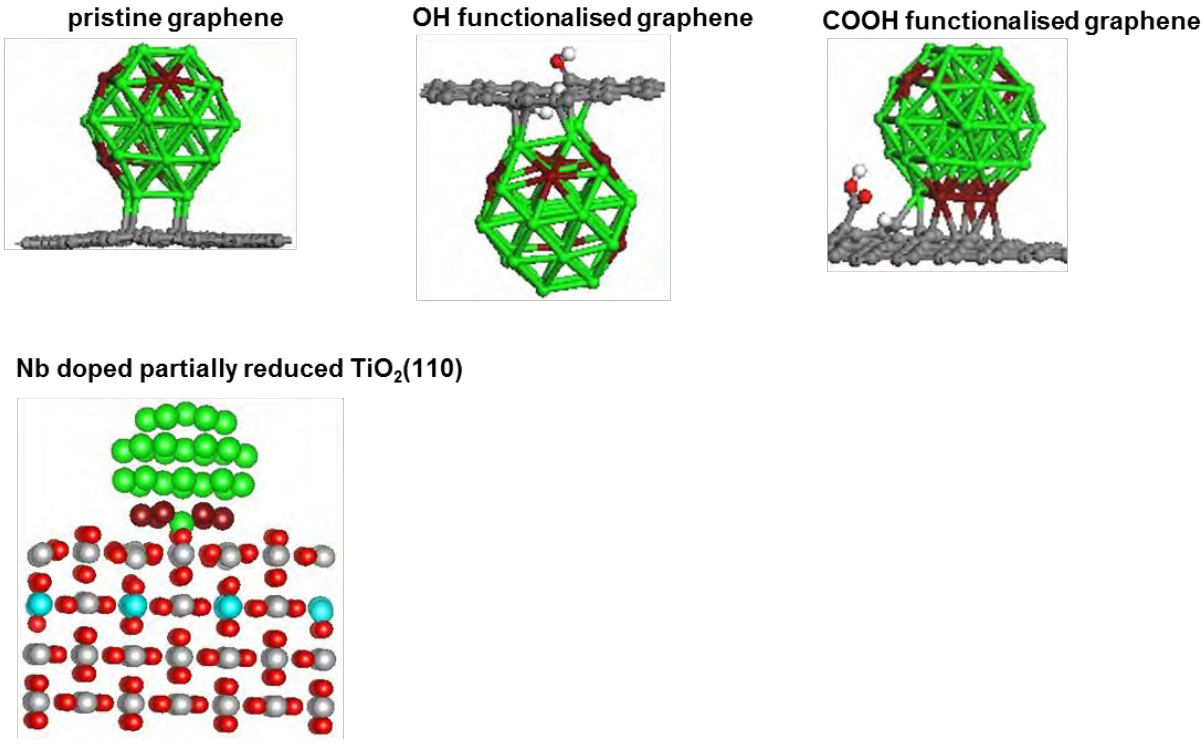


Figure 8.2: Adsorption geometries of the $Pt_{32}Pd_6$ cluster adsorbed on the graphene and $TiO_2$ based supports.

The activation energies to diffuse from the stable adsorption site at the functional group to the defect free site will be high indicating that the transition may not be feasible. Thus, the $Pt_{32}Pd_6$ cluster can be expected to be found trapped around the functional group on the graphene support than be located at the defect free sites of the graphene support.

The difference in energy between the functionalised site (i.e. OH and COOH) and the defect free site (i.e. pristine) for adsorption of the $Pt_{32}Pd_6$ cluster are higher than for adsorption of the $Pt_{38}$ cluster. For the $Pt_{32}Pd_6$ cluster the differences are: OH functionalised graphene (2.65 eV)

> COOH functionalised graphene (2.37 eV), the corresponding difference for the binding of the $Pt_{38}$ cluster are: OH functionalised graphene (1.78 eV) > COOH functionalised graphene (1.57 eV). The binding energy of the $Pt_{32}Pd_6$ cluster to OH and COOH functionalised graphene is more exothermic than the binding energy of the $Pt_{38}$ cluster to OH and COOH functionalised graphene. In contrast, the binding energy of the $Pt_{38}$ cluster to pristine graphene is less endothermic (more stable) than the binding energy of the $Pt_{32}Pd_6$ cluster to pristine graphene. Therefore, the likelihood of cluster detachment from the support is lower for the $Pt_{32}Pd_6$ cluster on the functionalised graphene support compared to the $Pt_{38}$ cluster. This is due to the stronger binding energy of the $Pt_{32}Pd_6$ cluster compared to the $Pt_{38}$ cluster on the functionalised graphene supports.

Irrespective of the functional group, the facet of approach of the $Pt_{32}Pd_6$ cluster to the graphene based supports is through the square facet. Adsorption of the $Pt_{32}Pd_6$ cluster to the Nb-doped partially reduced $TiO_2$(110) surface is through the hexagonal facet which results in maximisation of formation of Pt-Ti, Pd-Ti and Pd-O bonds on the surface. On OH functionalised graphene, the most stable adsorption geometry is of the $Pt_{32}Pd_6$ cluster approaching from underneath on the side not bearing the functional group (see Figure 8.2). For adsorption on COOH functionalised graphene, the stable adsorption geometry is where the $Pt_{32}Pd_6$ cluster approaches from the same side as the functional group but not directly bonding to the functional group.

The Pd-$O_{2c}$ distances for the $Pt_{32}Pd_6$ cluster adsorbed on the Nb-doped partially reduced $TiO_2$(110) surface are shorter than the Pt-C bond distances for the $Pt_{32}Pd_6$ cluster on the graphene based supports. This indicates that the $Pt_{32}Pd_6$ cluster is optimised closer to the Nb-doped partially reduced $TiO_2$(110) surface than the graphene based support surfaces. The shorter metal-support bond distances for the $Pt_{32}Pd_6$ cluster adsorbed on the Nb-doped partially reduced $TiO_2$(110) surface correlates with the stronger binding energy on this surface compared to the longer Pt-C distances on the graphene supports and the corresponding less exothermic binding energies.

The extent of d-band centre shift of the $Pt_{32}Pd_6$ cluster supported on functionalised graphene supports is slightly less than that of the $Pt_{38}$ cluster on the same supports. This indicates that the electronic properties of the $Pt_{32}Pd_6$ alloy cluster are modified differently to those of the monometallic $Pt_{38}$ cluster upon adsorption on the same supports. The smaller extent of d-band centre shift of the opposite facet of the $Pt_{32}Pd_6$ cluster supported on OH and COOH functionalised graphene (see Table 8.2) indicates that the support barely changes the d-band centre of the opposite facet. In comparison, there is higher shift of d-band centre of the

opposite facet of the $Pt_{38}$ cluster adsorbed on the functionalised graphene supports (see Table 8.1).

On the OH functionalised graphene support, there was no thermodynamic driving force for rearrangement of the supported $Pt_{32}Pd_6$ cluster. The preferred arrangement of the supported $Pt_{32}Pd_6$ cluster was the mixed arrangement, with Pd atoms occupying the centre of the hexagonal facets on the surface mixed with Pt atoms. This is the same preferred arrangement of the free standing unsupported $Pt_{32}Pd_6$ cluster. On the contrary, there was a thermodynamic driving force for rearrangement of the $Pt_{32}Pd_6$ cluster supported on COOH functionalised graphene. There was segregation of Pd atoms towards the cluster-support interface for the $Pt_{32}Pd_6$ cluster supported on COOH functionalised graphene (see Figure 8.2). The result of segregation of Pd towards the cluster-support interface, is higher fraction of Pt atoms are exposed on the surface of the cluster. The implication of the rearrangement of the $Pt_{32}Pd_6$ cluster supported on COOH functionalised graphene is the reactivity of the rearranged $Pt_{32}Pd_6$ cluster (with the square facet interacting with the support occupied by Pd atoms) maybe different to the reactivity of the mixed arrangement of the $Pt_{32}Pd_6$ cluster supported on OH functionalised graphene. The difference in reactivity maybe due to different arrangement of Pt and Pd atoms within the $Pt_{32}Pd_6$ cluster, this may affect the d-band properties of the different facets of the cluster.

The extent of d-band centre shift of the opposite facet for the $Pt_{32}Pd_6$ cluster supported on the Nb-doped partially reduced $TiO_2$(110) surface is higher than the d-band centre shift of the opposite facet for the $Pt_{32}Pd_6$ cluster supported on OH and COOH functionalised graphene (see Table 8.2). Thus, it can be expected that adsorbates may bind weaker on the $Pt_{32}Pd_6$ cluster supported on the Nb-doped partially reduced $TiO_2$(110) surface than on the functionalised graphene supported cluster. This is due to the higher extent of downward shift of the d-band centre of the opposite facet.

It is interesting to note that the extent of d-band centre downshift of the opposite facet of the $Pt_{32}Pd_6$ cluster supported on the Nb-doped partially reduced $TiO_2$(110) surface (-0.16 eV) is lower than the extent of upward shift of the opposite facet of the $Pt_{38}$ cluster supported on the defect containing $TiO_2$(110) surfaces (0.31 eV for partially reduced $TiO_2$(110) and 0.36 eV for hydroxylated $TiO_2$(110)). This indicates that the extent of the influence of the support in modifying the d-band properties of the facet not in direct contact with the support is lower for the $Pt_{32}Pd_6$ cluster than for the $Pt_{38}$ cluster. In addition, the binding strength of catalyst poisons such as CO is expected to be weaker on the $Pt_{32}Pd_6$ alloy cluster supported on the Nb-doped partially reduced $TiO_2$(110) surface than on the $Pt_{38}$ cluster supported on the partially reduced

or hydroxylated $TiO_2$(110) surfaces. The binding strength of adsorbates is expected to be stronger on the $Pt_{38}$ cluster supported on the partially reduced and hydroxylated $TiO_2$(110) surfaces.

On the Nb-doped partially reduced $TiO_2$(110) surface there was preferential segregation of Pd towards the cluster-support interface. The preferential segregation of Pd towards the cluster-support interface exposes more Pt atoms on the surface of the $Pt_{32}Pd_6$ cluster. This may result in different reactivity of the supported $Pt_{32}Pd_6$ cluster compared to the free unsupported $Pt_{32}Pd_6$ cluster in which the mixed alloy arrangement is preferred.

The implications for catalyst support choice from the $Pt_{32}Pd_6$ results are the following: The $Pt_{32}Pd_6$ cluster is attached strongly to the Nb-doped partially reduced $TiO_2$(110) surface than the graphene based supports. Therefore, the likelihood of particle detachment from the Nb-doped partially reduced $TiO_2$(110) surface is less compared to the graphene based supports. This implies higher durability on the Nb-doped partially reduced $TiO_2$(110) surface compared to the graphene based supports. The $Pt_{32}Pd_6$ cluster supported on Nb-doped partially reduced $TiO_2$(110) can be expected to have higher resistance to catalyst poisons compared to the $Pt_{32}Pd_6$ cluster supported on graphene based supports This is due to the expected weaker adsorption strength of adsorbates on the $Pt_{32}Pd_6$ cluster supported on Nb-doped partially reduced $TiO_2$(110) surface (manifested by the higher extent of downward shift of the d-band centre of the opposite facet) than graphene based supports.

If both alloy constituents are important for catalysing the reaction, then the OH functionalised graphene support is desirable as it does not lead to rearrangement of the $Pt_{32}Pd_6$ cluster which ensures mixed arrangement of the alloy. Alternatively, if the most important alloy constituent is Pt, then the COOH functionalised graphene support is desirable since it preferentially segregates Pd atoms towards the cluster-support interface thereby exposing more Pt atoms on the surface. The rearrangement of the $Pt_{32}Pd_6$ cluster exposing more Pt atoms on the surface may result in modified reactivity of the $Pt_{32}Pd_6$ cluster compared to the reactivity of a monometallic $Pt_{38}$ cluster.

If stronger attachment of the cluster to the support is desirable in order to minimise particle detachment, and Pt is the important alloy element for the desired reactivity (e.g. oxygen reduction reaction in polymer electrolyte fuel cells), then the Nb-doped partially reduced $TiO_2$ support is desirable since it binds the cluster strongly and exposes more Pt atoms on the surface of the cluster by segregating Pd towards the cluster-support interface.

In summary, it has been observed that defects on the support, i.e. both graphene and $TiO_2$ supports excluding the hydrogen adatoms on hydroxylated $TiO_2$(110) act as anchoring sites to stabilise binding of the cluster to the support. Therefore, the defects aid by strongly attaching clusters to the support ensuring that they are trapped at the defect sites, thereby minimising chances of cluster detachment from the support. In addition, the defects on the surface of graphene and $TiO_2$ supports alter the electronic structure of the active metal. The altered electronic properties of the supported clusters imply modification of the reactivity of the supported clusters. Worth mentioning is that even on the pristine graphene support, which is generally considered inert, the reactivity of the supported $Pt_{38}$ cluster is expected to be altered relative to that of the free standing $Pt_{38}$ cluster due to 0.41 eV upward shift of the d-band centre of the opposite facet exposed to adsorbates. For the $Pt_{32}Pd_6$ alloy cluster, the defects can alter arrangement of Pt and Pd atoms within the $Pt_{32}Pd_6$ cluster, thus affecting their segregation pattern. The altered arrangement of the alloy may display different reactivity compared to the unaltered arrangement of the $Pt_{32}Pd_6$ alloy cluster.

## 8.3 References

Jiang, D., Overbury, S.H. & Dai, S. (2012) Structures and energetics of Pt clusters on $TiO_2$: interplay between metal-metal bonds and metal-oxygen bonds. *J. Phys. Chem. C* **116**, 21880-21885.

Kim, G., Kawazoe, Y. & Lee, K.R. (2012) Controlled catalytic properties of platinum clusters on strained graphene. *J. Phys. Chem. Lett*. **3**, 1989-1996.

Lim, D.H. & Wilcox, J. (2012) Mechanisms of the oxygen reduction reaction on defective graphene-supported Pt nanoparticles from first-principles. *J. Phys. Chem. C* **116**, 3653-3660.

Maiti, R. & Ricca, A. (2004) Metal-nanotube interactions – binding energies and wetting properties. *Chem. Phys. Lett*. **395**, 7-11.

# Chapter 9: Concluding remarks

## 9.1 Overview

The study set out to gain fundamental understanding of the role of the support on supported metal clusters. The support can consist of defects and the present study was specifically aimed at understanding the role of defects on supported metal clusters. To achieve the objective two different types of supports were considered; carbon based and $TiO_2$ based supports. The carbon based support was modelled as a single graphene sheet. The defects considered on the graphene support were monovacancy defect, OH functionalised graphene and COOH functionalised graphene. Defect free or pristine graphene was also considered. The $TiO_2$ based support was modelled using the rutile $TiO_2$(110) surface and the defects considered were partially reduced $TiO_2$(110) surface with a surface bridge oxygen vacancy, hydroxylated $TiO_2$(110) surface with surface hydroxyl groups and Nb-doped $TiO_2$ (110). The defect free or stoichiometric $TiO_2$(110) surface was also investigated.

The metal clusters considered for investigation on the different supports were a monometallic Pt nanoparticle represented by a 38 atom truncated octahedron cluster, and a Pt-Pd nanoparticle represented by a 38 atom truncated octahedron cluster of composition $Pt_{32}Pd_6$.

Three hypotheses were formulated in the present study in order to address the objectives. Each hypothesis will be revisited in order to assess to what extent do the results of the present study support or reject it.

***Hypothesis 1***

*The presence of the oxygen surface functional groups OH and COOH on graphene will lead to enhanced binding of the $Pt_{38}$ and $Pt_{32}Pd_6$ clusters on functionalised graphene relative to binding on pristine graphene. The enhanced binding on functionalised graphene is due to the surface oxygen functional groups modifying the electronic properties of the carbon atoms in the vicinity of the attached functional groups, therefore leading to stronger binding of the clusters.*

The binding energy of the $Pt_{38}$ cluster was found to be enhanced on defect containing graphene than on pristine graphene. The binding energies followed the trend: monovacancy graphene > OH functionalised graphene > COOH functionalised graphene > pristine

graphene. The enhanced binding on OH and COOH functionalised graphene relative to pristine graphene indicates that even with the vacancy site occupied by the OH or COOH functional groups, the cluster binds stronger to the support than on pristine graphene. The implication of stronger binding on OH and COOH functionalised graphene is the functional groups aid in minimising sintering of the cluster on the graphene support.

Not only do the defects affect the binding strength of the $Pt_{38}$ cluster to the support, but they also modify the electronic properties of the supported $Pt_{38}$ cluster. The electronic properties of the defect containing graphene are also modified relative to those of pristine graphene. The modification of electronic properties of the defect containing graphene, i.e. monovacancy graphene, OH and COOH functionalised graphene is evidenced by different PDOS profiles of the defect containing graphene compared to that of pristine graphene.

The modified electronic properties of the supported $Pt_{38}$ cluster is manifested by different PDOS and d-band centre of the supported $Pt_{38}$ cluster compared to that of the free standing $Pt_{38}$ cluster. Upon binding of the $Pt_{38}$ cluster on the different graphene supports, there is a downward shift of the d-band centre of the entire $Pt_{38}$ cluster relative to that of the free standing $Pt_{38}$ cluster. In addition to the d-band centre shift of the entire cluster there is also downward shift of the d-band centre of the facet interacting with the cluster and an upward shift of the d-band centre of the opposite facet not interacting directly with the support. The change of the d-band centre of the entire $Pt_{38}$ cluster, the interacting and opposite facets indicate that the effect of the interaction of the cluster with the support is not localised to the interacting facet but affects the entire cluster. The electronic structure of the $Pt_{38}$ cluster is transformed from a discrete molecular like PDOS for the free standing cluster to a continuous metallic PDOS for the supported $Pt_{38}$ cluster.

The binding energy of the $Pt_{32}Pd_6$ cluster is enhanced on OH and COOH functionalised graphene relative to binding on pristine graphene. The binding of the $Pt_{32}Pd_6$ cluster is enhanced more on OH functionalised graphene than on COOH functionalised graphene. Similar to the case of the $Pt_{38}$ cluster adsorbed on functionalised graphene, there is a downward shift of the d-band centre of the supported $Pt_{32}Pd_6$ cluster on pristine graphene, OH and COOH functionalised graphene. Likewise, there is a downward shift of the d-band centre of the interacting facet for the $Pt_{32}Pd_6$ cluster supported on the different supports. The electronic structure of the $Pt_{32}Pd_6$ cluster is transformed from a discrete molecular like PDOS for the free standing cluster to a continuous metallic PDOS for the supported $Pt_{32}Pd_6$ cluster on pristine and functionalised graphene.

***Hypothesis 2***

*The modified electronic properties of the carbon atoms in the vicinity of the surface oxygen functional groups (i.e. OH and COOH) on functionalised graphene will lead to a different chemical ordering in the $Pt_{32}Pd_6$ cluster compared to the ordering in the unsupported $Pt_{32}Pd_6$ cluster. The preference of either Pt or Pd to bind to the support is expected to change the ordering in the $Pt_{32}Pd_6$ cluster supported on functionalised graphene.*

The most stable arrangement of the free standing $Pt_{32}Pd_6$ cluster is the mixed arrangement with Pd atoms on the surface mixed with Pt atoms. For the free standing $Pt_{32}Pd_6$ lowest energy arrangement structure, Pd atoms occupy the centre of hexagonal facets. Arrangements in which Pd atoms are on the surface and occupy one facet, either square or hexagonal thereby maximising the number of surface Pd-Pd bonds were found not to be lower in energy than the mixed arrangement where the are no surface Pd-Pd bonds.

On OH functionalised graphene there is no thermodynamic driving force for the rearrangement of the supported $Pt_{32}Pd_6$ cluster. The supported $Pt_{32}Pd_6$ cluster retained the same arrangement as the free standing $Pt_{32}Pd_6$ cluster. Rearranged structures were energetically unfavourable with positive segregation energies.

On COOH functionalised graphene there is thermodynamic driving force for rearrangement of the supported $Pt_{32}Pd_6$ cluster. There is preferential segregation of Pd towards the cluster-support interface with Pd atoms occupying the facet directly in contact with the support on COOH functionalised graphene, thereby exposing more Pt atoms on the surface. The different arrangement of the $Pt_{32}Pd_6$ cluster on COOH functionalised graphene which exposes more Pt atoms on the surface compared to the free standing $Pt_{32}Pd_6$ cluster is expected to result in different reactivity to the $Pt_{32}Pd_6$ cluster supported on OH functionalised graphene. On OH functionalised graphene the $Pt_{32}Pd_6$ cluster has the same arrangement as the free standing $Pt_{32}Pd_6$ cluster.

The rearrangement of Pd towards the cluster-support interface for the $Pt_{32}Pd_6$ cluster supported on OH and COO functionalised graphene was rationalised by considering the amount of charge loss from the interacting facet bearing Pd atoms. On OH functionalised graphene it was observed that the quantity of charge loss from Pd atoms on the facet interacting with the support is lower than charge loss from Pd atoms on the interacting facet on COOH functionalised graphene. Enhanced charge transfer from anchoring Pd atoms on the COOH functionalised graphene support favours rearrangement of the supported $Pt_{32}Pd_6$ cluster. The electronic properties of the OH functionalised and COOH functionalised graphene

supports are different as evidenced by different PDOS spectra. Therefore, owing to the different electronic structure of OH and COOH functionalised graphene, the $Pt_{32}Pd_6$ cluster interacts differently with both supports. The different interactions lead to enhanced charge transfer from Pd atoms interacting with the COOH functionalised graphene support compared to the OH functionalised graphene support.

***Hypothesis 3***

*Pd will segregate towards the cluster-support interface when the $Pt_{32}Pd_6$ cluster is supported on Nb-doped $TiO_2$(110). Pd will preferentially segregate towards the cluster-support interface due to its higher affinity for oxygen compared to Pt. The segregation of Pd towards the cluster-support interface will result in less Pd being exposed on the surface of the $Pt_{32}Pd_6$ cluster.*

The binding of the $Pt_{32}Pd_6$ cluster is enhanced on the Nb-doped partially reduced $TiO_2$(110) surface than on the pure undoped partially reduced $TiO_2$(110) surface. The segregation of Pd atoms towards the cluster-support interface depends on location of Nb dopant atoms within the partially reduced $TiO_2$(110) surface slab. In the absence of Nb dopant atoms, and with Nb dopant atoms located on the surface layer, segregation of Pd atoms towards the cluster-support interface is not thermodynamically favoured since the arrangement with Pt atoms located at the cluster support interface is the stable arrangement. As Nb dopant atoms are positioned in the second and third layers of the 4 layer thick partially reduced $TiO_2$(110) surface slab, the segregation of Pd towards the cluster-support interface becomes thermodynamically favoured. The highly exothermic segregation energy is attained when Nb atoms are positioned in the second layer of the partially reduced $TiO_2$(110) surface slab.

The presence of Nb dopant atoms result in enhanced electron transfer from the Nb-doped partially reduced $TiO_2$(110) surface to the adsorbed $Pt_{32}Pd_6$ cluster. The highest quantity of electron transfer from the Nb-doped partially reduced $TiO_2$(110) surface is obtained when the Nb dopant atoms are positioned in the third layer, with charge being redistributed to the surface and to layers above and below the third layer.

Preferential segregation of Pd atoms towards the cluster-support interface as Nb atoms are located in the second and third layers of the partially reduced $TiO_2$(110) surface slab indicates that more Pt atoms will be exposed on the surface of the cluster. The rearranged structure of the $Pt_{32}Pd_6$ cluster with Pd atoms at the cluster-support interface may result in different reactivity of the supported $Pt_{32}Pd_6$ cluster compared to the free unsupported $Pt_{32}Pd_6$ cluster. This is because more Pt atoms are exposed on the surface of the supported cluster. The

electronic structure of the $Pt_{32}Pd_6$ cluster is transformed from a discrete molecular like PDOS for the free standing cluster to a continuous metallic PDOS for the supported $Pt_{32}Pd_6$ cluster.

The preferential segregation of Pd atoms towards the cluster-support interface is not due to Pd having higher affinity for oxygen than Pt. We observe in the absence of Nb dopant atoms that preferential segregation of Pt towards the cluster-support interface is preferred over that of Pd. The preferential segregation of Pd towards the cluster-support interface becomes thermodynamically favourable as Nb atoms are positioned away from the surface and in layers 2 and 3 of the partially reduced $TiO_2$(110) surface slab. The preferential segregation of Pd towards the cluster-support interface is due to charge contribution from Nb dopant atoms positioned in layers 2 and 3 of the partially reduced $TiO_2$(110) surface. Charge contribution by Nb atoms contributes to the overall charge transferred to the adsorbed $Pt_{32}Pd_6$ cluster.

## 9.2 Recommendations/ future research

Results of the present study have indicated that the support material not only act as anchor for the supported metal particles, but depending on the surface composition (type of defect) can also change the d-band centre energy of the supported cluster. Change of the d-band centre of the cluster and of the facets of the cluster exposed to reactants imply that reactivity of the cluster towards adsorbates may be affected.

It would therefore be interesting to perform adsorption calculations with a probe molecule, e.g. $O_2$ and then determine dissociation activation energy of the adsorbed $O_2$ on the free standing and supported cluster. This would help ascertain if there is need to include or exclude the support in determining the activity of a catalyst, seeing that most catalysts are applied in supported form. Moreover, from this study it has been observed that the supported cluster can have different electronic properties to the free standing cluster (so by ignoring the effect of the support is the actual reactivity of the metal cluster correctly predicted?).

Furtheron, the study has also highlighted an important aspect in determining the activity of a supported $Pt_{32}Pd_6$ bimetallic cluster. It has been established that the $Pt_{32}Pd_6$ cluster can rearrange to a different arrangement of the Pt and Pd constituents on the support as opposed to the arrangement in the free standing $Pt_{32}Pd_6$ cluster. The implication of this finding is studying the activity of the $Pt_{32}Pd_6$ cluster without the presence of the support can lead to a different conclusion to the actual activity of the supported $Pt_{32}Pd_6$ cluster. This is so because

the supported $Pt_{32}Pd_6$ cluster can rearrange on the support thereby resulting in different activity to the lowest energy arrangement of the free standing $Pt_{32}Pd_6$ cluster.

Larger clusters should be considered to investigate if the effect of the support on the supported cluster is dependent on cluster size, e.g. will the shift of the d-band centre of the opposite facet not directly in contact with the support still be observed for larger cluster sizes.

# Appendices

# Appendix A: Mathematical formulation of Kohn-Sham theorem

## Kohn–Sham theorem

The central theme in the Kohn–Sham formulation is to solve the system of interacting electrons in an external potential $v_{ext}(r)$ by using a fictitious system of non-interacting Kohn–Sham particles in an effective potential $v_{eff}(r)$ (Mattsson et al., 2005). Thus the single effective single-particle potential $v_{eff}(r)$ of the Kohn–Sham theory can be regarded as that unique, fictitious external potential which leads for non-interacting particles, to the same physical density $n(r)$ as that of the interacting electrons in the physical external potential $v_{ext}(r)$ (Wang & Parr, 1993).

The Kohn–Sham equations consists of the following 3 equations:

$$\left(-\frac{1}{2}\nabla^2 + v_{eff}(r)\right)\varphi_j(r) = \epsilon_j\varphi_j \quad \text{(A.1)}$$

$$v_{eff}(r) = v(r) + \int \frac{n(r')}{|r-r'|}dr' + v_{xc}(r) \quad \text{(A.2)}$$

$$n(r) = \sum_{i=1}^{N} |\varphi_j(r)|^2 \quad \text{(A.3)}$$

The equations A.1, A.2 and A.3 are collectively termed the self-consistent Kohn–Sham equations which are solved iteratively until a desired convergence is satisfied.

The Kohn–Sham theorem is derived from the Hartree theory (Thomas, 1927; Fermi, 1927; Dirac, 1930) which presents single particle equations as the approximate description for the electronic structure of atoms. In the Hartree theory the electron is considered to be moving in an effective single particle potential $v_H(r)$.

$$v_H(r) = \frac{-Z}{r} + \int \frac{n(r')}{|r-r'|}dr' \quad \text{(A.4)}$$

The term $\frac{-Z}{r}$ represents the potential due to a nucleus of atomic number Z and the term $\int \frac{n(r')}{|r-r'|}dr'$ represents the potential due to the electron density $n(r)$. Each electron satisfies the single particle Schrödinger equation:

$$\left\{-\frac{1}{2}\nabla^2 + v_H(r)\right\}\varphi_j(r) = \varepsilon_j\varphi_j \quad \text{(A.5)}$$

$\varphi_j$ is the single particle wavefunction, from which the electron density can be determined.

$$n(r) = \sum_{i=1}^{N} |\varphi_j(r)|^2 \quad \text{(A.6)}$$

Equation A.5 is of the form of the Schrödinger equation of non-interacting electrons moving in an external potential $v_{eff}(r)$.

The central theme of the Kohn–Sham formulation is to derive the Hartree equation analogues from the Hohenberg–Kohn variational principle for energy (Kohn, 1999). Applying the Hohenberg–Kohn variational to A.5principle results in:

$$E_{v(r)}[n(r)] = \int v(r)n(r)dr + F[n(r)] \geq E \quad \text{(A.7)}$$

Applying Euler-Lagrange equations to equation A.7 cognisant that equation A.6 is stationery with respect to variation of $n(r)$ which ensures that the number of electrons remain unchanged result in the expression:

$$\delta E_{v(r)}[n(r)] = \delta n(r)\left\{v(r) + \frac{\delta}{\delta n(r)}T_s[n(r)] - \epsilon\right\}dr = 0 \quad \text{(A.8)}$$

$\epsilon$ is a Lagrange multiplier to assure particle conservation. The ground state energy and the electron density $n(r)$ can be obtained by calculating the eigenfunction $\varphi_j(r)$ and the eigenvalues $\epsilon_j$ of non-interacting single particle equations by solving the following equations:

$$\left(-\frac{1}{2}\nabla^2 + v(r)\right)\varphi_j(r) = \epsilon_j\varphi_j \quad \text{(A.9)}$$

$$E = \sum_{j=1}^{N}\epsilon_j \quad \text{(A.10)}$$

$$n(r) = \sum_{j=1}^{N}|\varphi_j(r)|^2 \quad \text{(A.11)}$$

For interacting electrons, the energy functional of the system is described by equation A.7, the universal functional $F[n(r)]$ can be further expressed by separating the long range classical Coulomb energy resulting in the expression:

$$F[n(r)] = \frac{1}{2}\int\frac{n(r)n(r')}{|r-r'|}drdr' + G[n(r)] \quad \text{(A.12)}$$

Thus the energy functional of the interacting electrons system is given by the expression:

$$E_{v(r)} = \int v(r)n(r)dr + \frac{1}{2}\int\frac{n(r)n(r')}{|r-r'|}drdr' + G[n(r)] \quad \text{(A.13)}$$

The universal functional of the density $G[n(r)]$ was approximated to contain the effects of correlation and exchange by Kohn and Sham (1965). The expansion of $G[n(r)]$ in terms of correlation and exchange effects is expressed as:

$$G[n(r)] = T_s[n(r)] + E_{xc}[n(r)] \quad \text{(A.14)}$$

With $T_s[n(r)]$ being the kinetic energy of the system of non-interacting electrons and $E_{xc}[n(r)]$ is the exchange correlation energy for interacting electrons in electron density $n(r)$. The expression for the universal functional $F[n(r)]$ becomes:

$$F[n(r)] = T_s[n(r)] + \frac{1}{2}\int \frac{n(r)n(r')}{|r-r'|} dr dr' + E_{xc}[n(r)] \quad \text{(A.15)}$$

Applying the Hohenberg–Kohn variational principle to the interacting electrons results in the energy expression:

$$E_v[n(r)] = \int v(r)n(r)dr + T_s[n(r)] + \frac{1}{2}\int \frac{n(r)n(r')}{|r-r'|} dr dr' + E_{xc}[n(r)] \geq E \quad \text{(A.16)}$$

Application of Euler-Lagrange equations to equation A.16 for a given total number of electrons results in the expression:

$$\delta E_v[n(r)] = \int \delta n(r) \left\{ v_{eff}(r) + \frac{\delta}{\delta n(r)} T_s[n(r)] - \epsilon \right\} dr = 0 \quad \text{(A.17)}$$

$$v_{eff}(r) = v(r) + \int \frac{n(r')}{|r-r'|} dr' + v_{xc}(r) \quad \text{(A.18)}$$

$$v_{xc}(r) = \frac{\delta}{\delta n(r)} E_{xc}[n(r)] \quad \text{(A.19)}$$

Comparison of equations A.17 and A.8 indicates that they are identical and of the same form. Therefore, the minimizing electron density $n(r)$ is given by solving the single particle equation:

$$\left(-\frac{1}{2}\nabla^2 + v_{eff}(r)\right)\varphi_j(r) = \epsilon_j \varphi_j \quad \text{(A.20)}$$

The electron density is given by equation A.11 and the effective potential $v_{eff}(r)$ by equation A.18. Equations A.11, A.18 and A.20 are known as the self-consistent Kohn–Sham equations which need to be solved iteratively until a desired convergence criterion is satisfied. The ground state energy of the system is given by:

$$E = \sum_j \epsilon_j + E_{xc}[n(r)] - \int v_{xc}(r) n(r) dr - \frac{1}{2}\int \frac{n(r)n(r')}{|r-r'|} dr dr' \quad \text{(A.21)}$$

Thus the single effective single-particle potential $v_{eff}(r)$ of the Kohn–Sham theory can be regarded as that unique, fictituos external potential which leads for non-interacting particles, to the same physical density $n(r)$ as that of the interacting electrons in the physical external potential $v(r)$ (Wang & Parr, 1993). The Kohn–Sham density functional theory in principle results in an exact electron density and the exact total energy of any interacting, correlated system (Becke, 2014). The accuracy of Kohn–Sham density functional theory calculations depends on the accuracy of the approximation of the exchange correlation energy functional, since there is no known explicit expression for it.

**References**

Becke, A.D. (2014) Perspective: Fifty years of density-functional theory in chemical physics. *J. Chem. Phys.***140**, 18A301-18A318.

Dirac, P.A.M. (1930). Note on the exchange phenomena in the Thomas atom. *Mathematical Proceedings of the Cambridge Philosophical Society* **26**, 376-385.

Fermi, E. (1927) Un metodo statistic per la determinazione di alcune prioprietà dell'Atomo. *Rend. Accad. Naz. Lincei* **6**, 602-607.

Kohn, W. (1999) Nobel lecture: electronic structure of matter–wave functions and density functionals. *Rev. Modern Phys.* **71**, 1253-1266.

Kohn, W. & Sham, L.J. (1965) Self-consistent equations including exchange and correlation effects. *Phys. Rev.* **140**, A1133-A1138.

Mattsson, A.E., Schultz, P.A., Desjarlias, M.P., Mattsson, T.R. & Leung, K. (2005) Designing meaningful density functional theory calculations in material science - a primer. *Modell. Simul. Mater. Sci. and Eng.* **13**, R1-R3.

Thomas, L.H. (1927) The calculation of atomic field. *Mathematical Proceedings of the Cambridge Philosophical Society* **23**, 542-548.

Wang, Y. & Parr, R.G. (1993) Construction of exact Kohn-Sham orbitals from a given electron density. *Phys. Rev. A* **47**, R1591-R1593.

# Appendix B: Unsupported $Pt_{32}Pd_6$

## B.1 Investigation of arrangement in free standing $Pt_{32}Pd_6$ cluster

$$E_{excess} = E_{Pt_{32}Pd_6} - \frac{6}{38}E_{Pd_{38}} - \frac{32}{38}E_{Pt_{38}}$$

$$E_{diff} = E_i - E_{reference}$$

$E_{reference}$ is the energy of the most stable arrangement with excess energy of -0.68 eV

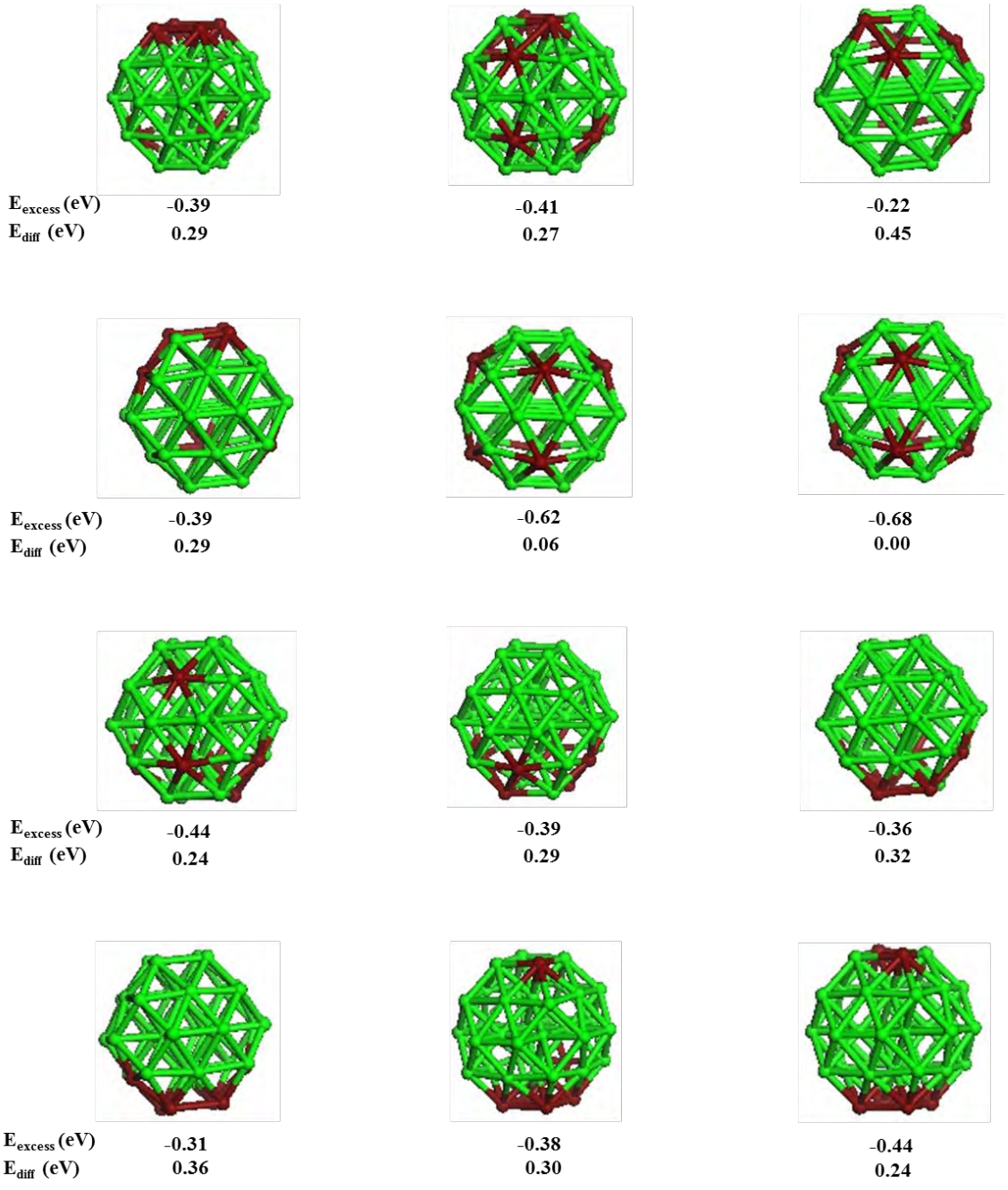


Figure B.1: Arrangements of the free standing $Pt_{32}Pd_6$ cluster with calculated excess energy and difference in energy to the lowest energy arrangement.

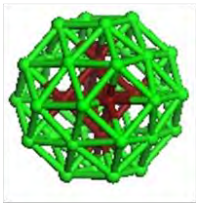

| | |
|---|---|
| $E_{excess}$ (eV) | 0.82 |
| $E_{diff}$ (eV) | 1.50 |

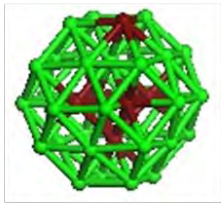

| | |
|---|---|
| $E_{excess}$ (eV) | 0.65 |
| $E_{diff}$ (eV) | 1.33 |

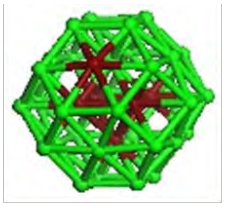

| | |
|---|---|
| $E_{excess}$ (eV) | 0.77 |
| $E_{diff}$ (eV) | 1.45 |

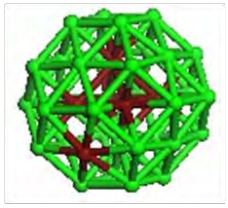

| | |
|---|---|
| $E_{excess}$ (eV) | 0.77 |
| $E_{diff}$ (eV) | 1.45 |

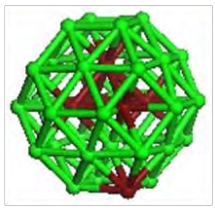

| | |
|---|---|
| $E_{excess}$ (eV) | 0.66 |
| $E_{diff}$ (eV) | 1.33 |

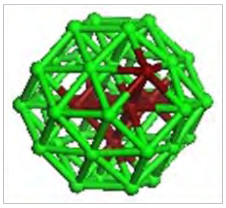

| | |
|---|---|
| $E_{excess}$ (eV) | 0.63 |
| $E_{diff}$ (eV) | 1.31 |

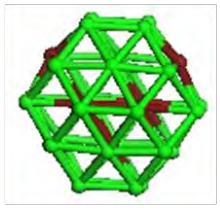

| | |
|---|---|
| $E_{excess}$ (eV) | 0.67 |
| $E_{diff}$ (eV) | 1.35 |

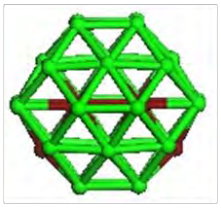

| | |
|---|---|
| $E_{excess}$ (eV) | 0.73 |
| $E_{diff}$ (eV) | 1.41 |

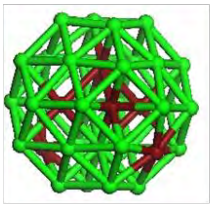

| | |
|---|---|
| $E_{excess}$ (eV) | 0.70 |
| $E_{diff}$ (eV) | 1.40 |

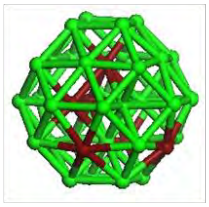

| | |
|---|---|
| $E_{excess}$ (eV) | 0.40 |
| $E_{diff}$ (eV) | 1.09 |

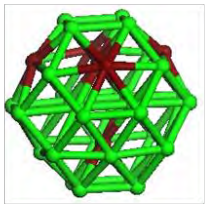

| | |
|---|---|
| $E_{excess}$ (eV) | 0.33 |
| $E_{diff}$ (eV) | 1.03 |

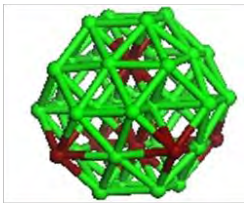

| | |
|---|---|
| $E_{excess}$ (eV) | 0.01 |
| $E_{diff}$ (eV) | 0.69 |

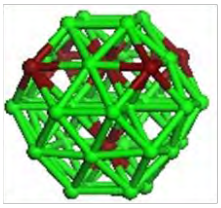

| | |
|---|---|
| $E_{excess}$ (eV) | 0.01 |
| $E_{diff}$ (eV) | 0.69 |

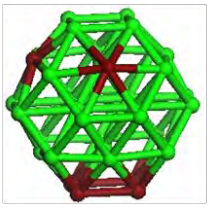

| | |
|---|---|
| $E_{excess}$ (eV) | -0.34 |
| $E_{diff}$ (eV) | 0.35 |

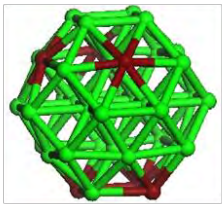

| | |
|---|---|
| $E_{excess}$ (eV) | -0.27 |
| $E_{diff}$ (eV) | 0.43 |

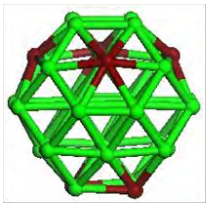

| | |
|---|---|
| $E_{excess}$ (eV) | -0.43 |
| $E_{diff}$ (eV) | 0.27 |

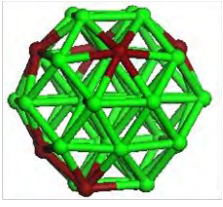

| | |
|---|---|
| $E_{excess}$ (eV) | -0.44 |
| $E_{diff}$ (eV) | 0.26 |

Figure B.1 continued*:* Arrangements of the free standing $Pt_{32}Pd_6$ cluster with calculated excess energy and difference in energy to the lowest energy arrangement.

## B.2. Definition of unique facets for the $Pt_{32}Pd_6$ cluster

Figure B.2 below indicates the labels of the unique facets of the lowest energy structure of the free standing $Pt_{32}Pd_6$ cluster (mixed arrangement).

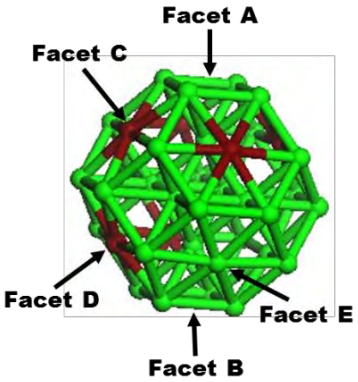


Figure B.2: Labelling of the unique facets of the $Pt_{32}Pd_6$ cluster

The unique facets are defined as follows:

**Facet A**: square facet consisting of 4 Pt atoms in the half of the cluster with 4 Pd atoms at the centre of hexagonal facets.

**Facet B**: square facet opposite facet A and also consisting of 4 Pt atoms.

**Facet C**: one of the hexagonal facet having a Pd atom at its centre in the half of the cluster having 4 Pd atoms at the centre of the hexagonal facet.

**Facet D**: hexagonal facet with a central Pd atom in the half of the cluster which has only 2 Pd atoms at the hexagonal facets.

**Facet E**: hexagonal facet consisting of Pt atoms only.

# Appendix C: $Pt_{32}Pd_6$ cluster interaction with graphene based supports

## C1: Approach of the $Pt_{32}Pd_6$ cluster with graphene based supports

The first set of calculations was to establish through which facet does the $Pt_{32}Pd_6$ cluster interacts favourably with pristine graphene, OH functionalised and COOH functionalised graphene. Once the most favourable facet of interaction with OH and COOH functionalised graphene has been established, the possibility of rearrangement of Pt and Pd atoms whilst not changing the lowest energy adsorption geometry (i.e. facet of interaction, atomic positions and distance between the cluster and the support) was investigated. This was done by changing the location of Pd and Pt atoms in the lowest energy adsorption geometry and re-optimising the structure with the new atomic locations.

**$Pt_{32}Pd_6$ interaction with pristine graphene**

To investigate the facet of interaction of the $Pt_{32}Pd_6$ cluster with pristine graphene 5, adsorption geometries were investigated. Owing to the symmetry of pristine graphene, only the ontop approach of the cluster on graphene was investigated. Each of the 5 unique facets of the $Pt_{32}Pd_6$ cluster approaching the centre of graphene sheet were investigated.

**$Pt_{32}Pd_6$ interaction with OH functionalised graphene**

To investigate the facet of interaction of the $Pt_{32}Pd_6$ cluster with OH functionalised graphene, 10 adsorption geometries were investigated. Similar to the case of $Pt_{38}$ interaction with functionalised graphene (section 4.2), two different approaches of the cluster were considered, i.e. ontop and underneath approach. For ontop approach the $Pt_{32}Pd_6$ cluster directly atop the functional group forming a linking metal-O-carbon bond was investigated. For bottom approach, the cluster was approaching from below the functional group and was therefore not directly interacting with the functional group. The adsorption geometries were confined to those where the cluster through its interacting facet were bonded to the carbon atoms in the vicinity of the added functional group and the saturating H atoms at the vacancy

site of graphene. Only the local region around the added functional group to the graphene was investigated for binding of the cluster to the support.

For both ontop and bottom approach, approach through the 5 unique facets were considered resulting in a total of 10 adsorption geometries.

Once the lowest energy structure for the $Pt_{32}Pd_6$ cluster on OH functionalised graphene was obtained, the possibility of rearrangement of Pt and Pd atoms within the $Pt_{32}Pd_6$ cluster was investigated. The assumption made in the calculations was that the facet of approach to the support during rearrangement does not vary from that obtained for the most favourable facet of approach of the $Pt_{32}Pd_6$ cluster on OH functionalised graphene. Different rearranged structures were investigated to assess if ordering in the unsupported $Pt_{32}Pd_6$ cluster was still the lowest energy structure while bound to OH functionalised graphene or whether the $Pt_{32}Pd_6$ cluster can rearrange to other arrangements on the OH functionalised graphene support.

Several rearrangements were considered. The first approach was to increase concentration of Pd atoms on the facet directly in contact with the support, i.e. having Pd atoms anchor the cluster to the support.

The second approach was to consider the extreme case of segregation between Pt and Pd atoms with core shell arrangement (all Pd atoms occupying the interior region of the cluster and exposing Pt atoms at the surface). Rearrangements in which the surface concentration of Pd atoms was gradually increased from the perfect core shell arrangement were also considered in the second approach.

The third approach was to consider arrangements in which Pd atom concentration is increased on the half of the cluster which is furthest away from the contact region with the support. This arrangement results in high concentration of Pt atoms on the half of the cluster closest to the support.

The fourth set of rearranged structures investigated was where 4 Pd atoms occupy corner sites of the hexagonal facet for both the top half and bottom half of the cluster with the rest of Pd atoms in the core region.

**$Pt_{32}Pd_6$ interaction with COOH functionalised graphene**

Similar to adsorption on OH functionalised graphene, ontop and underneath approach were investigated in order to establish which facet interacts favourably with the COOH functionalised graphene support. For ontop approach, two variants were considered. The first variant was identical to ontop geometries on OH functionalised graphene where the cluster was ontop of the functional group resulting in formation of metal-O-carbon bonds. The second variant considered was where the interacting facet was closer to graphene with the functional group on the same side as the cluster, with either facet C, facet D and facet E interacting directly with the functional group. For underneath approach, the 5 considered adsorption geometries are similar to those considered for adsorption on OH functionalised graphene.

Similar to interaction with OH functionalised graphene, the most favourable facet of approach of the $Pt_{32}Pd_6$ cluster to the COOH functionalised graphene support geometry was used to investigate rearrangement of the supported $Pt_{32}Pd_6$ cluster. Taking precedence from rearrangement on OH functionalised graphene, two approaches to rearrangement were explored. In the first approach the extreme case of core shell segregation with Pd atoms in the core was investigated. Subsequently the surface concentration of Pd was increased both to the half closer to the support and the half furthest from the support. The second approach was to increase concentration of Pd atoms on the facet interacting with the support thereby increasing the number of anchoring Pd atoms to the support.

# C2: Comparison of geometries between GGA-PW91 and vdW-OptPBE functionals

## C2.1 $Pt_{32}Pd_6$ on pristine graphene

The calculated binding energies using the GGA-PW91 functional, and the van der Waals functionals for the two lowest energy adsorption structures for the $Pt_{32}Pd_6$ cluster adsorbed on pristine graphene are presented in Table C1. The calculated bond lengths for the adsorption structures using the PW91 functional and the vdW-OptPBE functional are also presented in Table C1. Similar to $Pt_{38}$ cluster adsorption on pristine graphene, the binding energies calculated with the van der Waals functionals are exothermic. The van der Waals functionals can describe dispersion forces which are dominant in graphene systems (Fuentes-Cabrera et al., 2008) whereas the PW91 functional poorly describes dispersion forces. The difference in energy between the two structures calculated with the PW91 functional is the same as the

difference in energy with the vdW-TS-SCS functional with a difference of 0.34 eV. A slightly higher difference of 0.59 eV between the two structures is obtained for the vdW-OptPBE functional. The energy difference between the vdW-TS-SCS functional and the vdW-OptPBE functional is probably due to the different implementation of the van der Waals forces in the two functionals.

Table C.1: Optimised parameters for geometric structures of the $Pt_{32}Pd_6$ cluster adsorbed on pristine graphene.

| | **Facet A** | | **Facet B** | |
|---|---|---|---|---|
| **$E_{bind}$ (eV)** | | | | |
| GGA-PW91 | 1.05 | | 0.71 | |
| vdW-TS-SCS | -1.62 | | -1.96 | |
| vdW-OptPBE | -2.61 | | -3.20 | |
| | **PW91** | **vdW-OptPBE** | **PW91** | **vdW-OptPBE** |
| | 2.95 | 2.92 | 2.83 | 2.82 |
| | 2.87 | 2.83 | 2.81 | 2.81 |
| $d_{Pt\text{-}Pt}$ [1], Å | 2.96 | 2.86 | 2.86 | 2.82 |
| | 3.01 | 3.04 | 3.05 | 3.02 |
| | **PW91** | **vdW-OptPBE** | **PW91** | **vdW-OptPBE** |
| | 2.69 | 2.65 | 2.67 | 2.64 |
| | 2.68 | 2.59 | 2.66 | 2.63 |
| $d_{Pt\text{-}Pt}$ [2], Å | 2.70 | 2.65 | 2.67 | 2.64 |
| | 2.68 | 2.59 | 2.67 | 2.64 |
| | **PW91** | **vdW-OptPBE** | **PW91** | **vdW-OptPBE** |
| | 2.22 | 2.18 | 2.22 | 2.22 |
| | 2.21 | 2.16 | 2.21 | 2.22 |
| $d_{Pt\text{-}C}$ , Å | 2.25 | 2.19 | 2.20 | 2.22 |
| | 2.24 | 2.18 | 2.21 | 2.22 |

[1]Pt-Pt distance of the facet closest to graphene

[2] Pt-Pt distance of the facet opposite to the one interacting with graphene

The van der Waals contribution to the binding energy of the $Pt_{32}Pd_6$ cluster on pristine graphene with the vdW-OptPBE functional is 0.051 eV/C (4.91 kJ/mol C) for approach through facet A and 0.054 eV/C (5.24 kJ/mol C). These calculated van der Waals contributions are of the order of magnitude expected for van der Waals contributions on carbon systems (5 – 10 kJ /mol) (Tonigold & Groß, 2010; Rubeš et al., 2010; Klimeš & Michaelides, 2012).

From Table C.1 it is observed that calculated bond lengths for the interacting and opposite facets calculated with the PW91 and the vdW-OptPBE functionals are similar. For the $Pt_{32}Pd_6$ cluster interacting with pristine graphene through facet A, the highest difference between the

PW91 and vdW-OptPBE functionals calculated bond lengths is 0.10 Å. For the $Pt_{32}Pd_6$ cluster interacting with pristine graphene through facet B, the bond lengths between the two functionals are identical with the highest bond length difference being 0.04 Å. Identical bond lengths between the PW91 and vdW-OptPBE functionals in the present study indicates that there is no substantial difference in geometry of the $Pt_{32}Pd_6$ cluster on pristine graphene between the two functionals. Pt-C bond lengths are predicted to within 0.06 Å between the functionals.

Inclusion of van der Waals forces results in more negative binding energy of the $Pt_{32}Pd_6$ cluster to the OH functionalised graphene support (see Table C.2). The van der Waals contribution to the binding energy calculated with the vdW-OptPBE functional for the $Pt_{32}Pd_6$ cluster adsorbed on OH functionalised graphene are: 0.02 eV/C (1.89 kJ/mol C) for underneath approach through facet A and 0.03 eV/ C (2.61 kJ/mol C) for underneath approach through facet D. The van der Waals contribution to the binding of the $Pt_{32}Pd_6$ cluster to OH functionalised graphene is lower compared to the contribution to the binding energy on pristine graphene. The difference in energy between underneath approach through facet A and underneath approach through facet D calculated with the vdW-OptPBE functional is 0.36 eV whilst the difference with PW91 functional is 0.90 eV. Despite the smaller difference in energy calculated with the vdW-OptPBE functional the stability ranking is not changed, approach through facet A binds stronger than approach through facet D.

The calculated Pt-Pt bond lengths for the interacting and opposite facets of the $Pt_{32}Pd_6$ cluster approaching OH functionalised graphene through facet A are similar for the PW91 and vdW-OptPBE functionals. The largest bond difference between the PW91 and vdW-OptPBE functionals is 0.08 Å. Longer Pt-Pt and Pt-Pd bond lengths are calculated using the PW91 functional than the vdW-OptPBE functional for underneath approach of the $Pt_{32}Pd_6$ cluster through the hexagonal facet D. The highest calculated bond difference between the PW91 and vdW-OptPBE functional is 0.21 Å. The highest of extent of bond length difference is observed for diagonal Pt-Pd bond lengths of the interacting facet. The different bond lengths between the PW91 and vdW-OptPBE functional indicates that the Pt-Pd bonds are predicted differently by the two functionals, whilst there is no difference in prediction of Pt-Pt bond lengths by the two functionals.

Calculated Pt-C bond lengths for the $Pt_{32}Pd_6$ cluster adsorbed on OH functionalised graphene are similar between the PW91 and vdW-OptPBE functionals. The highest Pt-C bond distances between the PW91 and vdW-OptPBE functional is 0.07 Å, indicating similar Pt-C bond distance prediction between the two functionals.

Table C.2: Optimised parameters for the lowest energy geometric structures of the $Pt_{32}Pd_6$ cluster adsorbed onto OH functionalised graphene. Side length corresponds to corner to corner Pt-Pt lengths while diagonal length corresponds to corner to central Pd atom (Pd-Pt) on hexagonal facet.

| | **Facet A underneath** | | **Facet D underneath** | | | |
|---|---|---|---|---|---|---|
| **$E_{bind}$ (eV)** | | | | | | |
| GGA-PW91 | -1.94 | | -1.04 | | | |
| vdW-TS-SCS | -4.89 | | -4.22 | | | |
| vdW-OptPBE | -3.35 | | -2.99 | | | |
| | **PW91** | **vdW-OptPBE** | **PW91** | | **vdW-OptPBE** | |
| | | | Side length | Diagonal length | Side length | Diagonal length |
| $d_{Pt-Pt}$ [1], Å | 3.45 | 3.47 | 2.80 | 2.83 | 2.81 | 2.94 |
| $d_{Pd-Pt}$ [1], Å | 2.96 | 3.00 | 2.72 | 2.76 | 2.69 | 2.79 |
| | 2.87 | 2.84 | 2.72 | 2.70 | 2.75 | 2.74 |
| | 3.22 | 3.26 | 2.74 | 2.74 | 2.76 | 2.74 |
| | | | 2.89 | 2.88 | 3.00 | 3.06 |
| | | | 2.81 | 2.81 | 2.81 | 3.02 |
| | **PW91** | **vdW-OptPBE** | **PW91** | | **vdW-OptPBE** | |
| | | | Side length | Diagonal length | Side length | Diagonal length |
| $d_{Pt-Pt}$ [2], Å | 2.64 | 2.57 | 2.71 | 2.75 | 2.61 | 2.82 |
| $d_{Pd-Pt}$ [2], Å | 2.66 | 2.58 | 2.65 | 2.73 | 2.55 | 2.74 |
| | 2.67 | 2.66 | 2.70 | 2.72 | 2.53 | 2.71 |
| | 2.66 | 2.65 | 2.66 | 2.75 | 2.58 | 2.75 |
| | | | 2.72 | 2.74 | 2.61 | 2.77 |
| | | | 2.65 | 2.75 | 2.59 | 2.79 |
| | **PW91** | **vdW-OptPBE** | **PW91** | | **vdW-OptPBE** | |
| | 2.20 | 2.18 | | | | |
| | 2.23 | 2.23 | 2.15 | | 2.20 | |
| $d_{Pt-C}$ , Å | 2.16 | 2.13 | 2.34 | | 2.31 | |
| | 2.26 | 2.25 | 2.31 | | 2.30 | |
| | 2.15 | 2.20 | 2.35 | | 2.36 | |
| | 2.32 | 2.25 | 2.41 | | 2.40 | |
| | | | 2.37 | | 2.36 | |

[1]Pt-Pt and Pd-Pt distance of the facet closest to OH functionalised graphene

[2] Pt-Pt and Pd-Pt distance of the facet opposite to the one interacting with OH functionalised graphene

Inclusion of van der Waals forces within DFT does not alter the calculated stability ranking obtained using the PW91 functional on pristine and OH functionalised graphene. Stability ranking was also not varied on COOH functionalised graphene for adsorption of the $Pt_{38}$ cluster. Based on the above observations, van der Waals corrected DFT calculations were not performed for the $Pt_{32}Pd_6$ cluster on COOH functionalised graphene support. Van der Waals

forces are not dominant on the COOH functionalised graphene support hence we do not expect different stability ranking to that obtained using the PW91 functional.

**References**

Klimeš, J. & Michaelides, A. (2012) Perspective: Advances and challenges in treating van der Waals dispersion forces in density functional theory. *J. Chem. Phys*. **137**, 120901-120913.

Rubeš, M., Kysilka, J., Nachtigall, P. & Bludskỳ. (2010) DFT/CC investigation of physical adsorption on a graphite (0001) surface*. Phys. Chem. Chem. Phys*. **12**, 6438-6444.

Tonigold, K. & Groß, A. (2010) Adsorption of small aromatic molecules on the (111) surfaces of noble metals: A density functional theory study with Semiempirical corrections for dispersion effects. *J. Chem. Phys*. **132**, 224701-224711.

# Appendix D: Rutile $TiO_2$(110) surface

## D.1 Optimisation of bulk rutile $TiO_2$

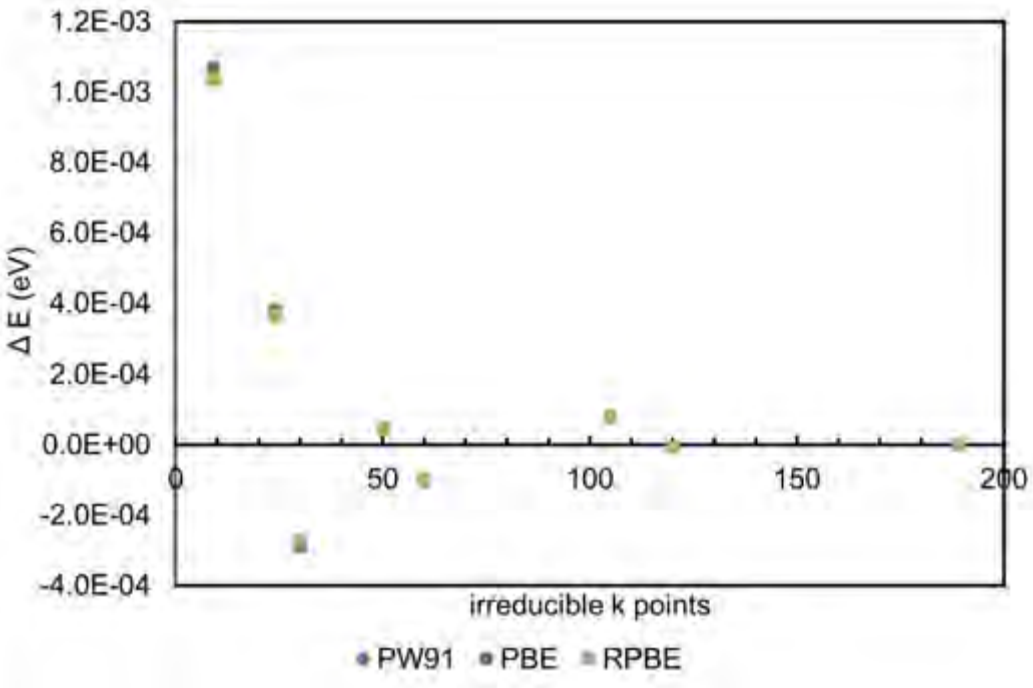


Figure D.1: k-point optimisation of bulk rutile $TiO_2$ calculated with different functionals.

From Figure D.1 it is observed that for the different functionals, i.e. PW91, PBE and RPBE, 50 irreducible k-points are sufficient to describe bulk $TiO_2$. The difference in energy is converged with respect to variation in number of irreducible k points beyond 50 irreducible points.

Figure D.2 indicates that a cut off energy of 400 eV is sufficient to describe bulk $TiO_2$ for all three functionals investigated. The difference in energy is converged with respect to change in cut off energy at 400 eV.

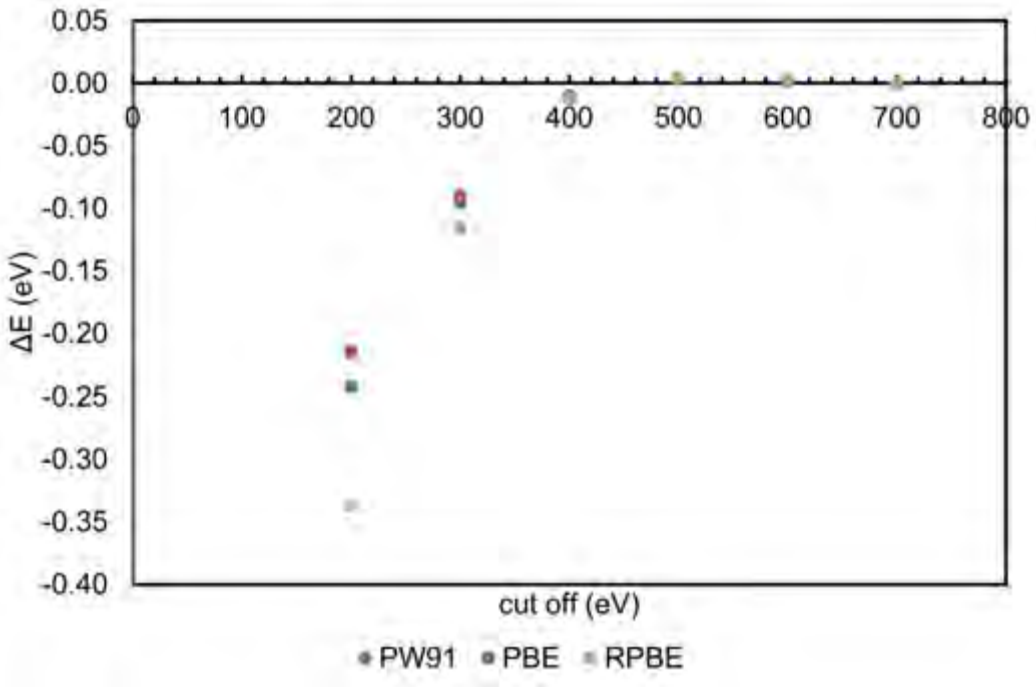


Figure D.2: Cut-off energy optimisation of bulk rutile $TiO_2$ calculated with different functionals.

**Lattice parameter optimisation**

Table D.1 presents the results of the automatic lattice parameter optimisation of bulk $TiO_2$ calculated with 3 different functionals.

Table D.1: Calculated lattice parameter of bulk $TiO_2$ and calculated percentage difference from the experimentally determined lattice parameter.

| | **Lattice parameter** | | | | |
|---|---|---|---|---|---|
| **Functional** | **a (Å)** | **% diff** | **c (Å)** | **% diff** | **c/a** |
| PW91 | 4.6040 | 0.44 | 2.9543 | 0.04 | 0.642 |
| PBE | 4.6090 | 0.50 | 2.9570 | 0.14 | 0.642 |
| RPBE | 4.6372 | 1.16 | 2.9724 | 0.66 | 0.641 |
| | | | | | |
| Experimental | 4.587 | - | 2.954 | - | 0.644 |

The lattice parameters predicted by the PW91 functional are closest to the experimentally determined values since they have the lowest percentage deviations. Therefore, the PW91 functional was chosen as the functional to proceed with for calculations on $TiO_2$.

## D.2 Optimisation of rutile $TiO_2$(110) surface

**Slab thickness optimisation**

Convergence of the binding energy of a single Pt atom on rutile $TiO_2$(110) surface as slab thickness is varied was used to determine the number of layers (tri-atomic layer) to describe the rutile $TiO_2$(110) surface. Figure D.3 shows variation of the binding energy of a Pt atom with variation in slab thickness and Figure D.4 shows variation of difference in binding energy between successive slab thickness (e.g. difference in binding energy between 3-layer slab and 2-layer slab, 4-layer slab and 3-layer slab, and so on). Single point energy calculations were used to calculate the binding energy.

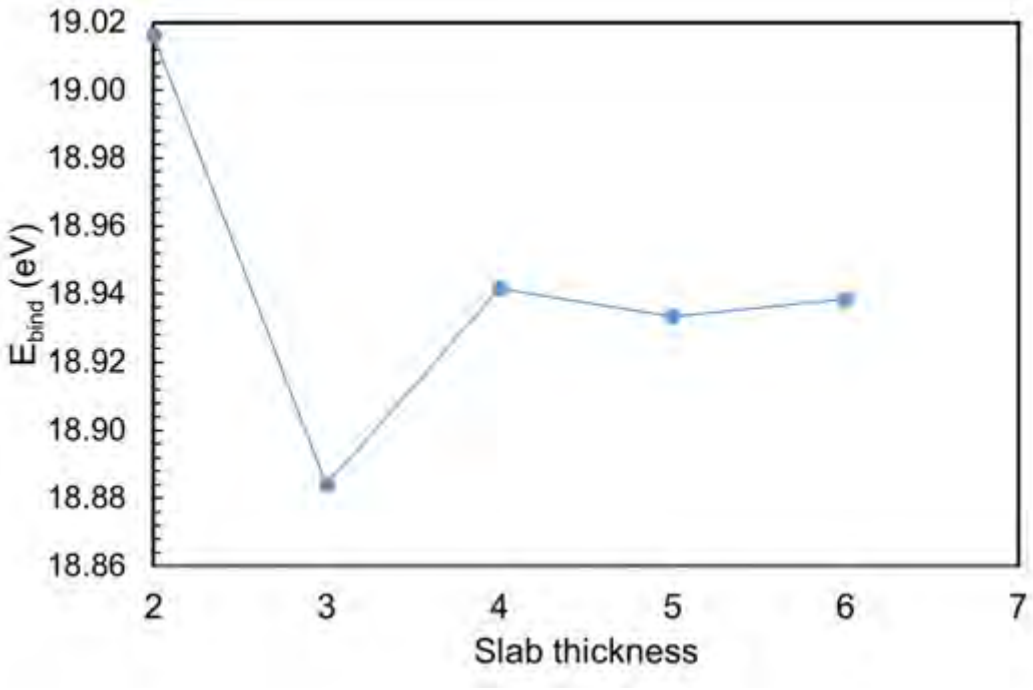


Figure D.3: Variation of binding energy of a Pt atom with slab thickness of the rutile $TiO_2$(110) surface.

Figure D.4 indicates that the difference in binding energy between successive slab thickness falls below 0.10 eV beyond a 4-layer (4 tri-atomic layer) thick slab. Also from Figure D.3 the binding energy for a single Pt atom is converged on a 4-layer thick slab. Therefore, in the present study the rutile $TiO_2$(110) surface is represented by a 4-layer (4 tri-atomic layer) thick slab.

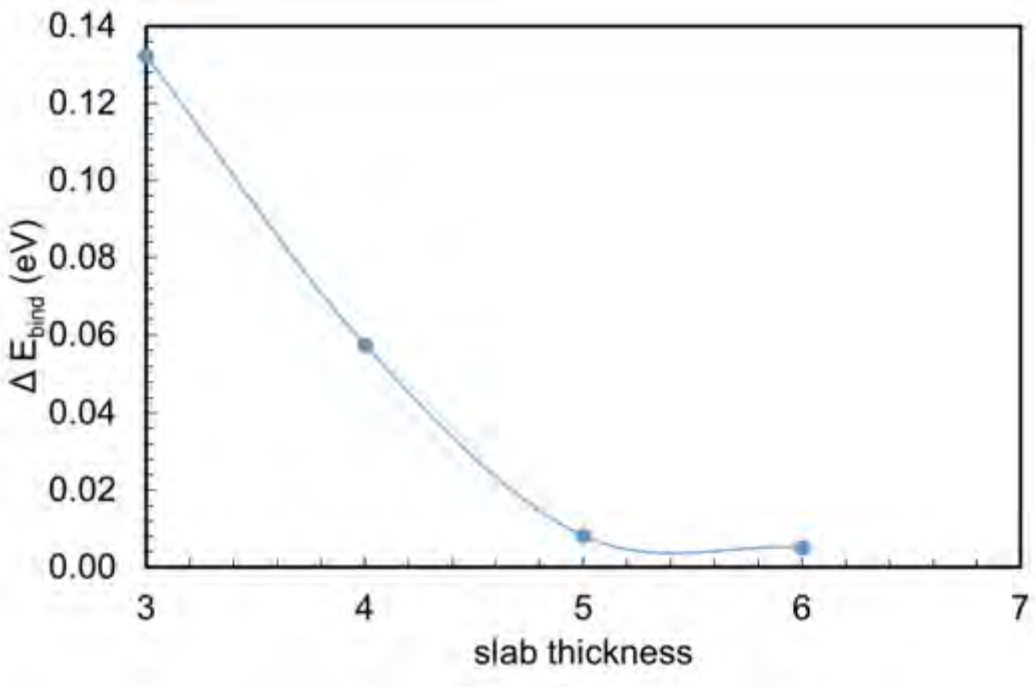


Figure D.4: Variation of difference in binding energy between successive slab thicknesses with slab thickness.

**U parameter optimisation**

The lattice parameter a and c varies with applied U parameter (see Figure D.5). In the present study the DFT+U method is used to get a good description of the peak in the band gap for the partially reduced $TiO_2$(110) surface, thus the lattice parameters used are those obtained for U = 0 eV. Morgan & Watson, (2007) have indicated that a compromise needs to be made with the choice of U since a U value which describes one feature well will not necessarily describe another feature equally well also. Thus, the U value chosen was based on description of the defect peak in the partially reduced $TiO_2$(110) surface not on how close the band gap is to the experimental value.

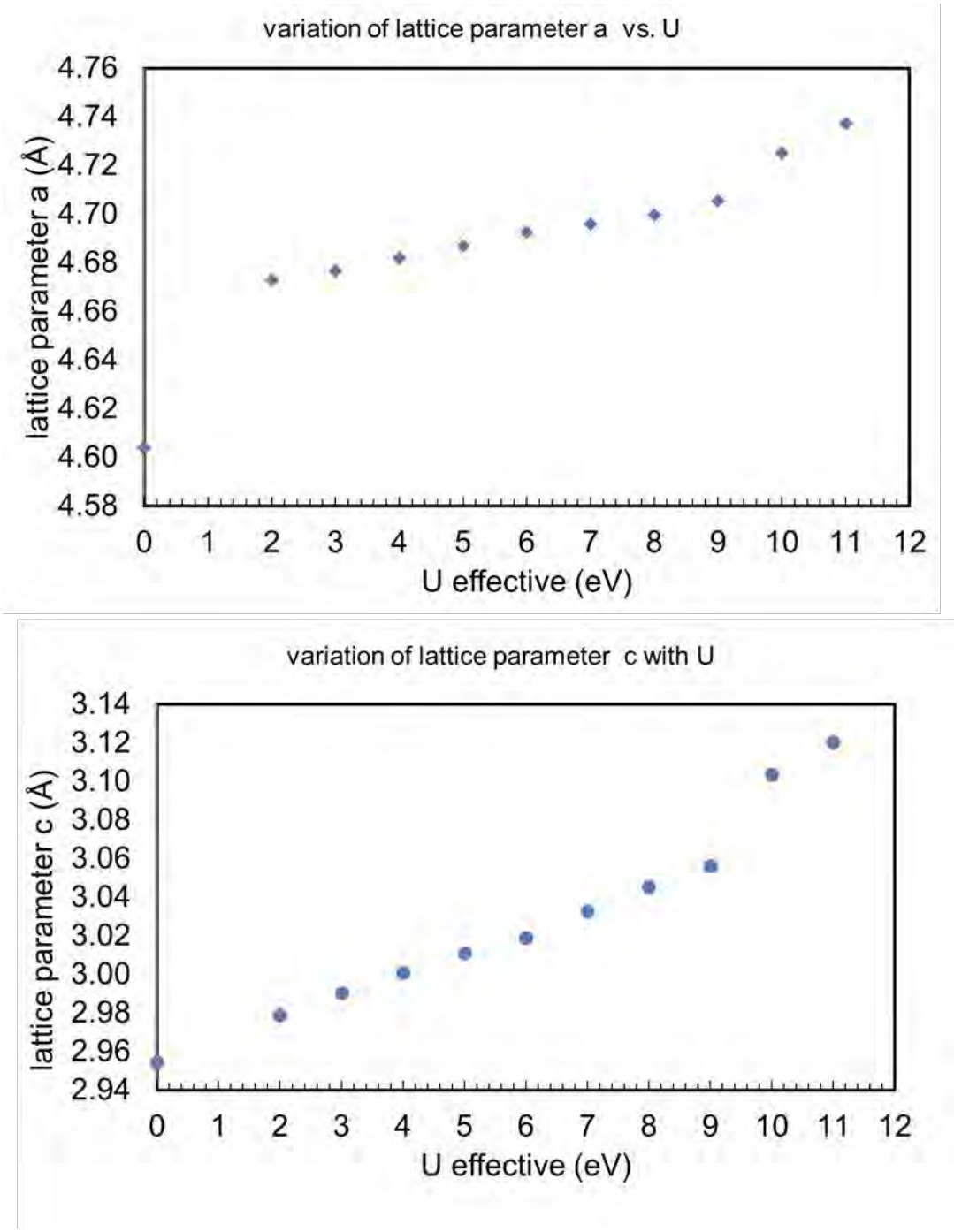


Figure D.5: variation of lattice parameter with U in the DFT+U method.

**U parameter for rutile $TiO_2$**

The band gap of rutile $TiO_2$ increases with increase in the U value (see Figures D.6 and D.7). However, for U values in the range 2-4 the increase in d-band gap as U increases is modest compared to other ranges of U. For U > 9 eV the band gap starts to decrease.

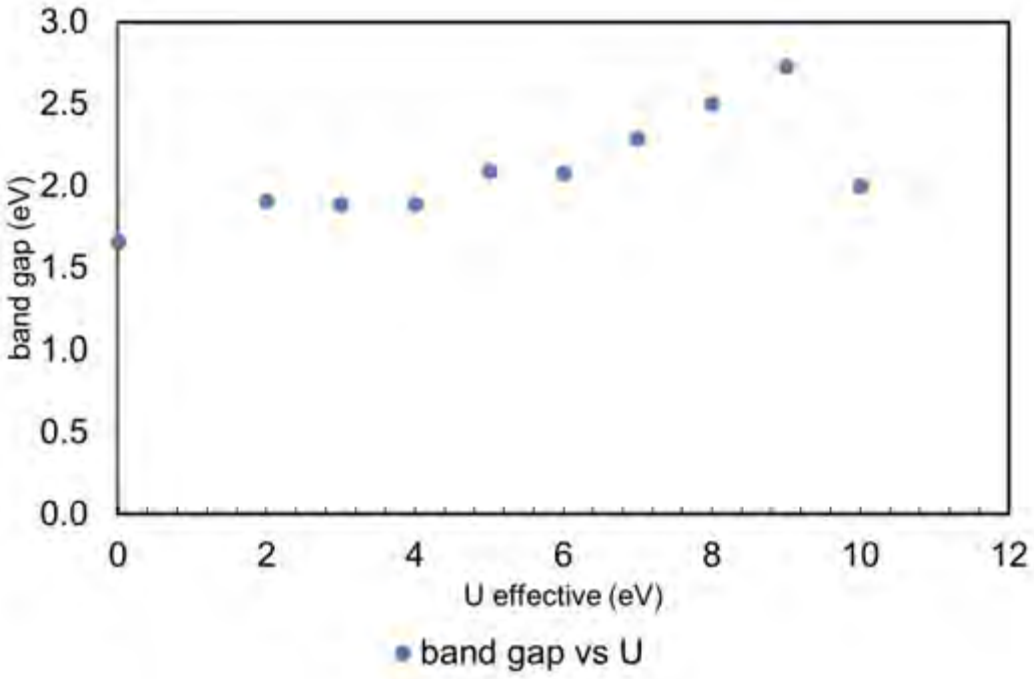


Figure D.6: band gap of rutile $TiO_2$ as the effective U parameter in the DFT+U method is varied.

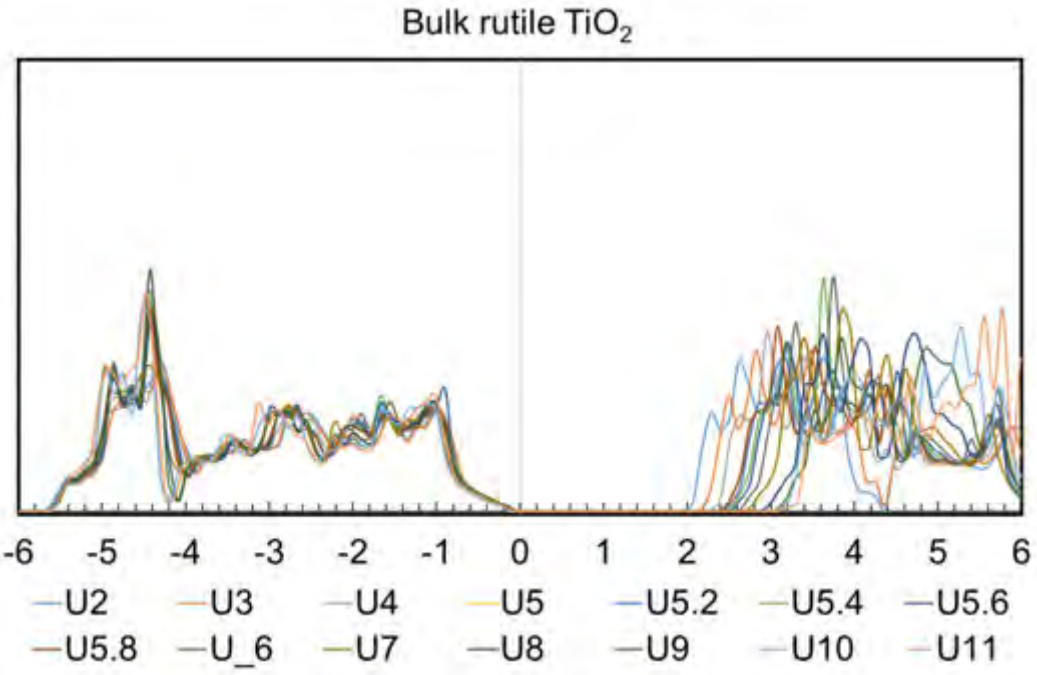


Figure D.7: PDOS of bulk $TiO_2$ as the effective U in the DFT+U method is varied.

The variation of the PDOS of the rutile $TiO_2$(110) surface with effective U parameter in the DFT+U method is presented in Figure D.8. It is observed that the band gap for the rutile $TiO_2$(110) surface is slightly smaller than that of bulk rutile $TiO_2$.

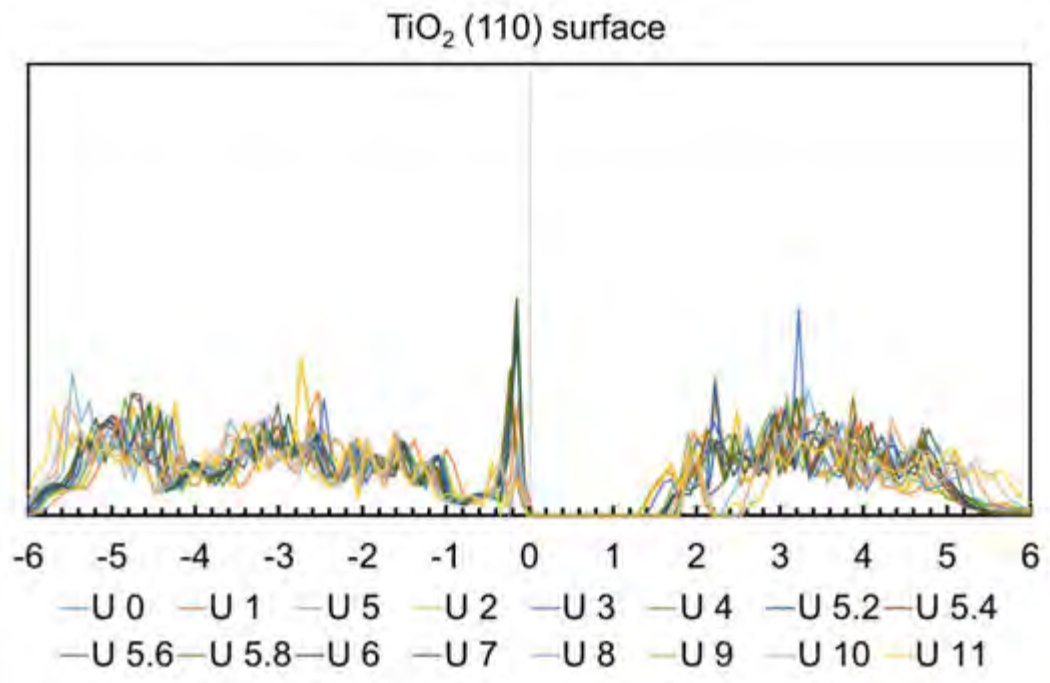


Figure D.8: PDOS of rutile $TiO_2$(110) surface as the effective U in DFT+U method is varied.

For the partially reduced $TiO_2$(110) surface the appearance of the defect peak in the band gap is dependent on the U parameter used. Morgan & Watson, (2007) have specified the range of U parameters which correctly position the defect peak in the band gap, the range is 4.2 eV ≤ U ≤ 6 eV. In addition, Morgan et al. (2009) found the same range of U (4.2 eV ≤ U ≤ 6 eV) applicable for the description of the PDOS of Nb and Ta doped rutile $TiO_2$, resulting in the defect peak due to dopants appearing in the band gap. For standard DFT the peak due to dopants is located at the bottom of the conduction band. In the present study, for the partially reduced $TiO_2$(110) surface, the hydroxylated $TiO_2$(110) surface and the Nb-doped partially reduced $TiO_2$(110) surface U = 4.5 eV was used as it falls within the range determined by Morgan & Watson, (2007).

**References**

Morgan, B.J. & Watson, G.W. (2007) A DFT+U description of oxygen vacancies at the $TiO_2$ rutile (110) surface. *Surf. Sci*. **601**, 5034-5041.

Morgan, B.J., Scanlon, D.O. & Watson, G.W. (2009) Small polarons in Nb- and Ta-doped rutile and anatase $TiO_2$. *J. Mater. Chem.* **19**, 5175-5178.

# Appendix E: $Pt_{32}Pd_6$ interaction with Nb-doped $TiO_2$(110) surface

A few select calculations for the interaction of the $Pt_{32}Pd_6$ cluster with the Nb doped stoichiometric $TiO_2$(110) surface and Nb-doped partially reduced $TiO_2$(110) surface were performed to investigate how the $Pt_{32}Pd_6$ cluster interacts with the Nb-doped $TiO_2$(110) surfaces. The aim of the study was to investigate if there will be preferential segregation of Pd towards the cluster support-interface when the $Pt_{32}Pd_6$ cluster is adsorbed onto Nb-doped $TiO_2$(110) surface. Therefore, not all unique facets of the $Pt_{32}Pd_6$ cluster interacting with the Nb-doped supports were investigated, but only a few and rearranged structures with Pd at the cluster support-interface were considered. The calculation time for geometry optimisation of the $Pt_{32}Pd_6$ cluster on the support is long, hence only a few select adsorption geometries were considered.

## E.1 Interaction of the $Pt_{32}Pd_6$ cluster with the Nb-doped $TiO_2$(110) surface

To investigate the binding of the $Pt_{32}Pd_6$ cluster on the Nb-doped $TiO_2$(110) surface, the bulk model of Nb-doped $TiO_2$(110) surface with Nb atoms located in the third tri-atomic layer was used. The (110) surface of rutile $TiO_2$ consists of two unique Ti sites, i.e. a six coordinated Ti atom ($Ti_{6C}$) and a five coordinated Ti atom ($Ti_{5C}$). The $Ti_{6C}$ atoms have bridging oxygen atoms above them, rendering them not exposed on the surface, whereas $Ti_{5C}$ atoms are exposed on the surface. In the present study it is desired to investigate the effect of the interaction of the dopant atoms with the supported $Pt_{32}Pd_6$ cluster. Therefore, Nb atoms are placed at the $Ti_{5C}$ sites.

The partially reduced Nb-doped $TiO_2$(110) surface slab was created by removing the central surface bridging oxygen atom of the *p*(6 × 3) unit cell as was done in chapter 6 to create the partially reduced surface. Removal of the central bridging oxygen atom results in a coverage of 1/18 ML or 0.06ML of monovacancy sites.

Owing to the size of the unit cell used in the present chapter, not all the unique facets of the $Pt_{32}Pd_6$ cluster were probed for interaction of the $Pt_{32}Pd_6$ cluster with the stoichiometric Nb-doped $TiO_2$(110). The binding energy of 3 different structures of the $Pt_{32}Pd_6$ cluster was calculated on the stoichiometric and partially reduced bulk model of Nb-doped $TiO_2$(110) surface to assess on which surface is the binding and formation energies most stable.

The 3 structures were as follows:

- **Structure one** is the lowest energy arrangement of the unsupported $Pt_{32}Pd_6$ cluster obtained in chapter 3 (mixed structure) interacting with the support via facet A.
- **Structure two** is the perfect core shell arrangement with 6 Pd atoms in the core and Pt atoms on the shell. The facet of approach to the support is through a hexagonal facet.
- **Structure three** is a rearranged form of structure two with three Pd atoms in the core and the other three Pd atoms at the corners of the hexagonal facet interacting with the support.

The other rearranged form of the $Pt_{32}Pd_6$ cluster investigated is the rearranged structure where the 6 Pd atoms occupies corners of the hexagonal facet interacting with the support. Interaction through facet B, facet C and facet E were also investigated on the partially reduced bulk model of the Nb-doped $TiO_2$(110) surface. Facet D was not investigated owing to its similarity to facet C.

## E2. Results for $Pt_{32}Pd_6$ interaction with stoichiometric and partially reduced Nb-doped $TiO_2$(110)

The optimised adsorption structures for the three probe structural arrangements of the $Pt_{32}Pd_6$ cluster on the bulk model of stoichiometric Nb-doped $TiO_2$(110) are presented in Figure E.1. The binding and formation energy of the three probe arrangements of the $Pt_{32}Pd_6$ cluster are exothermic on the stoichiometric bulk model of the Nb-doped $TiO_2$(110) surface. The formation energy of the $Pt_{32}Pd_6$ structure with facet C interacting with the support has the most exothermic formation energy of -3.85 eV. The perfect core shell arrangement with all 6 Pd atoms in the core has the least exothermic formation energy of -3.05 eV.

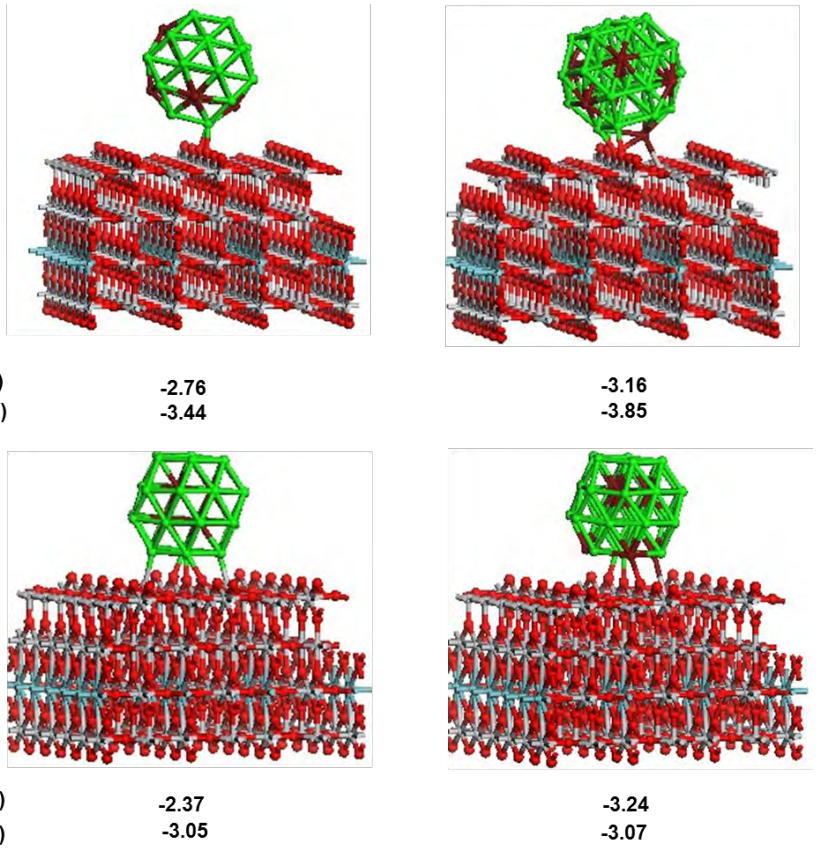


Figure E.1: Adsorption structures of the $Pt_{32}Pd_6$ cluster on the stoichiometric bulk model of Nb-doped $TiO_2$ (110) surface. Key: green represent Pt atoms, maroon Pd atoms, red oxygen atoms, grey titanium atoms and cyan Nb atoms.

Figure E.2 shows the adsorption structures of the $Pt_{32}Pd_6$ cluster on the bulk model of Nb-doped partially reduced $TiO_2$(110) with a vacant oxygen bridge atom on the surface. On the partially reduced bulk model of the Nb-doped $TiO_2$(110) surface, the binding and formation energies of the different arrangements of the $Pt_{32}Pd_6$ cluster are highly exothermic than on the stoichiometric bulk Nb-doped model of $TiO_2$(110) surface. This indicates that the surface oxygen bridge vacancy stabilises adsorption of the $Pt_{32}Pd_6$ cluster on the bulk model of Nb-doped $TiO_2$(110) surface compared to adsorption on the stoichiometric bulk model of Nb-doped $TiO_2$(110) surface. Thus, on Nb-doped $TiO_2$(110) surface, the surface oxygen bridge vacancy is vital for stabilising binding of the $Pt_{32}Pd_6$ cluster on the support.

The adsorption structures in the top row in Figure E.2 are for adsorption of the $Pt_{32}Pd_6$ cluster interacting with the support through three of the unique facets (facet A, facet B, facet C) of the lowest energy arrangement of the unsupported $Pt_{32}Pd_6$ cluster. The adsorption structure with approach through facet E is 0.03 eV less stable than the most stable formation energy structure which is through facet B, the 0.03 eV difference is negligible. Therefore, the adsorption structure of the $Pt_{32}Pd_6$ cluster through facet E which consists only of Pt atoms

anchoring the cluster to support was considered as the reference structure for the $Pt_{32}Pd_6$ cluster adsorbed on the bulk model of Nb-doped partially reduced $TiO_2$(110) surface. The adsorption structure with approach through facet E was also chosen as the reference structure since it would allow for comparison between the interacting facet with Pt atoms only and the interacting facet consisting of maximum number of Pd atoms.

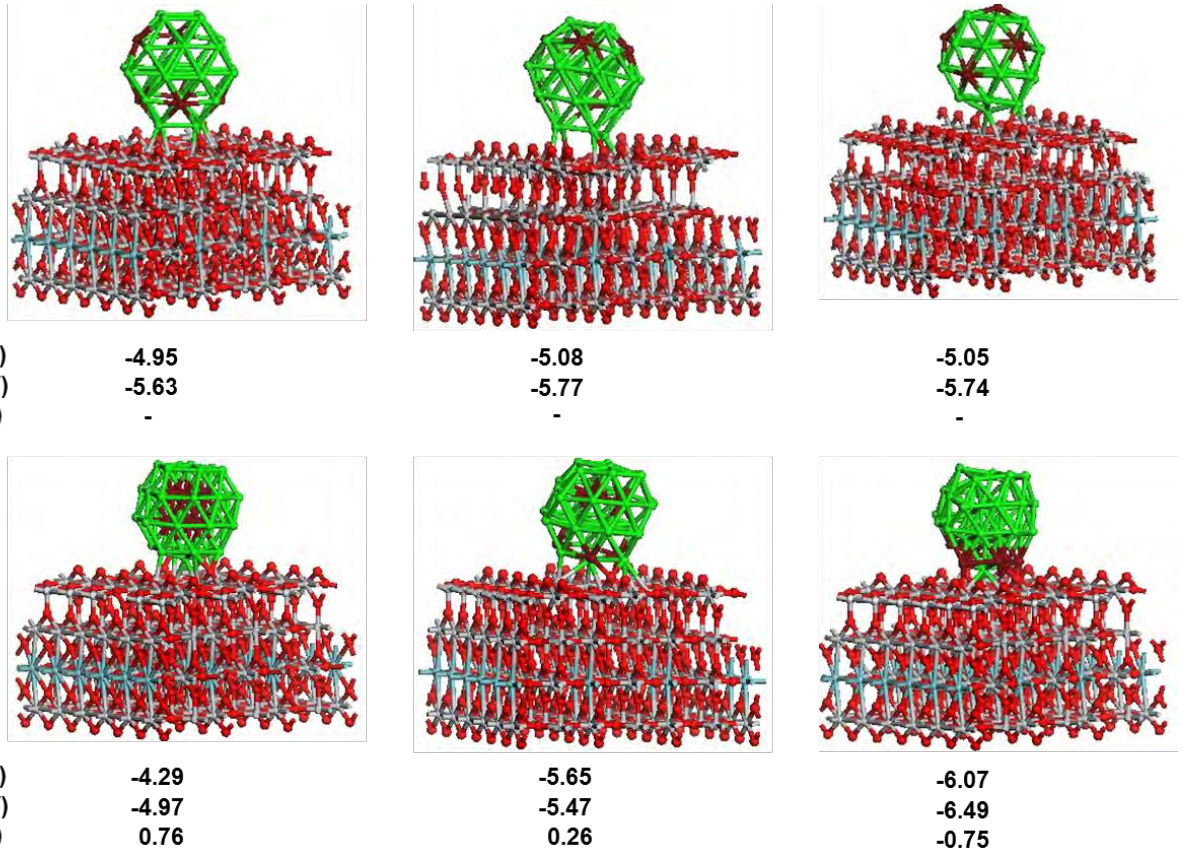


Figure E.2: Adsorption structures of the $Pt_{32}Pd_6$ cluster on the partially reduced Nb-doped $TiO_2$ (110) surface.

From Figure E.2 it is observed that the perfect core shell arrangement with all Pd atoms in the core has the least exothermic binding and formation energy together with the highest positive segregation energy. This is an indication that the perfect core shell arrangement is the least energetically favoured arrangement of the investigated arrangements in the present study on the bulk model of the Nb-doped partially reduced $TiO_2$(110). It will be recalled that the perfect core shell arrangement was the least energetically preferred arrangement of the unsupported $Pt_{32}Pd_6$ cluster, and on OH and COOH functionalised graphene.

Increasing the surface concentration of Pd atoms on the interacting facet while retaining some of Pd atoms in the core region results in a more exothermic formation energy than that of the perfect core shell arrangement. In addition, the arrangement results in a less endothermic

segregation energy compared to the perfect core shell arrangement. This observation corroborates the observations made in Chapter 3 where for the unsupported $Pt_{32}Pd_6$ cluster it was observed that arrangements which have some Pd atoms on the surface and some in the interior had more exothermic excess energies than the perfect core shell arrangement with all Pd atoms in the core. A similar observation was made for the $Pt_{32}Pd_6$ cluster supported on OH and COOH functionalised graphene in Chapter 5.

In the present chapter it is observed that the formation and binding energy of arrangements of the $Pt_{32}Pd_6$ cluster which have all Pd atoms on the surface are more exothermic than of the structure with 3 surface anchoring Pd atoms and other 3 Pd atoms in the core. These observations further strengthen the conclusion that Pd prefers to be on the surface than in the interior while alloyed with Pt irrespective of the presence and type of support.

The rearranged structure of the $Pt_{32}Pd_6$ cluster with all 6 Pd atoms on the hexagonal facet interacting with the bulk model of the Nb-doped partially reduced $TiO_2$(110) surface has a highly exothermic formation and binding energy than the reference structure for the $Pt_{32}Pd_6$ cluster. This structure also has a negative segregation energy of -0.75 eV which indicates that it is energetically more stable than the reference structure. In addition, this arrangement has a distorted truncated octahedron shape compared to the other investigated arrangements on the bulk model of the Nb-doped partially reduced $TiO_2$(110) surface which retains their truncated octahedron shape.